THE UNIVERSITY of ADELAIDE

Constraints on the timing and physical conditions of shale detachment faulting using natural examples

Rowan Hansberry

Geology and Geophysics
School of Physical Sciences
The University of Adelaide

October 2015

Table of Contents

Abstract

A detachment can be defined as a horizon or zone, centimetres to kilometres in thickness, which mechanically decouples deforming rocks or sediments from underlying, non-deforming sequences. Detachment zones accommodate thin-skinned deformation in fold and thrust belts across a variety of tectonic settings. Fold-thrust belts exhibit considerable variation in structural styles and vergence direction depending on the type (salt, overpressured shale, low-angle faults) and characteristics (thickness, strength, dip and dip direction) of the detachment horizon(s). Shale detachments have been previously described as largely ductile in their mechanism of deformation, however, increasing resolution of seismic imaging and understanding of these zones suggest brittle deformation may have a significant role in their internal behaviour and the deformation of overlying fold and thrust belts. Despite the critical influence on the structural style of fold and thrust belts, the precise nature by which detachments control deformation in FTBs is poorly constrained. Dependence on seismic imaging and other indirect or low-resolution study methods has resulted from the lack of outcropping shale detachment zones for detailed study. This study presents an investigation of the structural style and deformational mechanisms of a newly described shale detachment zone in the Khao Khwang Fold and Thrust Belt in Central Thailand, which is an exceptionally well-exposed shale detachment in the Sap Bon Formation shales. This is integrated with new data and structural interpretation from the Chrystalls Beach Complex (accretionary wedge) in southern Otago, New Zealand, and the Osen Røa thrust sheet (collisional) in the Norwegian Caledonides for comparison with results from the larger study in the Khao Khwang FTB.

Detailed field mapping and construction of cross-sections through the detachment zone reveals the deformational style and brittle nature of deformation. In the Sap Bon Formation detachment zone, cross-sections were sub-divided into structural domains based on the style and complexity of deformation. In particular, the 'proximal domain' located directly above the Eagle Thrust exhibited the most heavily deformed shales, and is interpreted to be acting as a detachment zone. The proximal domain is deformed in a continuous vs. discontinuous deformational style where the distribution of contrasting competency domains has governed the distribution of deformational mechanisms. Weak phases (incompetent domains composed of fine-grained shales) have localised strain and host shear-zone like faults which form an anastomosing network through the detachment zone. These shear zones characterise a three-dimensionally complex fault system in the proximal domain, surrounding three-dimensional lenses of competent rock. Extreme structural heterogeneity occurs both in-section and laterally through the proximal domain.

Analysis of the geochemistry of the Sap Bon Formation detachment zone through use of illite crystallinity, carbon and oxygen stable isotopes, vitrinite reflectance, and total organic carbon content analyses reveals a peak deformational temperature of between 160-220 °C. Higher illite crystallinity is observed in the continuously deformed incompetent domains, and is found to be directly linked to the finite strain. Finite strain throughout the Sap Bon Formation detachment zone (and the two comparison field areas) is shown to exhibit a strong correlation to $KI_{(CIS)}$ values, suggesting strain rate may play have a key influence in the development of illite crystallinity, as well as the prograde transformation of clay minerals.

Carbon and oxygen stable isotope mapping across the structural cross sections reveals fluid flow pathways through the evolution of the complex fault zone which constitutes the Sap Bon Formation detachment zone. Results indicate the basal Eagle Thrust, as well as other large faults constituted the primary source of permeability during orogenesis, once rock-matrix permeability had been lost. Oxygen stable isotope values from calcite mineralisation along these major structures are frequently as negative as -16.00 $\delta^{18}O$, indicating relatively hotter precipitating fluid temperatures that the background value of calcite mineralisation in the Sap Bon Formation (~10-12 $\delta^{18}O$). Burial > diagenetic > pre thrust deformation > orogenic association of carbon and oxygen stable isotope results and clay mineralogy provide a conceptual model for the development of the Sap Bon Formation through burial and into the formation of the detachment zone. The timing of this evolution is constrained by K-Ar illite age determinations, with burial occurring no later than 262±5.4 Ma, while faulting related to the onset of orogenesis began by 230±4.6 Ma, with deformation continuing as late as 208±4.1 Ma.

Declaration

I certify that this work contains no material which has been accepted for the award of any other degree or diploma in my name, in any university or other tertiary institution and, to the best of my knowledge and belief, contains no material previously published or written by another person, except where due reference has been made in the text. In addition, I certify that no part of this work will, in the future, be used in a submission in my name, for any other degree or diploma in any other university of tertiary institution without the prior approval of the University of Adelaide and where applicable, any partner institution responsible for the joint award of this degree.

I give consent to this copy of my thesis when deposited in the University Library, being made available for loan and photocopying, subject to the provisions of the Copyright Act 1968.

The author acknowledges that the copyright of published works contained within this thesis resides with the copyright holder(s) of those works.

I also give permission for the digital version of my thesis to be made available online, via the University of Adelaide's digital research repository, the Library Search, and also through search engines, unless permission has been granted by the University of Adelaide to restrict access for a period of time.

Rowan Hansberry

Journal Articles

Hansberry, R. L., King, R., Collins, A. S., & Morley, C. K. 2014. Complex structure of an upper-level shale detachment zone: Khao Khwang fold and thrust belt, Central Thailand. *Journal of Structural Geology*, *67*, 140-153.

Hansberry, R. L., Collins, A. S., King, R. C., Morley, C. K., Giże, A. P., Warren, J., Löhr, S. C., & Hall, P. A. 2015. Syn-deformation temperature and fossil fluid pathways along an exhumed detachment zone, khao khwang fold-thrust belt, Thailand. *Tectonophysics*, *655*, 73-87.

Arboit, F., Collins, A. S., King, R., Morley, C. K., & **Hansberry, R**. 2014. Structure of the Sibumasu–Indochina collision, central Thailand: A section through the Khao Khwang Fold and thrust belt. *Journal of Asian Earth Sciences*, *95*, 182-191.

Statement of Authorship

Title of Paper	Complex Structure of an upper-level shale detachment zone: Khao Khwang fold and thrust belt, Central Thailand
Publication Status	☑ Published ☐ Accepted for Publication ☐ Submitted for Publication ☐ Publication Style
Publication Details	Hansberry, Rowan Lawrence, et al. "Complex structure of an upper-level shale detachment zone: Khao Khwang fold and thrust belt, Central Thailand." Journal of Structural Geology 67 (2014): 140-153.

Principal Author

Name of Principal Author (Candidate)	Rowan Hansberry		
Contribution to the Paper	Completed fieldwork, collected and interpreted data, collected, prepared and analysed samples wrote manuscript, acted as corresponding author.		
Overall percentage (%)	80		
Signature		Date	15/10/15

Co-Author Contributions

By signing the Statement of Authorship, each author certifies that:

i. the candidate's stated contribution to the publication is accurate (as detailed above);

ii. permission is granted for the candidate in include the publication in the thesis; and

iii. the sum of all co-author contributions is equal to 100% less the candidate's stated contribution.

Name of Co-Author	Alan Collins		
Contribution to the Paper	Supervised fieldwork, aided in collection of data and samples, helped with data interpretation and manuscript revision.		
Signature		Date	15/10/15

Name of Co-Author	Rosalind King		
Contribution to the Paper	Supervised fieldwork, aided in collection of data and samples, helped with data interpretation and manuscript revision.		
Signature		Date	15/10/15

Name of Co-Author	Christopher Morley		
Contribution to the Paper	Supervised fieldwork, aided in collection of data, helped with data interpretation and manuscript revision.		
Signature		Date	28/08/2015

Statement of Authorship

Title of Paper	Syn-Deformation Temperature and Fossil Fluid Pathways along an Exhumed Detachment Zone, Khao Khwang Fold-Thrust Belt, Thailand
Publication Status	☑ Published ☐ Accepted for Publication ☐ Submitted for Publication ☐ Publication Style
Publication Details	Hansberry, Rowan L., et al. "Syn-Deformation Temperature and Fossil Fluid Pathways along an Exhumed Detachment Zone, Khao Khwang Fold-Thrust Belt, Thailand." Tectonophysics (2015).

Principal Author

Name of Principal Author (Candidate)	Rowan Hansberry		
Contribution to the Paper	Completed fieldwork, collected and interpreted data, collected, prepared and analysed samples wrote manuscript, acted as corresponding author.		
Overall percentage (%)	80		
Signature		Date	15/10/15

Co-Author Contributions

By signing the Statement of Authorship, each author certifies that:

i. the candidate's stated contribution to the publication is accurate (as detailed above);

ii. permission is granted for the candidate in include the publication in the thesis; and

iii. the sum of all co-author contributions is equal to 100% less the candidate's stated contribution.

Name of Co-Author	Alan Collins		
Contribution to the Paper	Supervised fieldwork, aided in collection of data and samples, helped with data interpretation and manuscript revision.		
Signature		Date	15/10/15

Name of Co-Author	Rosalind King		
Contribution to the Paper	Supervised fieldwork, aided in collection of data and samples, helped with data interpretation and manuscript revision.		
Signature		Date	15/10/15

Name of Co-Author	Christopher Morley		
Contribution to the Paper	Supervised fieldwork, aided in collection of data, helped with data interpretation and manuscript revision.		
Signature		Date	28/08/2015

Name of Co-Author	John Warren		
Contribution to the Paper	Provided discussion and insight in the preparation of the manuscript.		
Signature		Date	20/09/15

Name of Co-Author	Andy P. Giże		
Contribution to the Paper	Completed preparation and analysis of samples.		
Signature		Date	15/10/15

Name of Co-Author	Stefan C. Löhr		
Contribution to the Paper	Assisted in preparation and analysis of samples, helped with interpretation of results.		
Signature		Date	28/09/2015

Name of Co-Author	Tony A. Hall		
Contribution to the Paper	Assisted in analysis of samples.		
Signature		Date	19/10/15

Statement of Authorship

Title of Paper	Strain and Competency Contrasts in Shale Detachment Zones: An Examination of the Relationship between Finite Strain and Illite Crystallinity
Publication Status	☐ Published ☐ Accepted for Publication ☑ Submitted for Publication ☐ Publication Style
Publication Details	Hansberry, Rowan L., et al. "Syn-Deformation Temperature and Fossil Fluid Pathways along an Exhumed Detachment Zone, Khao Khwang Fold-Thrust Belt, Thailand." Tectonophysics (2015).

Principal Author

Name of Principal Author (Candidate)	Rowan Hansberry		
Contribution to the Paper	Completed fieldwork, collected and interpreted data, collected, prepared and analysed samples wrote manuscript, acted as corresponding author.		
Overall percentage (%)	80		
Signature		Date	15/10/15

Co-Author Contributions

By signing the Statement of Authorship, each author certifies that:

i. the candidate's stated contribution to the publication is accurate (as detailed above);

ii. permission is granted for the candidate in include the publication in the thesis; and

iii. the sum of all co-author contributions is equal to 100% less the candidate's stated contribution.

Name of Co-Author	Alan Collins		
Contribution to the Paper	Supervised fieldwork, aided in collection of data and samples, helped with data interpretation and manuscript revision.		
Signature		Date	15/10/15

Name of Co-Author	Rosalind King		
Contribution to the Paper	Supervised fieldwork, aided in collection of data and samples, helped with data interpretation and manuscript revision.		
Signature		Date	15/10/15

Name of Co-Author	Christopher Morley		
Contribution to the Paper	Supervised fieldwork, aided in collection of data, helped with data interpretation and manuscript revision.		
Signature		Date	28/08/2015

Name of Co-Author	Stefan C. Löhr		
Contribution to the Paper	Assisted in preparation and analysis of samples, helped with interpretation of results.		
Signature		Date	28/09/2015

Name of Co-Author	Tony A. Hall		
Contribution to the Paper	Assisted in analysis of samples.		
Signature		Date	19/10/15

Statement of Authorship

Title of Paper	K-Ar illite age constraints on the formation of a shale detachment zone
Publication Status	☐ Published ☐ Accepted for Publication ☐ Submitted for Publication ☑ Publication Style
Publication Details	Hansberry, Rowan L., et al. "Syn-Deformation Temperature and Fossil Fluid Pathways along an Exhumed Detachment Zone, Khao Khwang Fold-Thrust Belt, Thailand." Tectonophysics (2015).

Principal Author

Name of Principal Author (Candidate)	Rowan Hansberry		
Contribution to the Paper	Completed fieldwork, collected and interpreted data, collected, prepared and analysed samples wrote manuscript, acted as corresponding author.		
Overall percentage (%)	80		
Signature		Date	15/10/15

Co-Author Contributions

By signing the Statement of Authorship, each author certifies that:

i. the candidate's stated contribution to the publication is accurate (as detailed above);

ii. permission is granted for the candidate in include the publication in the thesis; and

iii. the sum of all co-author contributions is equal to 100% less the candidate's stated contribution.

Name of Co-Author	Horst Zwingmann		
Contribution to the Paper	Completed K-Ar analysis of samples, contributed towards manuscript completion and reviewed manuscript		
Signature		Date	15/10/15

Name of Co-Author	Alan Collins		
Contribution to the Paper	Supervised fieldwork, aided in collection of data and samples, helped with data interpretation and manuscript revision.		
Signature		Date	15/10/15

Name of Co-Author	Rosalind King		
Contribution to the Paper	Supervised fieldwork, aided in collection of data and samples, helped with data interpretation and manuscript revision.		
Signature		Date	15/10/15

Name of Co-Author	Christopher Morley		
Contribution to the Paper	Supervised fieldwork, aided in collection of data, helped with data interpretation and manuscript revision.		
Signature		Date	28/08/2015

Name of Co-Author	Stefan C. Löhr		
Contribution to the Paper	Assisted in preparation and analysis of samples, helped with interpretation of results.		
Signature		Date	28/09/2015

Acknowledgements

It's done. I'd like to say a huge thank you to my two brilliant supervisors Alan Collins and Rosalind King for all their help over the last three (and a bit) years. This thesis would not have been possible without their guidance, motivation (particularly in the early stages), and encouragement. They have both had a massive hand in helping me to develop the research and writing skills necessary to reach this point.

Secondly, I'd like to thank Christopher Morley, who has essentially been an extra supervisor, organising and mentoring my field work, providing an excellent introduction to Thailand, as well as continued discussion and guidance in research directions and manuscript preparation, along with his direct contributions to the work. I'd also like to acknowledge the staff, in particular Waitat Narabolobh, of Siam City Cement Company Limited for their generous access to field sites, and assistance in moving around their quarries.

I would like to thank all of the laboratory staff and collaborators at Adelaide Microscopy, the Department of Resource Management at the University of Melbourne, The Sprigg Geobiology Centre at the University of Adelaide, CSIRO ESRE in Perth, and the Department of Geosciences at the University of Oslo. With special thanks to Stefan Löhr for a great deal of technical assistance and discussion, Tony Hall, Russell Drysdale, Horst Zwingmann, Aoife McFadden, Ben Wade, Bjørn Larsen and Roy Gabrielsen .

I would like to thank Laurel Goodwin for a huge amount of help reviewing my first paper, and all the anonymous reviewers for helpful and constructive feedback which greatly improved the quality of my manuscripts.

I'd also like to thank my colleges and fellow PhD and honours students: Francesco and Rommy for being excellent and entertaining field work buddies to help survive blistering days in Thai quarries, Diana, Rob, Jeremy, Ben, Funny, Chris, Ouyang, and Jack for being great office mates over the last three years, and the S3 gang for making a wonderful research group and providing some memorable Christmas parties. As well as the other PhD, honours, and staff friends I've had along the way: Adam, Bonnie, Kat, Katherine, Lachy, Josh, Gilby, Alex, Donnelly, Morgan, Laura, Kieran, James, Romana, Stijn, Alec, John, Simon, Karin, Juraj, and all the people I've forgotten.

Finally, I'd like to thank my wonderful family for their love and support. My partner Georgy, the whole Falster family, my Grandparents, my Dad, and most of all, my extremely supportive Mum without whom this would not have been possible.

Chapter 1

1. What is a detachment zone and why is it important?

A detachment zone is defined as a zone or horizon which mechanically decouples deforming rocks or sediments from underlying, non-deforming sequences or basement. The term detachment is most commonly associated with a basal detachment, which delineates a deforming fold-thrust belt (FTBs) from the basement in thin-skinned tectonics (Davis et al., 1983; Dahlen et al., 1984). However, detachment zones satisfying the above definition also occur within deforming sequences, and often at multiple levels (Fig 1.) (e.g. Sherkati et al., 2005; Briggs et al., 2006). These intra-orogen detachments mechanically decouple rocks or packages of rocks with differing styles or amounts of deformation, often they may be linked by ramps, with separate detachment zones forming floor and roof thrusts of duplexes (Briggs et al., 2006; Watkins et al., 2014). Detachment zones acting as large scale slip-surfaces to accommodate a difference in shortening, may also accommodate significant shortening internally (Davis et al., 1983; Dahlen et al., 1984). Fold-thrust belts vary in structural style depending on the tectonic setting (passive margin, ocean-continent collision, continent-continent collision), but thin-skinned fold-thrust belts also vary significantly in structural style and vergence with the nature the detachment zone (or zones) which accommodate deformation (Fig 2) (Davis et al., 1983; Rowan et al., 2004; Simpson, 2009). Detachment zones are therefore a critical control on the geometry of FTBs, and an understanding of how they influence this geometry has implications for hydrocarbon exploration, through the influences that detachment zone characteristics may have on the formation of petroleum-trapping structures, and hydrocarbon migration pathways (Faulkner et al., 2010). Despite this importance the deformational mechanisms and precise nature by which shale detachment zones control deformation in FTBs is poorly constrained, and still an area of considerable speculation (van Rensbergen and Morley, 2003; Maloney et al., 2010; Morley et al., 2014). Present-day active basal detachment zones are usually located in inaccessible, submarine regions. The shallow portions (with sub surface depths of less than 1 km) of active detachment zones in accretionary wedges have been penetrated by the Integrated Ocean Drilling Program (IODP; e.g. Moore, et al., 2005; Screaton et al., 2009). These IODP studies are extremely valuable, and provide the foundation of our understanding of active accretionary complexes and the deformation processes that occur above detachment zones. However, there is no equivalent well data for basal detachments associated with other types of FTBs, such as those associated with the gravitational deformation of deltas (e.g. Bight Basin, Australia), and early stage continent-continent, or continent-arc collision zones (e.g. offshore Timor and Papua New Guinea). Detachment zone characteristics will differ significantly in different tectonic settings (Morley et al., 2011). Consequently it is unknown if the understandings gained of the nature of accretionary complex detachments developed from IODP studies can be directly applied to other FTB settings. Therefore, the major aim of this project is to investigate the characteristics of detachment zones in shales in order to understand the deformational processes in FTBs formed in all types of tectonic settings.

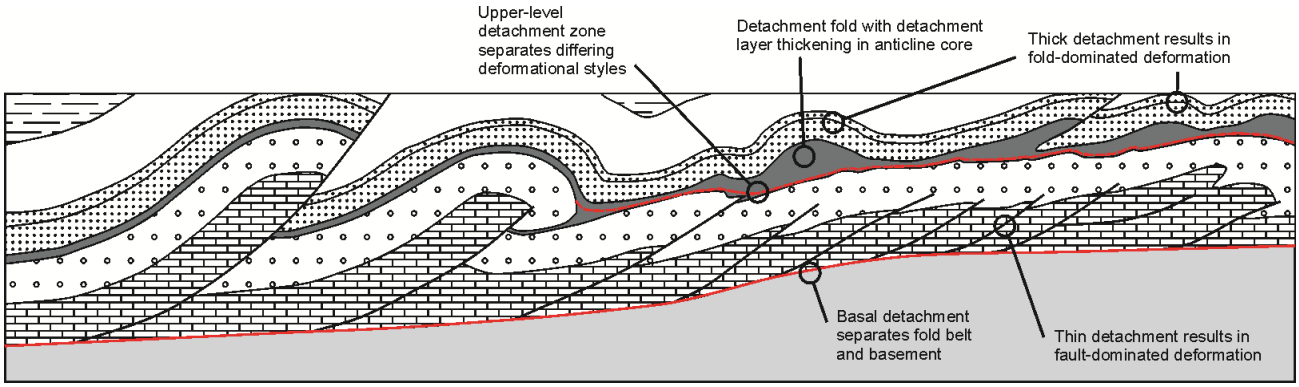

Fig 1. Schematic cross section of a think-skinned fold-thrust belt exhibiting multiple detachment levels.

2. Classification of shale detachments

Basal shale detachment zones tend to be thicker and accommodate greater shortening than 'upper-level' detachments within the deforming sequence, though the controlling factor on a detachment zones thickness and spatial extent is simply the extent of the relatively weaker lithological unit in which the detachment zone occurs (Morley et al., 2011). Therefore, detachment zones may vary from thin (cm) horizons to kilometre thick zones (Davis et al., 1983; Morley et al., 2011). Generally, shale detachment zones can be divided into four main categories: 1) compacted shales that act as zones or horizons of weakness due to the inherent material weakness of shale comparative to adjacent rocks, 2) compacted shale with high overpressure, 3) thin undercompacted shales of metres to tens of metres thickness with high overpressures and 4) thick undercompacted shales of 100s of metres to kilometres thickness with high overpressures (Morley et al., 2011). Shale detachments are widely associated with fluid overpressure, which can result from high sedimentation rates and low permeability that prevents water from escaping pore space during compaction (disequilibrium compaction), or hydrocarbon generation (van Rensbergen et al., 1999; Cobbold et al., 2009; Tingay et al., 2009).

3. Shale mobility

Detachment zones in shale have long been associated with a paradigm of "mobile shale", having broad similarities in material properties (e.g. viscosity), and structural effect (e.g. diapir formation), to mobile salt (Morley and Guerin, 1996; van Rensbergen et al., 1999). While this paradigm has shifted in recent years towards brittle deformation in shale detachment zones, the existence of relatively mobile shale, particularly in deep, under-compacted passive margin settings such as the Niger Delta is well established (Bilotti and Shaw, 2005; Corredor et al., 2005; Cobbold et al., 2009). However, as the quality of seismic imaging and understanding of the chemical diagenesis of shales has increased, it appears that mobile shale has been over interpreted in the past (van Rensbergen and Morley, 2003; Maloney et al., 2010). The most recent work suggest that while shales are in fact likely capable of viscous flow, large mobile masses and associated structures such as diapirs like those found in salt are improbable (Maloney et al., 2010). This is discussed further in chapter 2. Thickness variations and chaotic 2D seismic reflectors likely represent second

order (and smaller) faults, with complex geometries potentially involving a mixture of brittle and ductile deformational mechanisms (Morley, 2003; van Rensbergen and Morley, 2003; Maloney et al., 2010; Morley et al., 2011).

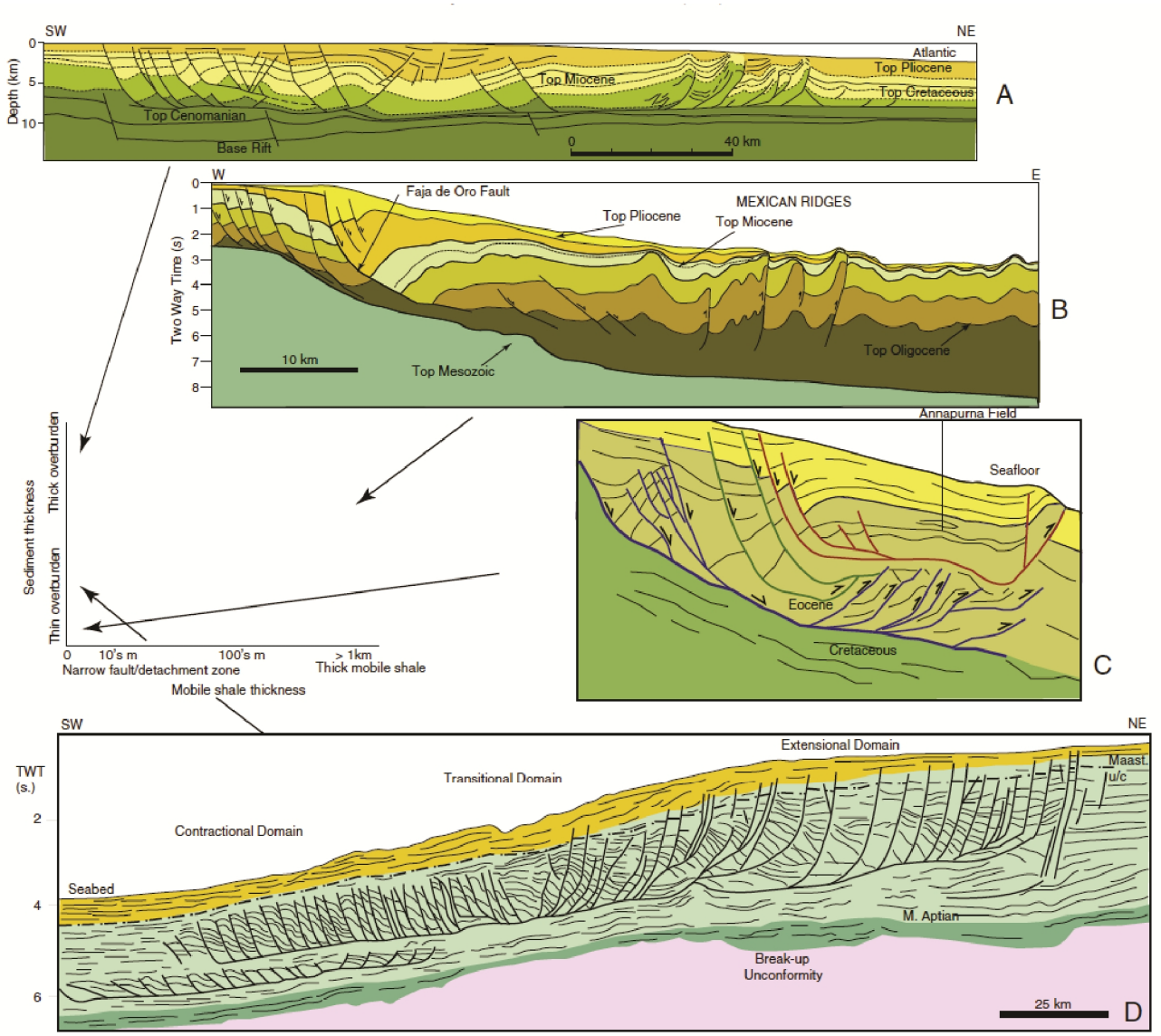

Fig 2. Range of styles of deformation in fold thrust belts associated with shale detachment zones. A = Amazon Fan, B = Mexican Ridges, C = Krishna-Godavari Basin, India, D = Orange Basin, and plot of structural styles and association to the thickness of detachment and of overburden (from Morley et al., 2011).

4. Fault zones and shear zones in shales

4.1 Deformation in fine grained rocks and sediments

Given the increasing role of brittle deformation attributed to deforming shale detachment zones, and the likelihood of mixed brittle/ductile deformational behaviour, it is important to assess not only the material properties and conditions of deforming shales, but also how the inherent heterogeneity of these attributes in shales can influence deformation. The term shear zone is often applied to higher (greenschist to granulite)

grade deformation, though similar foliation patterns are frequently observed in sub-greenschist facies deformation, as well as in fault gouge, and poorly lithified sediments (Maltman, 1994; Collins et al., 2000; Goodwin and Tikoff, 2002). Goodwin and Tikoff (2002) suggest that these are fundamental consequences of deforming heterogeneous rocks or sediments. In poorly lithified or incohesive sediments, shear foliations are typically defined by the alignment of clay minerals through either rotation of minerals or recrystallization in a common alignment (Wintsch, 1985; Agar et al., 1989; Labaume et al., 1997; Goodwin and Tikoff, 2002). Compositional banding is also frequently noted in many rock types including shales, in which this can be accommodated by particulate flow or with the aid of low-grade metamorphism through diffusive mass transfer (Rutter et al., 1986; Agar et al., 1989). Regardless of mechanism or the media in which it takes place, compositional banding is generally characterised by the segregation of the weakest phase: typically biotite and muscovite in supra-greenschist facies rocks, and clay minerals in sedimentary rocks or incoherent sediments (Goodwin and Tikoff, 2002). The banding of rheological different media in rocks is present in deformation of many rock types at a large range of conditions, and is likely independent of these conditions; it is probably a fundamental mechanism of deformation (Goodwin and Tikoff, 2002).

4.2 Competency contrast

Compositional banding as a result of deformation produces contrasting competencies; however, competency contrasts are also intrinsic to most rock types. Competency refers to the relative mechanical behaviour of a given media, in deforming rocks these often referred to as competent and incompetent domains (Goodwin and Tikoff, 2002). This can encompass many deformational processes, and similar mechanical behaviour can be observed in rocks deforming by vastly different deformational mechanisms (e.g. crystal-plastic flow, particulate flow, grain-boundary sliding, diffusion processes) (Goodwin and Tikoff, 2002). Deforming rock or sediment sequences composed of competency domains must be treated as interrelated systems, and the competency of individual domains can be affected by not only its internal properties, but the properties of adjacent domains, as well as changes through time (Turner and Weiss, 1963; Goodwin and Tikoff, 2002; Faulkner et al., 2010).

Competency domains can have a variety of characteristics and contributing parameters (Goodwin and Tikoff, 2002):

- Competency domains may be mono- or poly-minerallic, with relative competencies potentially depending on the bulk composition and/or distribution of mineralogy.

- Competency will depend partially on a domain's orientation to local stress, as well as internal orientation of minerals and structures.

- Material and orientation properties of a competency domain may change through time, as deformation can lead to changes in mineralogy (i.e. during diagenesis and/or metamorphism), and the orientation of

competency domains and their internal features will change as a deforming sequence evolves.

It is therefore possible for a feedback loop to exist between competency and deformation, as the former will influence the latter, which, in turn, influences many of the properties affecting the magnitude and distribution of competency contrast (Goodwin and Tikoff, 2002). Progressive segregation of incompetent phases within a deforming media into compositional banding (as described above) results in increasing incompetency in incompetent domains and partitioning of strain into them (Jordan, 1987). Generally materials with significant inherent competency contrast (such as shales) will therefore tend to develop proportionately highly partitioned deformation (Jordan, 1987; Goodwin and Tikoff, 2002).

High competency contrast between domains results in strain-rate incompatibilities at their boundaries, as materials of differing competency will deform at different strain rates (Goodwin and Tikoff, 2002). These incompatibilities may be accommodated by shearing along these boundaries, therefore, it follows that a largely competent package of rock will see deformation localised into in shear zones where weak phases exist and/or have been partitioned, while a largely incompetent package of rock will exhibit distributed strain throughout (Goodwin and Tikoff, 2002). These mechanisms are essentially scale

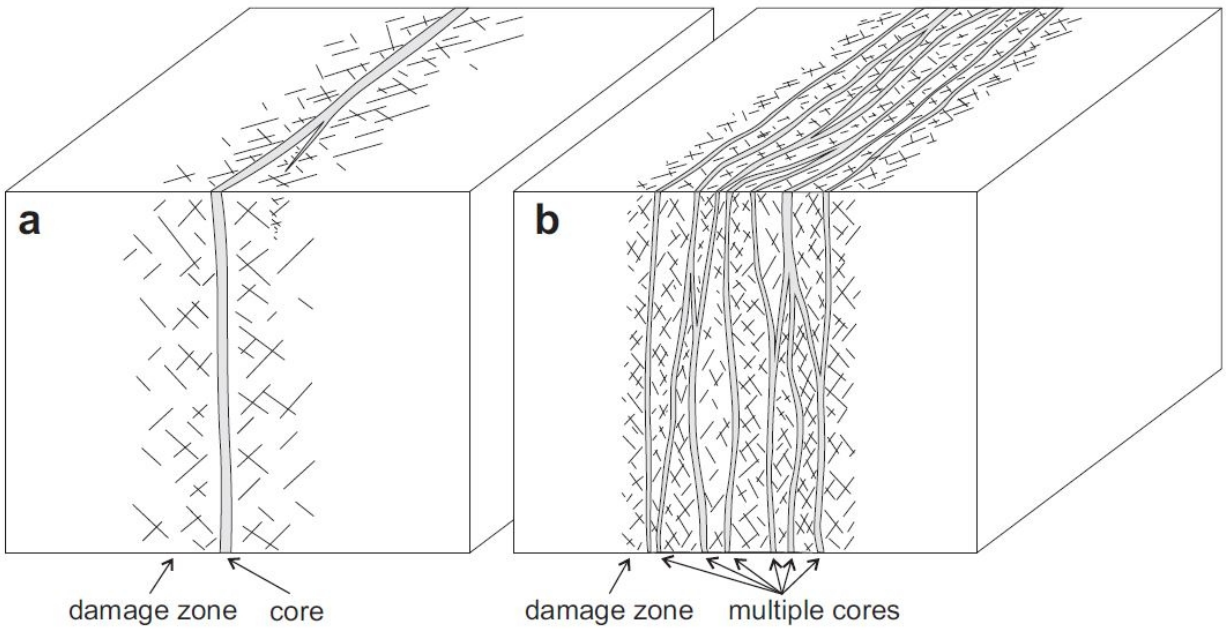

Fig 3. Models of fault zone development with single (a), and multiple (b) fault cores (from Faulkner et al., 2010).

independent, and therefore may be observed at a range of scales and magnitude through a deforming sequence (i.e. strain partitioned in weak phase minerals at the thin-section scale vs. metre-scale packages of clay-rich beds acting as shear zones surrounded by competent material).

All of the influences between competency contrast and deformation mechanisms (and vice versa) can be through of as influencing the three-dimensional flow of deforming media. Goodwin and Tikoff (2002) explain that in high competency contrast systems, proportionally high strain rate incompatibilities can result in

vastly different lineation orientations between adjacent domains. This agrees with the observation that many fault zones show significant structural variation along-strike and down dip, even over relatively short (metres) distances, resulting in complex and heterogeneous fault zone geometries (Faulkner et al., 2010; Fagereng, 2011b).

4.3 Influence on fault zone development

Understanding the evolution of fault zones and shear zones is key for understanding their influence on fold-thrust belt geometry, but also for understanding their potential as fluid flow pathways (Kirschner and Kennedy, 2001; Faulkner et al., 2010; Lacroix et al., 2014). For instance, the distribution of high and low permeability features through a geometrically complex fault zone may lead to extreme heterogeneity in both across- and along-fault permeability (Faulkner et al., 2010). A simplified conceptual model of how fault zones develop involves strain localisation within a fault core (or shear zone), which is then surrounded by a zone of brittle fractures and associated structures (fault damage zone) (Fig. 3). Fault zones may develop as a single damage zone around a fault core, or as interrelated multiple cores within a broader fault damage zone (Faulkner et al., 2010). This model related well to, and builds on, the understanding of the effects of competency contrast described above; fault cores exhibiting high-strain within low competency domains, where the fault damage zone consists of lower bulk-strain, with strain localised into discrete slip surfaces (Goodwin and Tikoff, 2002; Dellisanti et al., 2008; Faulkner et al., 2010). The fault cores themselves may in turn feature distributed strain across a shear zone, or consist of multiple high-strain slip surfaces, depending on the magnitude and distribution of competency contrast in the protolith rock (Faulkner et al., 2010; Rutter et al., 2013).

Much like seismic reflectors, with a shale detachment the brittle features of fault damage zones have previously been considered chaotic, however, detailed observations show they are highly ordered (Chester and Logan, 1986; Faulkner et al., 2010; Rutter et al., 2013). However, heterogeneity of these features, particularly along-fault variation is poorly understood, and requires a better understanding of the physical properties of the rocks involved (Faulkner et al., 2010).

4.4 Deformational conditions and rock properties

As discussed, a significant number of factors, many of which are interrelated, can affect the nature of deformation in shale detachments and associated fault zones. Mechanical competence, and heterogeneity of this property, exerts significant control of the 4D geometry and fluid flow potential of fault zones (Goodwin and Tikoff, 2002; Dellisanti et al., 2008; Faulkner et al., 2010; Rutter et al., 2013). This competence, essential rheology of a given domain of rock or sediment, can be influenced by a number of intrinsic and transient properties. Drawing from the shale detachment classification scheme of Morley et al. (2011), rheological weakness, allowing shale-rich rocks to localise strain and act as zones of detachment is generally influenced by

- Fluid overpressure (Cobbold et al., 2009; Suppe, 2014).

- Mineralogy, including the mineralisation of slip surfaces (Fagereng, 2011a; Rutter et al., 2013; Wells et al., 2014).

- Strain localisation during deformation (Goodwin and Tikoff, 2002; Haines et al., 2013).

As this study focussed on the analysis of outcropping, ancient, detachment zones where overpressure cannot be measured, only the effects of mineralogy and shear localisation are discussed here. Clay minerals are frictionally weak compared to other common rock forming minerals (Byerlee, 1978). The presence of organic carbon in shales also provides a significant source of weakness, with high TOC (total organic carbon) contents being associated with higher Poisson's ratios (Eseme et al., 2006). As discussed, competency contrast manifest in strain localisation. Additionally, weak phases within rocks such as clay minerals and organic carbon can result in a disproportionate reduction in friction compared to their bulk volume (Rutter et al., 2013). Clay minerals and organic content are frequently reported as the primary sources of weakness in shales; however, Wells et al. (2014) report vein calcite along fault planes as constituting the weak phase of a deforming shale sequence. This is achieved by plastically induced grain-size reduction of calcite, forming a network of ultrafine-grained calcite around more competent shale lenses, which acted as the incompetent phase (Wells et al., 2014). This example highlights the importance of a 4D understanding of fault zone development, as it shows how a property not intrinsic to the protolith shale, but rather a result of deformation, introduced a source of incompetency during the history of the fault zone. The pathways for fluid-flow, and therefore distribution of this introduced weak phase, were in turn governed by the geometry, heterogeneity, and competency contrast of the protolith shale.

The roles of mineralogy and the evolution of mineralogy through diagenetic and deformational process exert control on the competency contrast and heterogonous development of fault zones in shales. Considerable gaps still exist in the understanding of how these properties directly influence fault zone development, therefore, the main aim of this study is to analyse, in detail, the structure of an exhumed shale detachment zone, and characterise the influence of mineralogy, fluid-flow, and deformational conditions and processes through its evolution.

5. Thesis outline

5.1 Chapter 2

To date little work has focused of the detailed structure of shale detachment zones. The importance of understanding detachment zones and how they accommodate deformation in overlying sequences is fundamental in understanding the mechanics of fold-thrust belts in thin-skinned deformation (Davis et al., 1983; Dahlen et al., 1984; Rowan et al., 2004; Morley et al., 2011). An understanding of the detailed structure of these zones can help to fill the gap of sub-seismic scale information of the structural style and deformational mechanisms, of shale detachment zones. Observations of structural styles and geometries of deformed rocks can provide insight into the development

of deformation both spatially and through time, and the potential influences on this development (e.g. Fagereng, 2011; Watkins et al, 2014). Given the essentially inaccessible nature of active detachment zones, studies of their detailed structure are limited to ancient exhumed examples. The exposed Khao Khwang Fold-Thrust Belt in the Khorat Plateau of central-north east Thailand provides excellent exposures of shale detachments and detachment-like behaviour, resulting from deformation during the Triassic Indosinian Orogeny. This study focuses specifically on the Sap Bon Formation, a unit of shales and fine-grained arenites, heavily deformed above the Eagle Thrust, which delineates the Sap Bon Formation from the relatively undeformed underlying carbonates. Detailed mapping of cross-section exposures of the fault damage zone above the Eagle thrust is employed, detailing a primarily brittle, fault-dominated deformational style, with significant local variation of structural styles and orientations. Faults are heavily mineralised with calcite veins and slickenfibres throughout the fault damage zone, and give evidence for complex progressive development of structures. Three structural domains are described with the domain closest to the Eagle Thrust constituting a detachment zone. This proximal domain is characterised by complex three-dimensional deformational geometries of anastomosing shear zones. Stratigraphic heterogeneity of the Sap Bon Formation is suggested to have resulted in variation in competency and partitioning of strain, strongly influencing the progressive development of the fault zone.

5.3 Chapter 3

This chapter focuses on the factors controlling the deformational style and rheology of the detachment zone characterised in Chapter 2. The detachment zone in the Sap Bon Formation exhibits a strong rheological influence on the nature and mechanism of deformation, it is therefore important to investigate the potential influences on the rheology of these shales, and how rheological heterogeneity has influenced the development and behaviour of the detachment zone. A range of factors may contribute to the relative weakness of shales, including: tectonic setting and history, deformational temperature, mineralogy (and prograde/retrograde development thereof), competency contrast and distribution, strain rate, fluid overpressure, and fluid flow history (e.g. Simpson, 2009; Fagereng and Sibson, 2010; Wells et al., 2014). When investigating these properties it is important to consider deformational conditions, deformational mechanisms, rock properties, and the role of fluids as an interrelated system in a given fault zone. This study aimed to constrain the deformational temperature, document the mineralogy and its variation within the heterogeneous Sap Bon Formation, investigate total organic carbon levels, and constrain the history of syn-tectonic fluid flow within the detachment zone. These properties and conditions were then related to the deformational style and mechanisms present within the detachment zone. This study highlighted the difficulty of using vitrinite reflectance to constrain deformational temperature in highly sheared settings, while successfully using illite crystallinity to broadly constrain the maximum deformational temperature. Total organic carbon content was found to be notably higher within the detachment zone than the background Sap Bon

Formation levels, and a covariant trend of carbon and oxygen stable isotopic results from the syn-tectonic vein network established a burial and orogenic trend of mineralisation. From these results a fluid-flow history and model of fault zone development was synthesised.

5.4 Chapter 4

This chapter builds on the relationship noted in Chapter 3 (and various literature – e.g. Gutiérrez-Alonso and Nieto, 1996; Dellisanti et al., 2008) between illite crystallinity and strain rate, and focuses on investigating this relationship in the context of the Eagle Thrust detachment zone. Generally, the lack of mineral equilibrium-assemblages in diagenetic to very low-grade metamorphic settings means quantifying the conditions of deformation is problematic. Illite crystallinity is a widely used approximate palaeothermometer and forms a valuable tool in characterising the prograde smectite-illite conversion in clays (Frey et al., 1980; Kosakowski et al., 1999; Mählmann et al., 2012). The kinetics of this reaction are, however, poorly understood, and various authors note factors other than temperature affecting illite crystallinity, in particular tectonic strain (Gutiérrez-Alonso and Nieto, 1996; Dellisanti et al., 2008). Therefore, this study aimed to investigate the relationship between illite crystallinity and finite strain with a multi-setting approach: using data from the Eagle Thrust detachment zone, as well as from established ancient detachment zones in the Osen Røa Thrust Sheet in Oslo, Norway, and the Chrystalls Beach Complex in Southern Otago, New Zealand. Comparing the nature and conditions of deformation between contrasting structural domains is a valuable tool in understanding the evolution of a heterogeneous fault zone (Dellisanti et al., 2008). Therefore, the secondary aim of this study was to quantify finite strain within the Eagle Thrust detachment zone for comparison between structural domains (continuous vs. discontinuous deformation) described in Chapters 2 and 3. Finite strain was quantified using the Fry method of strain analysis as the shales of the Sap Bon Formation lacked appropriate strain markers. A strong correlation between illite crystallinity and finite strain across the three study areas was produced, with a similar finite strain value (RS = 1.693) found to correspond with the anchizone-epizone boundary commonly used in illite crystallinity studies, to that of previous work (RS = 1.5) (Gutiérrez-Alonso and Nieto, 1996). Results from this study built on the conclusion of Gutiérrez-Alonso and Nieto (1996) to suggest that illite crystallinity is an appropriate tool for tracking finite strain variation in fined grain rocks which have undergone a single phase of deformation, and exhibit diagenetic to sub-greenschist facies. The quantification of finite strain between contrasting zones of competency and deformational mechanism confirmed strain was heavily partitioned in the Eagle Thrust detachment zone, and supported the model of fault zone development developed in Chapter 3.

5.5 Chapter 5

This chapter builds on the understanding of the evolution of the Eagle Thrust detachment and associated fault damage zone by constraining the timing of deformation. Dating of fine-grained minerals such as those found in clays to provide constraints on the timing of mineral growth. By understanding the relationship of

mineral growth to structure, the timing of deformation can be constrained (Zwingmann et al., 2010; Viola et al., 2013; Torgersen et al., 2015). However, ages yielded by illite in shales can be essentially meaningless without constraints on the relationship of the dated illite to evolution of the fault zone (Pevear and Elliott, 1991). Ages obtained from illite within a shale sample, even one identified as being composed of fault gouge, are potentially influenced by detrital illites from the deposition of the protolith, diagenetic illites, and orogenic age illites formed during fault movement. To garner meaningful information from these dates it is necessary to constrain the 'end members' influences (detrital and authigenic) (Pevear and Elliott, 1991; Zwingmann and Mancktelow, 2004). This study uses the relationship of each dated sample to a suite of data used to indicate the stage of fault zone development. The sample's carbon and oxygen stable isotope signature is used to relate it to the stage of diagenetic to orogenic fluid flow evolution of the fault zone established in Chapter 3. X-ray diffraction based mineralogy, in particular chlorite chemistry and clay mineralogy is also employed to constrain the degree of detrital-diagenetic-orogenic illite component of each sample. Finally, these results are compared to recent geochronological work in the area in order to place the detrital and deformation ages into the regional geological context.

References

Agar, S. M., D. J. Prior, and J. H. Behrmann, 1989, Back-scattered electron imagery of the tectonic fabrics of some fine-grained sediments: implications for fabric nomenclature and deformation processes: Geology, v. 17, p. 901-904.

Bilotti, F., and J. H. Shaw, 2005, Deep-water Niger Delta fold and thrust belt modeled as a critical-taper wedge: The influence of elevated basal fluid pressure on structural styles: AAPG bulletin, v. 89, p. 1475-1491.

Briggs, S. E., R. J. Davies, J. A. Cartwright, and R. Morgan, 2006, Multiple detachment levels and their control on fold styles in the compressional domain of the deepwater west Niger Delta: Basin Research, v. 18, p. 435-450.

Byerlee, J., 1978, Friction of rocks: Pure and applied geophysics, v. 116, p. 615-626.

Chester, F., and J. Logan, 1986, Implications for mechanical properties of brittle faults from observations of the Punchbowl fault zone, California: Pure and applied geophysics, v. 124, p. 79-106.

Cobbold, P. R., B. J. Clarke, and H. Løseth, 2009, Structural consequences of fluid overpressure and seepage forces in the outer thrust belt of the Niger Delta: Petroleum Geoscience, v. 15, p. 3-15.

COLLINS, A.S., Zalasiewicz J.A. & Kryza, R., 2000. Macrofabric fingerprints of Late Devonian-Early Carboniferous subduction in the Polish Variscides, the Kaczawa complex, Sudetes. Journal of the Geological Society, London, 157, 283-288.

Corredor, F., J. H. Shaw, and F. Bilotti, 2005, Structural styles in the deep-water fold and thrust belts of the Niger Delta: AAPG bulletin, v. 89, p. 753-780.

Dahlen, F., J. Suppe, and D. Davis, 1984, Mechanics of fold-and-thrust belts and accretionary wedges: Cohesive Coulomb theory: Journal of Geophysical research, v. 89, p. 10087-10,101.

Davis, D., J. Suppe, and F. Dahlen, 1983, Mechanics of fold-and-thrust belts and accretionary wedges: Journal of Geophysical research, v. 88, p. 1153-1172.

Dellisanti, F., G. Pini, F. Tateo, and F. Baudin, 2008, The role of tectonic shear strain on the illitization mechanism of mixed-layers illite–smectite. A case study from a fault zone in the Northern Apennines, Italy: International Journal of Earth Sciences, v. 97, p. 601-616.

Eseme, E., R. Littke, and B. Krooss, 2006, Factors controlling the thermo-mechanical deformation of oil shales: implications for compaction of mudstones and exploitation: Marine and Petroleum Geology, v. 23, p. 715-734.

Fagereng, Å., 2011a, Fractal vein distributions within a fault-fracture mesh in an exhumed accretionary mélange, Chrystalls Beach Complex, New Zealand: Journal of Structural Geology, v. 33, p. 918-927.

Fagereng, Å., 2011b, Geology of the seismogenic subduction thrust interface: Geological Society, London, Special Publications, v. 359, p. 55-76.

Fagereng, Å., and R. H. Sibson, 2010, Melange rheology and seismic style: Geology, v. 38, p. 751-754.

Faulkner, D., C. Jackson, R. Lunn, R. Schlische, Z. Shipton, C. Wibberley, and M. Withjack, 2010, A review of recent developments concerning the structure, mechanics and fluid flow properties of fault zones: Journal of Structural Geology, v. 32, p. 1557-1575.

Frey, M., M. Teichmüller, R. Teichmüller, J. Mullis, B. Künzi, A. Breitschmid, U. Gruner, and B. Schwizer, 1980, Very low-grade metamorphism in external parts of the Central Alps: illite crystallinity, coal rank and fluid inclusion data: Eclogae Geologicae Helvetiae, v. 73, p. 173-203.

Goodwin, L. B., and B. Tikoff, 2002, Competency contrast, kinematics, and the development of foliations and lineations in the crust: Journal of Structural Geology, v. 24, p. 1065-1085.

Gutiérrez-Alonso, G., and F. Nieto, 1996, White-mica'crystallinity', finite strain and cleavage development across a large Variscan structure, NW Spain: Journal of the Geological Society, v. 153, p. 287-299.

Haines, S. H., B. Kaproth, C. Marone, D. Saffer, and B. van der Pluijm, 2013, Shear zones in clay-rich fault gouge: A laboratory study of fabric development and evolution: Journal of Structural Geology, v. 51, p. 206-225.

Jordan, P. G., 1987, The deformational behaviour of bimineralic limestone-halite aggregates: Tectonophysics, v. 135, p. 185-197.

Kirschner, D. L., and L. A. Kennedy, 2001, Limited syntectonic fluid flow in carbonate‐hosted thrust faults of the Front Ranges, Canadian Rockies, inferred from stable isotope data and structures: Journal of Geophysical Research: Solid Earth (1978–2012), v. 106, p. 8827-8840.

Kosakowski, G., V. Kunert, C. Clauser, W. Franke, and H. J. Neugebauer, 1999, Hydrothermal transients in Variscan crust: paleo-temperature mapping and hydrothermal models: Tectonophysics, v. 306, p. 325-344.

Labaume, P., A. Maltman, A. Bolton, D. Tessier, Y. Ogawa, and S. Takizawa, 1997, Scaly fabrics in sheared clays from the décollement zone of the Barbados accretionary prism: Proceedings of the Ocean Drilling Program. Scientific Results, p. 59-77.

Lacroix, B., A. Travé, M. Buatier, P. Labaume, T. Vennemann, and M. Dubois, 2014, Syntectonic fluid-flow along thrust faults: Example of the South-Pyrenean fold-and-thrust belt: Marine and Petroleum Geology, v. 49, p. 84-98.

Mählmann, R. F., Ö. Bozkaya, S. Potel, R. Le Bayon, B. Šegvić, and F. Nieto, 2012, The pioneer work of Bernard Kübler and Martin Frey in very low-grade metamorphic terranes: paleo-geothermal potential of variation in Kübler-Index/organic matter reflectance correlations. A review: Swiss Journal of Geosciences, v. 105, p. 121-152.

Maloney, D., R. Davies, J. Imber, S. Higgins, and S. King, 2010, New insights into deformation mechanisms in the gravitationally driven Niger Delta deep-water fold and thrust belt: AAPG bulletin, v. 94, p. 1401-1424.

Maltman, A., 1994, geological deformation of sediments, Chapman & Hall.

Moore, C., B. Dugan, P. Flemings, G. Iturrino, D. Sawyer, J. Behrmann, and C. John, 2005, Geological Consequences of Unequal Loading of Sedimentary Units, at Passive, Transform, and Convergent Margins: AGU Fall Meeting Abstracts, p. 01.

Morley, C., 2003, Mobile shale related deformation in large deltas developed on passive and active margins: Geological Society, London, Special Publications, v. 216, p. 335-357.

Morley, C., and G. Guerin, 1996, Comparison of gravity-driven deformation styles and behavior associated with mobile shales and salt: Tectonics, v. 15, p. 1154-1170.

Morley, C. K., R. King, R. Hillis, M. Tingay, and G. Backe, 2011, Deepwater fold and thrust belt classification, tectonics, structure and hydrocarbon prospectivity: A review: Earth-Science Reviews, v. 104, p. 41-91.

Morley, C. K., J. Warren, M. Tingay, P. Boonyasaknanon, and A. Julapour, 2014, Comparison of modern fluid distribution, pressure and flow in sediments associated with anticlines growing in deepwater (Brunei) and continental environments (Iran): Marine and Petroleum Geology, v. 51, p. 210-229.

Pevear, D., and W. Elliott, 1991, Illite Age Analysis: A Method for Interpreting Shale K/Ar Ages: LPI Contributions, v. 773, p. 124.

Rowan, M. G., F. J. Peel, and B. C. Vendeville, 2004, Gravity-driven fold belts on passive margins.

Rutter, E., A. Hackston, E. Yeatman, K. Brodie, J. Mecklenburgh, and S. May, 2013, Reduction of friction on geological faults by weak-phase smearing: Journal of Structural Geology, v. 51, p. 52-60.

Rutter, E., R. Maddock, S. Hall, and S. White, 1986, Comparative microstructures of natural and experimentally produced clay-bearing fault gouges: Pure and applied geophysics, v. 124, p. 3-30.

Screaton, E., G. Kimura, D. Curewitz, G. Moore, F. Chester, O. Fabbri, C. Fergusson, F. Girault, D. Goldsby, and R. Harris, 2009, Interactions between deformation and fluids in the frontal thrust region of the NanTroSEIZE transect offshore the Kii Peninsula, Japan: Results from IODP Expedition 316 Sites C0006 and C0007: Geochemistry, Geophysics, Geosystems, v. 10.

Simpson, G. D. H., 2009, Mechanical modelling of folding versus faulting in brittle–ductile wedges: Journal of Structural Geology, v. 31, p. 369-381.

Suppe, J., 2014, Fluid overpressures and strength of the sedimentary upper crust: Journal of Structural Geology, v. 69, p. 481-492.

Tingay, M. R., R. R. Hillis, R. E. Swarbrick, C. K. Morley, and A. R. Damit, 2009, Origin of overpressure and pore-pressure prediction in the Baram province, Brunei: AAPG bulletin, v. 93, p. 51-74.

Torgersen, E., G. Viola, H. Zwingmann, and I. H. Henderson, 2015, Inclined K – Ar illite age spectra in brittle fault gouges: effects of fault reactivation and wall ‐ rock contamination: Terra Nova, v. 27, p. 106-113.

Turner, F. J., and L. E. Weiss, 1963, Structural analysis of metamorphic tectonites, McGraw-Hill.

van Rensbergen, P., C. Morley, D. Ang, T. Hoan, and N. Lam, 1999, Structural evolution of shale diapirs from reactive rise to mud volcanism: 3D seismic data from the Baram delta, offshore Brunei Darussalam: Journal of the Geological Society, v. 156, p. 633-650.

van Rensbergen, P., and C. K. Morley, 2003, Re-evaluation of mobile shale occurrences on seismic sections of the Champion and Baram deltas, offshore Brunei: Geological Society, London, Special Publications, v. 216, p. 395-409.

Viola, G., H. Zwingmann, J. Mattila, and A. Käpyaho, 2013, K - Ar illite age constraints on the Proterozoic formation and reactivation history of a brittle fault in Fennoscandia: Terra Nova, v. 25, p. 236-244.

Watkins, H., C. E. Bond, and R. W. Butler, 2014, Identifying multiple detachment horizons and an evolving thrust history through cross-section restoration and appraisal in the Moine Thrust Belt, NW Scotland: Journal of Structural Geology, v. 66, p. 1-10.

Wells, R. K., J. Newman, and S. Wojtal, 2014, Microstructures and rheology of a calcite-shale thrust fault: Journal of Structural Geology, v. 65, p. 69-81.

Wintsch, R., 1985, The possible effects of deformation on chemical processes in metamorphic fault zones, Metamorphic reactions, Springer, p. 251-268.

Zwingmann, H., and N. Mancktelow, 2004, Timing of Alpine fault gouges: Earth and Planetary Science Letters, v. 223, p. 415-425.

Zwingmann, H., K. Yamada, and T. Tagami, 2010, Timing of brittle deformation within the Nojima fault zone, Japan: Chemical Geology, v. 275, p. 176-185.

Chapter 2

Published as Hansberry, R. L., King, R., Collins, A. S., & Morley, C. K., 2014. Complex structure of an upper-level shale detachment zone: Khao Khwang fold and thrust belt, Central Thailand. *Journal of Structural Geology*, *67*, 140-153.

Complex structure of an upper-level shale detachment zone: Khao Khwang fold and thrust belt, Central Thailand

Abstract

Shale detachment zones have been previously described as largely mobile in character; however, increasing resolution of seismic images and understanding of these zones suggest brittle deformation may have a significant role in their deformational behaviour and in the deformation of overlying fold and thrust belts. Dependence on seismic imaging and other indirect and low-resolution study methods has resulted from the lack of outcropping shale detachment zones, both active and ancient, for detailed study. However, a newly described upper-level detachment zone in a shale unit in the Khao Khwang Fold and Thrust Belt in Central Thailand is exceptionally well-exposed. We use detailed structural analysis to investigate deformational mechanisms of this ancient, exhumed detachment zone, as an analogue to active modern-day examples. Through detailed field mapping we were able to construct multiple cross-sections through the detachment zone. These cross-sections were subdivided into structural domains, which display an increase in density and complexity of deformational structures (folds, faults), and heterogeneity of their orientations toward the thrust at the base of the detachment zone. Contrasting strain rates in zones of continuous-discontinuous deformation result from contrasting rock-competencies through the sections. We conclude that the fault damage-zone in this study constitutes an upper-level detachment and is potentially analogous to those in active collisional fold and thrust belts. It displays mixed brittle-ductile deformation and a complex, three-dimensional anastomosing fault-system.

Key words: shale detachment, Thailand, brittle-ductile, damage-zone

1. Introduction

Thin-skinned fold and thrust belts occur across a variety of tectonic settings and have been the focus of extensive research and review (e.g. Davis et al., 1983; Rowan et al., 2004; Simpson, 2009; Morley et al., 2011). Davis et al. (1983) postulated that a thorough understanding of fold and thrust belt mechanics requires knowledge of the properties of two common features (Fig. 1):

1. A basal zone, above which material shows a large degree of horizontal contraction and below which there is little deformation (Davis et al., 1983; Dahlen et al., 1984; Dahlen, 1990; Rowan et al., 2004; Morley et al., 2011b).

2. A characteristic wedge-shape geometry of the overlying fold and thrust belt, described by critical taper wedge theory (Davis et al., 1983; Dahlen et al., 1984; Dahlen, 1990).

Detachment zones may vary from centimetres to kilometres in thickness and can accommodate a significant amount of deformation of the overlying rocks, as well as internally (Davis et al., 1983; Dahlen et al., 1984; Rowan et al., 2004; Briggs et al., 2006; Morley et al., 2011b). The physical properties of detachments, both at the base, and higher within the detachment zone, exert significant influence on the geometry of the fold and thrust belt above (Sherkati et al., 2005; Briggs et al., 2006). These properties affect the structural style of the fold and thrust belt, and how it accommodates shortening to reach a critical taper. Key factors that have been identified as controlling the rheological behaviour of a given detachment zone are its: 1) lithology, 2) stratigraphy (i.e. hetero- or homogeneity of lithology), 3) dip and dip direction, 4) deformational temperature, and 6) pore pressure.

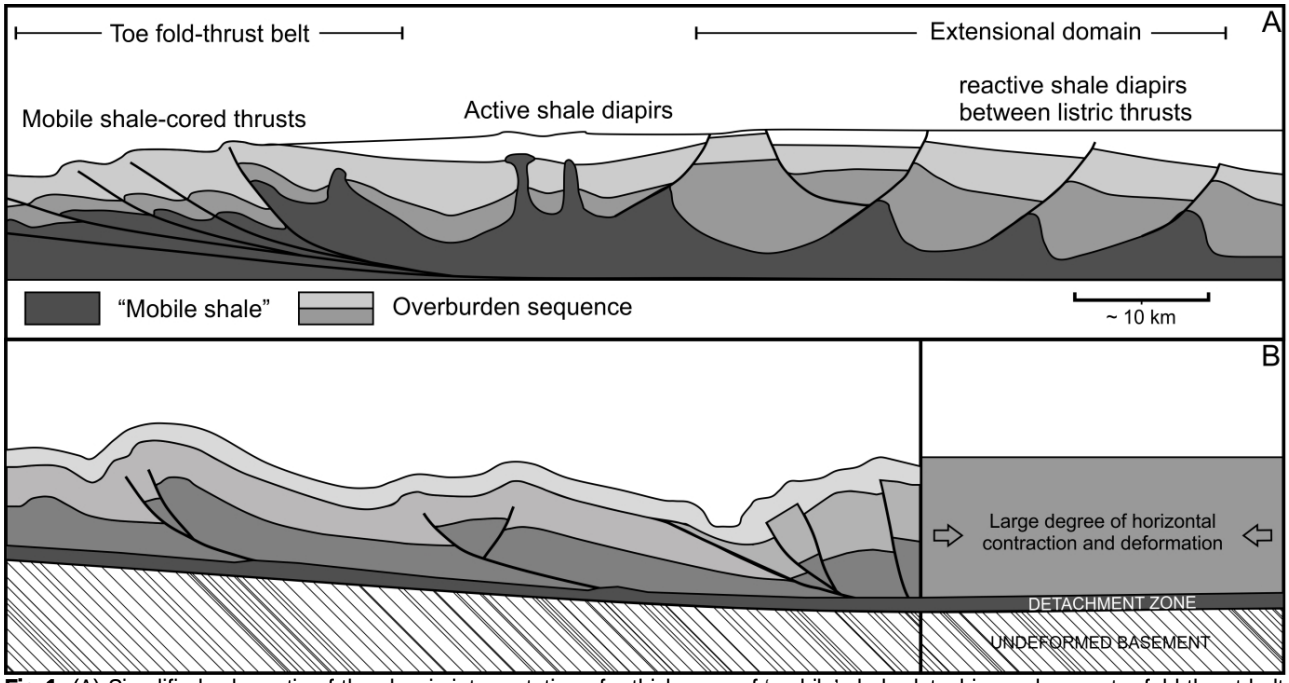

Fig 1. (A) Simplified schematic of the classic interpretation of a thick zone of 'mobile' shale detaching a deep-water fold-thrust belt. (B) Simplified schematic of a fold-thrust belt with a more vertically limited detachment zone within shales at the base of a folded and thrusted overburden sequence. After van Rensbergen and Morley (2003) King et al. (2010).

Detachment behaviour has been shown to significantly affect the geometries of fold and thrust belts, which have implications for hydrocarbon exploration and natural hazard assessment (Rowan et al., 2004; Briggs et al., 2006; Morley et al., 2011b). However, the majority of active fold and thrust belts occur in inaccessible, deep marine environments, thus studies of detachment zones have been largely indirect, and limited to employing seismic reflection data (van Rensbergen et al., 1999a; van Rensbergen and Morley, 2003; Corredor et al., 2005). Detachments are not exposed in active, sub-aerial fold and thrust belts, making detailed outcrop study of the detachments impossible. Little or no detailed structural analysis of detachment zones has been undertaken as the resolution of seismic data is generally too low, and detachment zones typically exhibit chaotic or no reflectors (e.g. Cohen and McClay, 1996; van Rensbergen et al., 1999a). The aim of this study of an ancient exhumed fold and thrust belt was to document the nature of deformation within a well-exposed shale detachment zone in central Thailand. The study focused on the mechanisms of deformation and how they varied both spatially, and with different lithologies.

Recent work in the Saraburi Province of Thailand has identified an exposure of a upper-level detachment zone within the fold and thrust belt, formed during the Triassic Indosinian Orogeny (Sone and Metcalfe, 2008; Morley et al., 2013). In this study we document the variation and nature of internal structure of a shale detachment zone in the Khao Khwang Fold and Thrust Belt and demonstrate the heterogeneity of deformation at a scale rarely documented in shale detachments (e.g. Needham, 2004; Fagereng, 2011).

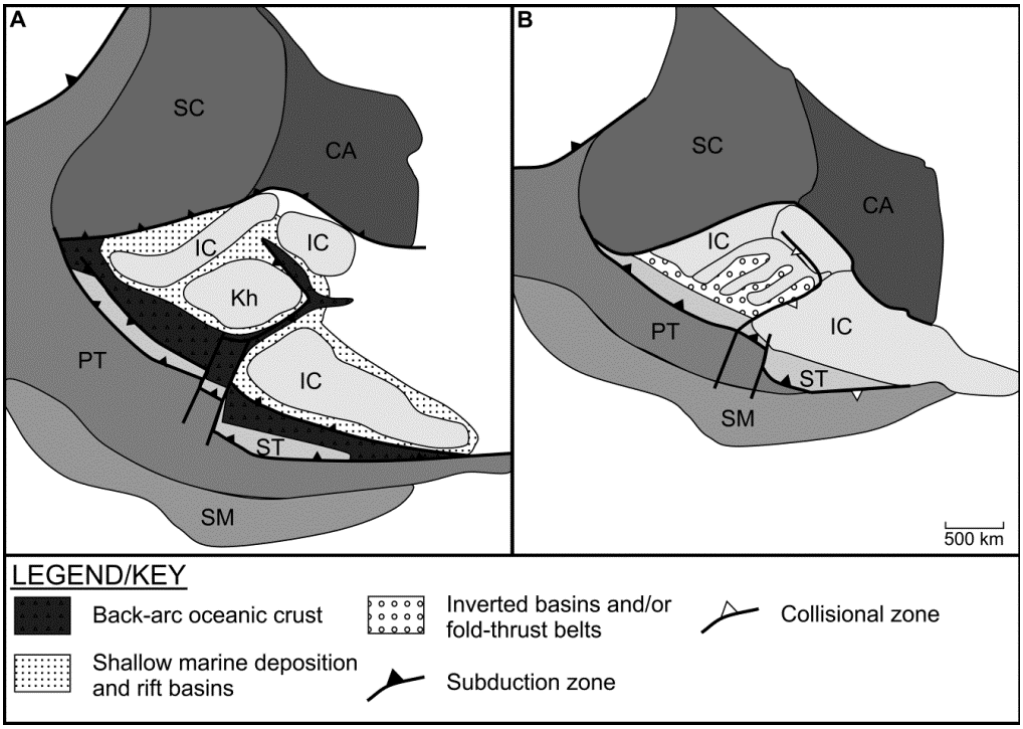

Fig 2. Simplified reconstruction of plate tectonic setting of fold and thrust belts on the Khorat Plateau in South-East Asia during the Early (A) and Middle (B) Triassic. Modified from Morley et al. (2013). IC = Indochina Block fragments including Khorat Plateau (Kh), SC = South China Block, CA = Cathaysian Block, SM = Sibumasu, ST = Sukhothai, PT = Palaeo-Tethys.

2. Geological setting of Central Thailand

The Indosinian orogeny occurred as a series of subduction and collision related events during the Late Permian to Early Jurassic (Sone & Metcalfe, 2008; Barber et al., 2011; Morley et al., 2013). A basic model for the Indosinian Orogeny in Thailand involves the Early Triassic closure of a back-arc basin, and collision of the Sukhothai Terrane with Indochina (Sone and Metcalfe, 2008). This was followed by the closure of the Palaeo-Tethys and collision of the outboard Sibumasu Terrane with the combined Sukhothai-Indochina Blocks during the Late Triassic (Fig. 2). Two stages of the Indosinian Orogeny have been described and related to unconformities in the relatively stable Khorat Plateau of NE Thailand (Sone and Metcalfe, 2008; Morley et al., 2013). Stage one defines much of the early deformation in the Indochina Block during the Early-Middle Triassic. Stage 2 deformation occurred within the Sibumasu Block during the Late Triassic to Early Jurassic (Morley et al., 2013). The Khao Khwang Fold and Thrust Belt of central and eastern Thailand (Fig. 3) is interpreted to have developed as the result of stage 1 on the southern margin of the Khorat Indochina fragment during the Early Triassic (Morley et al., 2013).

The Permian carbonates in the Saraburi-Pak Chong area form part of the Saraburi Group (Hinthong et al., 1985; Ueno and Charoentitirat, 2011; Morley et al., 2013). The Saraburi Group was originally defined as Permian carbonates and associated sediments along the margin of

the Indochina Block (Bunopas, 1981). The name was later restricted to the latest Carboniferous-Permian carbonates and associated clastics and siliciclastics on the Khao Khwang platform. Hinthong et al. (1985) identified six formations of the Saraburi Group in the Saraburi area. From oldest to youngest these are: the Phu Phe, Khao Khwang, Nong Poon, Pang Asok, Khao Khad and Sap Bon formations. Originally these formations were seen as a simple, younging-upwards succession. However, paleontological data has now shown that most of these formations are contemporaneous and an alternative hypothesis has emerged whereby the formations are coeval facies variations within the Saraburi Group (Ueno and Charoentitirat, 2011). The study described here focuses on outcrops of the Sap Bon and Khao Khad formations, which constitute the youngest unit of the originally proposed sequence (Fig. 4). The Khao Khad Formation consists of up to 1800 m of thin- to very thick-bedded bioclastic limestone with black chert nodules and minor interbeds of sandstone, siltstone and conglomerates (Ueno and Charoentitirat, 2011). The Sap Bon Formation makes up the originally uppermost formation of the Saraburi Group and comprises pale-green to pale-brown shale and sandstone, with interbeds of grey to dark-grey limestone and chert (Ueno and Charoentitirat, 2011). However, the formation was not well

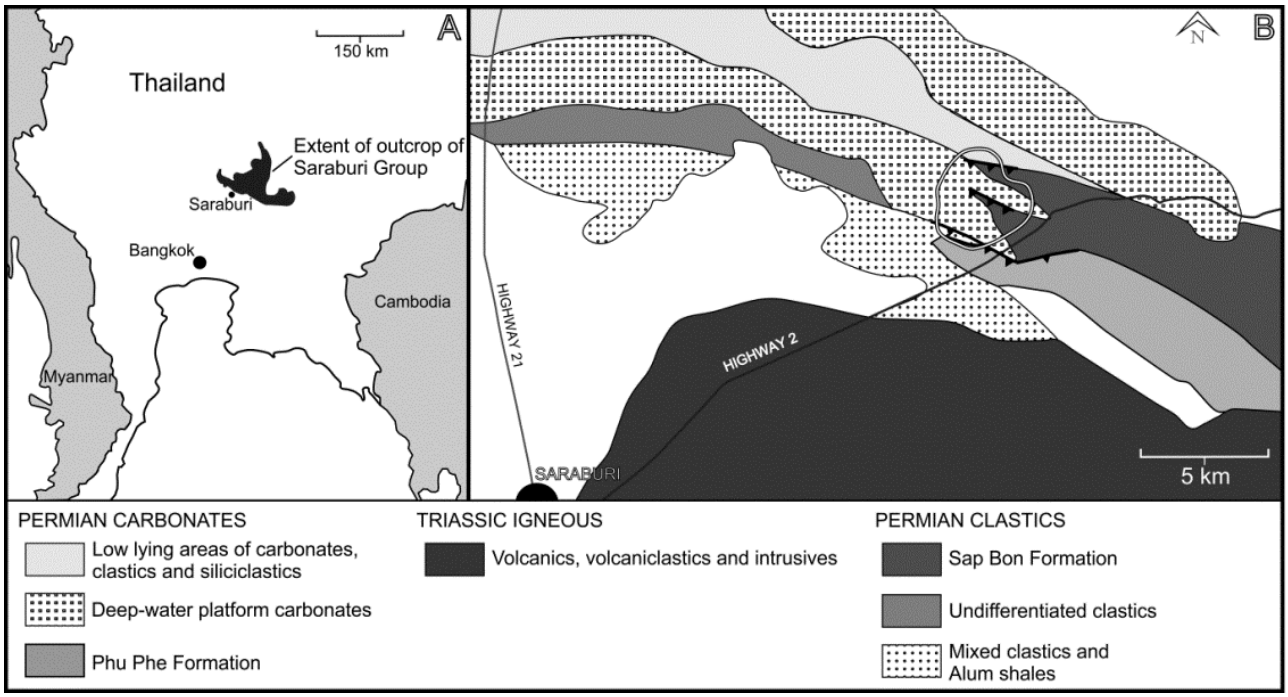

Fig 3. Location and extent of outcrop of the Saraburi Group in Thailand (A); location of Siam City Cement Quarry (outlined) within the context of outcrops of the Saraburi Group (B) (After Morley et al., 2013).

exposed where it was initially described. Exposures in study area indicate the Sap Bon Formation is of equivalent age, and even underlies the Khao Khad Formation.

A detailed understanding of the stratigraphy and structural evolution of the Saraburi area is still a work in progress, though this provides an overview of the regional geology. The basic depositional setting of the Saraburi Group is interpreted as a suite of Permian rift basins on the southern margin of the Indochina Block controlled by extensional faults (Morley et al., 2013). These filled with clastics and mixed clastic and carbonate sediments (e.g. Sap Bon, Pang Asok, and Nong Pong formations), which transitioned laterally into platform carbonates (e.g. Khao Khad, Phu Phe, and Khao Khwang

formations), which generally occupy high, intra-basinal areas (Fig. 4) (Morley et al., 2013). The rocks of the Saraburi Group are exposed as a chain of limestone hills and ridges through the Saraburi Province. Thick vegetation and high rainfall means good quality outcrop is spatially limited to active and recent quarries (e.g. Fig. 3). The study area in the Siam City Cement Quarry covers approximately 3 x 4 km, and lies 30 km NE of the city of Saraburi (Fig. 3). The northern-most of two large, northward-verging thrusts outcropping in the quarry forms a thrust contact between the Sap Bon Formation and the Khao Khad Formation (Morley et al., 2011a; Morley et al., 2013). This study presents detailed structural work on the shales of the Sap Bon Formation above this thrust, which are interpreted as constituting an upper-level detachment zone: shales above the thrust are heavily deformed whereas the carbonates underlying it are undeformed for 10s of meters, these show bedding parallel to the thrust, implying the thrust was originally horizontal.

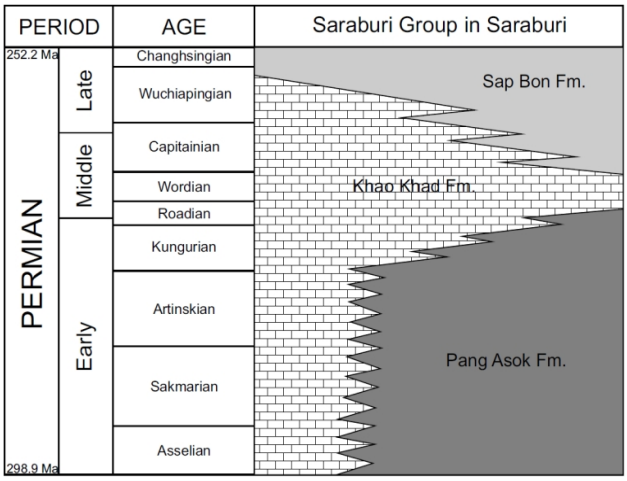

Fig 4. Ages and stratigraphy of the Saraburi Group in the Saraburi area after Ueno & Charoentitirat (2011) and Morley et al. (2013).

3. Detailed geology of the Eagle Thrust, Siam City Cement Quarry

3.1 Stratigraphy of the Siam City Cement Quarry

The Khao Khad Formation limestone in the Siam City Cement Quarry consists of thick-bedded bioclastic limestone with dark-grey to black chert nodules. Beds vary from centimetres to metres in thickness and commonly contain gastropods and bivalves. Crinoidal wackestone-packstone packages and rudstones are common. The Sap Bon Formation in the Siam City Cement Quarry consists of brown-grey interbedded siltstones and fine- to medium-grained sandstones with individual sandstone beds typically 5-15 centimetres thick. The thicknesses of siltstone beds are more variable and often difficult to define as these rocks exhibit well-developed foliations, often overprinting laminations, but beds generally vary from 1-10 millimetres.

3.2 Structure of the Sap Bon Formation

Figures 5 and 6 display the three cross sections constructed from observations made across strike of the northern-most thrust in the Siam City Cement Quarry – herein referred to as the Eagle thrust. These measured sections were constructed from data collected in the field, as well as photographs and sketches of each of the three benches (inset section map, Fig. 5 and 6). Each section (bench) displays the Eagle thrust to the right (north) and the deformed Sap Bon Formation shales over the limestones of the Khao Khad Formation.

The striking feature of the deformed shale exposed in the Siam City Cement Quarry is the complexity of the fault-dominated brittle appearance of deformation. Bedding in shale and sandstone layers throughout the section is broadly congruous with the orientation of the Eagle thrust, with a moderate dip to the S-SW (Fig. 5). However, significant local variation in orientation of bedding occurs due to the complexity of structural features through the section (Fig. 5 & 6). Variation in bedding orientation is locally controlled by decametre-scale faults and decimetre- to metre-scale folds.

Minor folds within the section are most commonly upright, or moderately inclined in the hanging wall of minor faults (e.g. Fig. 6H, labelled '11'); antiform-synform pairs are uncommon. Orientations of bedding planes are locally variable, particularly with proximity to the Eagle thrust, however they do broadly mirror the orientations of major faults with a W-SE spread of dip directions and a mean dip and dip direction of 66/193 (Fig. 7). Figure 7 also displays the orientations of faults; these have mean orientation of 65/194. Slickenfibres have a mean orientation of 47→156, with mineralized steps indicating a N-NW (43/336) movement direction. Two populations of fold hinges to the W and E, respectively, have axial traces which trend WNW to ESE (Fig. 7).

Throughout the section, both the Sap Bon and Khao Khad formations locally exhibit calcite mineralisation (Fig. 8). Veins parallel and orthogonal to the E-W to ENE-WSW strike of the Eagle thrust are observed in the underlying Khao Khad Formation. Within the Sap Bon Formation, calcite mineralisation is more restricted to planar orientations parallel to bedding and faults (Fig. 8, top left). In particular, the greatest concentration of mineralisation occurs along large faults, where multiple millimetre-thick layers of are commonly observed and discrete, individual calcite layers within 'stacks' preserve different slickenfibre orientations in some instances (Fig. 8, middle right). Calcite-filled tension gashes are also observed (Fig. 8, middle left).

Strain is strongly partitioned within the Sap Bon Formation, with shale layers exhibiting well-developed foliations and S-C fabrics. Fine-grained siltstones are heavily deformed and exhibit a fissility parallel to bedding (or potentially overprinting bedding), whereas packages of sandstone exhibit little evidence of foliation and internal strain (Fig. 8, top right).

Within the sandstone dominated packages, strain is accommodated by ramps and centimetre- to metre-scale fault propagation folds in the hanging walls of faults (Fig. 6E, labelled '6'). Faults in these packages occur as finite surfaces, lacking the shear zone-like foliations with S- and C-surfaces of finer-grained layers. The sheared and foliated packages in shale separate packages of relatively gently deformed sandstones (Fig. 6E, labelled '7'). Throughout the section, folds are largely fault-propagation folds in relatively competent layers above thrust faults (e.g. Fig. 6H, labelled '11'). Although the spacing and characteristics of deformational structures varies considerably with lithology, decreasing structural complexity and broader spacing of thrust faults is observed with increasing distance from the Eagle thrust. Simpler fold and thrust geometries are found outward of 130 meters from the Eagle thrust. We have used this change in structural style to divide the exposure of the Sap Bon Formation shales into three structural domains: proximal, intermediate and distal (with respect to the Eagle thrust).

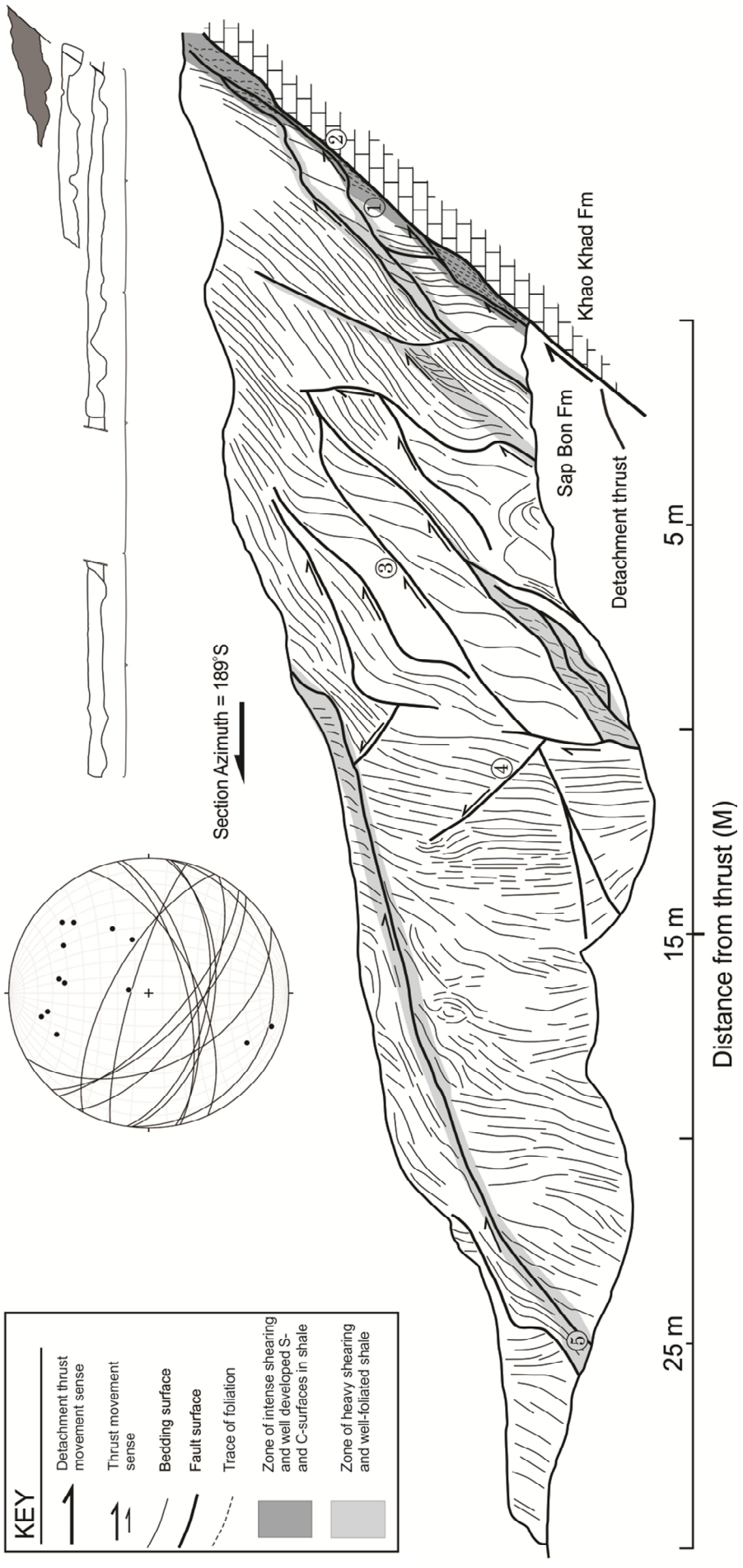

Fig. 5. Cross section through the top bench of Sap Bon Formation shale above the studied fault in Siam City Cement Quarry; inset section map displaying position and scale relative to other benches. Inset equal area stereonet displaying bedding orientations (great circles) and orientations of faults (poles to planes).

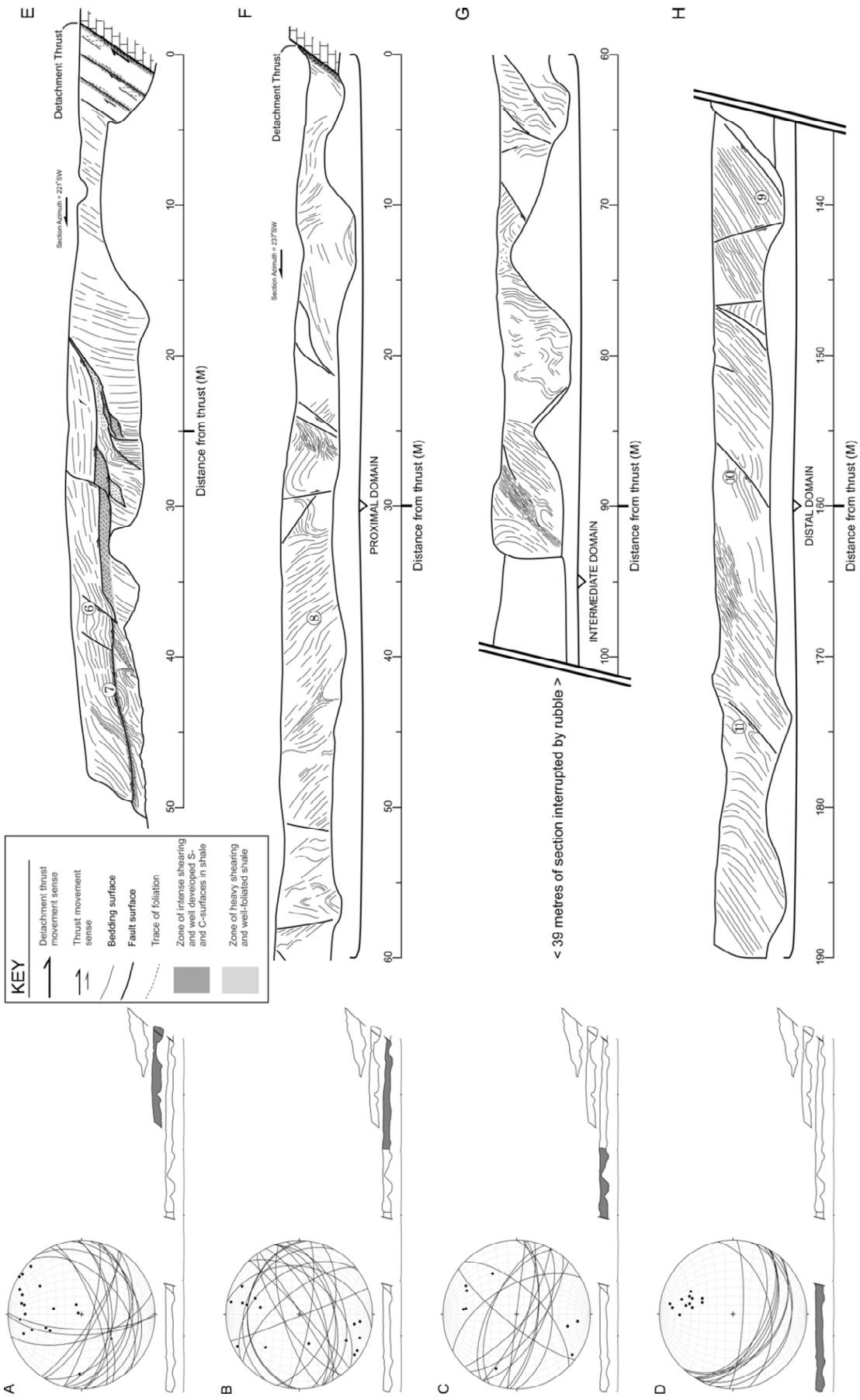

Fig 6. Cross section through the middle (top section) and bottom (divided into three lower sections) of Sap Bon Formation shale above the studied fault in Siam City Cement Quarry; inset section maps displaying position and scale relative to other benches. Inset equal area stereonets displaying bedding orientations (great circles) and orientations of slip faults (poles to planes)

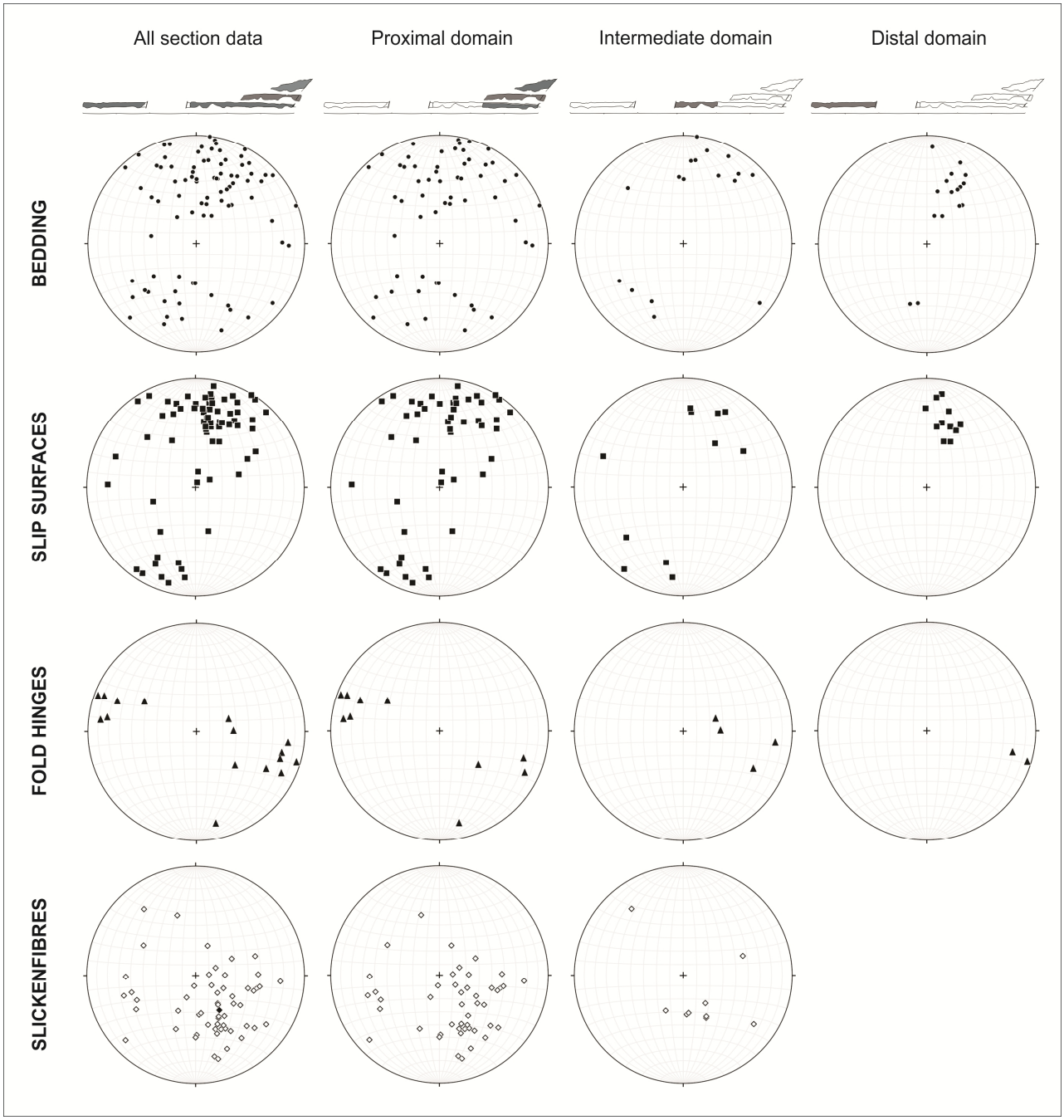

Fig 7. Lower hemisphere equal area stereographic projections of data sets from the Sap Bon Formation through the Siam City Cement Quarry cross sections. Data are separated into poles to bedding surfaces (circles), poles to slip surfaces (squares), fold hinge trends (triangles), and slickenfibre plunges = (hollow circles); each data set is separated for each domain. No slickenfibre data was recorded in the distal domain.

Fig. 8. Photographs of layer of heavily deformed shale above detachment thrust (top left); strain partitioning in finer layers of the Sap Bon Formation with S-C fabrics developed in shale (top right); calcite mineralisation in tension gashes (middle left); multiple orientations of slickenlines can be seen in discretely mineralised shears (middle right); meter scale duplexing in the top bench (Figure 5) of the cross section, note people for scale (bottom left and right).

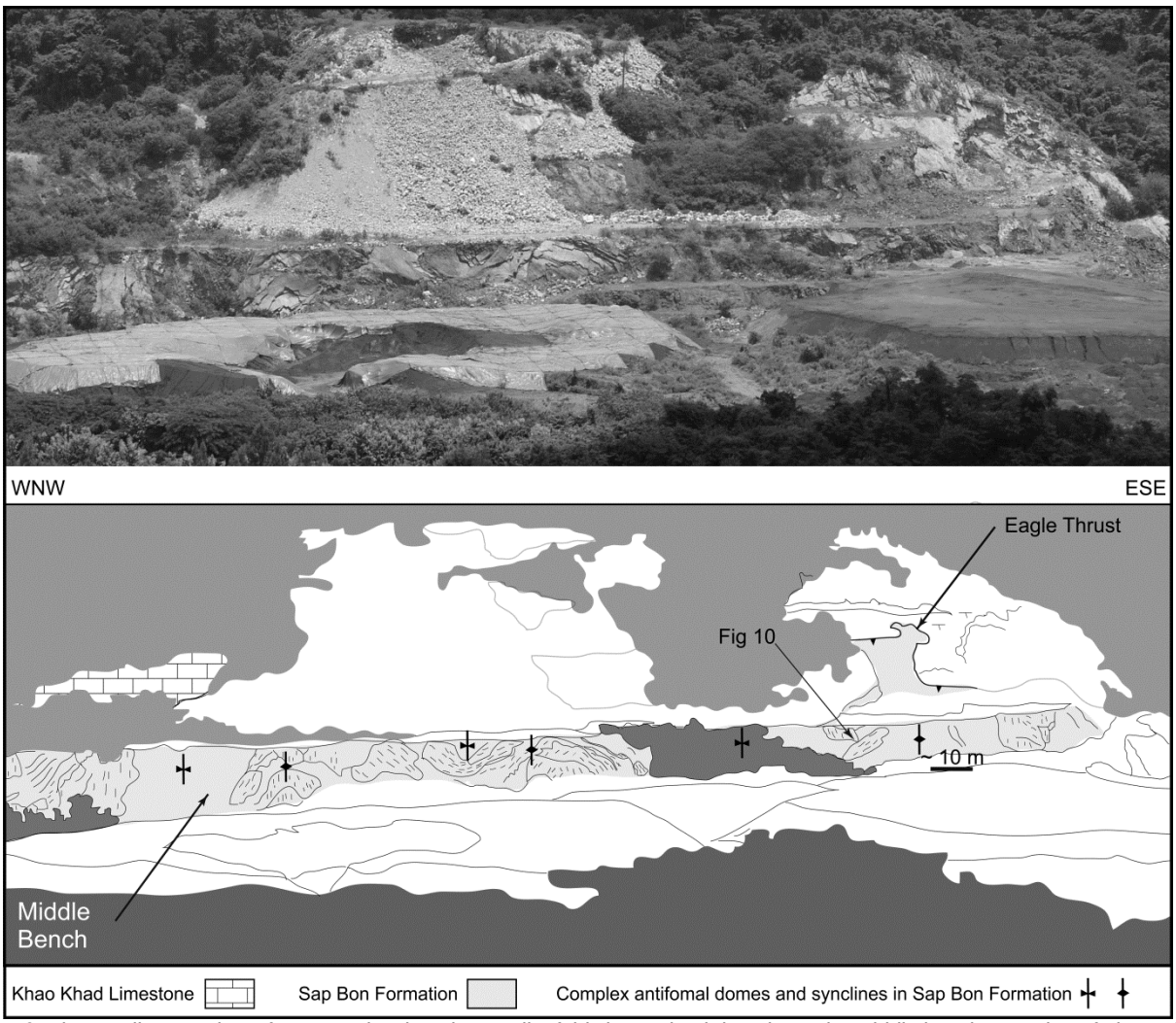

Fig. 9. Along-strike overview of outcrop showing along-strike folds in proximal domain on the middle bench. Location of Fig. 10 is shown

3.2.1 Proximal domain

The proximal domain extends from the Eagle thrust to approximately 60 metres south in the Sap Bon Formation. It is characterised by complex three-dimensional duplexes, significant local variations in orientation of structures, and heavily deformed, shale-rich layers exhibiting well-developed foliation and anastomosing faults (Fig. 5, labelled '5'). Poles to bedding in this domain show a significant spread in orientation (Fig. 7). Bedding planes generally dip toward the NNE to SSW but exhibit a range in strike from ~220° to 350°. Compared to the intermediate and distal domains, a significant number of bedding planes dip towards the north (antithetic) as well as the south (~350° to 020°). This variation is matched by significant spread in the orientation of faults (Fig. 7). The largest thrust fault exposed in the top and middle bench (Fig. 5, labelled '5'; Fig. 6E, labelled '7') juxtaposes bedding with two distinctly different orientations. Below the thrust, bedding dips approximately 40-60° to the S-SW, whereas above it beds are much shallower, dipping 5-20° to the S-SW. In a section of the bottom bench (Fig. 6F, labelled '8') approximately 30 to 60 metres from the Eagle thrust, beds dip back to the north at approximately 45-60°. This part of the section is likely the limb of a fold beyond the resolution of the section. Metre- to decametre-scale, curviplanar thrusts (like the one mentioned above) occur throughout the section in layers of finer grained, heavily-deformed material. These commonly exhibit a

10-30 centimetre wide, shear-zone like area of well-developed S- and C-surfaces on either side of the fault (Fig. 5, labelled '5'; Fig. 8). The low-angle, curviplanar, thrust in Fig. 5 (labelled '5') is interpreted to continue into the bench below (Fig. 6, labelled '7') and is marked by a zone of phyllite with a dominant S-C foliation. This zone is bounded above and below by zones of more competent sandstones. These features do not occur in the coarser packages where thrusts are discrete surfaces and lack the surrounding shear zone of the larger thrusts (Fig. 6E, labelled '6'). These smaller thrusts in the sandstone layers above and below the above mentioned thrust (as well as throughout the section) cut through and displace bedding on a small (centimetre to decimetre) scale (Fig. 11). These faults generally strike approximately ESE-WNW sympathetic to the Eagle thrust, verging to the N-NNE. They are also frequently associated with metre-scale fault-propagation folds (e.g. Fig. 6H, labelled '11'). The top bench (Fig. 5) presents a higher degree of detail than the rest of the section, displaying metre-scale duplexes (Fig. 8). The dominant deformational mechanism within the three domains appears to be fault-base contraction. However, the layer of shale directly above the Eagle thrust (Fig. 5, labelled '1') displays ductile deformational characteristics. The layer is 5-40 centimetres in thickness and exhibits very fine-grained, heavily-sheared, black shale (Fig. 8, top left). The layer varies in thickness below the structures of the overriding, more competent layers, thickening under hanging-wall flats and thinning in one point to form a shale weld (Fig. 5, labelled '2'). The structural style in the proximal domain is dominated by complex three-dimensional metre-scale duplexes, a high density of thrusts and heavily deformed packages of finer sediment. Thrust surfaces are tightly spaced on a metre scale (Fig. 5) and overlap to form roof and floor thrusts (Fig. 5, labelled '3'). These surfaces are also tightly laterally spaced.

3.2.1.1 Complex three-dimensional faulting

The cross-strike cross-sections do not entirely capture the complexity of the metre- to decametre-scale deformation in the top and middle benches. The middle bench (Fig. 6E) curves around to the west affording a virtually along-strike view of the Sap Bon Formation, where the complex three-dimensional nature of the deformed shale is visible. Figure 9 shows the overview of the outcrop where several short wavelength (decametres) along-strike anticlines and synclines are present, whose fold axes lie sub-parallel to the thrust transport direction (dip slip to the north). These anticlines are internally complex, with internal geometries that comprise imbricates, duplexes and out-of-sequence thrusts. The anticlines can be viewed as small-scale complex culminations. Figure 10 is a detail of one area in this zone (see Fig. 9 for location) displaying an along-strike view and an accompanying block diagram of the fault geometries in the proximal domain. Fault planes here define horses which exhibit a three-dimensional lozenge shape, and pinch out both across- and along-strike at the intersections of anastomosing faults. These faults commonly have mineral coatings of calcite which vary in thickness from millimetres to 5-10 centimetres. Individual fault planes exhibit mineral slickenfibre orientations, which are mostly consistent on each fault plane, but differ significantly compared to other fault planes (Fig. 10). However, some instances of multiple orientations of slickenfibres on the same fault plane do occur. A notable example exhibits a thick (~5 cm) mineral coating which has multiple levels of slickenfibres, each separated by several 3-5 millimetres of calcite (Fig. 8, middle right). Each individual layer in this 'stack' of slickenfibres has a different orientation. The mean orientation of these slickenfibres in the proximal domain (51→157) is consistent with the overall trend for the section. However, clearly 3D strain occurs locally in this zone.

3.2.2 Intermediate domain

The zone between 60 and 130 metres from the Eagle thrust displays a gradual transition between the structural characteristics of distal and proximal domains. Approximately 40 metres of section is unaccounted for due to rubble covering the outcrop. However, immediately south of this section break the structures transition into the simpler southward-dipping geometry of the distal domain. Bedding in this domain is less variably oriented than that of the proximal domain with a tighter cluster of poles to bedding (Fig.7) of southward dipping beds (dipping toward ~170° to 210°). This trend is mirrored by the orientation of faults (Fig. 6C & 7). In comparison to the proximal domain, heavily-deformed packages of finer-grained shales are less frequently observed. The large, curviplanar faults of the proximal zone, associated with these packages are therefore less common. Large faults are still common but they display a tendency towards more decametre than metre spacing, and duplex structures are less common than in the proximal domain.

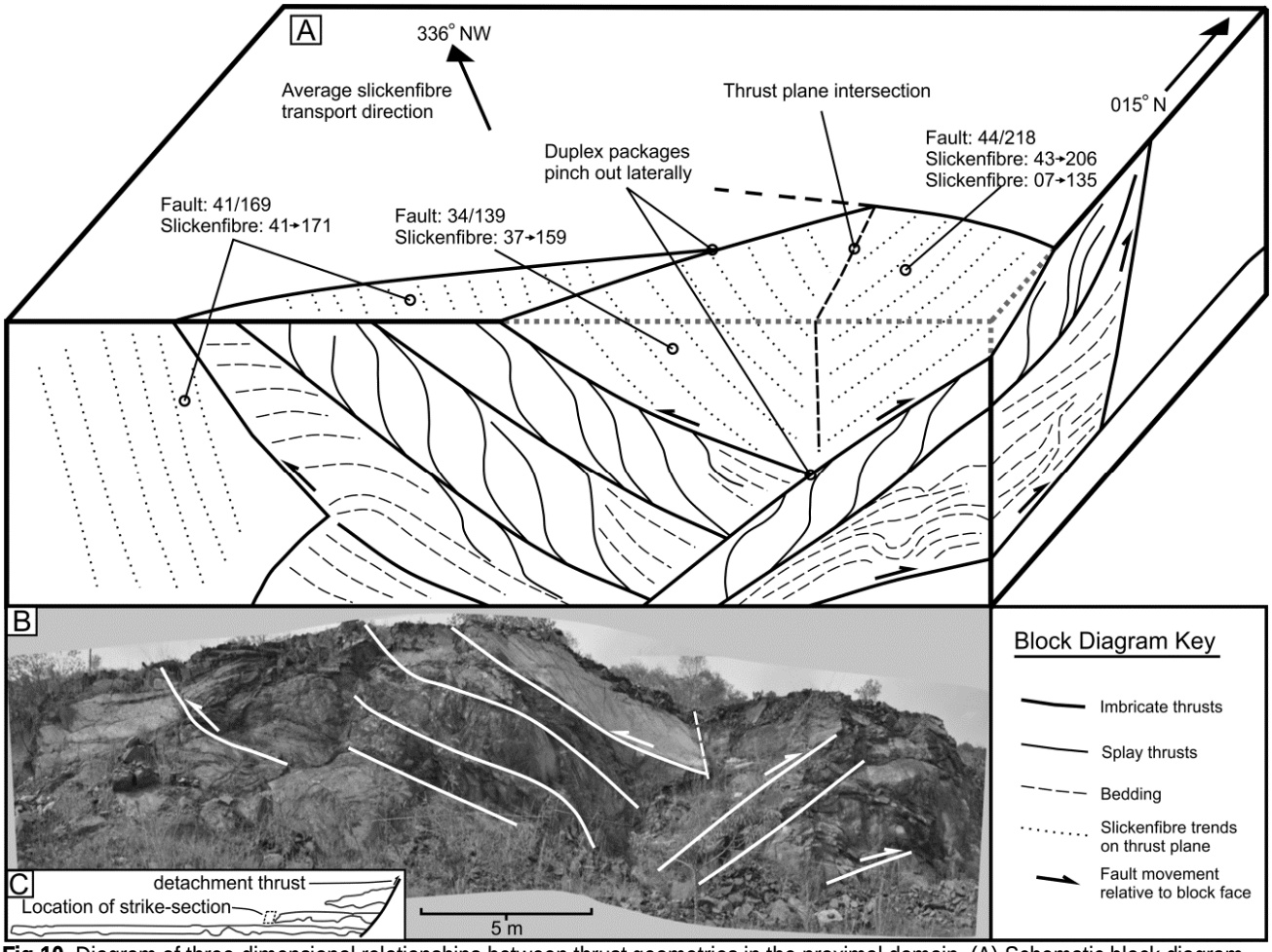

Fig 10. Diagram of three-dimensional relationships between thrust geometries in the proximal domain. (A) Schematic block diagram of strike-section through the deformed Sap Bon Formation illustrating variation in thrust orientation and pinch-out geometries of imbricates.

3.2.3 Distal domain

The distal domain extends from approximately 130 metres to 190 metres from the Eagle thrust and is characterised by much simpler deformational geometries than the proximal domain. Density of poles to bedding shows a tight distribution of south dipping beds, dipping toward ~180° to 210°. Foliations occur in zones of more heavily deformed, finer packages which are far less common than in the proximal domain. Thicker sandstone beds are much less

folded and variably orientated than in the proximal domain (comparison of Fig. 5 & 6H). Similarly to bedding, foliations are less variably oriented, consistently dipping toward S-SSW with a 15-50° dip. One section between 135 to 150 metres is in contrast to this trend with a high-angle-to-bedding pervasive cleavage with a steeply dipping NW-SE strike (Fig. 6, labelled '9'). A lack of any strike section in this domain means we can only speculate on the lateral variation of structures. In contrast to the proximal domain, the distal domain is characterised by simple thrust imbricates of consistent orientation (Fig. 6H) with major thrust surfaces that are spaced at a decametre-scale.

4. Discussion

Cases of outcropping shale detachment zones free of overprinting or intrusion are rare. These instances provide invaluable insight into the nature of these horizons at a scale and detail beyond the reach of modelling studies, well-data, or seismic data. A distinction must be made when using the term "detachment": this can referred only to a basal zone or surface which decouples and orogen from an undeformed foreland. However, the existence of detachments at lower and upper levels has long been defined (Dahlstrom, 1969) and a significant body of work (particularly in shales) on the identification and characterisation of multiple detachments lead the authors to use the term "upper-level detachment" to describe the shales in this study (Corredor et al., 2005; Briggs et al., 2006; Watkins et al., 2014). A detachment is defined as a horizon or zone that mechanically decouples deforming rocks or sediment from underlying non-deforming sequences. Upper-level detachments may act as roofs to splays from a basal detachment (floor thrust) as well has as influencing the structural style of overlying sequences. We determine the fault damage zone studied in the Khao Khwang Fold and Thrust Belt constitutes an upper-level detachment within the orogen, separating the highly and variably deformed Sap Bon Formation shales from the Khao Khad Formation packstones bellow, which exhibit comparatively minimal deformation.

Herein, we have presented detailed measured structural sections from the Siam City Cement Quarry, which demonstrate the deformational heterogeneity displayed in the outcropping Sap Bon Formation shale. The three structural domains (proximal, intermediate and distal) identified within the shale exhibit a relationship between spacing and complexity of deformational structures, and distance from the Eagle thrust at the base of the detachment. However, given the variability of deformation in the shale, distance from the detachment base is not the only control on deformational distribution.

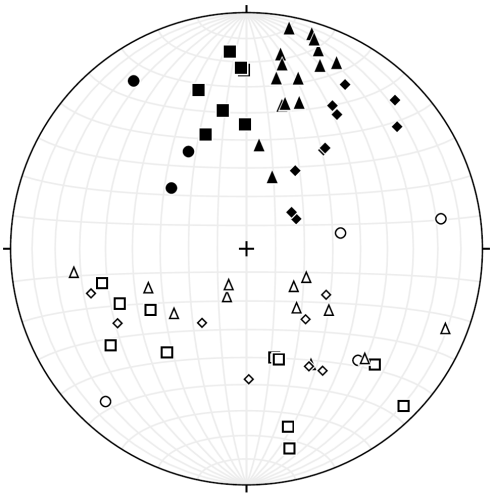

Fig 11. Lower hemisphere equal-area stereographic projections of poles to fault planes and slickenfibres associated with the three-dimensional fault damage in Figure 9. Poles to faults are plotted in solid colour, slickenfibres in hollow symbols. Each data set is divided into 30° swathes of fault plane dip directions: Circles dip toward 120-150°; squares dip toward 150-180°; triangles dip toward 180-210°; and diamonds dip toward 210-240°. Slickenfibres are plotted with the symbol of the fault plane on which they occur.

Spacing and complexity of deformational structures throughout the sections appears to be at least partially controlled by

thedistribution of finer, rheologically weaker shales. The words 'clay', 'mud' and 'shale' have widely been used interchangeably when referring to potentially mobile, fine-grained clastic sediments, without classification of consolidation or sediment/rock type (van Rensbergen and Morley, 2003). In this case we use the terms 'sand', 'silt' and 'clay' (and respectively sandstone, siltstone and shale) to simply describe the grain-size of the rock material (per the Wentworth scale (Wentworth, 1922)) independent of any interpretation on deformational style or 'shale mobility'.

Many authors support the existence of thick mobile shales characterised by undercompaction, overpressure and ductile deformational behaviour (Morley and Guerin, 1996; Van Rensbergen et al., 1999b; Van Rensbergen and Morley, 2000). However, there is evidence to suggest mobile shale has been over interpreted in the past (e.g. van Rensbergen and Morley, 2003). While this does not preclude the existence of deep, mobile shale, however, their prevalence and the nature of deformation in shales has come into recent debate due to the increasing quality of seismic data and further understanding of chemical diagenesis of shales (van Rensbergen and Morley, 2003; Cobbold et al., 2009; Maloney et al., 2010; Morley et al., 2014). While It is likely that shales are capable of viscous flow (Maloney et al., 2010), Morley et al. (2011) suggest that mobile masses of shale, like those found in salt detached systems, are unlikely and may have been interpreted over-frequently in the past. However, there remains a strong case for the existence of thick mobile shale acting as detachment surfaces or zones in fold and thrust belts (Corredor et al., 2005; Briggs et al., 2006; Cobbold et al., 2009; Maloney et al., 2010; Morley et al., 2011b). Investigation of mobile shale flow rates into anticlinal cores in the Niger Delta concluded that it is unlikely that deformation in mobile shale is accommodated entirely through ductile behaviour, and that the occurrence of mobile shale has been widely exaggerated (Maloney et al., 2010). This study calculated that the rate of flow into anticlinal cores was considerably greater than any measured rates of shale ejected from mud volcanoes and from this inferred ductile flow could not be the primary mechanism for the translation of observed volume of shale (Maloney et al., 2010). The thickened shale must therefore have another mechanism of internal structural thickening, likely through a mixture of brittle and ductile deformation (Maloney et al., 2010). It is suggested that thickness variations and other classic 2D indications of 'mobile shale' could be achieved through second-order (and smaller-scale) thrusting and folding within a detachment zone to form imbricate thrust stacks, resulting in the observed geometries of fold amplification and pinching of the detachment under synclines (van Rensbergen and Morley, 2003; Maloney et al., 2010; Morley et al., 2011b). The detachment zone in the Sap Bon Formation is an upper-level detachment zone and, it could be argued, not directly comparable to the thick, basal detachments of gravity driven systems in the aforementioned studies. However, we see no reason why the deformational mechanisms and structures formed in this upper-level detachment would differ from the basal detachment of the Khao Khwang Fold and Thrust Belt, or shale detachments in other collisional orogens.

The increasing observation and interpretation of shale detachments featuring complex, sub-seismic scale fault systems brings into question how complex deformational structures like those in the Siam City Cement Quarry evolve and accommodate shortening. While we have stated here that deformational behaviour appears to be influences by the distribution of fine-grained rock packages, as well as proximity to the Eagle thrust at the base of the detachment zone, it is not understood quantitatively how shortening is accommodated through the shale detachment zone. Shear zones in shales around decametre-

scale faults constitute a minimal thickness of the detachment zone, but it is possible these features within the proximal domain are responsible for a considerable portion of the overall shortening.

4.1 Complex three-dimensional structures

The three-dimensional deformation described in the proximal zone (Fig. 9 & 10) is characteristic of the complexity of fault damage zones in shales. Anastomosing fault systems are well documented, though they are more commonly described in normal and strike-slip fault systems and at a larger scale than this study (e.g. Sengör, 1979; Loveless and Meade, 2001). The differing apparent transport directions along differently orientated faults in this domain (inferred from slickenfibres) indicate they are not simply lateral and oblique ramps to the net transport direction. Slickenfibre 'stacks' in which changing transport direction is recorded along single faults

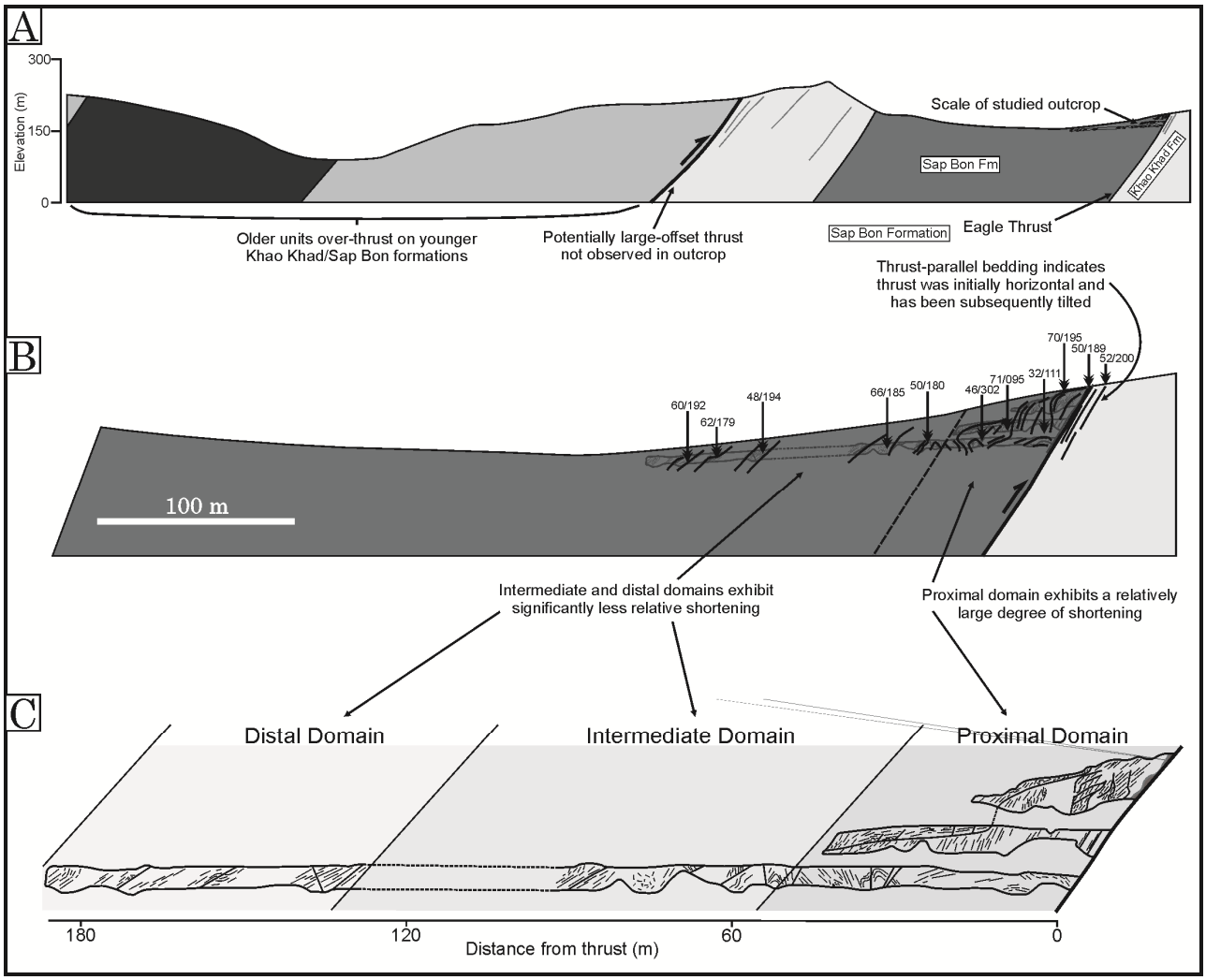

Fig 12. Summary of studied outcrop geometry in relation to geology of Siam City Cement Quarry. (A) Simplified cross section through the quarry showing position of Sap Bon Formation outcrop. (B) Blow-up of A showing overall variation in structural geometry and relative shortening in (C) the three structural domains of the cross sections of the Sap Bon Formation.

direction is recorded along single faults planes indicates a progressive change in local strain. Figure 11 displays slickenfibre orientations recorded on four fault sets, grouped according to the dip direction of their fault planes. No consistent transport direction is recorded for faults of any one orientation with slickenfibres from each fault set plotting roughly on a great

circle with a pole plunging toward the mean transport direction. One hypothesis is that these slickenfibres may have been rotated from and originally more consistent trend but as we observe no inflection points where folding of mineral-coated surfaces rotates slickenfibres, this is unlikely. Whether these locally (metre- to decametre-scale) differing transport directions are indicative of any lateral translation of material could not be determined as the complexity of deformation and lack of complete marker beds over even short distances makes shortening estimates impossible. We interpret that this system of anastomosing faults and record of variable local transport direction is the result of progressive non-plane strain deformation. It is possible that 'flow' or translation of material by faulting is complexly influenced, as faults within the system develop according to local strain within and overall NNW to SSE shortening regime, in turn influencing the local strain around them

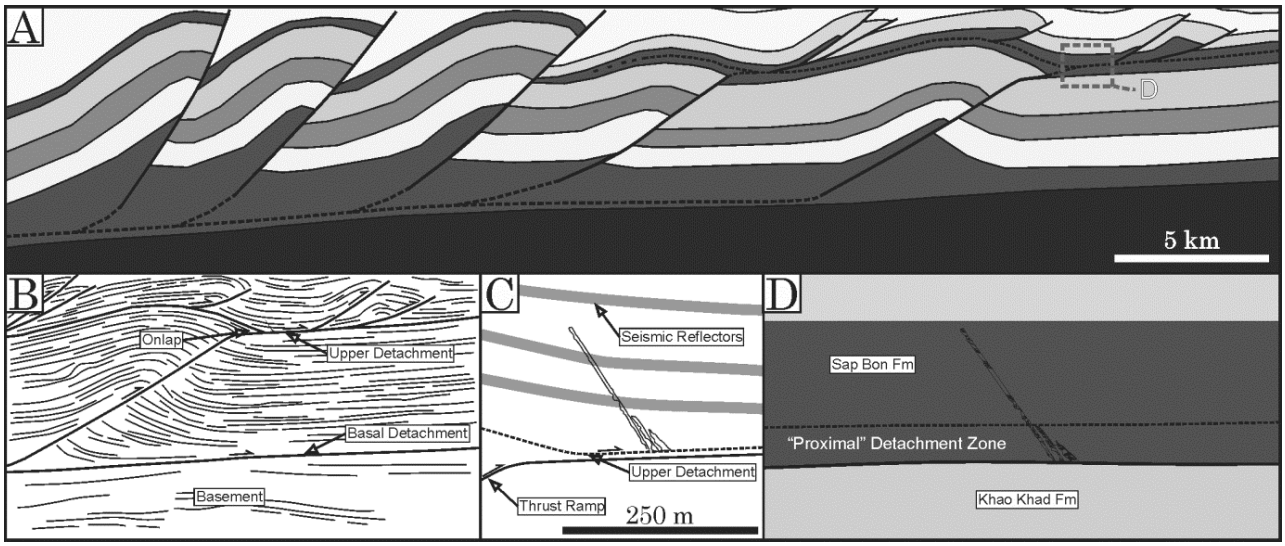

Fig. 13. Summary of the geometry and scale of cross-sections mapped within the Siam City Cement Quarry. (A) Schematic cross section through an idealised fold-thrust belt displaying multiple detachment levels. (B) Line drawing of seismic section through A, displaying broad geometries of upper-level detachment (after Corredor et al. 2005). (C) Blow-up of B showing scale of outcrop in this study in comparison with seismic reflectors. (D) Summary of interpretation of how the geometry of the outcropping Sap Bon Formation constitutes an upper-level detachment.

and the progressive development of the fault system (e.g. Fagereng et al. 2011). This would result in variation of transport directions and fault orientations observed, as well as the multiple shear senses along fault surfaces, apparently active at different times.

4.2 Deformational mechanisms

The Sap Bon Formation consists of interbedded siltstones to fine- to medium-grained sandstones, a compositional variation which results in variations in mechanical competency (Ramsay, 1982; Goodwin and Tikoff, 2002). Deformational style of fine-grained rocks may depend on the thickness and distribution of mechanically weaker shale layers, which influence how strain is partitioned within zones of deformation (Lister and Williams, 1983). The Sap Bon Formation is a deformed shale sequence comprised of layers of varying competency causing variations in shear strain rate (Goodwin and Tikoff, 2002; Fagereng and Sibson, 2010). Deformation in the Sap Bon Formation is partitioned into shale layers and these zones of low competency exhibit well-developed foliations, relatively uniform strain, and potentially viscous deformation. Conversely, displacement in more competent coarse-grained rocks is accommodated by discrete fractures (thrust faults) – more brittle

deformational structures. This contrast in strain rate may also be time dependant; the proximal domain exhibits a greater proportion of low-competency, continuous deformation layers (Fagereng and Sibson, 2010) in which lenses of competent material occur as boudins. This suggests more competent layers may have undergone cataclastic dismemberment in areas proximal to the Eagle thrust during progressive deformation. What ratio of overall shortening is accommodated by distributed shear strain in the lower competency layers (and potentially lower strain rates over a wider zone), compared to discrete faulting in competent layers, is not apparent. However, the largest faults within the cross-sections propagate through these low-competency shale layers, suggesting transient high rates of strain. This variation in shear strain rate between two end-member mechanisms (and competencies in between) affects the rheological response to stress and results in the mixture of viscous and brittle deformational behaviour observed (Fagereng and Sibson, 2010). Given the variation in strain rate and distribution of continuous (viscous) and discontinuous (brittle) deformation (after Fagereng and Sibson, 2010), delimiting a finite zone as the 'detachment zone' is arbitrary. We loosely classify the proximal domain as the upper-level detachment zone in this as it appears to constituent the greater degree of shortening and translation of material in the reference frame of the Siam City Cement Quarry (Fig. 12)

5. Conclusions

The structural observations of the shale detachment zone in the Khao Khwang Fold and Thrust Belt presented here indicate mixed ductile-brittle deformational behaviour (continuous-discontinuous (Fagereng and Sibson, 2010)) in an upper-level detachment zone. Distribution of deformational mechanisms appears to be influenced by stratigraphic distribution of competency (and potentially time dependant distribution in progressive deformation) as well proximity to the Eagle thrust at the base of the detachment zone. Anastomosing faults in the detachment zone characterise complex three-dimensional deformation with a potential for both longitudinal and transverse translation of material. These structures occur at a scale well beyond the resolution of seismic imaging (Fig. 13).

The distribution of continuous and discontinuous deformation as a factor of distance from the Eagle thrust has led to the subdivision of the observed outcrop into three structural domains:

- The proximal domain, characterised by low competency zones of continuous deformation, complex three-dimensional duplexing and significant variation in orientation of structures. Vergence of these structures displays a wide spread of data verging from ENE-NW through to WSW-SE with a frequent occurrence of antithetic faults.

- The intermediate domain, characterised by decreasing structural complexity, greater spacing between major fault surfaces and a decrease in the frequency and complexity of duplexes. Orientation of folding and faulting becomes less variable with a NNW-NE to SSE-SW vergence.

- The distal domain, characterised by significantly less-complex deformational geometries, few zones of low competency continuous deformation, simple thrust imbricates and fault-related folding with a much less variable, N-NNE vergence.

We propose that the Eagle thrust and associated shale detachment zone is potentially analogous to shale detachments in zones in other collisional orogens. Further investigation of mineralogy and deformational conditions of this detachment zone will provide a better understanding of its deformational mechanisms.

References

Briggs, S. E., R. J. Davies, J. A. Cartwright, and R. Morgan, 2006, Multiple detachment levels and their control on fold styles in the compressional domain of the deepwater west Niger Delta: Basin Research, v. 18, p. 435-450.

Bunopas, S., 1981, Paleogeographic History of Western Thailand and Adjacent Parts of South-East Asia: a Plate Tectonics Interpretation: Submitted for the Degree of Doctor of Philosophy at the Victoria University of Wellington, Victoria University of Wellington.

Cobbold, P. R., B. J. Clarke, and H. Løseth, 2009, Structural consequences of fluid overpressure and seepage forces in the outer thrust belt of the Niger Delta: Petroleum Geoscience, v. 15, p. 3-15.

Cohen, H. A., and K. McClay, 1996, Sedimentation and shale tectonics of the northwestern Niger Delta front: Marine and Petroleum Geology, v. 13, p. 313-328.

Corredor, F., J. H. Shaw, and F. Bilotti, 2005, Structural styles in the deep-water fold and thrust belts of the Niger Delta: AAPG bulletin, v. 89, p. 753-780.

Dahlen, F., 1990, Critical taper model of fold-and-thrust belts and accretionary wedges: Annual Review of Earth and Planetary Sciences, v. 18, p. 55.

Dahlen, F., J. Suppe, and D. Davis, 1984, Mechanics of fold-and-thrust belts and accretionary wedges: Cohesive Coulomb theory: Journal of Geophysical research, v. 89, p. 10087-10,101.

Dahlstrom, C., 1969, The upper detachment in concentric folding: Bulletin of Canadian Petroleum Geology, v. 17, p. 326-346.

Davis, D., J. Suppe, and F. Dahlen, 1983, Mechanics of fold-and-thrust belts and accretionary wedges: Journal of Geophysical research, v. 88, p. 1153-1172.

Fagereng, Å., 2011, Fractal vein distributions within a fault-fracture mesh in an exhumed accretionary mélange, Chrystalls Beach Complex, New Zealand: Journal of Structural Geology, v. 33, p. 918-927.

Fagereng, Å., and R. H. Sibson, 2010, Melange rheology and seismic style: Geology, v. 38, p. 751-754.

Goodwin, L. B., and B. Tikoff, 2002, Competency contrast, kinematics, and the development of foliations and lineations in the crust: Journal of Structural Geology, v. 24, p. 1065-1085.

Hinthong, C., S. Chuaviroj, W. Kaewyana, S. Srisukh, C. Pholprasit, and S. Pholachan, 1985, Geological map of Thailand 1: 250 000 (Changwat Phranakorn Sri Ayutthaya, ND 47–8): Geological Survey Division of the Department of Mineral Resources, Bangkok, Thailand.

Lister, G., and P. Williams, 1983, The partitioning of deformation in flowing rock masses: Tectonophysics, v. 92, p. 1-33.

Loveless, J. P., and B. J. Meade, 2011, Stress modulation on the San Andreas fault by interseismic fault system interactions: Geology, v. 39, p. 1035-1038.

Maloney, D., R. Davies, J. Imber, S. Higgins, and S. King, 2010, New insights into deformation mechanisms in the gravitationally driven Niger Delta deep-water fold and thrust belt: AAPG bulletin, v. 94, p. 1401-1424.

Morley, C., P. Ampaiwan, S. Thanudamrong, N. Kuenphan, and J. Warren, 2013, Development of the Khao Khwang Fold and Thrust Belt: implications for the geodynamic setting of Thailand and Cambodia during the Indosinian Orogeny: Journal of Asian Earth Sciences.

Morley, C., P. Ampaiwan, S. Thanudamrong, and J. Warren, 2011a, Structural Style and Evolution of the Saraburi Group (Khao Khwang Platform), PTTEP Chulalongkorn University

Morley, C. K., and G. Guerin, 1996, Comparison of gravity-driven deofrmation styles and behaviour associated with mobile shales and salt: Tectonics, v. 15, p. 1154-1170.

Morley, C. K., R. King, R. Hillis, M. Tingay, and G. Backe, 2011b, Deepwater fold and thrust belt classification, tectonics, structure and hydrocarbon prospectivity: A review: Earth-Science Reviews, v. 104, p. 41-91.

Morley, C. K., J. Warren, M. Tingay, P. Boonyasaknanon, and A. Julapour, 2014, Comparison of modern fluid distribution, pressure and flow in sedi **Fig 1.** Schematic cross section of a think-skinned fold-thrust belt exhibiting multiple detachment levels.
ments associated with anticlines growing in deepwater (Brunei) and continental environments (Iran): Marine and Petroleum Geology, v. 51, p. 210-229.

Needham, D., 2004, Deformation in Moffat Shale detachment zones in the western part of the Scottish Southern Uplands: Geological Magazine, v. 141, p. 441-453.

Ramsay, J. G., 1982, Rock ductility and its influence on the development of tectonic structures in mountain belts: Mountain Building Processes, Academic Press, London, p. 111-127.

Rowan, M. G., F. J. Peel, and B. C. Vendeville, 2004, Gravity-driven fold belts on passive margins.

Sengör, A., 1979, The North Anatolian transform fault: its age, offset and tectonic significance: Journal of the Geological Society, v. 136, p. 269-282.

Sherkati, S., M. Molinaro, D. Frizon de Lamotte, and J. Letouzey, 2005, Detachment folding in the Central and Eastern Zagros fold-belt (Iran): salt mobility, multiple detachments and late basement control: Journal of Structural Geology, v. 27, p. 1680-1696.

Simpson, G. D. H., 2009, Mechanical modelling of folding versus faulting in brittle–ductile wedges: Journal of Structural Geology, v. 31, p. 369-381.

Sone, M., and I. Metcalfe, 2008, Parallel Tethyan sutures in mainland Southeast Asia: new insights for Palaeo-Tethys closure and implications for the Indosinian orogeny: Comptes Rendus Geoscience, v. 340, p. 166-179.

Ueno, K., and T. Charoentitirat, 2011, Carboniferous and Permian: The Geology of Thailand. Geological Society, London, p. 71-136.

van Rensbergen, P., C. Morley, D. Ang, T. Hoan, and N. Lam, 1999a, Structural evolution of shale diapirs from reactive rise to mud volcanism: 3D seismic data from the Baram delta, offshore Brunei Darussalam: Journal of the Geological Society, v. 156, p. 633-650.

Van Rensbergen, P., and C. K. Morley, 2000, 3D Seismic study of a shale expulsion syncline at the base of the Champion delta, offshore Brunei and its implications for the early structural evolution of large delta systems: Marine and Petroleum Geology, v. 17, p. 861-872.

van Rensbergen, P., and C. K. Morley, 2003, Re-evaluation of mobile shale occurrences on seismic sections of the Champion and Baram deltas, offshore Brunei: Geological Society, London, Special Publications, v. 216, p. 395-409.

Van Rensbergen, P., C. K. Morley, A. D. W., T. Q. Hoan, and L. N. T., 1999b, Structural evolution of shale diapirs from reactive rise to mud volcanism: 3D siesmic data from the Baram delta offshore Brunei Darussalam: Journal of Structural Geology, v. 156, p. 633-650.

Watkins, H., C. E. Bond, and R. W. Butler, 2014, Identifying multiple detachment horizons and an evolving thrust history through cross-section restoration and appraisal in the Moine Thrust Belt, NW Scotland: Journal of Structural Geology, v. 66, p. 1-10.

Wentworth, C. K., 1922, A scale of grade and class terms for clastic sediments: The Journal of Geology, v. 30, p. 377-392.

Chapter 3

Published as Hansberry, R. L., Collins, A. S., King, R. C., Morley, C. K., Giże, A. P., Warren, J., Löhr, S. C., & Hall, P. A. 2015. Syn-deformation temperature and fossil fluid pathways along an exhumed detachment zone, khao khwang fold-thrust belt, Thailand. *Tectonophysics*, *655*, 73-87.

Syn-deformation temperature and fossil fluid pathways along an exhumed detachment zone, Khao Khwang Fold-Thrust Belt, Thailand

Abstract

Shale detachment zones, their influence on deformational style, and their internal mechanisms of deformation are an understudied aspect of fold-thrust belts. Properties such as deformational temperature, lithology, and mineralogy are often recognized as having a key influence on the rheology and deformational style of detachment zones and overlying fold-thrust belts. However, little work has been conducted on rock properties of known detachment zones. A recently described upper-level detachment zone in the exhumed Khao Khwang Fold-Thrust Belt of central Thailand provides an ideal natural laboratory for investigation of the deformation conditions of the detachment zone, and association with its complex deformational style. The low-grade metamorphic indicator illite crystallinity is used to broadly constrain deformational temperatures, while oxygen and carbon stable isotope analysis provides insight into fluid flow history and fluid-rock interaction. Illite crystallinity data indicate deep diagenetic, to low anchizonal conditions, and temperatures of ~160-210 °C in the shale detachment, interpreted as reflecting peak metamorphic conditions during the Triassic Indosinian Orogeny. No trend between the intensity (spacing, complexity) of structures and illite crystallinity is observed. However, shale shear zones of continuous-style deformation and inferred higher finite strain display uniformly higher illite crystallinity than surrounding packages of discontinuously faulted shales. We also note a positive association between total organic carbon content in the shales and the spacing and complexity of deformational structures. Data from limestones and syn-tectonic vein fills detail the history of fluid-rock interaction during early mesogenesis, through to orogenesis. The early covariant trend of increasingly negative $\delta^{13}C$ and $\delta^{18}O$ values is attributed to increasing burial, while a divergent orogenic trend of increasingly negative $\delta^{18}O$ values is interpreted as the result of a loss of matrix permeability and interruption of fluid-rock re-equilibration. These hottest fluids were concentrated along large thrusts which facilitated fluid movement during orogenesis.

Key words: Shale detachment, fluid flow, stable isotopes, illite crystallinity, Thailand

1. Introduction

The structural behaviour of detachment zones and their influence on the structural style of fold-thrust belts has been widely documented (Davis et al., 1983; Dahlen, 1990; Rowan et al., 2004; Corredor et al., 2005; Morley et al., 2011a). Detachment zones can vary significantly in thickness and spatial distribution, and occur at multiple levels in a fold-thrust belt. Previous studies have focused primarily on interpretation of seismic reflection data and well data from recent and active deepwater fold-thrust belts (DWFTBs) (e.g. Niger Delta – Bilotti et al., 2005; Briggs et al., 2006) or are reviews of structural style and detachment layer influence of active fold-thrust belts across a variety of settings (e.g. Rowan et al., 2004; Morley et al., 2011a). The thickness, spatial distribution and rheology of detachment zones have been shown to exert significant control on fold-thrust belt geometries (e.g. Stewart, 1996; Briggs et al., 2006; Simpson, 2009). The vast majority of studies on, or incorporating, detachment zone behaviour are also focused at

a foldbelt, or at least 10s of kms scale (e.g. Rowan et al., 2004; Sherkati et al., 2005; Maloney et al., 2010).

A considerable range of factors contribute to shale detachment weakness, some are interrelated. These factors include tectonic setting, burial history, temperature of deformation, mineralogy at both the time of deposition and the time of deformation (diagenesis/metamorphism), stratigraphic thickness, mechanical stratigraphic relationships with adjacent layers, strain rate and fluid-distribution/overpressure history (e.g. (Davis et al., 1983; Stewart, 1996; Simpson, 2009; Ding et al., 2012; Hansberry et al., 2014). Consequently there are considerable variations in the way shale detachments develop and behave. However, three main factors can be considered as contributing to shale weakness: 1) overpressured fluids (Hubbert and Rubey 1959; Dahlen, 1990; Davis et al., 1983; Morley, 1992; Bilotti and Shaw, 2005; Cobbold et al., 2013; Suppe, 2015); 2) bulk mineralogy characteristics (Byerlee, 1978; Maltman, 1994; Moore and Lockner, 2008); and 3) the efficiency of structure localization during deformation (Viti and Collettini, 2009; Rutter, et al., 2013). These mechanisms are not mutually exclusive, and can complement each other. However, some recent publications emphasize the importance of a particular mechanism. For example Suppe (2015), and Aydin and Engelder (2014) stress the importance of overpressure; Haines et al. (2013) point out the importance of shale fabrics in localizing zones of weakness in clay-rich rocks irrespective of specific clay mineral composition; and Rutter et al. (2013) discuss how a small percentage of low-friction minerals can become concentrated on slip surfaces and exert a disproportionately large effect on fault-rock strength.

The influences on the rheology of detachment zones and fault damage zones, in exhumed fold-thrust belts remain largely understudied, as a result of the generally inaccessible nature of deeply buried, active shale detachment zones for detailed study. Studies examining rheology, and structural response in fine-grained sediments (or independent of medium) provide insight into the effects of competency contrast (Goodwin and Tikoff, 2002; Simpson, 2009), bulk rheology (Fagereng and Sibson, 2010), vein development and fluid flow (Fagereng, 2011b, a; Wells et al., 2014), and deformational temperature and strain (Kisch, 1991a; Gutiérrez-Alonso and Nieto, 1996b). More broadly it is important to consider the structure, mechanism, and fluid flow properties of a fault zone or system as inter-related (Faulkner et al., 2010). Recently presented work on an exposed shale detachment zone analogue (and broader fault damage zone) in the Khao Khwang Fold and Thrust Belt (KKFTB), Central Thailand (Fig. 1), provides an opportunity to investigate the fluid flow history, influences on rheology, and structural behaviour of fault zones in shale at an outcrop scale (Hansberry et al., 2014).

The scope of this study is to (1) investigate the association between the maximum deformational temperature of the detachment zone, and the heterogeneity of deformational mechanisms therein. This is achieved by determining illite crystallinity, often used to evaluate very low-grade metamorphic conditions (VLGM); (2) document the mineralogical compositions of low and high competency rock packages that delimit

contrasting deformational mechanisms; (3) investigate any association between rock total organic carbon content (TOC) and variation in the deformational style within the detachment zone; (4) investigate flow history and temperature of fluids which precipitated calcite veins within the detachment zone, using δ13C and δ18O isotope analysis. Assessing deformational pore-pressure in a now

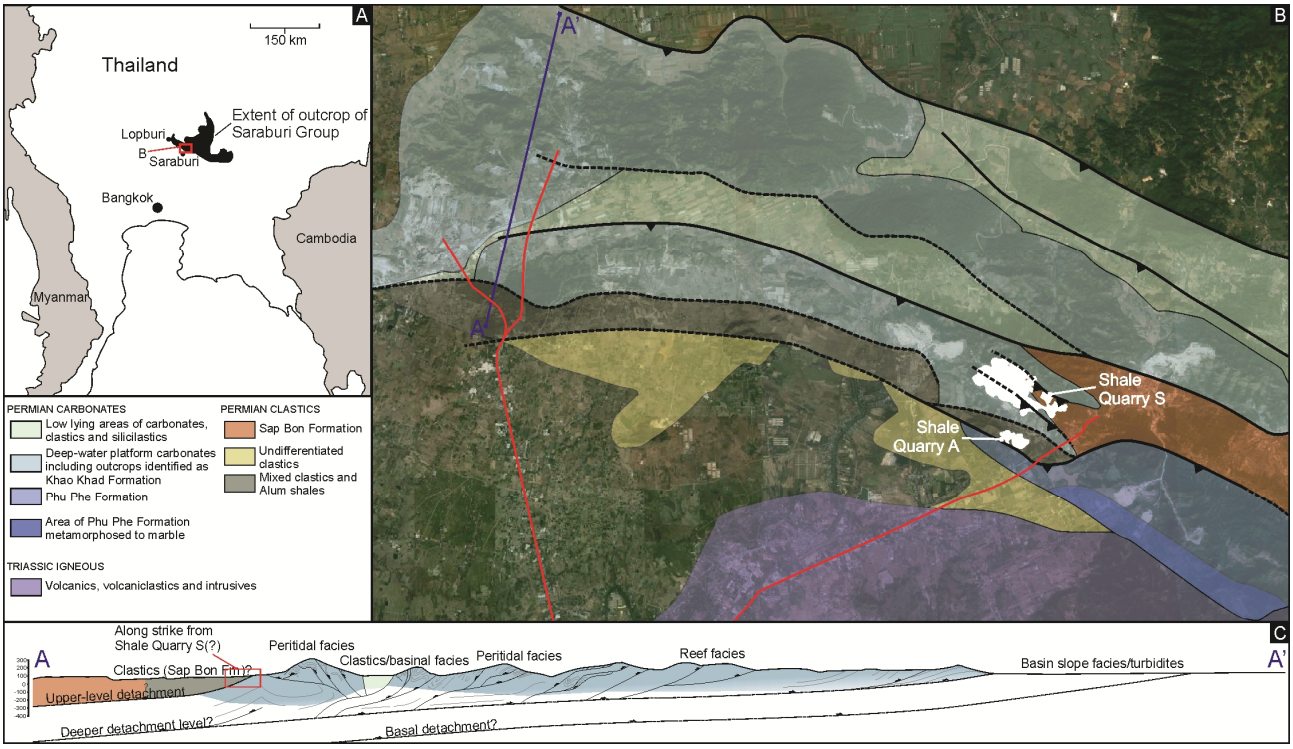

Fig. 1. (A) Location of outcropping Saraburi Group in the Khao Khwang Fold-Thrust Belt. (B) Geological map of the Saraburi area showing the locations of quarries in this study (white), major highways (red), and the location of the cross section A-A' (after Morley et al. 2013). (C) Cross-section A-A' along quarry exposures on highway 21, note multiple interpretation of the southernmost clastics as being equivalent to either the Sap Bon Fm, or the 'alum shales' found in shale quarries S and A respectively.

exhumed section is problematic (as no direct measure of palaeo-pore pressure exists) and has not been attempted in this study.

2. Geological setting

2.1 General framework

The geology of the Central Thailand KKFTB and surrounding Khorat Plateau is not extensively studied. The tectonic model of the Triassic Indosinian Orogeny, responsible for the formation of the fold belt and the deformation of the shale detachment in this study, has been broadly constrained by several authors (Sone and Metcalfe, 2008; Barber et al., 2011; Morley et al., 2011b), and is a focus of recent and ongoing work (Morley et al., 2013; Arboit et al., 2014). The Permian carbonates, clastics and siliciclastics in the Saraburi-Pak Chong area form part of the Saraburi Group, first defined by Bunopas (1981), then refined by Hinthong et al. (1985) to refer only to the latest Carboniferous-Permian sedimentary rocks on the Khao Khwang platform. Six formations in a simple younging up sequence (Phu Phe, Khao Khwang, Nong Poon, Pang Asok, Khao Khad and Sap Bon formations) have since been shown through paleontological data to be mostly

contemporaneous and potentially coeval facies variations (Ueno and Charoentitirat, 2011)(Fig. 2). Hansberry et al. (2014) described, in detail, the deformation in the Sap Bon Formation shales, constituting an upper-level detachment (Fig. 3).

2.2 Study Area

Hansberry et al. (2014) described a mixed continuous-discontinuous deformational style within a fault damage-zone in the Sap Bon Formation shales. This constitutes an upper-level detachment zone in the KKFTB, with the Eagle Thrust at its base (Figs. 3, 4). The exposure of the Sap Bon Formation shales is divided into three structural domains; this is based on increasing occurrence of 'shale shear zones', and increasing three-dimensional complexity of faulting and folding geometries with proximity to the Eagle Thrust (Hansberry et al., 2014)(Fig. 4). The three structural domains are described as:

- The Proximal Domain, characterised by low competency zones of continuous deformation, complex three-dimensional duplexing and significant variation in orientation of structures. Vergence of these structures varies widely, from ENE-NW through to WSW-SE with frequent occurrence of antithetic faults. This zone also features an anastomosing system of decametre-scale faults characterising complex three-dimensional deformation with a potential for both longitudinal and transverse translation of material (Hansberry et al., 2014).

- The Intermediate Domain, characterised by decreasing structural complexity, greater spacing between major fault surfaces and a decrease in the frequency and complexity of duplexes. Orientation of folding and faulting becomes less variable with a NNW-NE to SSE-SW vergence (Hansberry et al., 2014).

- The Distal Domain, characterised by significantly less-complex deformational geometries, few zones of low competency continuous deformation, simple thrust imbricates and fault-related folding with a much less variable, N-NNE vergence (Hansberry et al., 2014).

Fig. 2. Existing stratigraphy after Ueno and Charoentitirat (2011) in comparison to a time-space plot displaying the stratigraphic and structural relationships of rock formations outcropping in the Siam

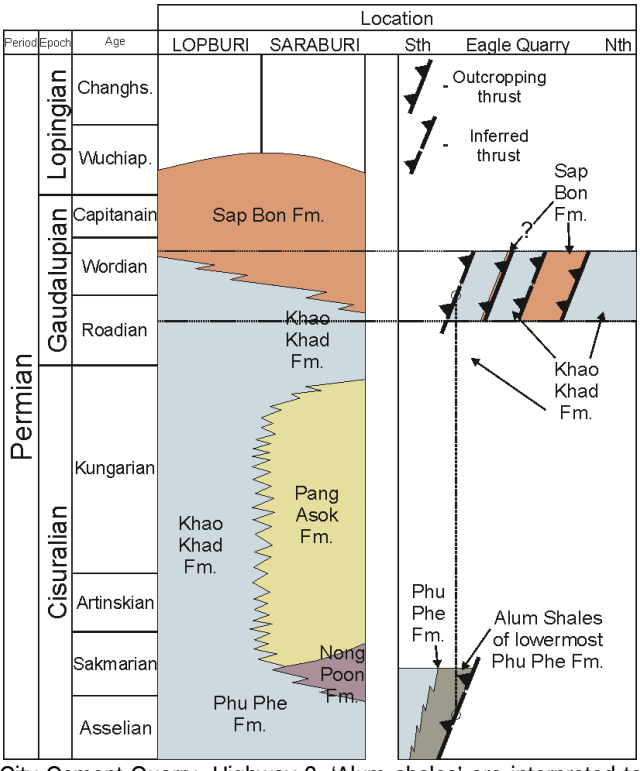

City Cement Quarry, Highway 2. 'Alum shales' are interpreted to be the lowest part of the Phu Phe Fm given the transitional stratigraphic contact between the two in Shale Quarry A (though this contact is also faulted). The Sap Bon Fm occurs mostly in the southern lowlands to the south of the Eagle Quarry but is interpreted here as in thrust contact with the Khao Khad Fm.

Shale shear zones or packages of low competency rock exhibiting relatively uniform strain contrast with packages of more competent coarse-grained rocks, where strain is accommodated by discrete fractures (Fig. 5). The shale shear zones exhibit well-developed foliations and the largest faults propagate through these layers, leading the authors to interpret transient high strain rates. The distribution of these two end-members of deformational mechanism (from here referred to as continuous or discontinuous deformation)

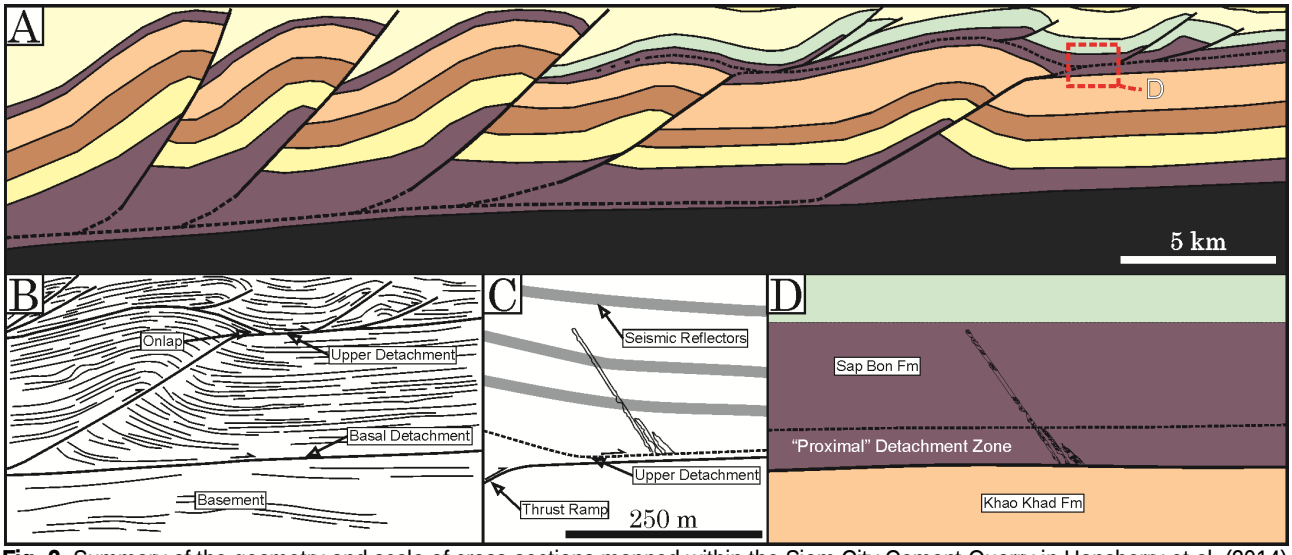

Fig. 3. Summary of the geometry and scale of cross-sections mapped within the Siam City Cement Quarry in Hansberry et al. (2014) (A) Schematic cross section through an idealised fold-thrust belt displaying multiple detachment levels. (B) Line drawing of seismic section through A, displaying broad geometries of upper-level detachment (after Corredor et al. 2005). (C) Blow-up of B showing scale of outcrop in this study in comparison with seismic reflectors. (D) Summary of interpretation of how the geometry of the outcropping Sap Bon Formation constitutes an upper-level detachment.

throughout the detachment zone is likely the result of stratigraphic variation, though a time-dependant distribution in progressive deformation is also posited (Hansberry et al., 2014).

3. Methods

A method for quantitative determination of temperature in diagenetic to very-low grade metamorphic (VLGM) conditions is not well constrained. This is a result of a number of problems encountered when interpreting low-temperature metamorphic reactions (Underwood et al., 1993; Kosakowski et al., 1999; Mählmann et al., 2012). The minerals involved are usually very fine-grained and occur in disequilibrium assemblages and metastable phases (Warr et al., 1996). Reactions may also be mostly influenced by kinetics (Warr et al., 1996; Kosakowski et al., 1999). Most studies deal with metamorphism above 350 °C where the formation of minerals such as biotite and chlorite can constrain temperature (Mählmann et al., 2012). However, standardised illite crystallinity is widely used as a method to broadly constrain temperature under diagenetic and VLGM conditions (Frey et al., 1980; Guthrie et al., 1986; Warr et al., 1996; Ji and Browne, 2000; Hara et al., 2009). Previous studies have mainly used either the 'Kübler Index' (Kübler, 1968; Frey et al., 1980; Kisch, 1991b) or the 'Crystallinity Index Standard' (Warr and Rice, 1994) to define metamorphic

grade zones based on established illite crystallinity boundaries. Given the uncertainty of constraining VLGM conditions with illite crystallinity data alone, the last couple of decades have seen many authors employ multiple analytical techniques (e.g. vitrinite reflectance, chlorite crystallinity) to better constrain temperature and pressure conditions of VLGM (Barker and Halley, 1986; Guthrie et al., 1986; Pollastro, 1986; Hesse and Dalton, 1991).

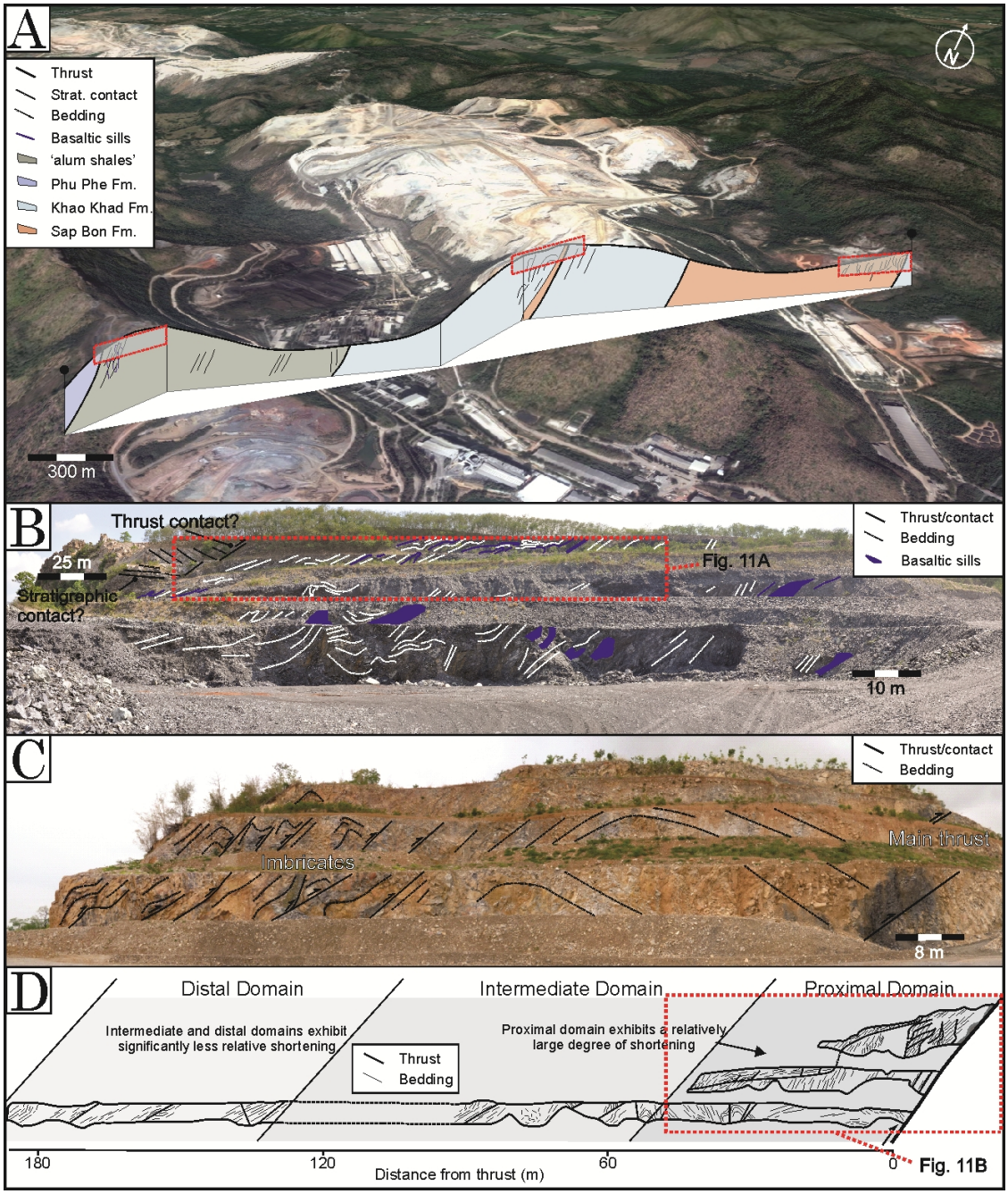

Fig. 4. (A) Cross-section through a 3D isometric view of the Siam City Cement Quarry showing the broad geology and the locations of B, C, and D. (B) Cross-section overlay of the alum shales and Phu Phe Fm packstones in Shale Quarry A, note the stratigraphic contact between the shales and packstone is faulted out to the left of the thrust in the top right of the section. (C) Cross-section overlay through the quarry's middle ridge displaying a large-scale fault-propagation fold along a thrust hosted in a thin shale bed, overlaid by imbricates. (D) measured-section through the Sap Bon Fm in Shale Quarry S (after Hansberry et al. 2014) displaying the three structural domains identified by variation in structural style.

The increasing amount of published illite crystallinity data and its comparison to with other techniques has also been used to correlate illite crystallinity to absolute temperatures, albeit with significant error margins (Underwood et al., 1993; Kosakowski et al., 1999). Optical vitrinite reflectance is frequently used in basin analysis and VLGM studies to constrain thermal maturation of sediments, as well as burial and metamorphic temperature (Samuelsson and Middleton, 1998; Sakaguchi et al., 2007). However, this can be problematic in deformed terranes as organic macerals are susceptible to shearing in deformed rocks, leading to poor statistics on reflectance measurements, and potentially misleading data.

3.1 Sampling

The shale detachment exposed above the Eagle Thrust is comprised of the heavily and variably deformed Sap Bon Formation shales; while underlying the thrust, the Khao Khad Formation limestones are relatively undeformed (Hansberry et al., 2014) (Fig. 4). The Sap Bon Formation consists of interbedded mudstones, siltstones and sandstones, as well as bioclastic limestones. Starting at the Eagle Thrust and moving south, samples were taken at regular intervals (where possible), across the exposure of the Sap Bon Formation, herein referred to as 'Shale Quarry S' (Fig. 4). Samples were taken from beds identified as shales, with all three analyses being carried out on the same subsample of each sample. The syn-deformational vein cements in the Sap Bon Formation shales record evidence for fluid flow during the Indosinian deformation, and can provide information from their geochemistry (Fig 7) (Hansberry et al., 2014). Sampling for $\delta^{13}C$ and $\delta^{18}O$ stable isotopes analysis was also carried out with consistent spacing through Shale Quarry S, as well as the nearby exposure of alum shales (Shale Quarry A) to the south-east of Shale Quarry S (Fig. 4). Samples were taken from calcite vein material throughout the Sap Bon Formation and alum shales, along thrusts, bedding planes and in tension gashes (see below for further textural description). Samples were also taken from bioclastics in the Khao Khad Formation in Shale Quarry S, as well as the Phu Phe Formation in Shale Quarry A (Fig. 4, 7C-D). In all, we collected 45 samples from Shale Quarry S; nine from the Khao Khad Formation below the Eagle Thrust (both packestone and veins were sampled), 15 of calcite veins in the shales, and 19 of shale samples. 10 of the shale samples were specifically taken from within the low-competency and high-competency packages (five from each) to directly compare the contrasting deformational mechanisms (Fig. 5). We also collected 97 samples from Shale Quarry A, 93 of calcite veins in the alum shales and associated basaltic sills, and four from the overlying Phu Phe Formation packstones.

3.2 Illite crystallinity

Determining illite crystallinity by X-Ray Diffraction (XRD) is an easy and rapid technique for broadly constraining the temperature conditions of VLGM (Frey et al., 1980; Frey, 1987; Mählmann et al., 2012). It is widely established that deep burial and incipient metamorphism causes diagenetic alteration of expandable smectite into non-expandable illite (Kennedy et al., 2014). Smectite consists of an octahedral silicate layer between two

tetrahedral layers, and an expandable interlayer available to water, organics and ions (Sposito et al., 1999; Brigatti et al., 2006; Kennedy et al., 2014). The process of illitization involves substitution of Al for Si in tetrahedral sheets, dehydration, collapse of the expandable interlayer,

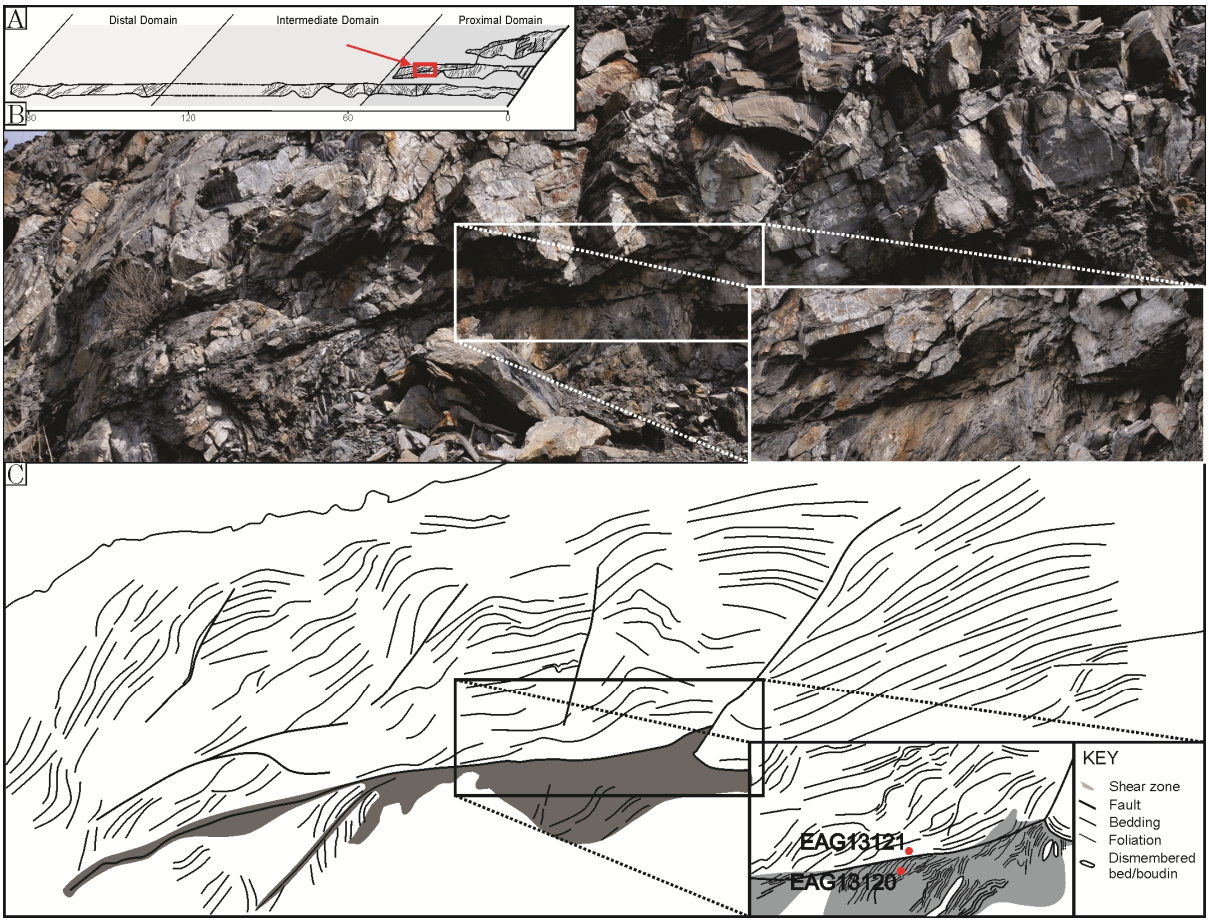

Fig. 5. Comparison of deformational styles: continuous deformational style characterised by fine, dark shales, well-developed foliations, and a relatively homogeneous strain profile; in comparison with discontinuous deformational style characterised by more competent, carbonate-cemented siltstones and sandstones, a heterogeneous strain profile dominated by low strain zones between discrete fractures. (A) Location of the photo in B on the cross section through the Sap Bon Formation in Shale Quarry S. (C) Line drawing of structure in B, with blow-up illustrating foliation development in shale shear zone. Locations of paired samples of the two zones are shown in red.

and replacement of exchangeable ions and organics with fixed K+ and/or NH4+, though it should be mentioned there is currently no agreement on how this proceeds at the crystal-scale (Lindgreen et al., 2000; Clauer et al., 2014; Kennedy et al., 2014). This mechanism of reaction facilitates a change from smectite, and mixed-layer illite-smectite, to pure illite during burial and inferred temperature increase. Experimental results have shown variation in illitization with increasing temperature and it is widely accepted this reaction series is complicated by many variables other than a simple increase in temperature (Clauer et al., 2014). For example: fluid pressure, tectonic stress, heating rate,

lithology, and original clay mineral chemistry have been suggested as potential factors in increasing illitization, indirectly measured by the shape of the 10Å (001) illite peak (Frey, 1987; Underwood et al., 1993; Kübler and

Jaboyedoff, 2000). In spite of these limitations IC remains a widely used and standardised method of determining the temperature conditions of burial diagenesis and onset of VLGM conditions (Frey et al., 1980; Pollastro, 1986; Warr et al., 1996).

Illite crystallinity is measured by XRD as the 'full width at half-peak height' of the 10-Å illite peak, expressed in units of Δ°2θ (Kübler, 1968; Kisch and Frey, 1987; Warr et al., 1996). This measure is then

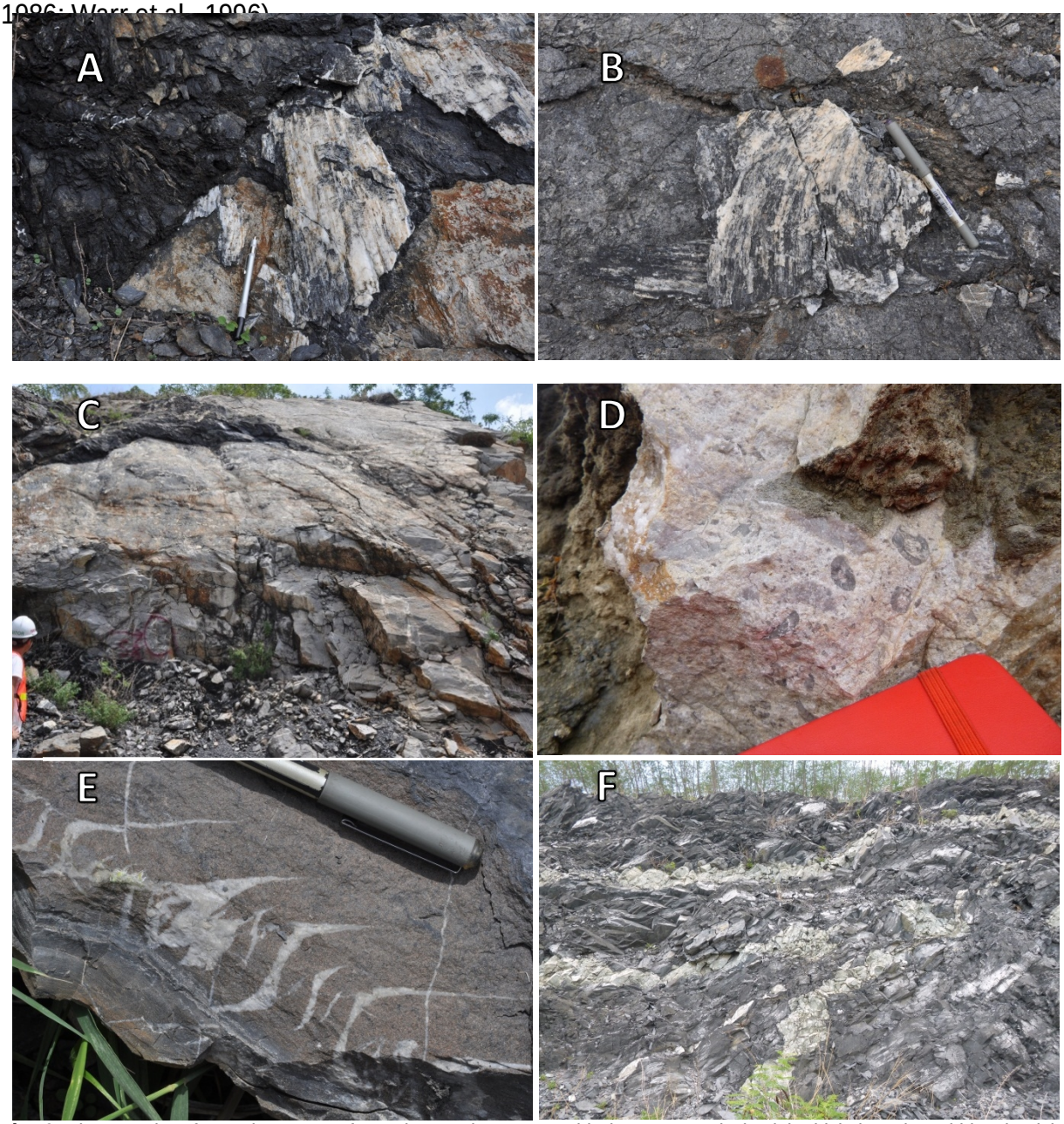

Fig. 6. Photographs of sample textures for carbon and oxygen stable isotopes analysis. (A) Thick (5 cm), multi-level calcite veins along the Eagle thrust with well-developed slickenfibres. (B) Well-developed slickenfibres of multiple orientations in a thick (2-3 cm) calcite vein along a major thrust plane in the Sap Bon Fm. (C) Khao Khad Fm wackestone with calcite veins below (north of) the Eagle thrust. (D) Phu Phe Fm packstone above the alum shales in Shale Quarry A. (E) Tension gashes in the Sab Bon Fm in Shale Quarry S. (F) Basaltic sills in the alum shales hosting calcite veins.

converted to the 'Kübler-Index' (KI) through measurement of a set of rock standards for calibration (Kübler, 1968). The importance of standardisation of sample preparation and

machine settings has been well documented (Kisch and Frey, 1987; Robinson et al., 1990; Kisch, 1991b; Warr and Rice, 1994). Warr and Rice (1994) proposed a calibration approach to the standardisation of IC data using rock chip standards to allow for quantitative interlaboratory comparison of data sets, and presented the 'Crystallinity Index Standard' (CIS). Mählmann et al. (2012) suggests care in the use of available standards: A large body of IC work and data

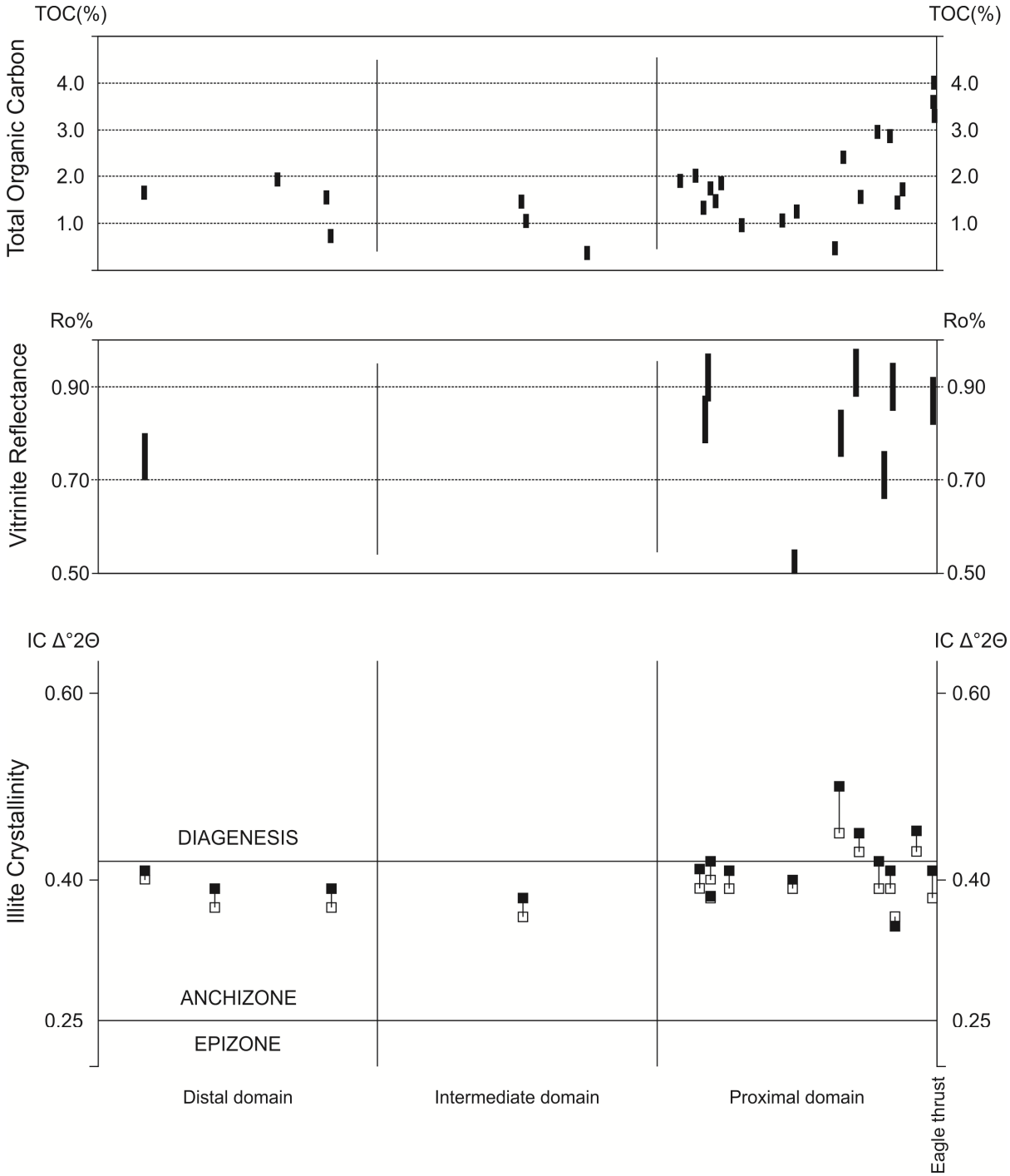

Fig. 7. Results from clay analyses of the Sap Bon Fm shales plotted vs distance from the Eagle thrust. (bottom) Illite crystallinty (IC) of 16 samples showing air-dried (solid) and glycolated (hollow) preparations. (middle) Ro% from vitrinite reflectance of 9 samples; the height of each bar is the error margin given by poor reflectance statistics. (top) TOC content of 26 samples with a 0.2% error (bar height).

through the central Alps has used the polished rock slab standards of Kübler (1968) to define results by the KI (Frey et al., 1980; Frey, 1987). Mählmann et al. (2012) discuss the discrepancy between data using these standards and those of Warr and Rice (1994), and that the two should not be compared. They recommend that studies not needing comparison to these existing KI standardised data sets use the CIS calibration of Warr and Rice (1994). We have therefore calibrated our IC data to the CIS.

A set of 15 samples were prepared as per recommendations of Kisch (1991). Samples were washed, then milled to break up large sample fragments (>2mm). Carbonate was removed from the sample using a 1M sodium acetate buffer at pH 5 and a heat bath at 90 °C. Organic matter was then removed with a solution of hypochlorite bleach at pH 9.5 and a heat bath at 90 °C. Samples were thoroughly washed and separated from these solutions by centrifugation. The ≤2 μm clay fraction was then separated by gravity settling and centrifugation (per Stokes' Law) before being pipetted si slides as orientated preparations for XRD analysis. Samples were analysed using a Bruker D8 Advance X-Ray diffractometer at the University of Adelaide using the following measurement conditions: CuKα radiation at 40 kV and 40 mA. Sample slides were then treated with ethylene glycol to remove possible overlap of the peak effect of remaining smectite in the sample. For interlaboratory calibration, the six rock standards of Warr and Rice (1994) were prepared and analysed in the same manner. These values were then plotted against those provided by Warr and Rice (1994) and a regression was determined to correct our raw data to CIS (Table 1).

3.3 Vitrinite reflectance

Vitrinite reflectance or 'coal rank' is a widely used method for broadly constraining thermal conditions in basins, geothermal settings and orogenic wedges (Barker and Halley, 1986; Samuelsson and Middleton, 1998; Sakaguchi et al., 2007). The optical reflectance of polished vitrinite macerals, as measured by optical microscopy is a function of increasing coalification of organic matter (Stach and Murchison, 1982; Kosakowski et al., 1999). This increasing coalification and subsequent reflectance is believed to be primarily a function of the maximum temperature the organic matter has experienced (Teichmüller, 1987). Vitrinite reflectance ('Ro%') is determined from multiple measurements within a sample resulting in the mean Ro% value. Multiple correlations between vitrinite reflectance and absolute palaeotemperature have been modelled and presented (Guthrie et al., 1986; Barker et al., 1998; Kosakowski et al., 1999). The chemical kinetic model of Burnham and Sweeney (1989; 1990) allows for vitrinite reflectance (up to 4.5%) to be calculated as a function of temperature and heating time (Price, 1983; Barker, 1988; Sweeney and Burnham, 1990). This method was chosen to potentially correlate to illite crystallinity in order to provide more robust estimates of deformational temperature.

A set of nine samples were prepared as polished blocks as per the ASTM D 278 protocol on "Dispersed Organic Matter Vitrinite Reflectance". Samples were measured for reflectance using a Zeiss UMSP 50 with immersion oil no. 1.515. Measuring wavelength was set to 545 ± 10 nm with a reflectance spot size of 7.63 μm (Table 1).

3.4 Carbon and oxygen stable isotopes

Fluid-rock interactions and fluid flow can be of significant importance in understanding the structural and tectonic development of fold-thrust belts (Wiltschko et al., 2009; Lacroix et al., 2014; Warren et al., 2014). Oxygen and carbon stable isotope data can help to constrain the origin and temperature of fluids involved in the structural development of a deforming sequence (Dietrich et al., 1983; Kirschner et al., 1995; Warren et al., 2014). Warren et al. (2014) implemented a regional carbon and oxygen stable isotope study, specifically sampling a variety of textures of carbonate cement and limestones in the deformed Saraburi Group sediments of the KKFTB. They focused on comparison of isotopic signatures from several areas over a 50-60 km span of the KKFTB, to define an evolution of burial and deformational fluid derived cements within a regional isotopic framework. They were able to define a stepwise diagenetic-to-orogenic fluid-history expressed in the isotopic ratios of different generations and orientations of vein cements (Warren et al., 2014). We use a similar process of analysis of the isotopic compositions of the Khao Khad Formation and Phu Phe Formation limestones, and calcite vein cements within the Sap Bon Formation and alum shales (Fig. 6). We define the fluids that precipitated these vein cements within the context of the regional framework of Warren et al. (2014), as well as investigate the burial to orogenic fluid-flow evolution of the study area, and the implications for the structural evolution of the Sap Bon Formation shales.

The set of 121 samples of calcite vein cements and limestones from the two quarry locations were categorised into four groups according to their texture; either by their lithology or in the case of samples from vein cements, according to their deformational association and orientation: 1) thrust plane associated and thrust-parallel veins (Fig. 6A-B); 2) syn-kinematic tension gashes (Fig. 6E); 3) veins with orthogonal, or no relationship to thrust/bedding orientation, and; 4) veins associated with tuff beds within the alum shales (Fig. 6F).

Sample powders of were extracted from vein cements using a dental technician's drill. Carbonate mineralogy (calcite) was confirmed by thin section analysis; no significant quantity of dolomite was present in any samples. Samples were analysed by the stable isotope mass spectrometer facility at The University of Melbourne.

TABLE 1. DETERMINATIONS OF ILLITE CRYSTALLINTY AND TOTAL ORGANIC CARBON CONTENT VALUES OF SAMPLES FROM SHALE QUARRIES 'S' AND 'A'

Sample	Location	Structural association	Texture	Original Rock TOC	$KI_{(CIS)}$ $\Delta 2\theta$	KI 'Grade'	Def. Temp. (***)
EAG12008	Shale Quarry S	Eagle thrust surface	Fissile/sheared shale in CDZ*	4.01	0.38	Low anchizone	196
EAG12010	Shale Quarry S	Eagle thrust surface	Fissile/sheared shale in CDZ	3.62			
EAG12012	Shale Quarry S	Eagle thrust surface	Calcite veins/interlayered fissile shale	3.30			
EAG12014	Shale Quarry S	Fault horse directly above Eagle thrust	Undeformed carbonate cemented shale in DDZ	-	0.43	Deep diagenetic	169
EAG12016	Shale Quarry S	Undeformed bed/limb in shale	Carbonate cemented siltstone and sandstone interbeds in DDZ**	1.44	0.39	Low anchizone	191
EAG12018	Shale Quarry S	Shear zone/continuously deformed shale	Fissile/sheared shale in CDZ	2.86	0.36	Low anchizone	208
EAG12019	Shale Quarry S	Undeformed bed/limb in shale	Carbonate cemented siltstone and sandstone interbeds DDZ	2.96	0.40	Low anchizone	187
EAG12020	Shale Quarry S	Shear zone/continuously deformed shale	Fine dark shale lacking foliation	1.58	0.43	Deep diagenetic	171
EAG12023	Shale Quarry S	Fault surface, associated veins/slickenfibres	Calcite veins/interlayered fissile shale	1.90			
EAG12024	Shale Quarry S	Fault surface, associated veins/slickenfibres	Calcite veins/interlayered fissile shale	2.01			
EAG12027	Shale Quarry S	Fault surface, associated veins/slickenfibres	Calcite veins/interlayered fissile shale	1.33			
EAG12028	Shale Quarry S	Fault surface, associated veins/slickenfibres	Calcite veins/interlayered fissile shale	1.74			
EAG12031	Shale Quarry S	Undeformed bed/limb in shale	Tension gash/surrounding undeformed shale	1.48			
EAG12032	Shale Quarry S	Undeformed bed/limb in shale	Undeformed carbonate cemented shale in DDZ	1.85			
EAG12033	Shale Quarry S	Shear zone/continuously deformed shale	Fissile/sheared shale in CDZ	0.97	0.40	Low anchizone	187
EAG12034	Shale Quarry S	Fault surface, associated veins/slickenfibres	Calcite veins/interlayered fissile shale	1.05			
EAG12035	Shale Quarry S	Undeformed bed/limb in shale	Undeformed carbonate cemented shale in DDZ	2.41	0.45	Deep diagenetic	162
EAG12036	Shale Quarry S	Eagle thrust surface	Brecciated shale along thrust zone	1.73			
EAG12041	Shale Quarry S	Fault surface, associated veins/slickenfibres	Sheared shale and packstone interbeds with calcite veins in DDZ	0.47			
EAG12042	Shale Quarry S	Limb in shale	Partially sheared shale in zone of mixed deformational style	1.24	0.39	Low anchizone	191
EAG12044	Shale Quarry S	Shear zone/continuously deformed shale	Calcite vein	0.37			
EAG12045	Shale Quarry S	Shear zone/continuously deformed shale	Fissile/sheared shale	1.05			
EAG12046	Shale Quarry S	Undeformed bed/limb in shale	Undeformed shale	1.45	0.36	Low anchizone	211
EAG12047	Shale Quarry S	Relatively under formed bed/limb in shale	Shale with a well-developed cleavage outside of CDZ	0.74	0.37	Low anchizone	203
EAG12048	Shale Quarry S	Fault surface, associated veins/slickenfibres	Calcite veins/interlayered fissile shale	1.55			
EAG12049	Shale Quarry S	Fault surface, associated veins/slickenfibres	Calcite veins/interlayered fissile shale	1.96			
EAG12051	Shale Quarry S			-	0.50	Deep diagenetic	141
EAG12053	Shale Quarry S	Slightly fissile shale in fault core	Fissile/sheared shale outside of CDZ	1.64	0.40	Low anchizone	188
EAG13120	Shale Quarry S	Shear zone/continuously deformed shale	Fissile/sheared shale in CDZ	-	0.37	Low anchizone	201
EAG13121	Shale Quarry S	Undeformed bed/limb in shale	Carbonate cemented siltstone and sandstone interbeds DDZ	-	0.40	Low anchizone	187

* Continuous deformation zone **Discontinuous deformation zone ***Per equation of Kosakowski et al. (1999)

3.5 Total organic carbon content

A link between high organic matter content and the propensity for developing brittle fractures has recently been identified (Ding et al., 2012). Variation in TOC content of otherwise geodynamically and mineralogically similar rocks is a potentially important factor affecting fracture development (Hill et al., 2004; Ding et al., 2012). We examine variation of TOC content within the Sap Bon Formation and associated detachment analogue to investigate potential correlation to the density of fractures (and structural heterogeneity). A set of 24 samples were analysed using a PE 2400 CHNS elemental analyser and pressure calcimeter test to calculate TOC. The original source rock TOC (TOCO) was estimated using the calculator of Pepper and Corvi (1995).

4. RESULTS

4.1Illite crystallinity

The results from 15 samples for which illite crystallinity (measured air dried sample preparations as well as after ethylene glycol treatment) was determined is shown in Table 1, the spatial distribution of these results within the structural framework of the Sap Bon Formation is shown in Figure 7. The determined values fall between 0.45 and 0.36 Δ°2θ (CIS) corresponding to deep diagenetic zone and low anchizone (after Arkai et al. 1995). The IC values for the diagenesis-anchizone and anchizone-epizone boundaries are 0.42 Δ°2θ and 0.25 Δ°2θ, respectively. Metamorphic facies estimates are difficult without pressure constraints and given the potential error involved in illite crystallinity-grade determination, though values in this study likely correspond to zeolite to lower greenschist facies.

Values vary significantly between air dried preparations and slide preparations treated with ethylene glycol, with glycolated samples display higher crystallinity (lower Δ°2θ). The bulk of the data occurs in the Proximal Domain adjacent to the Eagle Thrust (Figs. 4 and 8). A significant spreads of values occurs in this domain, with no strong spatial correlation, though the highest degree of crystallinity (0.36 Δ°2θ) occurs within several metres of the thrust plane. However, when comparing IC values of samples with differing deformational mechanisms, a trend is apparent. Illite crystallinity values from shale samples in zones of low-competency, continuous deformation exhibit higher IC values than samples of shale from high-competency, discontinuous deformation (Hansberry et al., 2014) (Figs. 5 and 8). In four locations, samples were taken in pairs from shear zones and the surrounding rock (Fig. 5); here, IC values were noticeably higher in samples from shear zones (samples EAG12008, EAG12018, EAG12033, and EAG13120) while IC values were lower in samples from the surrounding, relatively undeformed rock (samples EAG12014, EAG12020, EAG12035, and EAG13121) (Table 1).

4.2 Vitrinite reflectance

The results from the nine samples used for vitrinite reflectance analysis demonstrated the difficulty of using this technique in highly deformed settings. While generally good polishes were obtained, and samples contained high concentrations of organic matter, shearing

has frequently rendered the vitrinite macerals too fine-grained for reflectance measurement (Fig. 8). As many as possible were measured, however, the minimum target of 100 measurements per sample was never reached. Inertinite was assumed to be the high reflectance macerals present in several samples (Fig. 8), it was observed and measured in all samples with the exception of EAG12053. Bireflectance measurements were severely hampered by the small grain size of vitrinites; interpretation of any results must therefore be cautioned by the lack of bireflectance measurements.

Mean vitrinite reflectance of the nine samples range from 0.71 to 0.93 Ro% but given the poor statistics due to lower than ideal number of reflectance measurements and a lack of bireflectance measurements, an error of 0.1 Ro% is inferred (Table 1).

4.3 Fluid evolution from texture-aware isotopic sampling

When the stable isotopic values determined for all samples of each texture set are charted on a δ13CPDB vs δ18OPDB crossplot, a generally covariant trend of increasingly negative carbon and oxygen values plotting away from an estimated Permian sea water value is observed (Fig. 9). Samples from Shale Quarry S are split into those from the Khao Khad Formation (limestones and veins), and those from the Sap Bon Formation (veins only). Values from limestones (Phu Phe Formation and Khao Khad Formation packestones) plot closest to the Permian sea water estimate (Veizer et al., 1999) (Fig. 9). Calcite vein fills in the Khao Khad Formation, below the Eagle Thrust plot at the most oxygen-negative end of this plot field (Fig. 9). Vein fills in the Sap Bon Formation plot along a trend of increasingly negative C-O values from values from the Khao Khad Formation. Values from veins related to thrusts cluster around +2.0 δ13C and -11.0 δ18O, with values from veins orthogonal to, or unrelated to, faulting plotting closer to those from the Khao Khad Formation in this plot field (Figure 9). Samples from Shale Quarry A are predominantly from veins in the alum shales (and associated folded sills (Fig. 4 & 6)), with four samples from the Phu Phe Formation (packestones and veins). Values from vein fill in the alum shales plot broadly across the C-O crossplot (Fig. 9). However, several trends are apparent: Values from vein fills orthogonal to (or not spatially related to) thrusting plot between +4.8 to +0.5 δ13C and -6.5 to -11.0 δ18O, continuing the covariant trend of increasingly negative C-O values (Fig. 9). Vein fills in thrust planes and parallel to thrust planes and/or fold axial planes plot with more negative oxygen values (-9.0 to -17.0 δ18O) than non-thrust related veins, and with similar δ13C values (Fig. 9). There is some overlap between these trends, but a clear covariance of increasingly negative δ13C and δ18O values is seen for non-thrust related vein cements, while vein cements along thrust and exhibiting evidence of precipitation during deformational accommodation of fluid flow (slickenfibres) show relatively stable δ13C values, yet strongly increasingly negative δ18O values (Fig. 9).

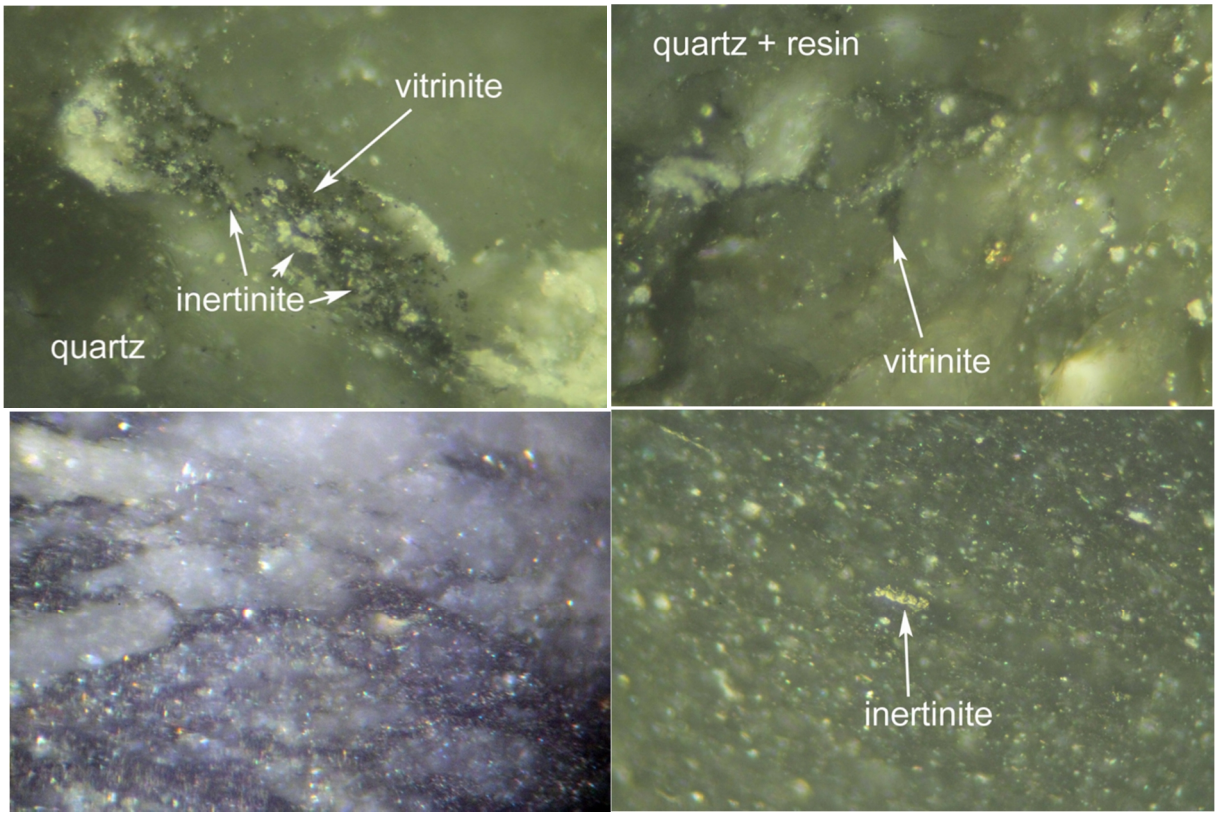

Fig. 8. Microphotographs of organic matter in samples from the Sap Bon Fm shales. (top left) highly reflective large Inertinite grain surrounded by disseminated Inertinite and virtirnite. (top right) dark vitrinite grain in quartz large enough for reflectance measurement. (bottom left) fine interstitial vitrinite in quartz, heavily fragmented making measurement difficult. (bottom right) Dark bands of finely ground Inertinite, vitrinite often too small to measure and/or filled with high-reflectance inclusions leading to erroneous readings.

The complete data set from the two quarries exhibits two distinct trends. Firstly, a covariant trend of increasingly negative δ13C and δ18O values plotting away from an approximated sea water value, through bioclastics (+5.0 to +4.0 δ13C and -6.5 to -9.0 δ18O), non-thrust related veining such as tension gashes and bedding/thrust-orthogonal vein arrays (+4.5 to +0.5 δ13C and -6.5 to -11.0 δ18O), and the bulk of thrust related veining in the Sap Bon Formation (+3.5 to +1.0 δ13C and -10.5 to -12.0 δ18O). The second trend plots with relatively stable carbon values (+5.0 to +2.5 δ13C) and increasingly negative oxygen values, diverging from the first trend at values of approximately -11.0 δ18O (Fig. 9), these values come from thrust-related vein fills in Shale Quarry A (as well as values from the Eagle Thrust plane in Shale Quarry S) .

4.4 Total organic carbon content

The results from the 24 samples used for TOC analysis were run through the calculator of Pepper and Corvi (1995) to obtain TOC0 values for the data set (Table 1). Unlike IC values, TOC values do not exhibit a trend between different structural mechanisms, no systematic change in TOC content is noted between those samples taken from continuous deformation shear zones and those taken from competent layers deforming by discrete faulting and associated folding. However, the data do exhibit a trend of

increasing TOC content with proximity to the Eagle Thrust (Fig. 7). Distance from the thrust and TOC content are not statistically significantly correlated, but a noticeable increase (2% to 4%) in TOC values occurs in the Proximal Domain, within 20-30 m of the thrust.

5. Discussion

5.1 Palaeotemperature indicators

Illite crystallinity is widely used as a VLGM palaeothermometer, however, as a single technique it lacks precision, and interpretation is limited to allocating values to broad grade divisions (Mählmann et al., 2012). Various authors have proposed multi-technique analysis as a way of increasing the accuracy of IC analysis. This can be through comparison with results from independent techniques which also constrain palaeotemperature, in order to increase reliability of determinations (Árkai et al., 1995; Árkai and Ghabrial, 1997), or correlations to independent techniques providing absolute palaeotemperature, and therefore, potential calibration of IC to temperature (Underwood et al., 1993; Kosakowski et al., 1999). In the latter case, vitrinite reflectance and its established relationship to temperature has been used to attempt calibration of IC (or the diagenetic-anchizone, anchizone-epizone boundaries) with absolute palaeotemperatures. While temperature estimations using IC have significant inherent errors (as the kinetics of this relationship are poorly constrained), it appears primarily controlled by temperature and is often well-correlated with other VLGM indicators, permitting calibration and broad temperature estimates (Kosakowski et al., 1999). However, the results presented here illustrate the difficulty of using vitrinite reflectance as an independent parameter for calibration in highly deformed rocks, so that no IC-palaeotemperature relationship could be determined (Fig. 7). Vitrinite reflectance and IC are frequently well-correlated, however, the well-established logarithmic relationship between Ro% and temperature is not observed in any known IC data (Underwood et al., 1993). The use of relationships derived in these studies to calculate temperature in different geological settings and conditions is cautioned against (Underwood et al., 1993; Kosakowski et al., 1999). While it was not possible to establish the relationship between IC and Ro% (and therefore temperature) in this study, we provide temperature calculations as per the equation of Kosakowski et al. (1999) as an inexact indication of temperature, though we suggest that the error is in the order of 20-50 °C (Table 1):

$$IC = 2.24 - 0.81 \log(T)$$

While estimates of deformational temperature from the data in this study are limited to illite crystallinity-grade determination, we do observe a trend in IC with respect to deformational mechanism. Samples taken from within zones of continuous deformation exhibit a uniformly higher degree of IC ($\Delta°2\theta$ 0.38, 0.36, 0.40, 0.37) than the corresponding samples taken from adjacent discontinuously deformed rock ($\Delta°2\theta$ 0.39, 0.40, 0.45, 0.40). These values are taken from locations within the Sap Bon Formation where it was possible to sample shale material from continuous- and discontinuous-deformational styles in close proximity (Fig. 5).

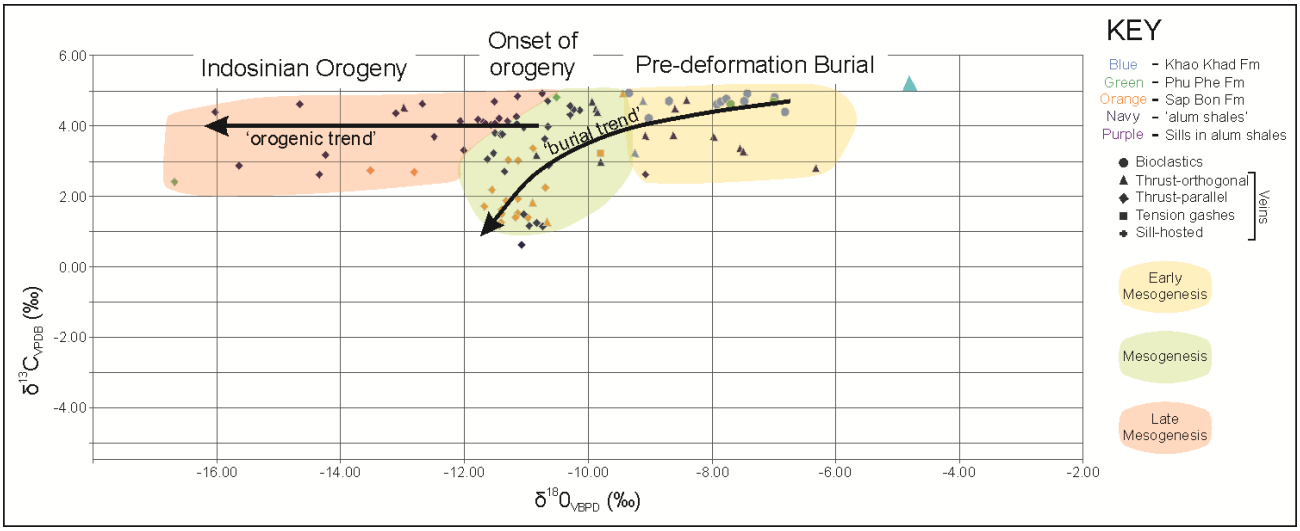

Fig. 9. Carbon and oxygen stable isotopes crossplot of data from Shale Quarries S and A. Symbol colour indicates the sample or vein-hosting lithology and symbol shape indicates the texture of the sample. Burial and orogenic trends after Warren et al. (2014) regional study. Teal triangle in the top right of the plot indicates $\delta^{13}C$ and $\delta^{18}O$ values for average tropical Permian seawater (Veizer et al. 1999).

Potential influences on differing IC values from these opposing end members of deformational style are varied; while increased crystallinity could reflect differences in maximum deformational temperature, strain rate, lithology and mechanical reduction of crystallite size could also be a factor (Eberl and Hower, 1976; Roberts et al., 1991; Fernández-Caliani and Galán, 1992).

The relationship between an increase in illite crystallinity and an increase in strain has been well documented (Merriman and Roberts, 1985; Roberts et al., 1991; Fernández-Caliani and Galán, 1992). Higher illite crystallinity (smaller $\Delta°2\theta$) have been observed in areas of inferred higher-strain, in the centre of anticlines and adjacent to, or within, shear zones in otherwise texturally and lithologically uniform rocks (Merriman and Roberts, 1985; Fernández-Caliani and Galán, 1992). Roberts et al. (1991) discuss a similar deformational style to that of the Sap Bon Formation, in that the location of high-strain shear zones in fine-grained clastic rocks is likely controlled by competency contrasts within the stratigraphy. They concluded that it is likely that the growth of white-mica is accelerated above the burial-related 'background' rate via annealing processes within the high-strain zones. A qualitative relationship between finite strain calculations (RS) and illite crystallinity has also been demonstrated (Gutiérrez-Alonso and Nieto, 1996a). Gutiérrez-Alonso and Nieto (1996) go on to suggest that this relationship is suitable for documenting strain variation in rocks lacking appropriate strain markers. Hansberry et al. (2014) do not demonstrate that the shear zones of continuous deformation in the Sap Bon Formation are quantitatively of higher strain than the rest of the dominantly discontinuously deformed cross-section (Fig. 4). However, it is likely that they do exhibit relatively higher-strain given the development of a strong schistosity in these zones and uniformly higher IC (Fig. 5).

5.2 δ18O composition of fluids and fault related fluid flow

The regional carbon and oxygen stable isotopic study implemented by Warren et al. (2014) defined a series of trends from eogenesis (shallow burial) through mesogenesis (deep burial) and orogenesis. This was achieved by plotting δ13C and δ18O values from samples of know texture and context (e.g. best preserved deep-water carbonates) and examining the trends produced by these data with the aim of defining the fluid and texture-based diagenetic or orogenic evolution of the KKFTB (Warren et al., 2014). Their data defined a typical covariant trend of increasingly negative δ13C and δ18O values during burial, passing into a deformation trend of increasingly negative δ18O values in the areas closest to the quarries in this study. Early burial occurred with a permeable matrix (as well as vein cements) re-equilibrating under the influence of warming fluids, until the burial-induced temperature reached δ18O values equivalent to -8 to -10‰.

The orogenic and burial trends diverge at ~-9‰ δ18O as matrix permeability decreased, with matrix-fluid re-equilibration ceasing completely beyond temperatures equivalent to δ18O -10 to -12‰. Matrix permeability cemented and only thrust-related veins continued to facilitate fluid movement and only cements from these veins preserve δ18O values more negative than -12‰.

In comparison to the data of Warren et al. (2014), δ13C and δ18O values from Shale Quarry S and Shale Quarry A plot in the early mesogenesis, through pre-thrust deformation and finally orogenesis plot-space of Warren et al. (2014). Values from packestones and wackestones in the Phu Phe and Khao Khad formations (~ +4.0 δ13C, -7.0 δ18O) plot in the early mesogenesis plot space of Warren et al. (2014) (Fig. Values from tension gashes and non-thrust hosted vein cements (~ +5.0 to 1.0 δ13C, -7.0 to -10.0 δ18O) correspond to values for pre-thrust deformation and ongoing burial as matrix-fluid interaction decreases with decreasing permeability. The burial and orogenic trends appear to diverge at approximately -10.0 δ18O, as more negative δ18O values occur only in thrust-hosted vein cements as matrix-permeability had ceased.

This relationship is clearly apparent in Figure 10, where δ18O values are overlain on the host geology of shale quarries A and S. δ18O values were gridded over the X-Y plane of the cross section using Surfer Surface Mapping Software. These grids were constructed by using carefully measured cross-sections allowing each sample location to be allocated an X-Y coordinate for gridding. Figure 10 exhibits 'hottest' most δ18O negative samples occurring along the major, lithology-bounding fault in each section. Second-order structures are also highlighted by negative δ18O signatures: A continuous deformation shear zone through the middle bench of the Sap Bon Formation cross-section exhibits a more negative δ18O trend (~ -12.5 δ18O) than the background value of syn-tectonic vein fill precipitate in the surrounding rock (~ -10.5 δ18O) (Fig. 10). The least negative δ18O values in each cross-section (~-7.0 to -8.5 δ18O) are associated with samples of matrix material from packestones and wackestones in the footwall (Shale Quarry S) and hangingwall (Shale Quarry A) respectively of the major thrusts in each section (Fig. 10).

These trends provide stark contrast in isotopic trends across these two faults, providing further evidence for a loss of matrix permeability and fluid-rock re-equilibration in carbonates, and continued thrust related permeability as major structures acted as conduits for hotter fluids driven by orogenesis.

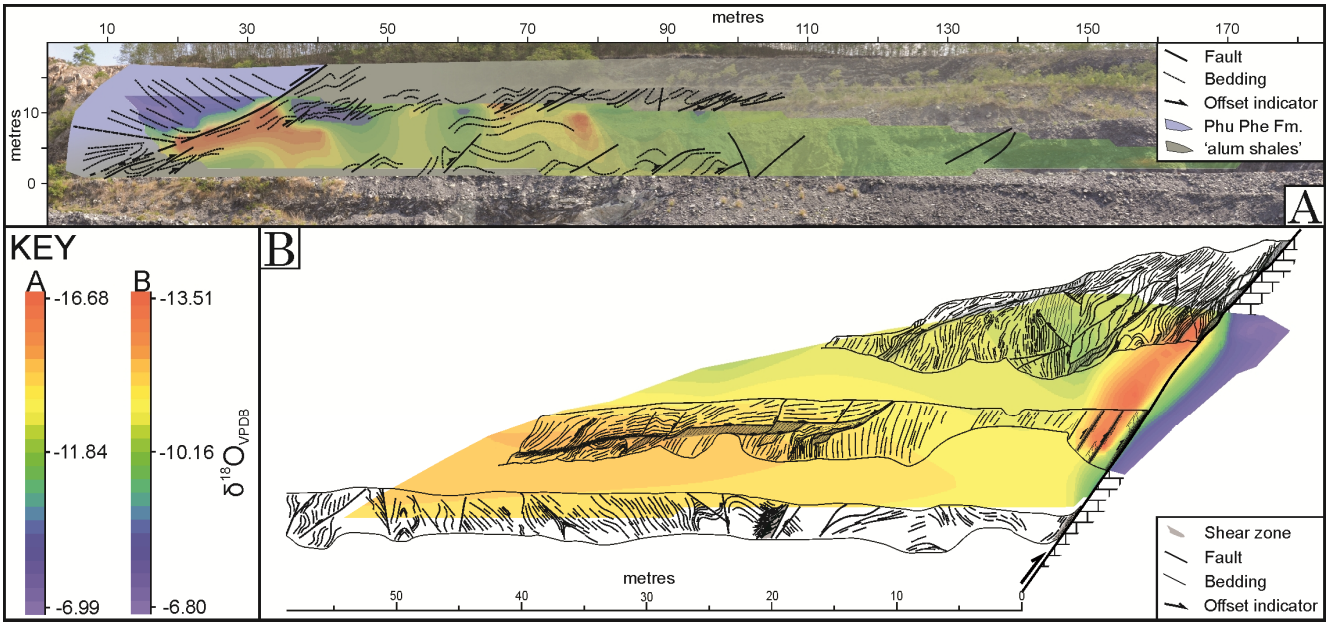

Fig. 10. Gridded values of $\delta^{18}O$ overlaid on cross sections from Shale Quarries A (A) and S (B). Both grids indicate the most negative oxygen stable isotopic ratios are from samples along the major thrust in each section. The Sap Bon Fm Section (B) also exhibits a similar trend (light-dark orange) along the largest thrust in the shale, propagating through a continuous deformational zone shaded in grey.

5.3 Total organic carbon content and fracture density

An increase in total organic carbon content with proximity to the base of the detachment zone is observed in the Sap Bon Formation shales (Fig. 8). It is unclear whether a higher TOC content in the exposed strata of the Sap Bon Formation created rheological weakness which were exploited by the Eagle Thrust, or if the higher values are simply related to the formation, and not a direct influence on deformation. However it is clear that the higher TOC values are associated with the zone of most closely-spaced faults and related structures (essentially fracture density), a relationship which has been previously established and potentially represents a controlling factor on the development and density of structural features (Hill et al., 2004; Ding et al., 2012). Based on structural observation, stable isotope data and TOC data, we propose a deformation and fluid flow history for the Eagle Thrust and associated shale detachment zone:

1) Burial heating corresponding to early mesogenesis as pore fluids increase in CaCO3 concentration. A permeable rock matrix and vein development allowed matrix-fluid re-equilibration during ongoing burial (Warren et al., 2014).

2) Pre-thrust deformation corresponding to mesogenesis. Strain partitioning initiates as a result of existing competency contrasts in the rock packages of the Sap Bon Formation, with TOC rich layers

contributing to low competency (Goodwin and Tikoff, 2002). Strain-rate discontinuities at boundaries between contrasting competencies lead to strain localisation and shear failure, with shear surfaces becoming conduits for fluid flow as matrix permeability decreases (Goodwin and Tikoff, 2002; Fagereng, 2011b; Warren et al., 2014).

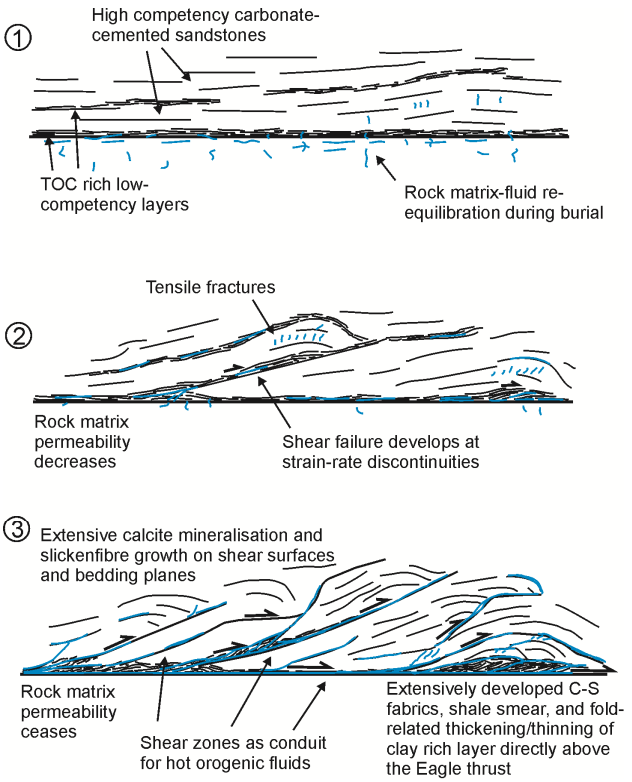

Fig. 11. Schematic model of fault zone and detachment fault evolution in the Sap Bon Formation. Fluid flow as evidenced by calcite mineralisation is represented in blue.

3) Orogenic deformation characterised by shear failure, as calcite precipitation and slickenfibre growth along shear zones increases and impedes matrix permeability further. Shear zones become the primary conduit for hot orogenic fluids as matrix permeability ceases (Warren et al., 2014). Calcite precipitation potentially increased weakness along zones of shear failure, contributing to a feedback loop of increasing competency contrast and strain-rate discontinuity (Wells et al., 2014). High contrasts in competency likely influenced the complex asymmetry of structural geometries in the deformed Sap Bon Formation (Goodwin and Tikoff, 2002).

6. Conclusions

- New illite crystallinity data provide broad constrains on the deformational temperature within an upper-level shale detachment of the Khao Khwang Fold-Thrust Belt, resulting from the Triassic Indosinian Orogeny. Data indicate temepratures in the range of 160-220 °C (±20 °C).

- A higher degree of illite crystallinity and inferred temperature is associated with shale shear zones of continuous deformation (Δ°2θ 0.38, 0.36, 0.40, 0.37) than the corresponding samples taken from adjacent discontinuously deformed rock (Δ°2θ 0.39, 0.40, 0.45, 0.40) within the detachment zone. These zones are interpreted as having higher finite strain relative to the surrounding discontinuously deformed rocks.

- Carbon and oxygen stable isotope values from limestones and syn-tectonic vein fills exhibit a strong trend of fluid-rock interaction during early mesogenesis, through to orogenesis (Fig. 9). Hottest fluids were concentrated along large thrusts and related structures, which facilitated fluid movement during orogenesis, as matrix permeability ceased.

- Total organic carbon content exhibits an association with density and complexity of structures within the Sap Bon Formation detachment zone (Fig. 7).

References

Arboit, F., A. S. Collins, R. C. King, C. K. Morley, and R. L. Hansberry, 2014, Structure of the Sibumasu-Indochina Collision, Central Thailand: A section through the Khao Khwang Fold and Thrust Belt: Journal of Asian Earth Sciences, v. 90.

Árkai, P., and D. S. Ghabrial, 1997, Chlorite crystallinity as an indicator of metamorphic grade of low-temperature meta-igneous rocks; a case study from the Bukk Mountains, Northeast Hungary: Clay Minerals, v. 32, p. 205-222.

Árkai, P., F. P. Sassi, and R. Sassi, 1995, Simultaneous measurements of chlorite and illite crystallinity; a more reliable tool for mo **Fig 1.** Schematic cross section of a think-skinned fold-thrust belt exhibiting multiple detachment levels.

nitoring low-to very low grade metamorphisms in metapelites; a case study from the Southern Alps (NE Italy): European Journal of Mineralogy, v. 7, p. 1115-1128.

Aydin, M. G., and T. Engelder, 2014, Revisiting the Hubbert–Rubey pore pressure model for overthrust faulting: Inferences from bedding-parallel detachment surfaces within Middle Devonian gas shale, the Appalachian Basin, USA: Journal of Structural Geology, v. 69, p. 519-537.

Barber, A., M. Ridd, and M. Crow, 2011, The origin, movement and assembly of the pre-Tertiary tectonic units of Thailand: The Geology of Thailand, Geological Society, London, p. 507-537.

Barker, C. E., 1988, Geothermics of petroleum systems: Implications of the stabilization of kerogen thermal maturation after a geologically brief heating duration at peak temperature: Petroleum systems of the United States: US Geological Survey Bulletin, v. 1870, p. 26-29.

Barker, C. E., Y. Bone, and M. D. Lewan, 1998, Fluid inclusion and vitrinite-reflectance geothermometry compared to heat-flow models of maximum paleotemperature next to dikes, western onshore Gippsland Basin, Australia: International Journal of Coal Geology, v. 37, p. 73-111.

Barker, C. E., and R. B. Halley, 1986, Fluid inclusion, stable isotope, and vitrinite reflectance evidence for the thermal history of the Bone Spring Limestone, southern Guadalupe Mountains, Texas: Roles of organic matter in sediment diagenesis: Society of Economic Paleontologists and Mineralogists Special Publication, v. 38, p. 190-203.

Brigatti, M., E. Galan, and B. Theng, 2006, Structures and mineralogy of clay minerals: Handbook of clay science, v. 1, p. 19-69.

Briggs, S. E., R. J. Davies, J. A. Cartwright, and R. Morgan, 2006, Multiple detachment levels and their control on fold styles in the compressional domain of the deepwater west Niger Delta: Basin Research, v. 18, p. 435-450.

Byerlee, J., 1978, Friction of rocks: Pure and applied geophysics, v. 116, p. 615-626.

Clauer, N., L. B. Williams, and A. E. Fallick, 2014, Genesis of nanometric illite crystals elucidated by light-element (hydrogen, lithium, boron and oxygen) isotope tracing, and K-Ar and Rb-Sr dating: Chemical Geology.

Cobbold, P. R., A. Zanella, N. Rodrigues, and H. Løseth, 2013, Bedding-parallel fibrous veins (beef and cone-in-cone): worldwide occurrence and possible significance in terms of fluid overpressure, hydrocarbon generation and mineralization: Marine and Petroleum Geology, v. 43, p. 1-20.

Corredor, F., J. H. Shaw, and F. Bilotti, 2005, Structural styles in the deep-water fold and thrust belts of the Niger Delta: AAPG bulletin, v. 89, p. 753-780.

Dahlen, F., 1990, Critical taper model of fold-and-thrust belts and accretionary wedges: Annual Review of Earth and Planetary Sciences, v. 18, p. 55.

Davis, D., J. Suppe, and F. Dahlen, 1983, Mechanics of fold-and-thrust belts and accretionary wedges: Journal of Geophysical research, v. 88, p. 1153-1172.

Dietrich, D., J. A. McKenzie, and H. Song, 1983, Origin of calcite in syntectonic veins as determined from carbon-isotope ratios: Geology, v. 11, p. 547-551.

Ding, W., C. Li, C. Li, C. Xu, K. Jiu, W. Zeng, and L. Wu, 2012, Fracture development in shale and its relationship to gas accumulation: Geoscience Frontiers, v. 3, p. 97-105.

Eberl, D., and J. Hower, 1976, Kinetics of illite formation: Geological Society of America Bulletin, v. 87, p. 1326-1330.

Fagereng, Å., 2011a, Fractal vein distributions within a fault-fracture mesh in an exhumed accretionary mélange, Chrystalls Beach Complex, New Zealand: Journal of Structural Geology, v. 33, p. 918-927.

Fagereng, Å., 2011b, Geology of the seismogenic subduction thrust interface: Geological Society, London, Special Publications, v. 359, p. 55-76.

Fagereng, Å., and R. H. Sibson, 2010, Melange rheology and seismic style: Geology, v. 38, p. 751-754.

Faulkner, D., C. Jackson, R. Lunn, R. Schlische, Z. Shipton, C. Wibberley, and M. Withjack, 2010, A review of recent developments concerning the structure, mechanics and fluid flow properties of fault zones: Journal of Structural Geology, v. 32, p. 1557-1575.

Fernández-Caliani, J., and E. Galán, 1992, Influence of tectonic factors on illite crystallinity; a case study in the Iberian pyrite belt: Clay Minerals, v. 27, p. 385-388.

Frey, M., 1987, Low temperature metamorphism, Blackie.

Frey, M., M. Teichmüller, R. Teichmüller, J. Mullis, B. Künzi, A. Breitschmid, U. Gruner, and B. Schwizer, 1980, Very low-grade metamorphism in external parts of the Central Alps: illite crystallinity, coal rank and fluid inclusion data: Eclogae Geologicae Helvetiae, v. 73, p. 173-203.

Goodwin, L. B., and B. Tikoff, 2002, Competency contrast, kinematics, and the development of foliations and lineations in the crust: Journal of Structural Geology, v. 24, p. 1065-1085.

Guthrie, J. M., D. W. Houseknecht, and W. D. Johns, 1986, Relationships among vitrinite reflectance, illite crystallinity, and organic geochemistry in Carboniferous strata, Ouachita Mountains, Oklahoma and Arkansas: AAPG bulletin, v. 70, p. 26-33.

Gutiérrez-Alonso, G., and F. Nieto, 1996a, White-mica'crystallinity', finite strain and cleavage development across a large.

Gutiérrez-Alonso, G., and F. Nieto, 1996b, White-mica'crystallinity', finite strain and cleavage development across a large Variscan structure, NW Spain: Journal of the Geological Society, v. 153, p. 287-299.

Haines, S. H., B. Kaproth, C. Marone, D. Saffer, and B. van der Pluijm, 2013, Shear zones in clay-rich fault gouge: A laboratory study of fabric development and evolution: Journal of Structural Geology, v. 51, p. 206-225.

Hansberry, R. L., R. C. King, A. S. Collins, and C. K. Morley, 2014, Complex Structure of an Upper-level Shale Detachment Zone: Khao Khwang Fold and Thrust Belt, Central Thailand: Journal of Structural Geology.

Hara, H., K. Wakita, K. Ueno, Y. Kamata, K.-i. Hisada, P. Charusiri, T. Charoentitirat, and P. Chaodumrong, 2009, Nature of accretion related to Paleo-Tethys subduction recorded in northern Thailand: constraints from mélange kinematics and illite crystallinity: Gondwana Research, v. 16, p. 310-320.

Hesse, R., and E. Dalton, 1991, Diagenetic and low - grade metamorphic terranes of Gaspé Peninsula related to the geological structure of the Taconian and Acadian orogenic belts, Quebec Appalachians: Journal of Metamorphic Geology, v. 9, p. 775-790.

Hill, D. G., T. E. Lombardi, and J. P. Martin, 2004, Fractured shale gas potential in New York: Northeastern Geology and Environmental Sciences, v. 26, p. 57-78.

Hubbert, M. K., and W. W. Rubey, 1959, Role of fluid pressure in mechanics of overthrust faulting I. Mechanics of fluid-filled porous solids and its application to overthrust faulting: Geological Society of America Bulletin, v. 70, p. 115-166.

Ji, J., and P. R. Browne, 2000, Relationship between illite crystallinity and temperature in active geothermal systems of New Zealand: Clays and Clay Minerals, v. 48, p. 139-144.

Kennedy, M. J., S. C. Löhr, S. A. Fraser, and E. T. Baruch, 2014, Direct evidence for organic carbon preservation as clay-organic nanocomposites in a Devonian black shale; from deposition to diagenesis: Earth and Planetary Science Letters, v. 388, p. 59-70.

Kirschner, D. L., Z. D. Sharp, and H. Masson, 1995, Oxygen isotope thermometry of quartz-calcite veins: Unraveling the thermal-tectonic history of the subgreenschist facies Morcles nappe (Swiss Alps): Geological Society of America Bulletin, v. 107, p. 1145-1156.

Kisch, H., 1991a, Development of slaty cleavage and degree of very - low - grade metamorphism: a review: Journal of Metamorphic Geology, v. 9, p. 735-750.

Kisch, H., 1991b, Illite crystallinity: recommendations on sample preparation, X - ray diffraction settings, and interlaboratory samples: Journal of Metamorphic Geology, v. 9, p. 665-670.

Kisch, H., and M. Frey, 1987, Appendix: Effect of sample preparation on the measured 10 Å peak width of illite (illite-"crystallinity"): Low temperature metamorphism, p. 301-304.

Kosakowski, G., V. Kunert, C. Clauser, W. Franke, and H. J. Neugebauer, 1999, Hydrothermal transients in Variscan crust: paleo-temperature mapping and hydrothermal models: Tectonophysics, v. 306, p. 325-344.

Kübler, B., 1968, Evaluation quantitative du metamorphism par la cristallinite de l'Illite: Bull. Centre Rech. Pau-SNPA, v. 2, p. 385-397.

Kübler, B., and M. Jaboyedoff, 2000, Illite crystallinity: Comptes Rendus de l'Académie des Sciences-Series IIA-Earth and Planetary Science, v. 331, p. 75-89.

Lacroix, B., A. Travé, M. Buatier, P. Labaume, T. Vennemann, and M. Dubois, 2014, Syntectonic fluid-flow along thrust faults: Example of the South-Pyrenean fold-and-thrust belt: Marine and Petroleum Geology, v. 49, p. 84-98.

Lindgreen, H., V. A. Drits, B. A. Sakharov, A. L. Salyn, P. Wrang, and L. G. Dainyak, 2000, Illite-smectite structural changes during metamorphism in black Cambrian Alum shales from the Baltic area: American Mineralogist, v. 85, p. 1223-1238.

Mählmann, R. F., Ö. Bozkaya, S. Potel, R. Le Bayon, B. Šegvić, and F. Nieto, 2012, The pioneer work of Bernard Kübler and Martin Frey in very low-grade metamorphic terranes: paleo-geothermal potential of variation in Kübler-Index/organic matter reflectance correlations. A review: Swiss Journal of Geosciences, v. 105, p. 121-152.

Maloney, D., R. Davies, J. Imber, S. Higgins, and S. King, 2010, New insights into deformation mechanisms in the gravitationally driven Niger Delta deep-water fold and thrust belt: AAPG bulletin, v. 94, p. 1401-1424.

Maltman, A., 1994, geological deformation of sediments, Chapman & Hall.

Merriman, R., and B. Roberts, 1985, A survey of white mica crystallinity and polytypes in pelitic rocks of Snowdonia and Llyn, North Wales: Mineralogical Magazine, v. 49, p. 305-319.

Moore, D. E., and D. A. Lockner, 2008, Talc friction in the temperature range 25–400 C: Relevance for fault-zone weakening: Tectonophysics, v. 449, p. 120-132.

Morley, C., P. Ampaiwan, S. Thanudamrong, N. Kuenphan, and J. Warren, 2013, Development of the Khao Khwang Fold and Thrust Belt: implications for the geodynamic setting of Thailand and Cambodia during the Indosinian Orogeny: Journal of Asian Earth Sciences.

Morley, C., P. Ampaiwan, S. Thanudamrong, and J. Warren, 2011a, Structural Style and Evolution of the Saraburi Group (Khao Khwang Platform), PTTEP Chulalongkorn University

Morley, C. K., R. King, R. Hillis, M. Tingay, and G. Backe, 2011b, Deepwater fold and thrust belt classification, tectonics, structure and hydrocarbon prospectivity: A review: Earth-Science Reviews, v. 104, p. 41-91.

Pepper, A. S., and P. J. Corvi, 1995, Simple kinetic models of petroleum formation. Part I: oil and gas generation from kerogen: Marine and Petroleum Geology, v. 12, p. 291-319.

Pollastro, R. M., 1986, Application of clay-mineral, vitrinite reflectance, and fluid inclusion studies to the thermal and burial history of the Pinedale anticline, Green River basin, Wyoming.

Price, L. C., 1983, Geologic time as a parameter in organic metamorphism and vitrinite reflectance as an absolute paleogeothermometer: Journal of Petroleum Geology, v. 6, p. 5-38.

Roberts, B., R. Merriman, and W. Pratt, 1991, The influence of strain, lithology and stratigraphical depth on white mica (illite) crystallinity in mudrocks from the vicinity of the Corris Slate Belt, Wales: implications for the timing of metamorphism in the Welsh Basin: Geological Magazine, v. 128, p. 633-645.

Robinson, D., L. Warr, and R. Bevins, 1990, The illite 'crystallinity'technique: a critical appraisal of its precision: Journal of Metamorphic Geology, v. 8, p. 333-344.

Rowan, M. G., F. J. Peel, and B. C. Vendeville, 2004, Gravity-driven fold belts on passive margins.

Rutter, E., A. Hackston, E. Yeatman, K. Brodie, J. Mecklenburgh, and S. May, 2013, Reduction of friction on geological faults by weak-phase smearing: Journal of Structural Geology, v. 51, p. 52-60.

Sakaguchi, A., A. Yanagihara, K. Ujiie, H. Tanaka, and M. Kameyama, 2007, Thermal maturity of a fold–thrust belt based on vitrinite reflectance analysis in the Western Foothills complex, western Taiwan: Tectonophysics, v. 443, p. 220-232.

Samuelsson, J., and M. F. Middleton, 1998, The Caledonian foreland basin in Scandinavia: constrained by the thermal maturation of the Alum Shale: GFF, v. 120, p. 307-314.

Sherkati, S., M. Molinaro, D. Frizon de Lamotte, and J. Letouzey, 2005, Detachment folding in the Central and Eastern Zagros fold-belt (Iran): salt mobility, multiple detachments and late basement control: Journal of Structural Geology, v. 27, p. 1680-1696.

Simpson, G. D. H., 2009, Mechanical modelling of folding versus faulting in brittle–ductile wedges: Journal of Structural Geology, v. 31, p. 369-381.

Sone, M., and I. Metcalfe, 2008, Parallel Tethyan sutures in mainland Southeast Asia: new insights for Palaeo-Tethys closure and implications for the Indosinian orogeny: Comptes Rendus Geoscience, v. 340, p. 166-179.

Sposito, G., N. T. Skipper, R. Sutton, S.-h. Park, A. K. Soper, and J. A. Greathouse, 1999, Surface geochemistry of the clay minerals: Proceedings of the National Academy of Sciences, v. 96, p. 3358-3364.

Stach, E., and D. G. Murchison, 1982, Stach's Textbook of coal petrology.

Stewart, S., 1996, Influence of detachment layer thickness on style of thin-skinned shortening: Journal of Structural Geology, v. 18, p. 1271-1274.

Suppe, J., 2014, Fluid overpressures and strength of the sedimentary upper crust: Journal of Structural Geology, v. 69, p. 481-492.

Sweeney, J. J., and A. K. Burnham, 1990, Evaluation of a Simple Model of Vitrinite Reflectance Based on Chemical Kinetics (1): AAPG bulletin, v. 74, p. 1559-1570.

Teichmüller, M., 1987, Organic material and very low-grade metamorphism: Low temperature metamorphism, p. 114-161.

Ueno, K., and T. Charoentitirat, 2011, Carboniferous and Permian: The Geology of Thailand. Geological Society, London, p. 71-136.

Underwood, M. B., M. M. Laughland, and S. M. Kang, 1993, A comparison among organic and inorganic indicators of diagenesis and low-temperature metamorphism: Thermal evolution of the Tertiary Shimanto Belt, Southwest Japan: An example of ridge-trench interaction, v. 273, p. 45.

Veizer, J., D. Ala, K. Azmy, P. Bruckschen, D. Buhl, F. Bruhn, G. A. Carden, A. Diener, S. Ebneth, and Y. Godderis, 1999, $^{87}Sr/^{86}Sr$, $\delta^{13}C$ and $\delta^{18}O$ evolution of Phanerozoic seawater: Chemical Geology, v. 161, p. 59-88.

Viti, C., and C. Collettini, 2009, Growth and deformation mechanisms of talc along a natural fault: a micro/nanostructural investigation: Contributions to Mineralogy and Petrology, v. 158, p. 529-542.

Warr, L., and A. Rice, 1994, Interlaboratory standardization and calibration of day mineral crystallinity and crystallite size data: Journal of Metamorphic Geology, v. 12, p. 141-152.

Warr, L. N., R. O. Greiling, and E. Zachrisson, 1996, Thrust - related very low grade metamorphism in the marginal part of an orogenic wedge, Scandinavian Caledonides: Tectonics, v. 15, p. 1213-1229.

Warren, J., C. Morley, T. Charoentitirat, I. Cartwright, P. Ampaiwan, P. Khositchaisri, M. Mirzaloo, and J. Yingyuen, 2014, Structural and fluid evolution of Saraburi Group sedimentary carbonates, central Thailand: A tectonically driven fluid system: Marine and Petroleum Geology.

Wells, R. K., J. Newman, and S. Wojtal, 2014, Microstructures and rheology of a calcite-shale thrust fault: Journal of Structural Geology, v. 65, p. 69-81.

Wiltschko, D. V., G. R. Lambert, and W. Lamb, 2009, Conditions during syntectonic vein formation in the footwall of the Absaroka Thrust Fault, Idaho–Wyoming–Utah fold and thrust belt: Journal of Structural Geology, v. 31, p. 1039-1057.

Chapter 4

Strain and competency contrasts in shale detachment zones: An Examination of the relationship between finite strain and illite crystallinity

Abstract

The characterisation of the smectite to illite transformation through measurement of illite crystallinity is the most widely used technique for constraining the metamorphic grade of sub-greenschist facies rocks. Temperature is widely accepted to exert the most significant control on the prograde transformation from smectite to illite, and accompanying decrease in illite crystallite size. Despite its widespread application, the kinetics of this reaction remain poorly constrained, with various other factors such as strain, heating period, and lithology reported as controls on illite crystallinity. The role of tectonic strain is subject to conflicting evidence, with authors variously reporting strong to absent correlations with illite crystallinity. However, it is established that an increase in strain can lower the activation threshold for the recrystallization of illite, potentially inducing an increased illite crystallinity in rocks subject to otherwise identical conditions. We use the Fry method of finite strain analysis and X-ray Diffraction of the ≤2 μm fraction of deformed shale samples to investigate the relationship between finite strain and illite crystallinity across three ancient, exhumed shale detachment zones in various geological settings. Results from the Sap Bon Formation detachment zone in the Khao Khwang Fold-Thrust belt of central Thailand are compared to the Osen Røa thrust-sheet of the Oslo Region, Norway, as well as the Chrystalls Beach Complex of Southern Otago, New Zealand. Results from across the three field areas exhibit a strong linear correlation between illite crystallinity and finite strain. However, when separated the results from each area provide a different degree of correlation and the overall trend is best captured in the Chrystalls Beach Complex, which was sampled on a region scale, where a demonstrable increase in metamorphic grade is well established. Comparison of illite crystallinity and finite strain on a smaller scale, in the contrasting continuous vs. discontinuous deformational styles of the Sap Bon Formation and outcrop scale sampling of the Chrystalls Beach Complex, indicates illite crystallinity has potential as a tool for tracking finite strain variation with fine grained rocks; relatively high-strain domains within both field areas exhibit consistently higher illite crystallinity than the surrounding low-strain domains.

Key words: Illite crystallinity, strain, shale detachment, QEMSCAN

1. Introduction

Investigation of the tectonic evolution of deforming sequences in orogens requires an understanding of the conditions (temperature, pressure, fluid flow) and the material properties (lithology, rheology, chemistry) of those sequences. The integration of metamorphic petrography and structural geology is a powerful tool in determining these conditions and their impacts on deformation (Poyatos et al., 2001). In medium- to high-grade metamorphic rocks, this is simplified by the existence of equilibrium assemblages with established relationships to physical parameters (e.g. temperature and pressure paths) (e.g. Kelsey and Hand, 2015). However, a method for quantitative determination of temperature in diagenetic to very low-grade metamorphic (VLGM) conditions is not well

constrained (Warr et al., 1996; Mählmann et al., 2012; Hansberry et al., 2014).

Characterisation of the prograde clay mineral transformation of smectite → mixed-layers illite smectite → illite, and measurements of ' illite crystallinity ' (calibrated to various inter-laboratory standards), is the most widely used and accepted method for evaluation of metamorphic grade within diagenetic and VLGM zones, both in sedimentary successions and structurally deformed sequences (Frey et al., 1980; Warr et al., 1996; Hara et al., 2009). Increase in temperature is considered to be the most significant control on the illitization process (Kübler, 1968; Árkai et al., 1995). However, it is widely accepted that the variables of this kinetic relationship are not well understood (Mählmann et al., 2012). Other factors, such as lithology, heating period, fluid flow, K+ ion availability, tectonic strain, and mechanical reduction of crystallite size have been suggested as potentially influencing illite crystallinity (Frey, 1987; Underwood et al., 1993; Kosakowski et al., 1999; Dellisanti et al., 2008). The role of strain in affecting the illite crystallinity measurements of diagenetic and VLGM rocks has been a matter of debate and the subject of contrasting evidence (Roberts et al., 1991; Dellisanti et al., 2008). In a review on the influence of stress on illite crystallinity, Frey (1987) references various studies that found increased illite crystallinities in shear zones as opposed to adjacent, unsheared rocks. More recent studies have built on this relationship and concluded that strain is an important variable in the development of illite crystallinity (Roberts et al., 1991). Some studies report variable results in measuring illite crystallinity across strain variation (Poyatos et al., 2001), while others demonstrate a clear relationship between finite strain and the development of illite crystallinity (Gutiérrez-Alonso and Nieto, 1996; Dellisanti et al., 2008). Gutiérrez-Alonso & Nieto (1996) found a close inverse relationship between increasing finite strain and the illite crystallinity value (Kübler Index in units of Δ°2θ), which they concluded was robust enough to use illite crystallinity as a proxy for measuring strain variation in siliciclastic rocks.

Recent work on a newly defined, exhumed shale detachment zone in the Khao Khwang Fold and Thrust Belt (KKFTB), Thailand, has presented an opportunity to study the use of illite crystallinity in characterising conditions in a deformed, fine-grained sequence (Hansberry et al., 2014; 2015). The aim of this study is twofold: 1) to investigate the relationships between illite crystallinity and finite strain in fine-grained rocks; and 2) to characterise these relationships in the context of deformational styles in heterogeneously deformed shale detachment zones. In addition to data from the KKFTB in Thailand, samples were taken from two other detachment zones within exhumed settings, and where the nature of deformation has been more thoroughly established: the Chrystalls Beach Complex in southern Otago, New Zealand; and the Osen-Røa detachment in Caledonides of the Oslo Region, Norway (Figs. 2,3).

2. Geological setting

2.2 The Khao Khwang Fold-Thrust Belt, Central Thailand

The KKFTB of the Khorat Plateau in Central Thailand (Fig. 1A) is understudied and the focus of recent and ongoing works (Morley et al., 2013; Arboit et al., 2014; Warren et al., 2014). Carboniferous-Permian carbonates, clastics, and siliciclastics were deposited in a series of rift-basins formed on the southern margin of the Indochina Block (Fig. 1B) (Bunopas, 1981; Hinthong et al., 1985). These basins were inverted and deformed during the Triassic Indosinian

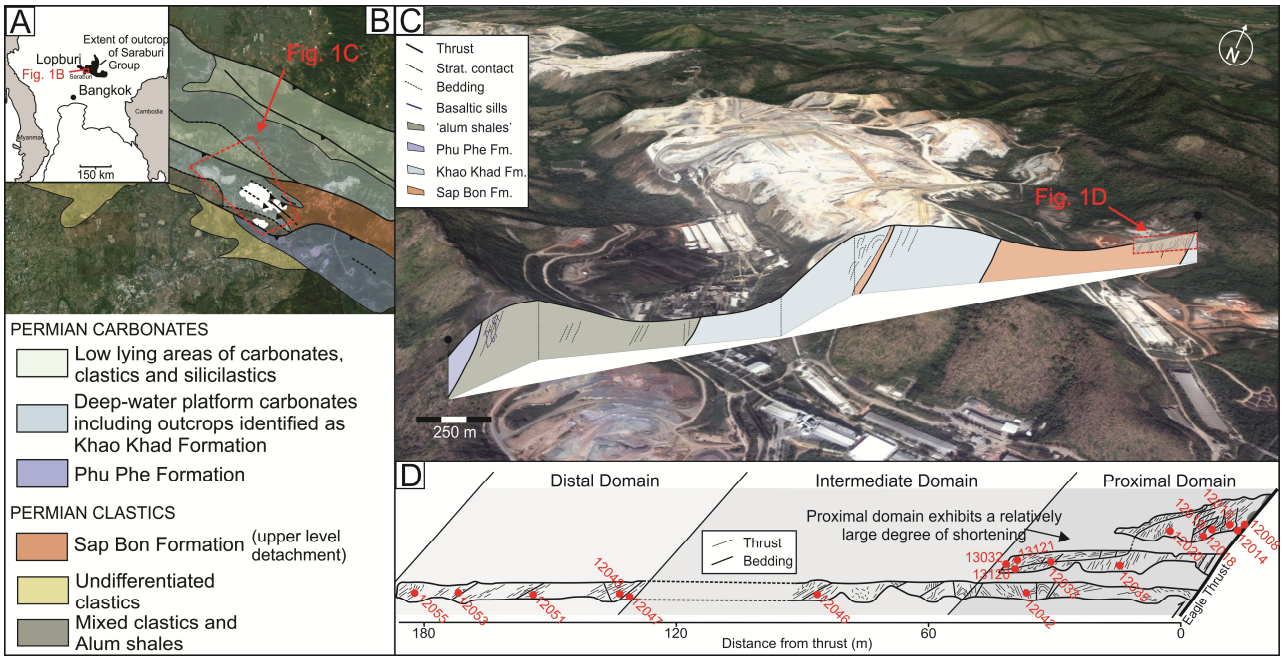

Fig. 1. Location and geological setting of the Eagle Thrust detachment zone in central Thailand. (A) Extent of Saraburi Group outcrop in Central Thailand. (B) Simplified geological map of the area surrounding the Siam City Cement quarry. (C) Cross-section through the quarry showing location Fig. 1D. (D) Detailed cross-section and sample locations of the detachment zone in the Sap Bon Formation above the Eagle Thrust (after Hansberry et al. 2014).

Orogeny as a result of a series of subduction and collision related events (Sone and Metcalfe, 2008; Ueno and Charoentitirat, 2011; Morley et al., 2013). Hansberry et al. (2014) define an upper-level detachment within the Sap Bon Formation shales (Fig. 1B), exhibiting a mixed continuous-discontinuous deformational style featuring complex three-dimensional fault geometries within the fault damage-zone of the Eagle Thrust, exposed in the Siam City Cement Quarry (Fig 1). Geometric complexity and spacing of deformational structures, as well as the occurrence of continuous deformation shear zones decrease with increased distance from the base of the detachment zone at the Eagle Thrust (Fig. 1D) (Hansberry et al., 2014). Stable isotope data indicate a concentration of hot, orogenic fluids along the base of the detachment zone and larger faults associated with continuous deformation shear zones (Hansberry et al., 2015). Illite crystallinity data indicate approximate maximum deformational temperatures between 160-210°C and exhibit a potential correlation between illite crystallinity

value and inferred strain contrast between continuously and discontinuously deformed rocks (Hansberry et al., 2015). In this study, we refer to these zones characterised by a contrast in deformational mechanism (which are likely the result of a ductility contrast between interbeds of the formation), as 'shear domains' and 'fault domains'.

2.3 The Chrystalls Beach Complex, Southern Otago, New Zealand

The Chrystalls Beach Complex is interpreted as accretionary melange exposed along the south-eastern Otago coastline on the South Island of New Zealand (Fig. 2). It formed as part of the Otago Schist accretion-collision assemblage during Triassic-Jurassic subduction along the Gondwana continental margin (Nelson, 1982; Mortimer, 1993; Fagereng, 2011b). It is an exhumed analogue of a 'subduction channel', comprising a mix of cherts, terrigenous muds and sands, and minor volcanogenics in a 'block-in-matrix' style melange (Fagereng and Sibson, 2007). The main sandstone-shale assemblage accounts for >90% of the Chrystalls Beach Complex and these rocks are intensely sheared in a continuous-discontinuous deformational style (Fagereng, 2011a, b). Competent sandstone beds are dismembered through layer parallel extension into asymmetric phacoids, surrounded by a relatively incompetent 'matrix' of cleaved mudstone (Fig. 2D) (Fagereng and Sibson, 2007). The Chrystalls Beach Complex is interpreted to have formed below (or within) a subduction interface detachment zone as indicated by layer-parallel extension and an inferred vertical $\sigma 1$ (Fagereng, 2011b). The assemblage has been progressively deformed through pre-lithification to exhumation, with metamorphism reaching estimated syn-tectonic peak conditions of c. 550 MPa and 300°C, with grade increasing northward towards the centre of the Otago Schist (Fagereng and Cooper, 2010; Fagereng, 2011a).

2.4 The Osen Røa Thrust Sheet, Oslo Region, Norway

Another fossil detachment zone occurs in the Oslo Region, Norway, referring to an area extending approximately 115 km to the north and south of Oslo (Fig. 3). Caledonian deformation during the early Devonian has folded and thrusted a Cambro-Silurian sequence of dark black-grey shales and thin limestones (Morley, 1987, 1994). The underlying Precambrian basement is undeformed by these events, as the thrust sheet is detached in the Late Cambrian Alum Shales Formation (Fig. 3C) (Hossack and Cooper, 1986; Morley, 1987, 1994). This structure called the Osen Røa detachment underlies the entire Oslo region and is characterized by intense deformation and numerous bed-parallel slip planes, as well as disharmonic folding of wavelengths varying from centimetres to hundreds of metres (Fig. 3) (Morley, 1994; Bruton et al., 2010). The Cambro-Middle Devonian sequence is characterized by numerous thrust, back-thrusts and associated fold structures and imbrication (Fig. 3) (Morley, 1986, 1987). Fold-generated faulting (break-thrusts) have also been interpreted as propagating from within the sequence down toward the Osen Røa detachment (Morley, 1994). The Mid Ordovician-Silurian sequence is deformed in broad buckle-folds (Morley, 1987).

The basement cover contact and Alum Shales Formation are accessible along the western coast of the Oslofjord, near Slemmestad and Nærsnes (Fig. 3A). Fluid inclusion data indicates that the Alum Shale Formation in Denmark, southern Sweden and Norway was subjected to temperatures of 200-220°C in the Silurian-Carboniferous, while in central Sweden these temperatures are much lower (95-110°C) (Thomsen et al., 1983; Jensenius, 1987; Lindgreen et al., 2000). Lindgreen et al. (2000) note that despite the temperatures indicated, crystallisation of the illite polytypes 2M1 (200-300°C) or the lower temperature 1M had not taken place. Thicknesses of coherent scattering domains as well as particle shape determined by atomic force microscopy lack evidence for the transition from diagenesis to anchimetamorphic conditions (Lindgreen et al., 2000). The succession also features a series of Upper Palaeozoic dykes, sills, and lavas resulting in localised metamorphism, with temperatures exceeding 300°C, based on Ordovician samples (Bruton et al., 2010).

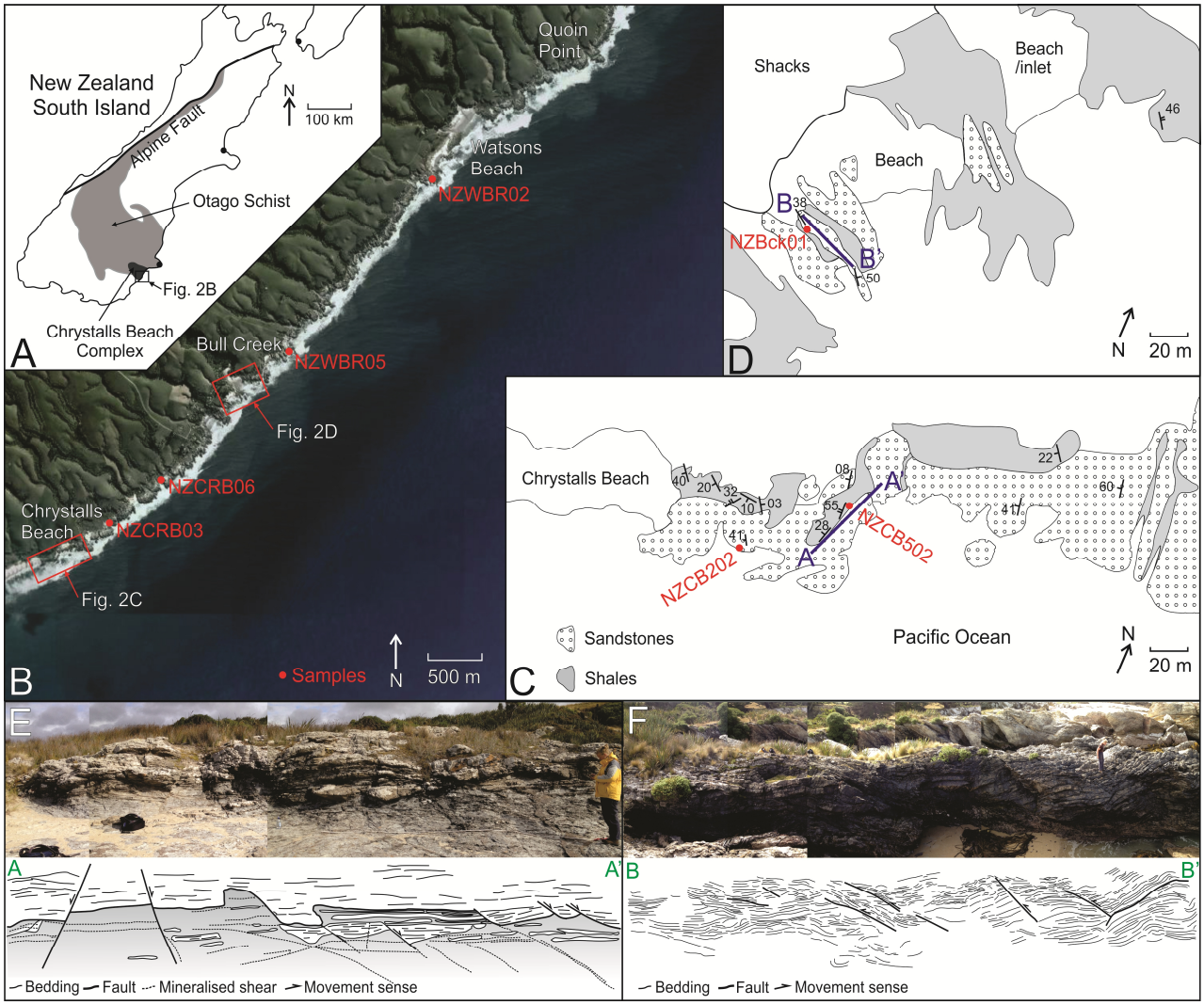

Fig. 2. (A) Location of the Chrystalls Beach Complex and Otago Schist on the South Island, New Zealand. (B) Chrystalls Beach Complex from Chrystalls Beach to Quoin Point along the southern Otago coast. (C) and (D) simplified geological maps of exposures at Chrystalls Beach and Bull Creek, as well as sample locations. (E) and (F) Cross-sections through the areas indicated in Figures 2C and 2D with the mudstone matrix in grey, and sandstones in white.

3. Methods

3.1 Sample materials

The upper-level shale detachment zone exposed above the Eagle Thrust is extremely structurally and lithologically heterogeneous (Fig. 1D) (Hansberry et al., 2014; Hansberry et al., 2015). The Sap Bon Formation consists of interbedded, mudstones, siltstones, and carbonate-cemented sandstones, which are variably sheared and juxtaposed by complex fold and thrust geometries (Hansberry et al., 2014). Samples 1-18 (Table 1) for

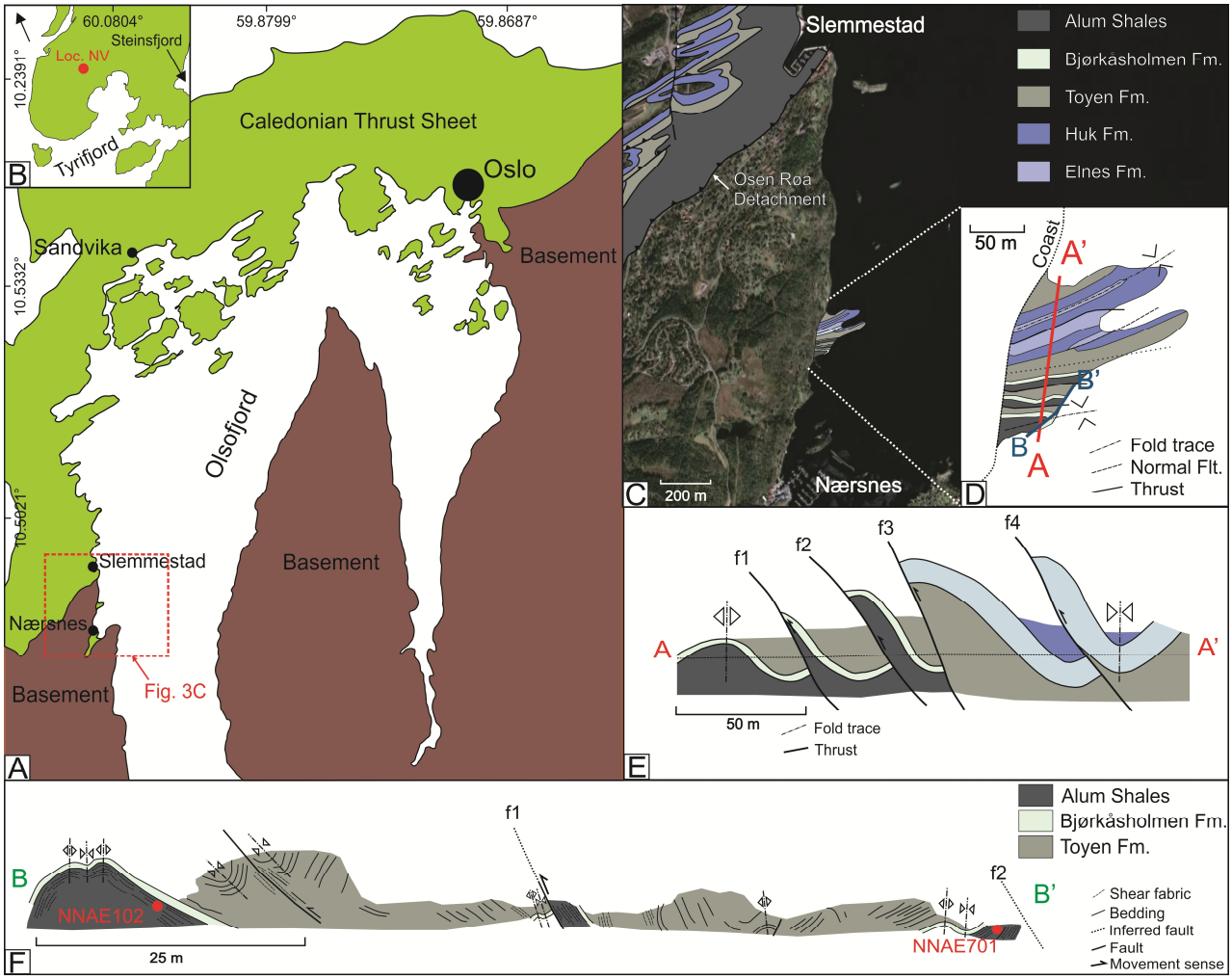

Fig. 3. (A) Location of the Osen Røa thrust sheet in the Oslo Region, Norway. (B) Inset of the sampling location of the Venstøp Formation in Hole, 35 kilometres northwest of Oslo. (C) Slemmestad-Nærsnes region on the west coast of Oslofjorden, showing the basement-cover contact (Osen Røa detachment) south of Slemmestad. (D) Expanded geological map of the Grundvik Peninsula at Nærsnes exposing the basal sequence of the Osen Røa thrust sheet. (E) Cross section through the Grundvik Peninsula (line A-A' in Fig. 3D) (after Morley 1994). (F) Detailed cross-section through the lowermost stratigraphy exposed on the Grundvik Peninsula (line B-B' in Fig. 3D) showing sample locations.

XRD analysis were taken from the contrasting packages of rock that constitute the detachment zone: both the low-competency, continuously deformed shear domains around mineralised shear planes, and the more competent and discontinuously deformed (faulted) surrounding rocks (Fig. 4). Where possible, these samples were taken as shear

domain/fault domain pairs in close proximity to each other. Eighteen samples from the Sap Bon Formation were analysed by XRD and in all cases the samples' associated deformational mechanism was noted (Table 1).

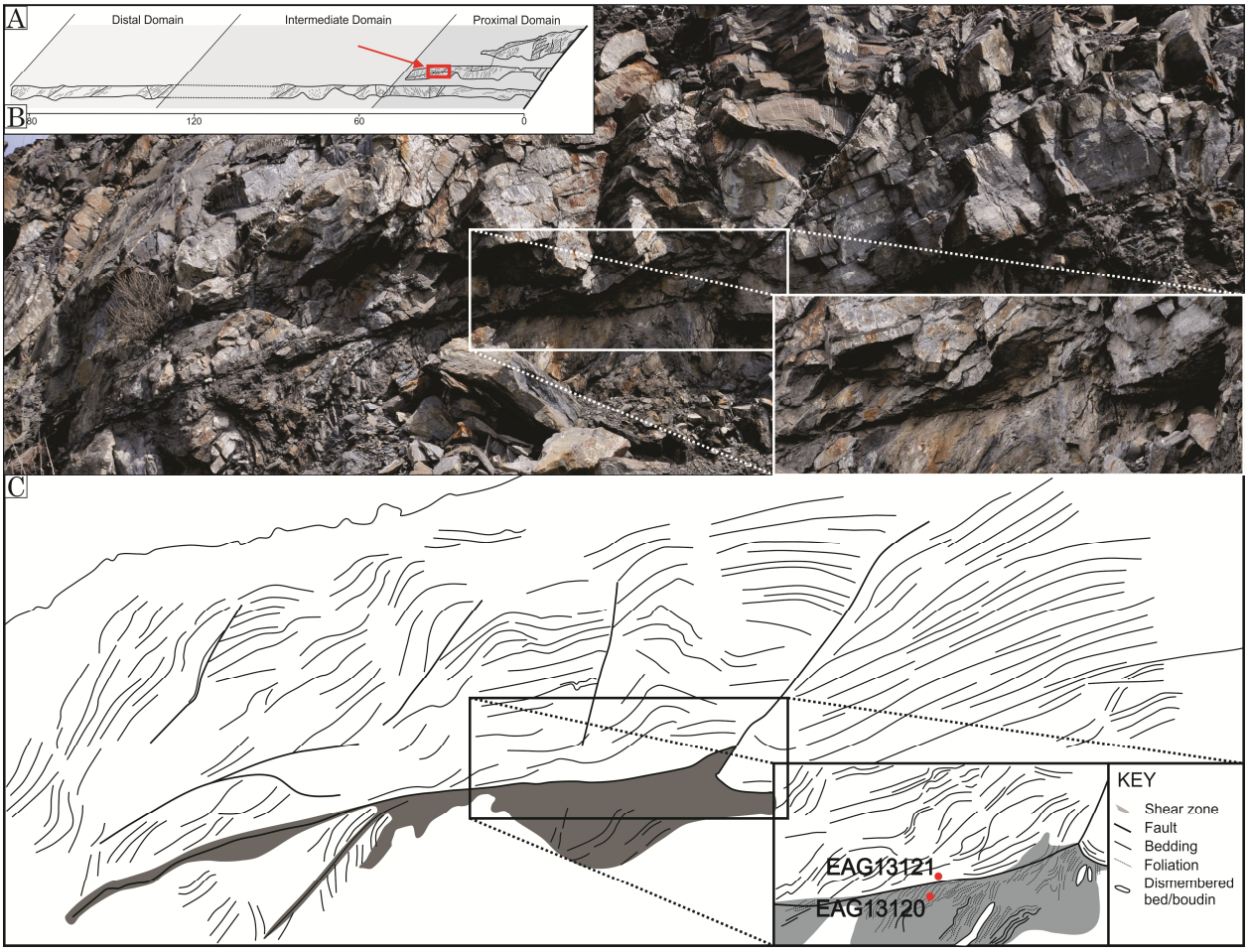

Fig. 4. Illustration of the different deformational mechanism in the Eagle Thrusts detachment zone. (A) Location of (B) and (C) in the cross-section through the Sap Bon Formation. (B) Photograph and (C) line drawing of the contrast between shear domains (grey) and fault domains (white) in the Sap Bon Formation, sample locations indicated inset.

Quoin Point (Fig. 2) (Mortimer, 1993; Fagereng and Sibson, 2007; Fagereng, 2011b). Seven samples were taken in total with three directly from the cross-section locations at Chrystalls Beach and Bull Creek (Fig. 2C, D). Samples were taken from continuously deformed shale matrix in each location.

Two locations were sampled in the Oslo Region (Fig. 3). Two samples of the Alum Shales Formation were taken at the Nærsnes Beach cross-section (Fig. 3F) and two samples of the Venstøp Formation shales that lie stratigraphically higher in the Osen Røa thrust sheet (Upper Ordovician) (Fig. 3B). The Venstøp Formation was used as it is not found in proximity to the Upper Palaeozoic magmatism, and comparison to the Alum Shales Formation may indicate if the latter has undergone

Samples 23-29 (Table 1) from the Chrystalls Beach Complex were taken on a regional scale in a NE-SW transect covering the extent of the accretionary melange from Chrystalls Beach to

alteration of illite crystallinity as a result of contact metamorphism.

3.2 Illite crystallinity by X-ray diffraction

X-ray diffraction of orientated preparations of the $\leqslant 2\ \mu m$ fraction was used to acquire mineralogical and crystallographic data from the 29 samples. These samples were prepared as per the recommendations reported in Kisch (1991). Samples were washed to remove weathered material then milled for <10 second in a disc mill at 2 mm aperture to break up large fragments. Carbonates were removed from the sample using a 1 M sodium acetate buffer and pH 5 and a heat bath at 90 °C. Organic matter was then removed from the samples using a pH 9.5 solution of hypochlorite bleach and the heat bath. Samples were thoroughly washed between and after the purifications with deionised water before the $\leqslant 2\ \mu m$ fraction was separated by centrifugation (per Stokes ' Law). The suspended $\leqslant 2\ \mu m$ fraction was then pipetted onto silicon wafer slides and analysed using a Bruker D8 Advance X-Ray Diffractometer. Instrument conditions were as follows: CuKα radiation at 40 kV/40 mA; 0.6 mm divergence slit; 0.05 (2θ) step size, 1.5s counting time. Diffraction patterns were collected from 3.5 to 45° 2θ. Patterns were collected again after ethylene glycol treatment of the orientated preparations to account for smectite in mixed layer illite-smectite (I-S). Results were calibrated to the Crystallinity Index Standard (CIS) of Warr and Rice (1994) by first recording the XRD patterns of the six rock standards provided by Warr and Rice (1994), using the same sample preparation and instrumental conditions as for the 29 samples in this study. The illite crystallinity values from these patterns were plotted against those provided by Warr and Rice (1994) and a regression was determined to correct our raw data to CIS (Table 1). Values for illite crystallinity are presented as Kübler Index values, corrected to the Crystallinity Index Standard (KI(CIS)).

3.3 Finite strain analysis

In the absence of suitable marker grains or other ovoids, the Fry method of point-to-point strain analysis was employed to determine the finite strain each of the 19 samples used in XRD analysis (Fig. 5) (Fry, 1979; Erslev, 1988). All samples were orientated in the field and thin sections were cut parallel to lineation (X-axis) and perpendicular to foliation (XY plane) in order to assess finite strain in the XZ plane of the finite strain ellipsoid, providing the greatest change in strain, and in the direction of transport (Ramsay and Huber, 1987). Sample material for XRD analysis was taken from as close as possible to the thin section slice so as to be directly comparable. Each thin section was photographed under an optical microscope with five photographs at x10 zoom taken of each 20x40 mm thin section and analysed using the software GeoFryplots. Two analyses were run on each photograph for a total of 10 per sample, with each analysis using between 80-200 grains. The 10 RS values for the strain ellipse were then averaged for each sample and a standard error calculated (Table 1).

Results of XRD of <2 µm Fraction and Strain Analysis

	Characteristic Minerals*				Illite Polytype Ratio	Deformational Association (Sap	Illite crystallinity			Strain	
Sample (ref no.)	Smectite	Illite	Kaolinite	Chlorite	(2M:1M) **	Bon Fm. only)***	KI(CIS) Δ°2θ	Metamorphic grade	Tmax****	R_S	SE
EAG12008 (1)	0%	86%	6%	8%	-	s	0.38	Low anchizone	200	2.06	0.085
EAG12014 (2)	-	-	-	-	58%	f	0.43	Deep diagenetic	170	-	-
EAG12016 (3)	0%	91%	t	7%	-	f	0.39	Low anchizone	190	1.66	0.068
EAG12018 (4)	-	-	-	-	-	s	0.36	Low anchizone	210	-	-
EAG12019 (5)	0%	91%	t	8%	-	f	0.40	Low anchizone	190	1.78	0.032
EAG12020 (6)	-	-	-	-	-	f	0.43	Deep diagenetic	170	-	-
EAG12032 (7)	-	-	-	-	75%	s	0.39	Low anchizone	190	-	-
EAG12033 (8)	t	89%	3%	7%	-	s	0.40	Low anchizone	190	1.63	0.038
EAG12035 (9)	3%	75%	0%	23%	-	f	0.45	Deep diagenetic	160	1.39	0.031
EAG12042 (10)	6%	85%	0%	9%	-	s	0.39	Low anchizone	190	1.82	0.030
EAG12046 (11)	-	-	-	-	55%	f	0.36	Low anchizone	210	-	-
EAG12047 (12)	-	-	-	-	-	f	0.37	Low anchizone	200	-	-
EAG12048 (13)	-	-	-	-	89%	s	0.37	Low anchizone	200	-	-
EAG12051 (14)	-	-	-	-	54%	f	0.36	Low anchizone	210	-	-
EAG12053 (15)	11%	75%	t	12%	-	s	0.40	Low anchizone	190	-	-
EAG12055 (16)	-	-	-	-	72%	s	0.42	Low anchizone	180	-	-
EAG13120 (17)	t	72%	t	25%	-	s	0.37	Low anchizone	200	2.00	0.052
EAG13121 (18)	9%	85%	t	5%	-	f	0.40	Low anchizone	190	1.47	0.032
NNAE1002 (19)	0%	98%	0%	t	-	-	0.49	Deep diagenetic	140	1.21	0.023
NNAE7001 (20)	0%	95%	t	4%	-	-	0.55	Deep diagenetic	120	1.13	0.013
NV001 (21)	0%	84%	0%	16%	-	-	0.58	Deep diagenetic	110	1.03	0.010
NV004 (22)	0%	83%	0%	17%	-	-	0.54	Deep diagenetic	120	1.04	0.007
NzBCk1001 (23)	0%	78%	22%	0%	-	-	0.26	High anchizone	280	2.79	0.046
NZCB2002 (24)	t	90%	5%	4%	-	-	0.43	Deep diagenetic	170	1.26	0.021
NZCB5002 (25)	t	90%	9%	0%	-	-	0.44	Deep diagenetic	170	1.34	0.021
NZCBR003 (26)	0%	80%	3%	17%	-	-	0.29	High anchizone	250	2.51	0.034
NZCBR006 (27)	t	82%	17%	0%	-	-	0.34	Low anchizone	220	2.13	0.023
NZWBR002 (28)	0%	82%	10%	8%	-	-	0.30	Low anchizone	250	2.43	0.028
NZWBR005 (29)	0%	88%	4%	8%	-	-	0.31	Low anchizone	240	2.50	0.048

* Determined by the method of Poppe et al. (2001), intended as relative estimates only, with 't' indicating trace amount (<3%). ** Determined my RockJock software on randomly orientated powders.
*** 's' denotes 'shear domain, 'f' denotes 'fault domain'. *** Temperature per equation of Kosakowski et al. (1999).

3.4 QEMSCAN mineralogy mapping

To investigate the mineralogy of contrasting of low competency shear domains and high competency fault domains the QEMSCAN system located at the Ian Wark Research Institute was employed. The system integrates the Zeiss Evo scanning electron microscope with two Bruker Silicon Drift Detectors (SDD) and iDiscover software. This fully automated instrument provides the capabilities for rapid characterisation of minerals and non-crystalline phases with distinct elemental composition. Two thin sections (one from a fault domain – EAG12016, and one from an adjacent shear domain – EAG12019) were measured with 10 µm spacing resolution, with each of the thin sections split into a grid. The analysed fields (1000 µm in size each) were then stitched into a single composite image allowing mineral associations to be visually represented for interpretation. In this study, a voltage of 25keV and a beam current of 5nA were used. During the QEMSCAN analyses, 1000 count X-ray spectra were collected from each analytical point and

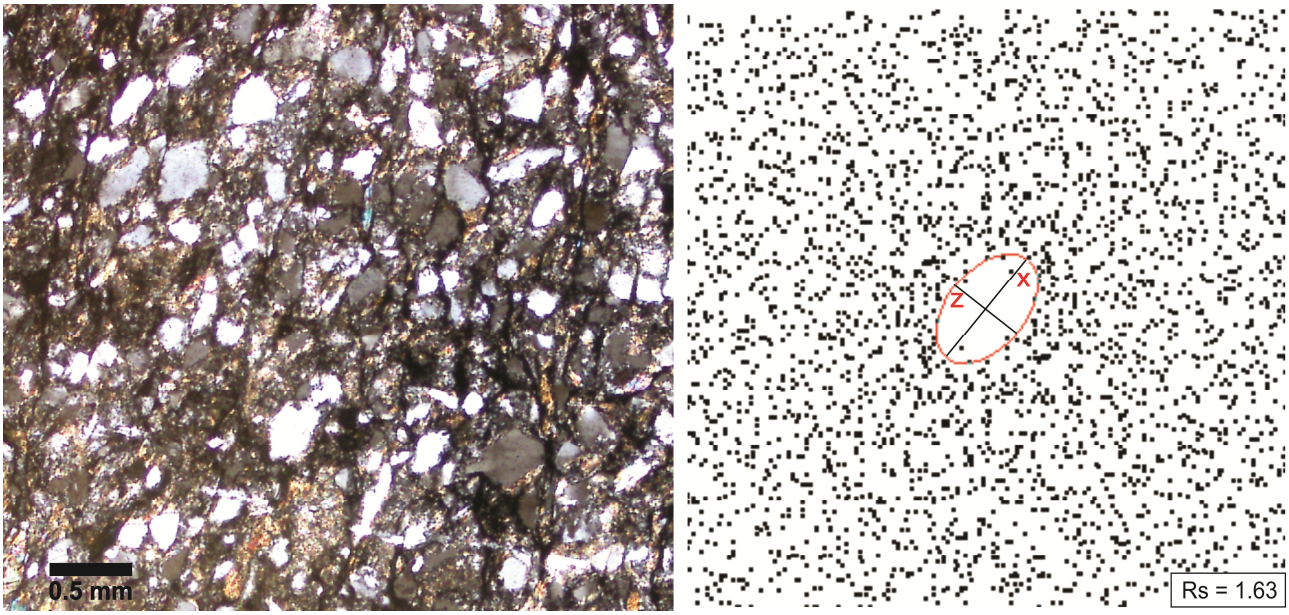

Fig. 5. Example of Fry method of finite strain analysis on sample EAG12042. This is one of 10 measurements taken for this (and each) sample analysed.

were automatically compared against the mineral phases present in the SIP (Species Identification Protocol). The SIP contains also the 'boundary phase' entries which refer to the EDX data collected from the boundaries between two (or more) inter-grown phases.

4. Results

4.1 Illite crystallinity

Results from the 29 samples for which illite crystallinity was determined are shown in Table 1 and Figure 6. Semi-quantitative mineralogy for comparison between samples were calculated from the weighted basal-peak method of Poppe et al. (2001), giving the ubiquitous phyllosilicate mineral assemblage (quartz) + illite ± kaolinite ± chlorite ± smectite (Table 1). For six samples the relative percentage of 1M to 2M illite polytypes were determined using the software RockJock to fit XRD patterns from randomly-orientated

powders on a low-background silicon mount (Table 1) (Eberl, 2003). Illite crystallinity from the 29 samples range from 0.26 to 0.58 Δ°2θ, with the value in the Sap Bon Formation in Thailand and the Chrystalls Beach Complex being largely anchizonal, and results from the Alum Shales Formation and Venstøp Formation in the Oslo Region being diagenetic (Fig. 6). Results from the Sap Bon Formation appear to have no relation to proximity to the Eagle Thrust (Fig. 1) but are related to the deformational association (shear domain/fault domain) of the sample. Results from the Chrystalls Beach Complex show an increase in illite crystallinity towards the NW, consistent with the document increase in grade towards the centre of the Otago Schist (Fagereng and Cooper, 2010; Fagereng, 2011a). Results from the Oslo Region show illite crystallinity ranging from 0.49 to 0.58 Δ°2θ, with marginally lower crystallinity in the Venstøp Formation than the Alum Shales Formation, though from a very small sample size. This is consistent with the relative stratigraphic positions of the Venstøp and Alum Shales formations within the thrust sheet, with the more deeply buried (and possibly heated by intrusion) Alum Shales expected to show a higher degree of crystallinity. However, these values are lower than expected given the deformational temperature range expected (200+ °C), and are more in line with conditions reported for Osen Røa Thrust Sheet in central Sweden (Thomsen et al., 1983; Jensenius, 1987; Lindgreen et al., 2000). These results would also indicate the samples were unaffected by the Upper Palaeozoic magmatism.

4.2 Finite strain

Results from the 19 strain determinations are shown in Table 1 and Figure 6. RS values range from 1.03 to 2.79, with ranges for each field area being 1.39 to 2.06 in the Sap Bon Formation, 1.03 to 1.21 in the Oslo Region, and 1.26 to 2.51 in the Chrystalls Beach Complex. Again, results in the Sap Bon Formation are unrelated to the changes in deformational complexity (spacing, geometry of shears) documented in Hansberry et al. (2014) but are related to the deformational domain, with higher RS values occurring in shear domains than in the fault domains (Fig. 7). The RS values from the Chrystalls Beach Complex are consistent with the documented NW increase in grade (Fagereng and Cooper, 2010; Fagereng, 2011a), with the lowest values occurring in the southern-most Chrystalls Beach area, and values increasing to the NW. Results from the Oslo Region show considerably lower RS values than the other areas, with very little change in strain recorded. These are consistent with the lower (in comparison to the Sap Bon Formation and the Chrystalls Beach Complex) illite crystallinity values recorded in these samples, which is consistent with the illite crystallinity results. A slightly higher RS value is recorded in the Alum Shales Formation than the Venstøp Formation though again interpretation is limited by sample size.

4.3 QEMSCAN mineralogy mapping

Results from the QEMSCAN mapping of the two thin section samples can be seen in Figure 8. Modal mineralogy from each sample as well as a mineralogical and porosity map is shown, and the mapped area of each thin section is

highlighted. Notable differences between the two samples include a much higher percentage of illite/muscovite in the shear domain sample than the fault domain (41.37% and 12.98% respectively), and lower percentage of chlorite/smectite in the shear domain (Fig. 8). Illite/muscovite appears to be relatively evenly distributed through the undeformed fault domain sample while in the shear domain the higher illite/muscovite percentage is concentrated in the highest strain areas featuring the most well developed shear fabric (Fig. 8). Porosity in the fault domain sample is both significantly less in total volume (1.78% compared to 5.03% in the shear domain) and is also less effective, with the porosity maps exhibiting a lack of connection between relatively large pore spaces in the undeformed rock, compared to much finer-scale, but well connected porosity in the shear domain (Fig. 8).

5. Discussion

Reports of observable trends between illite crystallinity and stages of cleavage development (as a proxy for the progression of tectonic deformation, being largely a function of total strain) are widespread, though little evidence has been presented to derive a quantitative relationship between deformation and the development of illite crystallinity (Kisch, 1991a; Fernández-Caliani and Galán, 1992; Gutiérrez-Alonso and Nieto, 1996). The influence of

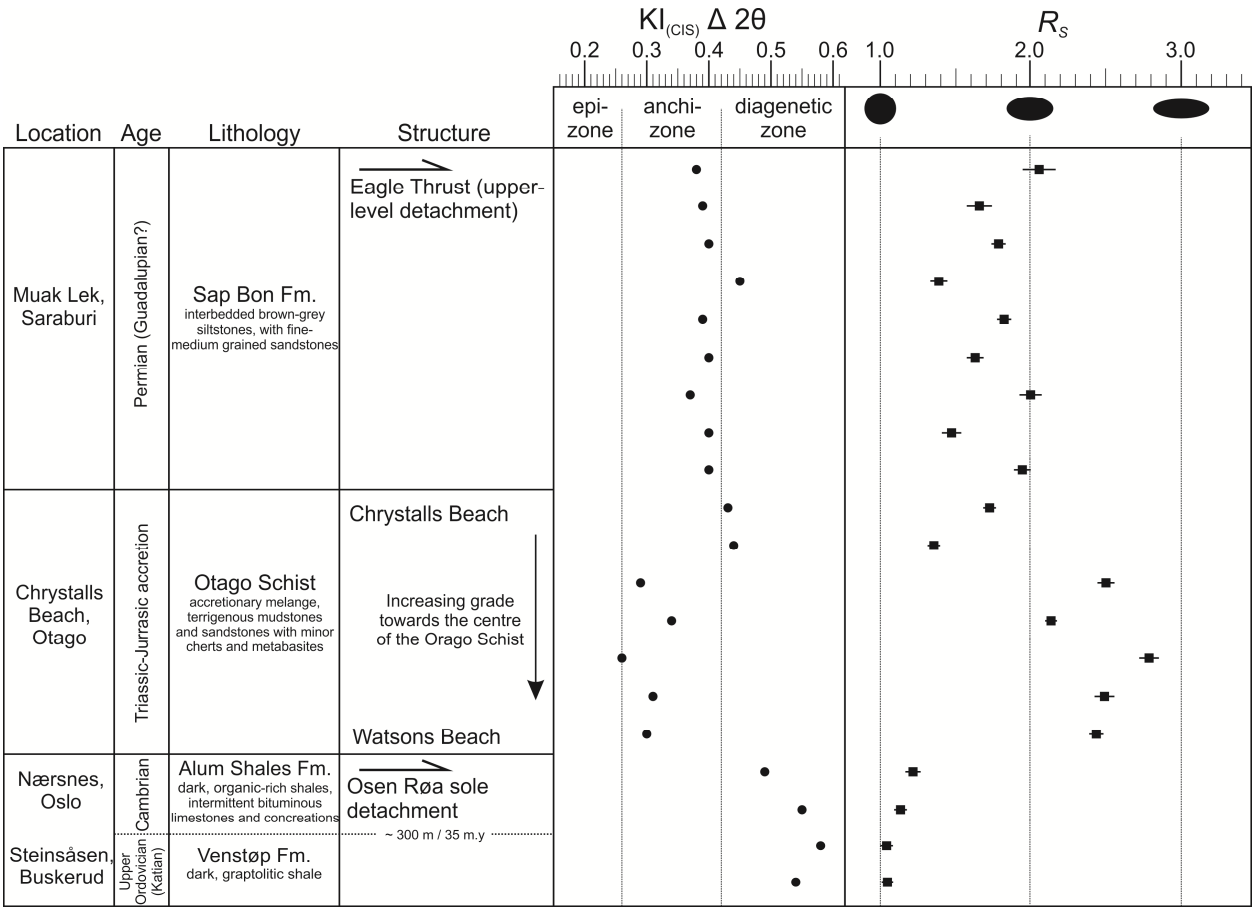

Fig. 6. Results of illite crystallinity and finite strain analysis for 20 samples across the three field areas along with associated geological framework. Error bars of finite strain analysis for each sample are shown.

tectonism as a variable is not always easy to quantify, and establishing a directly measureable relation between strain and metamorphic-grade indicators is often a problem (Gutiérrez-Alonso and Nieto, 1996). Previous studies have focused on investigating variation in illite crystallinity across well-understood tectonic structures and metamorphic profiles (Kisch, 1991a; Árkai et al., 1997), or in relation to the appearance of cleavage and qualitative, or not directly comparable estimates of strain (Gutiérrez-Alonso and Nieto, 1996; Dellisanti et al., 2008). Examples of areas where a quantitative or qualitative relationship between strain and illite crystallinity has been reported include the Otago Schist, New Zealand (Norris and Bishop, 1990); the Helvetic Nappes, Switzerland (Kisch, 1991a); the Corris Slate Belt, Wales (Roberts et al., 1991), the Narcea antiform, Cantabrian Mountains, Spain (Gutiérrez-Alonso and Nieto, 1996); and the Northern Apennines, Italy (Dellisanti et al., 2008).

5.1 Deformational Style and illite crystallinity

Dellisanti et al. (2008) report comparisons of illite crystallinity and tectonic strain from a regional-scale tectonic lineament in the Northern Apennines, Italy. They describe a mylonite-like fault zone dominated by scaly cleavage domains around anastomosing P, R, and D shear planes, which delineate shear lenses at a centimetre scale, as well as at the metre- to tens of metres scale. Illite crystallinity measurements were taken from the three structural domains observed within this fault zone: non-deformed, cleavage domain, and lithon core (centre of shear lenses). Dellisanti et al. 2008 noted that while there was not a significant difference in the range of illite crystallinity data from different domains, the non-deformed samples produced a wider range of illite crystallinity values, while the lithon core and cleavage domain samples produced a narrower range of results, respectively, at the high and low range of KI values from the non-deformed rocks. By comparison, data from this study show a similar trend (Table 1, Fig. 7).

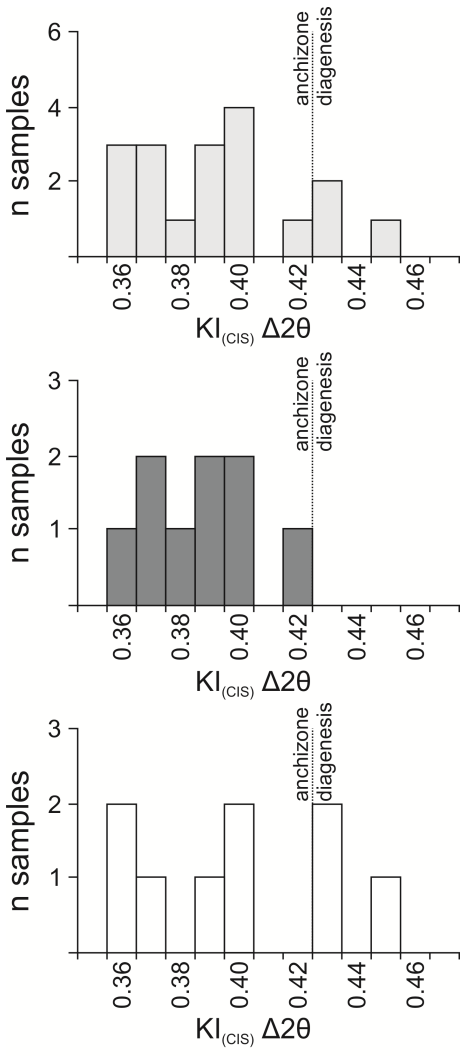

Fig. allinity against deformational domains.

Modal mineralogy

Mineral Volume(%)	Sample	EAG12019	EAG12016
	Porosity	5.03	1.78
	Silicates (C)	1.85	0.8
	Quartz	41.54	74.6
	Illite/Muscovite	41.37	12.98
	Pyrophyllite	0.74	1.21
	Biotite	1.56	1.33
	Kaolinite	0.41	0.38
	Chlorite/Smectite	0.78	1.21
	K Feldspars	0.92	0.56
	Albite	0.07	0.15
	Fe Ox/CO3	0.96	0.87
	Carbonates	3.31	3.41
	Ti(Fe) Oxides	0.96	0.58
	Al Oxides	0	0
	Pyrite	0.36	0.03
	Others	0.13	0.11

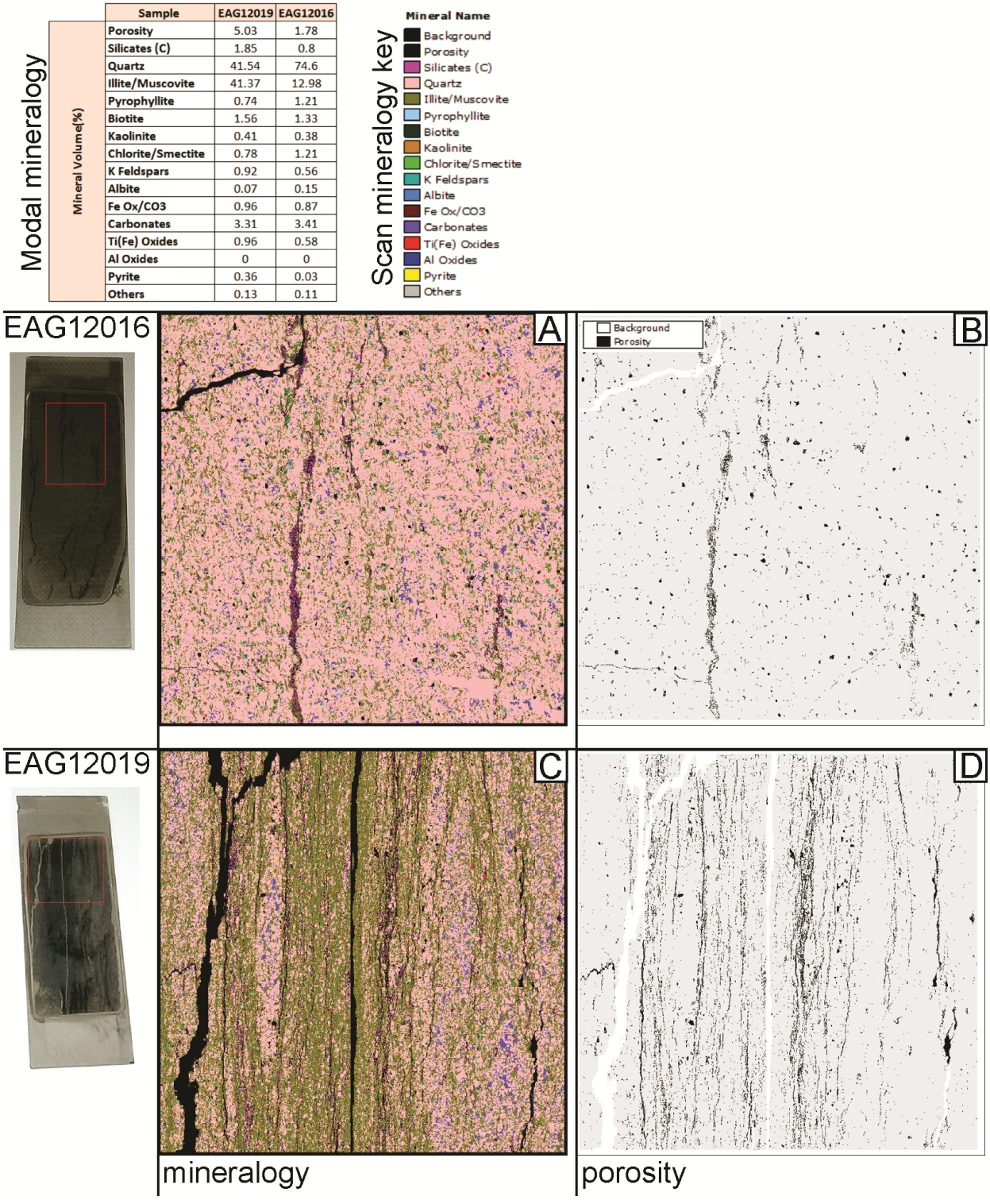

Fig. 8. Modal mineralogy and mineralogy maps from QEMSCAN analysis of fault domain (A, B) and shear domain (C, D) samples. Images A and C show the mineralogy of the scanned area of each thin section, while B and D show the porosity of each sample.

Given the similarity between shale shear zones around anastomosing shear planes in the Sap Bon Formation and descriptions of the cleavage domains of Dellisanti et al. (2008) a similar

relationship between deformational association and illite crystallinity is observed (Fig. 7) (Hansberry et al., 2014). Data from samples of undeformed fault domain rocks (discontinuous deformation) produce a range of KI(CIS) values of 0.36 to 0.45 Δ°2θ with a standard deviation of 0.98 Δ°2θ; data from the continuous deformation shear zones range from 0.36 to 0.42 Δ°2θ with a standard deviation of 0.57 Δ°2θ. Dellisanti et al. (2008) suggest comparison between different structural domains in fault rocks as an efficient tool in investigation of the effects of tectonic strain, fluid flow, and mineralogical evolution. Clear trends are observed in the percentage of illite, and illite in mixed illite-smectite layers, between cleavage domains and the relatively undeformed lithon cores (Dellisanti et al., 2008). Only six samples in this study produced enough of the $\leqslant 2$ μm fraction for XRD analysis of randomly orientated powders for illite polytype quantification.

However, all samples from continuous deformation zones have a significantly higher ratio of 2M to 1Md illite, indicating a more partial prograde development of illite mineralogy outside of continuous deformation zones (Kennedy et al., 2014). This is likely driven by higher strain, and significant fluid flow along shear zones acting as conduits for hot orogenic fluids (evident from significant mineralisation of shear planes) (Hansberry et al., 2014). Results from the QEMSCAN mapping would appear to support this conclusion, with higher volume and effectiveness of porosity found in the sampled shear domains that in surrounding fault domains, as well as well-developed strain fabric in the shear domains contrasting with no sign of any structural fabric in the fault domains (Fig. 8). Modal mineralogy from QEMSCAN also indicates the shear domains have a higher percentage of illite/muscovite than fault domains, and a higher ratio of illite/muscovite to smectite/chlorite suggesting greater prograde development of the smectite → illite transformation (Fig. 8).

5.2 Finite strain and illite crystallinity

The influence of finite strain on the development of illite crystallinity is well documented (Frey, 1987; Roberts et al., 1991; Fernández-Caliani and Galán, 1992). With the exception of the well-established, though also un-quantified, relationship with temperature, strain is inferred to be a more fundamental factor affecting development of white mica recrystallization and illite crystallinity than other controls, such as lithology (Roberts et al., 1991). This appears to be particularly true in rocks undergoing very low-grade metamorphism (sub-greenschist) where strain rate may exceed the rate of burial related (heating) recrystallization (Giorgetti et al., 2000). Increased strain lowers the activation threshold for recrystallization of illite, and therefore, the temperature at which progressive development of illite crystallinity can occur (Kisch, 1991a; Roberts et al., 1991). However, this relationship may be complicated by the order of geological events that have affected the rock: shear related recrystallization after burial heating to anchizonal-to-epizonal conditions may lead to retrogressive decrease in illite crystallinity (increase in KI(CIS))

(Kisch, 1991a; Árkai et al., 2002). Therefore, it is likely that the progressive influence of finite strain on illite crystallinity should only be considered in areas with a simple and single-phase tectonic history (Gutiérrez-Alonso and Nieto, 1996). A clear qualitative relationship is reported between finite strain and white mica crystallinity in the interbedded sandstones and slates of the Cantabrian Zone of the Narcea Antiform (Gutiérrez-Alonso and Nieto, 1996). However, as a result of illite crystallinity and finite strain being determined from equivalent positions but different samples across the studied transect, no comparative analysis is possible. The relationship is, however, reported as suitable for tracking strain variations where other indicators are absent, and indicative of a finite strain value of RS = 1.5 as being comparable to the 0.42 Δ°2θ KI(CIS) anchizone-epizone boundary (Frey, 1987; Árkai et al., 1995; Gutiérrez-Alonso and Nieto, 1996). Results in this study may be more directly compared as illite crystallinity and strain were determined from the same internally homogenous samples, with material used for ⩽2 μm fraction separation taken as rock chips from within less than 2 cm of the thin-section cut. The relationship between illite crystallinity and finite strain from the 19 samples across the three field areas (Figs. 1, 2, 3 and Table 1) exhibits a strong linear correlation (r2 = 0.904, P-value = 1.34 x 10-10 at the 95% confidence interval) with and RS value of 1.693 being equivalent to the anchizone-epizone boundary (Fig. 9). Variation of this trend is noted when samples from each field area are considered separately, with samples from the Oslo Region showing a slightly steeper negative correlation (r2

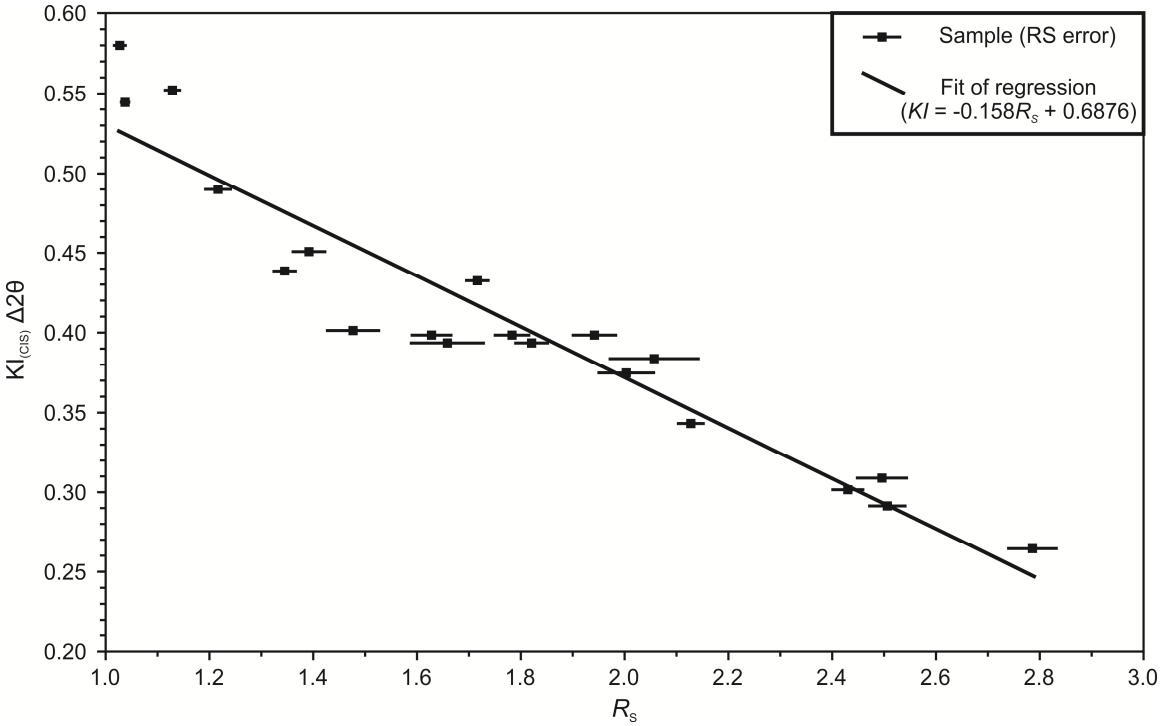

Fig. 9. Scatter-plot of illite crystallinity versus finite strain. Standard error bars for each finite strain analysis are shown. Linear regression line and equation are shown, with this fit predicting a finite strain value of 1.693 R_S as corresponding to the 0.42 Δ°2θ $KI_{(CIS)}$ diagenesis-anchizone boundary.

= 0.75), and samples from the Sap Bon Formation showing a slightly shallower correlation (r2 = 0.59). Data from the Chrystalls Beach Complex appears more representative of the overall trend and shows a similarly strong correlation (r2 = 0.956, P-value = 1.4 x 10-4 at the 95% confidence interval). Potential factors influencing the poorer correlations within the other two samples sets are smaller sample size (Oslo Region), and a higher standard error of strain measurements (Sap Bon Formation). However it is possible given the range of illite crystallinity measurements in both subsets (0.36 to 0.45 Δ°2θ in the Sap Bon Fm. and 0.49 to 0.58 Δ°2θ in the Oslo Region, compared to 0.26 to 0.44 Δ°2θ in the Chrystalls Beach Complex, Table 1), that a different response to finite strain occurs in diagenetic to low-anchizone conditions compared to that in low-anchizone to anchizone-epizone conditions. These differences may also be result of strain rate (i.e. Giorgetti et al. 2000). Multiple authors have found no clear correlation between finite strain and illite crystallinity, therefore the application of the correlation found in this study to other geological settings is cautioned (Árkai et al., 1997; Burkhard and Badertscher, 2001; Abad et al., 2003). The potential for retrogressive influence of strain on KI(CIS) (e.g. Árkai et al. 2002; Abad et al. 2003) indicates that even in settings with a simple burial-deformation history, correlation of finite strain and illite crystallinity (and therefore metamorphic grade) requires a thorough analysis of the potential influences on either parameter. Nevertheless, given the statistical significance of the correlation between finite strain and illite crystallinity in the Chrystalls Beach Complex, and the data set as a whole, we suggest that in diagenetic to anchizonal conditions in single-phase deformation, the illite crystallinity (KI(CIS)) in shales is directly influenced by tectonic strain (Fig. 9). This supports the conclusions of Gutiérrez-Alonso and Nieto (1996): that this relationship is an appropriate proxy for tracking strain variation in fine-grained siliciclastic rocks in the absence of other markers.

6. Conclusions

- Illite crystallinity can be used as a proxy for finite strain in rocks that have undergone a single phase of deformation, and lack appropriate strain markers.

- The relationship between strain and illite crystallinity is not straight forward, and likely varies with dependence on other conditions, such as the pressure-temperature range involved.

- Finite strain data from this relationship, as well as clay mineralogy, indicates strain has been partitioned into shear domains in the Sap Bon Formation, which exhibit much higher finite strain than the surrounding rock.

References

Abad, I., G. Gutiérrez-Alonso, F. Nieto, I. Gertner, A. Becker, and A. Cabero, 2003, The structure and the phyllosilicates (chemistry, crystallinity and texture) of Talas Ala-Tau (Tien Shan, Kyrgyz Republic): comparison with more recent subduction complexes: Tectonophysics, v. 365, p. 103-127.

Arboit, F., A. S. Collins, R. C. King, C. K. Morley, and R. L. Hansberry, 2014, Structure of the Sibumasu-Indochina Collision, Central Thailand: A section through the Khao Khwang Fold and Thrust Belt: Journal of Asian Earth Sciences, v. 90.

Árkai, P., K. Balogh, and M. Frey, 1997, The effects of tectonic strain on crystallinity, apparent mean crystallite size and lattice strain of phyllosilicates in low-temperature metamorphic rocks. A case study from the Glarus overthrust, Switzerland: Schweizerische Mineralogische und Petrographische Mitteilungen, v. 77, p. 27-40.

Árkai, P., R. Mahlmann, V. Suchy, K. Balogh, I. Sykorova, and M. Frey, 2002, Possible effects of tectonic shear strain on phyllosilicates: a case study from the Kandersteg area, Helvetic domain, Central Alps, Switzerland: Schweizerische Mineralogische und Petrographische Mitteilungen, v. 82, p. 273-290.

Árkai, P., F. P. Sassi, and R. Sassi, 1995, Simultaneous measurements of chlorite and illite crystallinity; a more reliable tool for monitoring low-to very low grade metamorphisms in metapelites; a case study from the Southern Alps (NE Italy): European Journal of Mineralogy, v. 7, p. 1115-1128.

Bruton, D. L., R. H. Gabrielsen, and B. T. Larsen, 2010, The Caledonides of the Oslo Region, Norway–stratigraphy and structural elements: Norwegian Journal of Geology/Norsk Geologisk Forening, v. 90.

Bunopas, S., 1981, Paleogeographic History of Western Thailand and Adjacent Parts of South-East Asia: a Plate Tectonics Interpretation: Submitted for the Degree of Doctor of Philosophy at the Victoria University of Wellington, Victoria University of Wellington.

Burkhard, M., and N. Badertscher, 2001, Finite strain has no influence on the illite crystallinity of tectonized Eocene limestone breccias of the Morcles nappe, Swiss Alps: Clay Minerals, v. 36, p. 171-180.

Dellisanti, F., G. Pini, F. Tateo, and F. Baudin, 2008, The role of tectonic shear strain on the illitization mechanism of mixed-layers illite–smectite. A case study from a fault zone in the Northern Apennines, Italy: International Journal of Earth Sciences, v. 97, p. 601-616.

Eberl, D., 2003, User guide to RockJock-A program for determining quantitative mineralogy from X-ray diffraction data, US Geological Survey.

Erslev, E. A., 1988, Normalized center-to-center strain analysis of packed aggregates: Journal of Structural Geology, v. 10, p. 201-209.

Fagereng, Å., 2011a, Fractal vein distributions within a fault-fracture mesh in an exhumed accretionary mélange, Chrystalls Beach Complex, New Zealand: Journal of Structural Geology, v. 33, p. 918-927.

Fagereng, Å., 2011b, Geology of the seismogenic subduction thrust interface: Geological Society, London, Special Publications, v. 359, p. 55-76.

Fagereng, Å., and A. F. Cooper, 2010, Petrology of metabasalts from the Chrystalls Beach accretionary mélange-implications for tectonic setting and terrane origin: New Zealand Journal of Geology and Geophysics, v. 53, p. 57-70.

Fagereng, Å., and R. H. Sibson, 2007, Is the Chrystalls Beach Accretionary Melange a Fossil Subduction Channel Shear Zone, American Geophysical Union, Fall Meeting.

Fernández-Caliani, J., and E. Galán, 1992, Influence of tectonic factors on illite crystallinity; a case study in the Iberian pyrite belt: Clay Minerals, v. 27, p. 385-388.

Frey, M., 1987, Low temperature metamorphism, Blackie.

Frey, M., M. Teichmüller, R. Teichmüller, J. Mullis, B. Künzi, A. Breitschmid, U. Gruner, and B. Schwizer, 1980, Very low-grade metamorphism in external parts of the Central Alps: illite crystallinity, coal rank and fluid inclusion data: Eclogae Geologicae Helvetiae, v. 73, p. 173-203.

Fry, N., 1979, Random point distributions and strain measurement in rocks: Tectonophysics, v. 60, p. 89-105.

Giorgetti, G., I. Memmi, and D. Peacor, 2000, Retarded illite crystallinity caused by stress-induced sub-grain boundaries in illite: Clay Minerals, v. 35, p. 693-708.

Gutiérrez-Alonso, G., and F. Nieto, 1996, White-mica'crystallinity', finite strain and cleavage development across a large Variscan structure, NW Spain: Journal of the Geological Society, v. 153, p. 287-299.

Hansberry, R. L., A. S. Collins, R. C. King, C. K. Morley, A. P. Giże, J. Warren, S. C. Löhr, and P. A. Hall, 2015, Syn-Deformation Temperature and Fossil Fluid Pathways along an Exhumed Detachment Zone, Khao Khwang Fold-Thrust Belt, Thailand: Tectonophysics, v. 645.

Hansberry, R. L., R. C. King, A. S. Collins, and C. K. Morley, 2014, Complex Structure of an Upper-level Shale Detachment Zone: Khao Khwang Fold and Thrust Belt, Central Thailand: Journal of Structural Geology.

Hara, H., K. Wakita, K. Ueno, Y. Kamata, K.-i. Hisada, P. Charusiri, T. Charoentitirat, and P. Chaodumrong, 2009, Nature of accretion related to Paleo-Tethys subduction recorded in northern Thailand: constraints from mélange kinematics and illite crystallinity: Gondwana Research, v. 16, p. 310-320.

Hinthong, C., S. Chuaviroj, W. Kaewyana, S. Srisukh, C. Pholprasit, and S. Pholachan, 1985, Geological map of Thailand 1: 250 000 (Changwat Phranakorn Sri Ayutthaya, ND 47–8): Geological Survey Division of the Department of Mineral Resources, Bangkok, Thailand.

Hossack, J., and M. Cooper, 1986, Collision tectonics in the Scandinavian Caledonides: Geological Society, London, Special Publications, v. 19, p. 285-304.

Jensenius, J., 1987, Regional studies of fluid inclusions in Paleozoic sediments from southern Scandinavia: Bulletin of the Geological Society of Denmark, v. 36, p. 221-235.

Kelsey, D. E., and M. Hand, 2015, On ultrahigh temperature crustal metamorphism: Phase equilibria, trace element thermometry, bulk composition, heat sources, timescales and tectonic settings: Geoscience Frontiers, v. 6, p. 311-356.

Kennedy, M. J., S. C. Löhr, S. A. Fraser, and E. T. Baruch, 2014, Direct evidence for organic carbon preservation as clay-organic nanocomposites in a Devonian black shale; from deposition to diagenesis: Earth and Planetary Science Letters, v. 388, p. 59-70.

Kisch, H., 1991a, Development of slaty cleavage and degree of very - low - grade metamorphism: a review: Journal of Metamorphic Geology, v. 9, p. 735-750.

Kisch, H., 1991b, Illite crystallinity: recommendations on sample preparation, X - ray diffraction settings, and interlaboratory samples: Journal of Metamorphic Geology, v. 9, p. 665-670.

Kosakowski, G., V. Kunert, C. Clauser, W. Franke, and H. J. Neugebauer, 1999, Hydrothermal transients in Variscan crust: paleo-temperature mapping and hydrothermal models: Tectonophysics, v. 306, p. 325-344.

Kübler, B., 1968, Evaluation quantitative du metamorphism par la cristallinite de l'Illite: Bull. Centre Rech. Pau-SNPA, v. 2, p. 385-397.

Lindgreen, H., V. A. Drits, B. A. Sakharov, A. L. Salyn, P. Wrang, and L. G. Dainyak, 2000, Illite-smectite structural changes during metamorphism in black Cambrian Alum shales from the Baltic area: American Mineralogist, v. 85, p. 1223-1238.

Mählmann, R. F., Ö. Bozkaya, S. Potel, R. Le Bayon, B. Šegvić, and F. Nieto, 2012, The pioneer work of Bernard Kübler and Martin Frey in very low-grade metamorphic terranes: paleo-geothermal potential of variation in Kübler-Index/organic matter reflectance correlations. A review: Swiss Journal of Geosciences, v. 105, p. 121-152.

Morley, C., 1986, The Caledonian thrust front and palinspastic restorations in the southern Norwegian Caledonides: Journal of Structural Geology, v. 8, p. 753-765.

Morley, C., 1987, Lateral and vertical changes of deformation style in the Osen-Røa thrust sheet, Oslo Region: Journal of Structural Geology, v. 9, p. 331-343.

Morley, C., 1994, Fold-generated imbricates: examples from the Caledonides of Southern Norway: Journal of Structural Geology, v. 16, p. 619-631.

Morley, C., P. Ampaiwan, S. Thanudamrong, N. Kuenphan, and J. Warren, 2013, Development of the Khao Khwang Fold and Thrust Belt: implications for the geodynamic setting of Thailand and Cambodia during the Indosinian Orogeny: Journal of Asian Earth Sciences.

Mortimer, N., 1993, Geology of the Otago Schist and adjacent rocks, Institute of Geological and Nuclear Sciences.

Nelson, K. D., 1982, A suggestion for the origin of mesoscopic fabric in accretionary melange, based on features observed in the Chrystalls Beach Complex, South Island, New Zealand: Geological Society of America Bulletin, v. 93, p. 625-634.

Norris, R., and D. Bishop, 1990, Deformed conglomerates and textural zones in the Otago schists, South Island, New Zealand: Tectonophysics, v. 174, p. 331-349.

Poppe, L., V. Paskevich, J. Hathaway, and D. Blackwood, 2001, A laboratory manual for X-ray powder diffraction: US Geological Survey Open-File Report, v. 1, p. 1-88.

Poyatos, D. M., F. Nieto, A. Azor, and J. F. Simancas, 2001, Relationships between very low - grade metamorphism and tectonic deformation: examples from the southern Central Iberian Zone (Iberian Massif, Variscan Belt): Journal of the Geological Society, v. 158, p. 953-968.

Ramsay, J. G., and M. I. Huber, 1987, The techniques of modern structural geology: Folds and fractures, v. 2, Academic press.

Roberts, B., R. Merriman, and W. Pratt, 1991, The influence of strain, lithology and stratigraphical depth on white mica (illite) crystallinity in mudrocks from the vicinity of the Corris Slate Belt, Wales: implications for the timing of metamorphism in the Welsh Basin: Geological Magazine, v. 128, p. 633-645.

Sone, M., and I. Metcalfe, 2008, Parallel Tethyan sutures in mainland Southeast Asia: new insights for Palaeo-Tethys closure and implications for the Indosinian orogeny: Comptes Rendus Geoscience, v. 340, p. 166-179.

Thomsen, E., H. Lindgreen, and P. Wrang, 1983, Investigation on the source rock potential of Denmark, Petroleum Geology of the Southeastern North Sea and the Adjacent Onshore Areas, Springer, p. 221-239.

Ueno, K., and T. Charoentitirat, 2011, Carboniferous and Permian: The Geology of Thailand. Geological Society, London, p. 71-136.

Underwood, M. B., M. M. Laughland, and S. M. Kang, 1993, A comparison among organic and inorganic indicators of diagenesis and low-temperature metamorphism: Thermal evolution of the Tertiary Shimanto Belt, Southwest Japan: An example of ridge-trench interaction, v. 273, p. 45.

Warr, L., and A. Rice, 1994, Interlaboratory standardization and calibration of day mineral crystallinity and crystallite size data: Journal of Metamorphic Geology, v. 12, p. 141-152.

Warr, L. N., R. O. Greiling, and E. Zachrisson, 1996, Thrust ‐ related very low grade metamorphism in the marginal part of an orogenic wedge, Scandinavian Caledonides: Tectonics, v. 15, p. 1213-1229.

Warren, J., C. Morley, T. Charoentitirat, I. Cartwright, P. Ampaiwan, P. Khositchaisri, M. Mirzaloo, and J. Yingyuen, 2014, Structural and fluid evolution of Saraburi Group sedimentary carbonates, central Thailand: A tectonically driven fluid system: Marine and Petroleum Geology.

Chapter 5

K-Ar illite age constraints on the formation of a shale detachment zone

Abstract

K-Ar dating of the clay mineral illite in fault gouge is a useful tool for constraining the timing of brittle fault movement. However, this technique is best used in protoliths which are unlikely to contaminate the sample with material from the fault wall, and its use in clay-rich rocks is problematic. Techniques exist to constrain the influence of non-authigenic illites within a sample; however, this typically requires extensive dating of multiple size-fractions of each sample. This study employs a mutli-analytical approach to discerning the association of fault gouge samples from a shale detachment fault zone, to the depositional and tectonic evolution of the fault zone. K-Ar dating of the ≥2 μm fraction of six samples from the Sap Bon Formation detachment zone and surrounding imbricates in the Khao Khad Fold-Thrust Belt of Central Thailand yielded an age range of 208±4.6 to 262±5.4. SEM petrography was used to confirm the presence and morphology of illite in the ≥2 μm fraction used for K-Ar dating. The fault zone evolution association of each sample is then characterised using XRD mineralogy, and carbon and oxygen stable isotopes. Through these analyses we are able to correlated age determinations to one of three stages of fault zone evolution, and likely source of dated illite: detrital, diagenetic, and orogenic. Orogenic association of the youngest dates in the Sap Bon Formation agree with recently published zircon province data indicating that Sap Bon Formation had been incorporated into the Kho Khwang Fold-Thrust Belt by the Middle-Upper Triassic, with deformation continuing as late as the Rhaetian.

Key words: shale detachment, K-Ar dating, brittle fault timing

1. Introduction

Dating of fine-grained minerals, such as clays, can provide constraints on timing of fault movement in the shallow crust (van der Pluijm et al., 2001; Zwingmann and Mancktelow, 2004; Pleuger et al., 2012). K-Ar dating is a reliable tool to constrain authigenic formation of fine-grained illite clay minerals in brittle faults (Torgersen et al., 2015). K-Ar ages for fine grained illite clay fractions (< 10 μm) are frequently reported as 'inclined age spectra' with respect to different grain-size fractions (e.g. Torgensen et al., 2015). K-Ar ages decrease with the grain size of the fraction from which they are obtained and the relationship is interpreted to reflect the mixing of inherited ages and authigenic ages (Pevear, 1999; Viola et al., 2013). The percentage of 1M/1Md to 2M1 illite polytypes can be considered in relation to K-Ar ages in an 'illite age analysis' plot (Pevear, 1999). This technique can be used to constrain the influence of fault host rock on the mineralogy of dated fault gauge material (van der Pluijm et al., 2006; Zwingmann et al., 2010; Yamasaki et al., 2013), or to quantify the influence of authigenic (1M) vs. detrital (2M1) component of the clay fraction (Elliott et al., 1991). Plots of K-Ar ages vs. the percentage of total illite that is diagenetic give a linear correlation, which can be extrapolated to 0% and 100% detrital illite end-members, to give the diagenetic and detrital ages, respectively (Pevear and Elliott,

1991). Complications arise if the fault host rock contains mineralogy that may contaminate clay fractions and influence the K-Ar ages (e.g. Torgersen et al., 2014; 2015); this is particularly true in shales, where it can be difficult to distinguish if ages: 1) reflect the formation of fault-gouge (authigenic illite); 2) are detrital ages; or 3) reflect the diagenetic formation of illite between deposition and fault activation.

This study presents K-Ar ages of <2 µm fraction clay separates from fault-gouges in an exhumed detachment zone (and one from the overlying imbricate) in the Khao Khwang Fold-Thrust belt in central Thailand (Fig. 1). To combat the aforementioned difficulties of K-Ar dating of illites in shales, XRD derived mineralogy, and associations with several proxies for temperature and stage of fault-zone development (carbon and oxygen stable isotopes, chlorite chemistry) are used to decipher ages from the six samples, similar to an approach discussed by Torgersen et al. 2014.

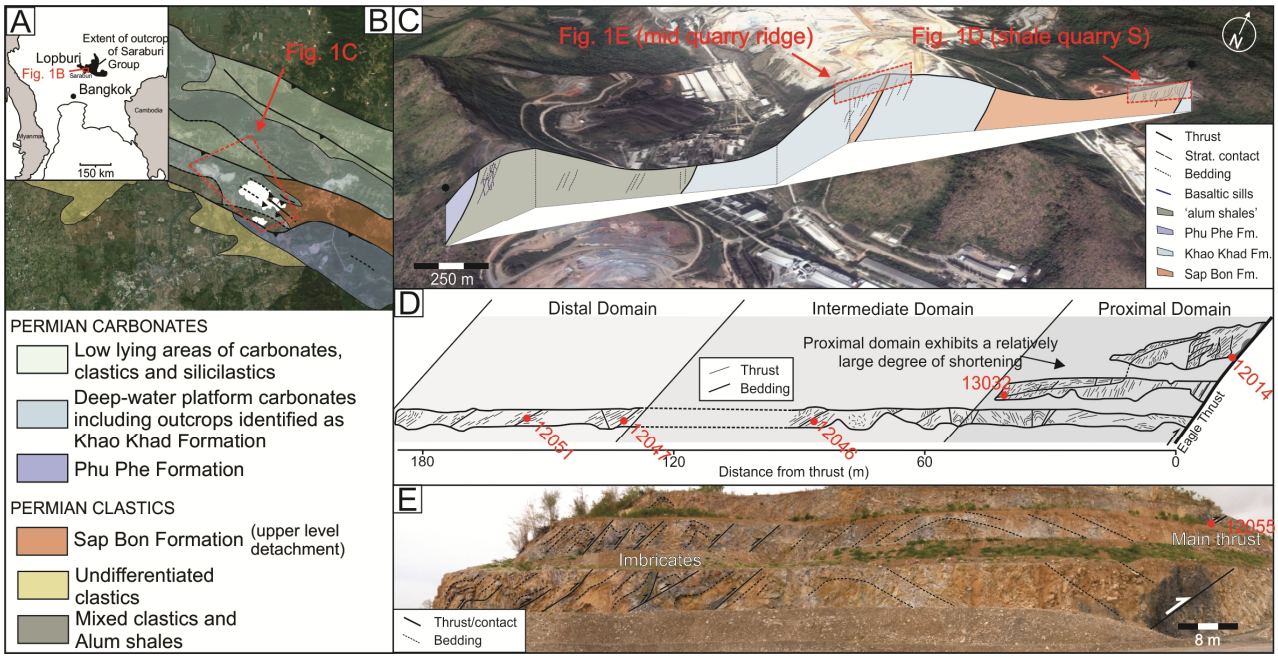

Fig. 1. Location of study area in the Khao Khwang Fold-Thrust Belt, central Thailand. (A) Location within Thailand and (B) simplified geology of the exposed Saraburi Group with Siam City Cement Quarry in white; (C) simplified cross-section through the Siam City Cement Quarry showing the locations of the 'mid quarry ridge' and 'shale quarry S' study areas; (D) and (E) simplified cross-sections through the mid quarry ridge and shale quarry S illustrating sample locations.

2. Geological setting

The study area is a fault damage zone associated with an exhumed upper-level detachment thrust in the Sap Bon Formation of the Khao Khwang Fold-Thrust Belt (KKFTB) of central Thailand (Fig. 1). The detachment zone is exposed in the Siam City Cement Quarry, in the Muak Lek District of Saraburi Province, Thailand (Fig. 1). The detachment zone is characterised by variably deformed shales described in detail below and carbonate cemented arenites deformed during the Triassic Indosinian Orogeny above a detachment fault referred to as the Eagle Thrust (Hansberry et al., 2014). The area is understudied, with constraining the tectonic evolution of the KKFTB the focus of ongoing work (e.g. Morley et al., 2013; Arboit et al.,

2014; 2015; Hansberry et al., 2015). Recent work by Arboit et al. (2014; 2015, in press) has focused on revision of the Saraburi Group stratigraphy and improving understanding of the timing of Indosinian orogenesis. U-Pb detrital zircon ages indicate a middle Permian (275 ± 4 Ma, Kungurian) maximum depositional age (MDA) for the Sap Bon Formation in the quarry in this study. An MDA of 205 ± 6 Ma (Rhaetian) in a clastic unit interpreted as deposited in a thrusting-related piggyback basin north of Siam City Cement Quarry indicates the Indosinian Orogeny was active into the Latest-Triassic (Arboit et al., 2015). Competency contrast within the Sap Bon Formation has influenced the formation of shear zones at strain rate discontinuities, these shear zones characterise the fault damage zone that constitutes an upper-level detachment zone (Hansberry et al., 2015a; Hansberry et al., 2015b). Within the fault damage zone, the most continuous thrusts are surrounded by well-developed shear zones and fault gouges, which we refer to as 'shear domains' (Hansberry et al., 2014). These shear zones are characterised by well-developed foliations and C-S fabrics, and vary in thickness from a few millimetres around discrete fractures to ~50 centimetre wide shear zones (Fig. 2).

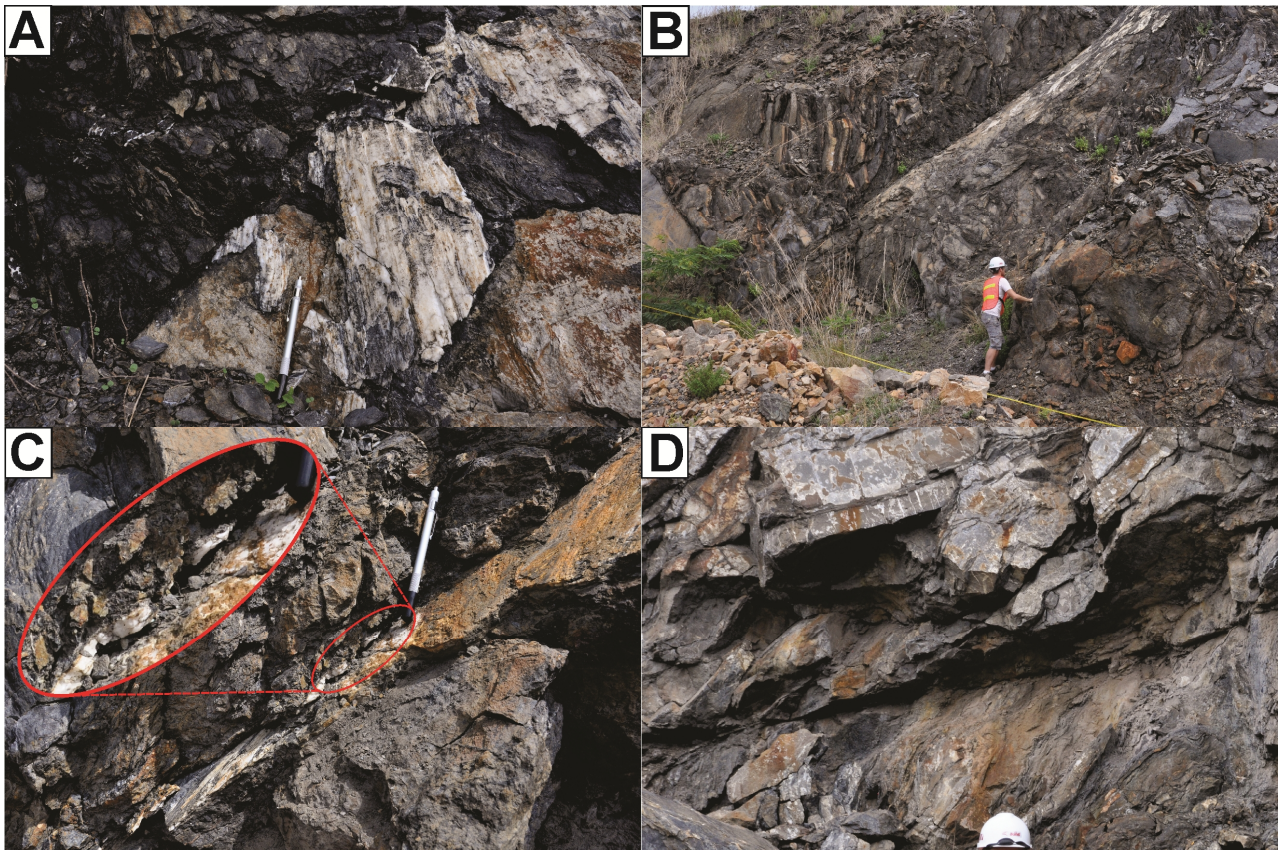

Fig. 2. (A) Shale smear, fault gouge and slickenfibres along the shear zone above the Eagle Thrust; (B) shear zone with mineralised fault surface in the Eagle Thrust damage zone; (C) discrete fault surface with little surrounding shear zone; (D) calcite filled tension fractures in competent rock packages above a shear zone with prominent C-S fabrics in the Eagle Thrust damage zone.

3. Sampling and methods

Fifty one samples were collected from the Sap Bon Formation in the Siam City Cement Quarry. From these samples 6 samples were selected for illite K-Ar dating in this study. To avoid weathering contamination, samples were collected directly from the deformation zone ~30 cm below the surface as recommended by Emery and Robinson (1993). GPS sample locations are listed in Table 1. Samples were taken from five locations in the exposure of the Sap Bon Formation fault damage zone (here referred to as 'shale quarry S') and one from the thrust imbricate overlying it (here referred to as the 'mid-quarry thrust'). Four of these samples come from shear zone material surrounding major faults (Fig. 2) while the other two are from zones of discontinuously deformed rock, where sample material came from immediately adjacent to discrete fault fractures (Fig. 2). These later two samples (EAG12046 and EAG12051) are therefore likely to contain host rock material. In all cases, kinematic indicators from slickenfibres of exposed parts of slip surfaces indicate consistent movement senses, sympathetic to the Eagle Thrust at the base of the Sap Bon Formation exposure, which strikes NW-SE, dipping at 50°, and has a top-to-the-NE transport direction (Fig. 2) (Hansberry et al., 2014). All of the sampled faults exhibit calcite mineralisation with slickenfibres and less frequently, tension gashes in the adjacent, more competent rock packages (Fig. 2). An extended description of each sample can be found in Table 1.

3.1 Scanning electron microscope petrography

Freshly broken surfaces of rock chips from samples EAG12014 and EAG12032 were carbon-coated and examined using an FEI Quanta 450 FEG scanning electron microscope (SEM), with an EDAX energy dispersive system (EDS) X-ray analyser at Adelaide Microscopy.

3.2 X-ray diffraction analysis

X-Ray Diffraction (XRD) of both orientated preparations and randomly orientated powders was used to characterise the mineralogy of each sample (Table 2). Samples were prepared as per the recommendations by Kisch (1991) and diffraction patterns were collected using a Bruker D8 Advance X-Ray Diffractometer at the following instrument settings: CuKα radiation at 40 kV/40 mA; 0.6 mm divergence slit; 0.05 (2θ) step size, 1.5s counting time. Diffraction patterns were collected from 3.5° to 45° 2θ. Semi-quantitative mineralogy for comparison between samples was calculated from the weighted basal-peak method of Poppe et al. (2001), giving the ubiquitous phyllosilicate mineral assemblage (quartz) + illite ± kaolinite ± chlorite ± smectite (Table 2). An error margin of 5% is suggested for this data.

Sample GPS locations (WGS 84)			
Sample	Latitude	Longitude	Quarry location
EAG12014	14°38'27.9"	101°05'24.9"	shale quarry S
EAG12032	14°38'26.4"	101°05'25.4"	shale quarry S
EAG12046	14°38'25.0"	101°05'24.5"	shale quarry S
EAG12047	14°38'25.0"	101°05'24.5"	shale quarry S
EAG12051	14°38'24.1"	101°05'24.8"	shale quarry S
EAG12055	14°38'064"	101°05'04.0"	Mid-quarry thrust

Sample Descriptions	
Sample	Description
EAG12014	Fault gouge material directly above the Eagle Thrust
EAG12032	Fault gouge material in ~30-50 cm shear zone surrounding large, continuous fault
EAG12046	Host-rock and minor gouge material from discrete fault with thin (1-2 cm) shear zone
EAG12047	Fault gouge material from ~10-20 cm shear zone around fault
EAG12051	Host-rock and fault gouge material from discrete fault with thin (3-10 cm) shear zone
EAG12055	Heavily sheared shale and fault gouge material in broad (up to 1 m) shear zone

Table 1. Table of sample locations and geological descriptions.

	Characteristic Minerals*					Illite polytype Ratio (2M:1M) **	Carbon & oxygen stable isotopes					
							$\delta^{18}O_{(VPDB)}$			$\delta^{13}C_{(VPDB)}$		
Sample	Smectite (%)	Illite (%)	Kaolinite (%)	Chlorite (%)	Chlorite Fe:Mg ratio		1	2	3	1	2	3
EAG12014	t	86	t	10	0.86		-13.51	-11.29	-11.12	2.73	3.05	3.02
EAG12032	t	83	t	14	0.83		-11.41	-11.98	-12.39	1.50	1.20	1.87
EAG12046	t	69	t	29	1.00		-10.18	-9.44	-9.01	4.93	4.20	3.38
EAG12047	4	81	t	15	0.95		-10.88	-10.90	-11.14	1.84	1.94	1.68
EAG12051	6	72	t	19	1.00		-9.93	-10.01	-10.27	2.18	1.94	2.78
EAG12055	t	93	7	0	N.D.		N.D.	N.D.	N.D.	N.D.	N.D.	N.D.

* Determined by the method of Poppe et al. (2001), intended as relative estimates only, with 't' indicating trace amount (≤3%).
** Determined by RockJock software on randomly orientated powders. N.D. = not determined

Table 2. Table of results from x-ray diffraction analysis and carbon and oxygen stable isotopes analysis from the six samples.

Sample [<2 µm]	K(%)	Rad. ^{40}Ar (mol/g)	Rad. ^{40}Ar (%)	Age (Ma)	Error (Ma)
EAG12014	4.67	1.9870E-09	94.1	230.0	4.6
EAG12032	4.86	2.0207E-09	95.1	225.1	4.6
EAG12046	3.86	1.8883E-09	93.7	262.1	5.4
EAG12047	4.38	1.9050E-09	93.4	234.8	4.9
EAG12051	3.07	1.3789E-09	94.8	242.0	5.1
EAG12055	5.24	2.0088E-09	92.0	208.5	4.4

Argon standard data						
Sample ID	K [%]	Rad. 40Ar [mol/g]	Rad. 40Ar [%]	Age [Ma]	Error [Ma]	Remark [%] *
HD-B1-112	7.96	3.3820E-10	93.69	24.34	0.39	+ 0.54%
HD-B1-113	7.96	3.3357E-10	92.38	24.01	0.36	- 0.83%
HD-B1-122	7.96	3.3607E-10	92.17	24.19	0.38	- 0.08%
HD-B1-123	7.96	3.3590E-10	92.07	24.18	0.37	- 0.12%

Airshot data		
Airshot ID	40Ar/36Ar	+/-
AS108-AirS-1	297.59	0.51
AS109-AirS-1	294.57	0.27
AS119-AirS-1	296.36	0.34
AS119-AirS-2	294.76	0.30

* error to reference (Hess and Lippolt, 1994)

Table 3. Table of results from K-Ar dating of the ≤2 µm fraction of the six samples.

3.3 Stable isotope analysis

Three samples of calcite veins and slickenfibres were taken from the slip surfaces of each of the six faults (Fig 2A), providing three data points for each fault sample (Fig. 3). Sample powders were extracted from vein cements using a dental drill. Carbonate mineralogy (calcite) was confirmed by thin section analysis; no significant quantity of dolomite was present in any samples. Each sample was analysed in duplicate at the stable isotope mass spectrometer facility at The University of

Melbourne with a standard uncertainty of ±0.10‰.

3.4 K-Ar dating

The analytical method for separating and dating the illite in the samples is described in detail in Zwingmann and Mancktelow (2004). Approximately 20 mg of sample material was required for Argon analyses. During the course of the study 4 HD-B1 standards (Hess and Lippolt, 1994) and airshot values were measured (n=4). The K-Ar dating and standard results are summarised in Table 3. The error for Argon analyses is below 1 % and the 40Ar/36Ar value for airshots averaged 295.82 ± 0.35 (2σ n=4). The K-Ar ages were calculated using 40K abundance and decay constants recommended by Steiger and Jäger (1977).

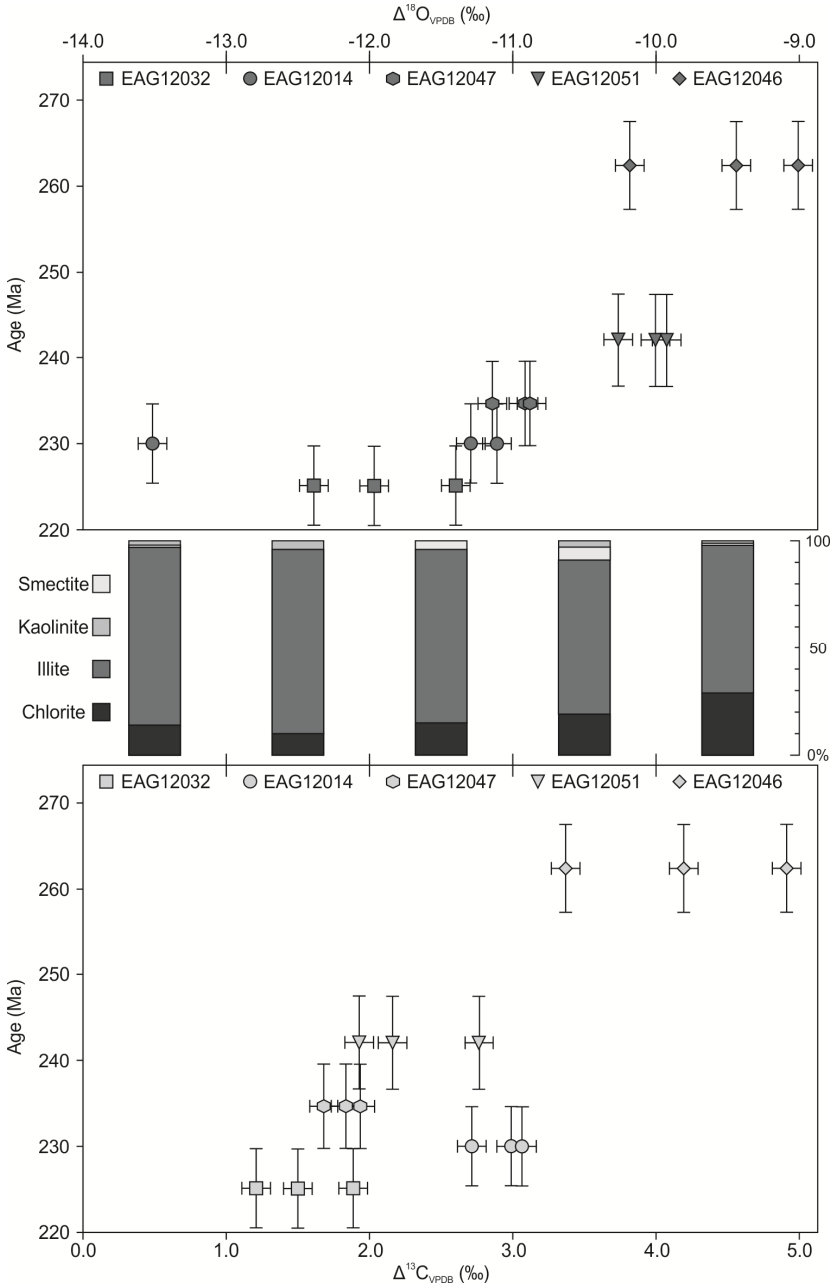

Fig. 3. Plots of carbon and oxygen stable isotope results vs. K-Ar age of illite in each of the five samples in shale quarry S. Mineralogy of the dated <2 µm fraction for each sample is also shown.

4. Results

4.1 Scanning electron microscope petrography

Images from SEM analysis of representative clay mineral sample assemblages are summarised in Figure X. Figure XA and XB highlight the morphology and clay mineral melange comprising mainly platy illite and chlorite. Both illite and chlorite crystallites indicate a strong preferred orientation and exhibit regular, euhedral boundaries (Fig. XA, XC). The hexagonal and prismatic morphologies of the illite and chlorite plates imply in-situ neocrystalisation. Euhedral particle outlines are typical of an authigenic or diagenetic origin (Fig. XC, XE), in contrast to the more irregular or diffuse outlines characteristic of a detrital origin (Clauer and Chaudhuri, 1995). EDS spectra confirm illite and chlorite mineralogy. Due to the intimate mixture of illite and chlorite Fe and K peaks were used to distinguish the clay mineral phases.

4.2 Mineralogical characterisation of clay fractions by X-ray diffraction

All of the samples from shale quarry S contain chlorite (10-29%) while the sample from the overlying thrust imbricate to the south east does not. All samples contain illite, as well as trace and/or small (4-7%) amounts of smectite and kaolinite (Table 2). Results of ROCKJOCK (Eberl, 2003) full pattern-fitting software indicated the majority of chlorite present in the five samples from shale quarry S is Fe-chlorite, though samples EAG12047, EAG12032 and EAG12014 exhibit increasing amounts for Mg-chlorite, from 5-17% of the total chlorite in each sample (Table 2).

4.3 Stable Isotopes

Carbon and oxygen stable isotopes were used to investigate the history of fluid-rock interaction along the five sample faults in shale quarry S, as well as using δ18O as a proxy for the relative temperature at which syn-tectonic calcite mineralisation occurred (i.e. Warren et al., 2014; Hansberry et al., 2015). Three samples were taken from each fault sampled for K-Ar dating of illite, with δ18OVPDB values range from -13.51 to -9.01, while δ13CVPDB values range from 4.93 to 1.20 ‰.

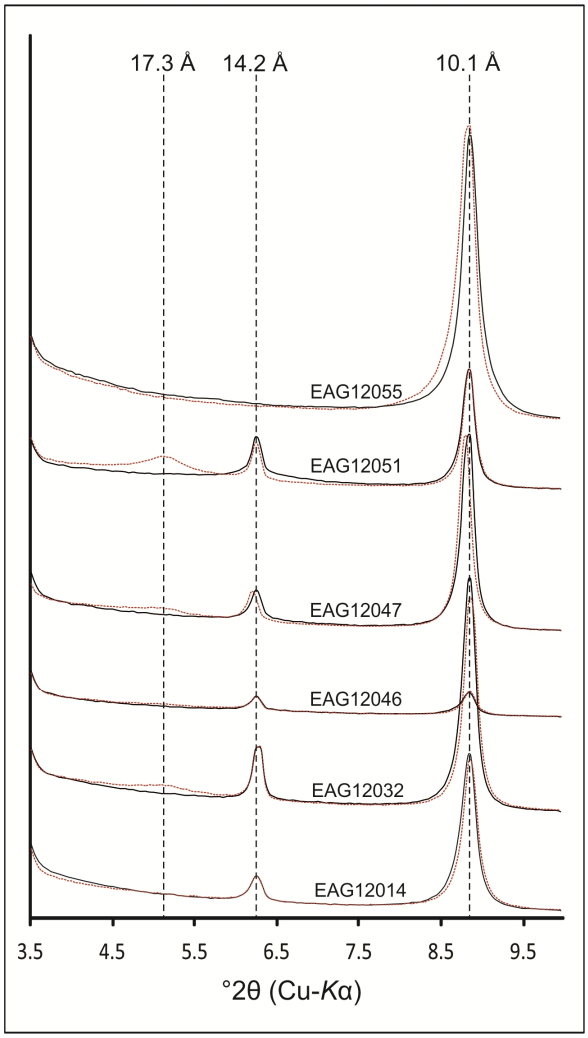

Fig. 4. X-Ray diffractograms taken from orientated preparations of the six samples from 3.5-10 °2θ. Air dried preparations are in black while runs on samples treated with ethylene glycol are in dashed red. Peaks for smectite (17.3 Å), chlorite (14.2 Å), and illite (10.1 Å) are highlighted.

4.4 K-Ar dating

The <2 µm fraction of six samples was dated by K-Ar analysis (Table 3). Samples from shale quarry S yield ages ranging from 262.1 Ma ± 5.4 Ma (Permian-Guadalupian) to 225.1 Ma ± 4.6 Ma (Upper Triassic-Carnian). The sample from the mid-quarry thrust yield an age of 208.5 Ma ± 4.4 Ma (Upper Triassic-Norian). Ages are referred to the Gradstein et al. (2004) timescale. Radiogenic 40Ar content ranges from 92.0 to 95.1% indicating reliable analytical conditions for all analyses. K contents range from 3.07% for sample EAG12051, to 5.24% for sample EAG12055 <2 µm. The relatively high K content of most illite fractions is consistent with an authigenic origin. Variable Potassium concentration in the size fractions is caused by mixture with other mineral phases, such as quartz and chlorite, which is supported by XRD data.

5. Discussion

The assumptions and limitations of K-Ar dating of fault gouge material to constrain fault timing have been discussed in various recent publications (e.g. Zwingmann and Mancktelow, 2004; Zwingmann et al., 2004; Haines and van der Pluijm, 2008; Torgersen et al., 2014; Mancktelow et al., 2015). In particular, it is best applied in areas where the host-rock does not contain mineralogy similar to the authigenic fault gouge mineralogy, and is therefore, usually applied to studying the timing of fault reactivation in metamorphic and igneous host-rocks (Zwingmann et al., 2010; Torgersen et al., 2015). The application of this technique in shales is therefore complicated by the fact that the clay size fraction of the host-rock can be expected to contain phyllosilicates (I/S, illite, muscovite), which will likely contaminate the fault gouge material. It is therefore important in interpreting the age data obtained in this study, to consider the likely effect of a detrital illite component in the ages (Pevear, 1999). It is well established that illite in shales is a mixture of detrital mica (2M1) with diagenetic illite (1M/1Md) precipitated from pore fluids (Pevear, 1999). Finer grain size fractions exhibit a greater abundance of 1M illite in the mixed 2M1/1M in shales, and these finer fractions also give younger ages (diagenesis) , while coarser fractions can yield ages older than deposition, as shale tend to inherit a range of detrital ages (Bailey et al., 1962; Pevear, 1999). Similarly, numerous studies of inclined illite 'age-grain-size spectra' exhibit that the finest grain size fractions contain a greater proportion of authigenic illite (1M/1Md), and produce the youngest age (Zwingmann et al., 2010; Viola et al., 2013; Torgersen et al., 2015). The finest particle separates (<0.1-2 µm) contain material derived from the ends of filamentous grains and should, theoretically, represent the most recently grown illite in gouge rocks. This does illustrate the problem with the dating of illites from shales in studies, such as this one, with uncertainties regarding the origin of illite in fault gouge material: the ages of bulk mixtures of detrital/diagenetic/authigenic illites yield essentially meaningless dates without a constraint on the end-member dates of this mixture (Pevear, 1999).

An understanding of fluid-rock interaction history can be useful to constrain the development of a fold-thrust belt (Wiltschko et al., 2009; Lacroix et al., 2014). Carbon and oxygen stable isotope data has been used to

investigate the relative temperatures at which carbonates and vein cements precipitated, and characterise the stage of burial-diagenesis-orogenesis recorded (Lacroix et al., 2014; Warren et al., 2014; Hansberry et al., 2015a). Recent work in the Saraburi Province (Warren et al., 2014) and the Sap Bon Formation in particular has defined a fluid-rock interaction history and model of the structural/fluid-flow evolution of the upper-level detachment zone (Hansberry et al., 2015a). Diagenetic to late orogenic isotopic signatures are defined and the large, continuous faults (and associated shear zones) are found to have acted as conduits for high temperature orogenic fluids once matrix permeability had ceased (Hansberry et al., 2015a). Samples of syn-tectonic calcite vein fills along these fault planes, and immediately adjacent to dated fault gouge material are plotted against age in Figure 3. Both δ13C and δ18O show a trend of increasingly negative isotopic signature with decreasing age. The transition from burial to orogenic conditions is reported as exhibiting temperatures equivalent to -10.00 to -12.00 δ18O, signatures which come exclusively from slickenfibres and vein fills along large faults (Warren et al., 2014; Hansberry et al., 2015a). This trend of younger ages associated with orogenic temperatures may indicate that the younger ages from samples EAG12032, EAG12014 and EAG12047 reflect the age of authigenic illite formed in fault gouges during orogenic movement and formation of these faults (Fig. 4). The older ages from samples EAG12051 and EAG12046 are interpreted to represent a bulk mixture age less dominated by authigenic illite.

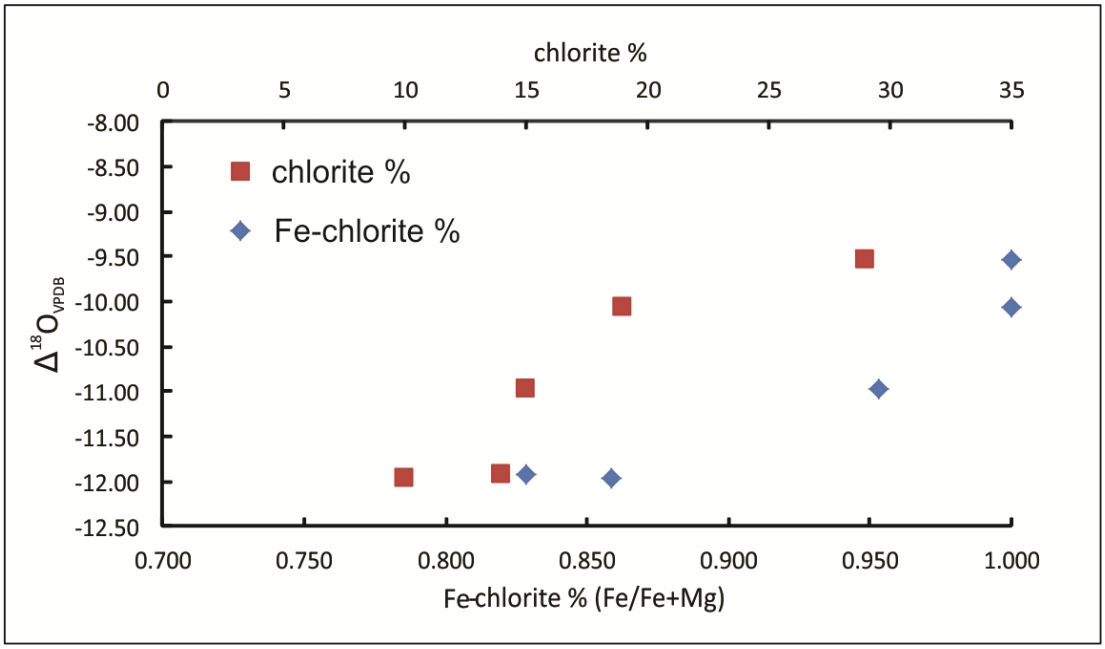

Fig. 5. Plot of sample chlorite mineralogy vs oxygen stable isotope results. Upper x-axis displays the percentage of chlorite in the <2 µm fraction of the sample and the lower x-axis displays the ratio of Fe:Mg-chlorite in that percentage.

X-Ray Diffraction patterns from orientated preparations were run as both air-dried and treated with ethylene glycol to highlight the presence of expandable smectite layers (e.g. Lanson et al., 2009). The occurrence of peaks in the glycol treated samples at 4.9-5.3 Δ°2θ highlights the presence of smectite layers in mixed-layers in all but one (EAG12014) of the

samples (Fig. 4). The five samples from the Eagle Thrust damage zone generally show a decreasing quantity of smectite, and a less prominent ~5 Δ°2θ diffractograms peak, with decreasing K-Ar age (Fig. 4).

All five samples from the Eagle Thrust damage zone show a consistent decrease in chlorite content with decreasing age; while the sample from the overlying thrust imbricate (EAG12055) contains no chlorite (Table 2). The majority of chlorite present in the five samples from the shale quarry S is Fe-chlorite, however, the ratio of Fe-chlorite to Mg-chlorite decreases with K-Ar age, as well as relative temperature indicated by δ18O results (Fig. 5). Generally, Fe-chlorites are considered to form at relatively low (diagenetic) temperatures while Mg-chlorites are considered higher temperatures, and have been variously reported to begin forming from 130-165° to 220-290°C (Weaver, 1989). Given the increase of Mg:Fe ions in the chlorites is well correlated with the δ18O temperature proxy (Fig. 5) we interpret that the majority of the chlorites in the samples from Shale Quarry S are diagenetic, and decrease in abundance as age decreases and relative temperature increases. Data from illite crystallinity indicate a maximum deformational temperature range of 160-210° ± 20°C, allowing for the development of Mg-chlorites during orogenesis (Hansberry et al., 2015a). As relative temperature increases (Fig. 3) the percentage of illite in the <2 µm fraction increases, replacing chlorite and mixed layer illite-smectite-chlorite.

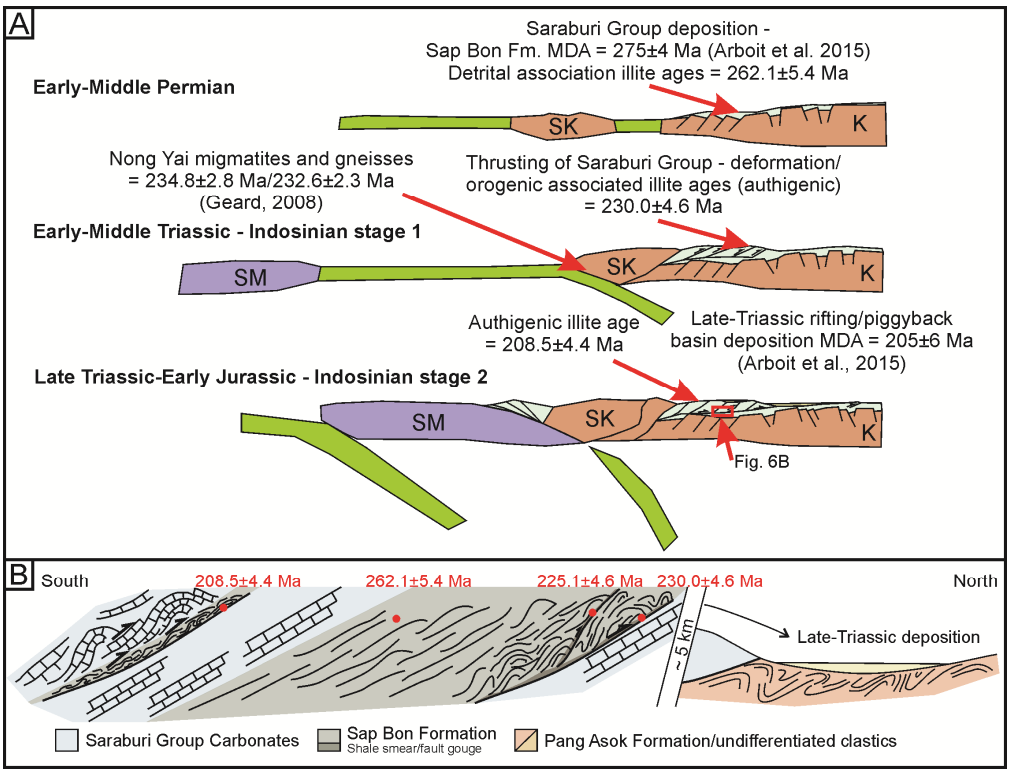

Fig.6. Summary of K-Ar illite ages within the framework of regional tectonics. (A) Tectonic cartoon of the development of the Khorat Plateau from deposition of the Saraburi Group to deformation during stage 1 and 2 of the Indosinian Orogeny. (B) Simplified cross section through the Siam City Cement Quarry showing K-Ar illite ages and deposition in a piggyback basin to the north contemporaneous with the youngest illite age.

5.1 Geochronological constraints on the study area

Arboit et al., (2015) used U-Pb ages and Hf isotopes of detrital zircons to better constrain the stratigraphy of the Saraburi Group, as well as identifying deposition into syn-tectonic basins as a consequence of Indosinian orogenesis into the Late Triassic. The maximum depositional age of the Sap Bon Formation in the Siam City Cement Quarry is constrained as Middle-Permian. This is consistent with the interpretation that the 262.1 ± 5.4 Ma age of illite in sample EAG12046 being largely influenced by detrital illite. The foredeep basin (or series of basins) containing the Sap Bon Formation was incorporated into the KKFTB by 240 Ma, placing this as the earliest likely age of growth of authigenic illite in fault zones (Fig. 6) (Arboit et al., 2015). While no record of sedimentation is present in the southern portion of the KKFTB during the Upper Triassic, the northward advancing thrust front is interpreted as being active and responsible for deposition in piggyback or thrust-top satellite basins as late as the Rhaetian (Fig. 6) (Arboit et al., 2015). While no direct evidence from other studies indicates ongoing deformation in the southern KKFTB, where the focus area of this study is located (Fig. 2B), it is possible that the 208.5 ± 4.6 age of illite in sample EAG12055 is a reflection of out-of-sequence thrusting, a feature that has been identified in the area by Morley et al. (2013), thus supporting the described model in this study.

6. Conclusions

By constraining the association of the K-Ar dates produced in this study to proxies and indicators of the stage of development (detrital, to diagenesis, to orogenesis) of the fault damage zone of the Eagle Thrust, we are able to conclude:

- The youngest ages in Shale Quarry S (225.1±4.6 to 230.0±4.6 Ma) are likely reflective of the age of orogenic fault movement and illite formation. These youngest dates are associated with hotter (relative to the rest of the fault damage zone) orogenic fluid, high temperature chlorites, less diagenetic chlorite and mixed layer phyllosilicates, and a higher % of uncontaminated illite, all indicative of a higher maturity of clay mineralogy (Figs. 3, 4, & 5). These dates are also consistent with the accepted age at which the basin containing the Sap Bon Formation was incorporated into the KKFTB (Fig. 6) (Arboit et al., 2015).

- Older dates between 242.0±5.1 to 262.1±5.4 are likely to represent a bulk mixture age of the Sap Bon Formation, potentially consisting of orogenic illites, but also influenced by a diagenetic and detrital component. In particular, the oldest age, from sample EAG12046 of largely host-rock material, is consistent with the 268 Ma age of deposition of the Sap Bon Formation (Arboit et al., 2015).

- The 208 ± 4.6 Ma illite age from the mid-ridge thrust in the Siam City Cement Quarry (Fig. 1) is concurrent with deposition in syn-tectonic basins in the mid-northern KKFTB, inferring ongoing, potentially out-of-sequence deformation, brittle fault movement, and authigenic illite growth in the Sap Bon Formation as late as the Latest-Triassic (Fig. 6).

- The K-Ar ages from illites in this study are consistent with recently published detrital zircon age data and help to further constrain the age of Indosinian deformation in the southern KKFTB.

References

Arboit, F., A. S. Collins, R. C. King, C. K. Morley, and R. L. Hansberry, 2014, Structure of the Sibumasu-Indochina Collision, Central Thailand: A section through the Khao Khwang Fold and Thrust Belt: Journal of Asian Earth Sciences, v. 90.

Bailey, S., P. Hurley, H. Fairbairn, and W. Pinson, 1962, K-Ar dating of sedimentary illite polytypes: Geological Society of America Bulletin, v. 73, p. 1167-1170.

Eberl, D., 2003, User guide to RockJock-A program for determining quantitative mineralogy from X-ray diffraction data, US Geological Survey.

Elliott, W. C., J. L. Aronson, G. Matisoff, and D. L. Gautier, 1991, Kinetics of the Smectite to Illite Transformation in the Denver Basin: Clay Mineral, K-Ar Data, and Mathematical Model Results (1): AAPG bulletin, v. 75, p. 436-462.

Emery, D., and A. Robinson, 1993, Inorganic Geochemistry: Applications to Petroleum Geology. Blackwells, Oxford.

Haines, S. H., and B. A. van der Pluijm, 2008, Clay quantification and Ar–Ar dating of synthetic and natural gouge: application to the Miocene Sierra Mazatán detachment fault, Sonora, Mexico: Journal of Structural Geology, v. 30, p. 525-538.

Hansberry, R. L., A. S. Collins, R. C. King, C. K. Morley, A. P. Giże, J. Warren, S. C. Löhr, and P. A. Hall, 2015a, Syn-Deformation Temperature and Fossil Fluid Pathways along an Exhumed Detachment Zone, Khao Khwang Fold-Thrust Belt, Thailand: Tectonophysics, v. 645.

Hansberry, R. L., R. King, A. S. Collins, S. C. Löhr, C. K. Morley, P. A. Hall, R. H. Gabrielsen, and B. T. Larsen, 2015b, Strain and Competency Contrasts in Shale Detachment Zones: An Examination of the Relationship between Finite Strain and Illite Crystallinty: In Preparation.

Hansberry, R. L., R. C. King, A. S. Collins, and C. K. Morley, 2014, Complex Structure of an Upper-level Shale Detachment Zone: Khao Khwang Fold and Thrust Belt, Central Thailand: Journal of Structural Geology.

Hess, J., and H. Lippolt, 1994, Compilation of K-Ar measurements on HD-B1 standard biotite 1994 status report: Phanerozoic time scale.(Odin, GS; editor). Bulletin of Liaison and Informatics. IGCP project, v. 196, p. 19-23.

Lacroix, B., A. Travé, M. Buatier, P. Labaume, T. Vennemann, and M. Dubois, 2014, Syntectonic fluid-flow along thrust faults: Example of the South-Pyrenean fold-and-thrust belt: Marine and Petroleum Geology, v. 49, p. 84-98.

Lanson, B., B. A. Sakharov, F. Claret, and V. A. Drits, 2009, Diagenetic smectite-to-illite transition in clay-rich sediments: A reappraisal of X-ray diffraction results using the multi-specimen method: American Journal of Science, v. 309, p. 476-516.

Morley, C., P. Ampaiwan, S. Thanudamrong, N. Kuenphan, and J. Warren, 2013, Development of the Khao Khwang Fold and Thrust Belt: implications for the geodynamic setting of Thailand and Cambodia during the Indosinian Orogeny: Journal of Asian Earth Sciences.

Pevear, D., and W. Elliott, 1991, Illite Age Analysis: A Method for Interpreting Shale K/Ar Ages: LPI Contributions, v. 773, p. 124.

Pevear, D. R., 1999, Illite and hydrocarbon exploration: Proceedings of the National Academy of Sciences, v. 96, p. 3440-3446.

Pleuger, J., N. Mancktelow, H. Zwingmann, and M. Manser, 2012, K–Ar dating of synkinematic clay gouges from Neoalpine faults of the Central, Western and Eastern Alps: Tectonophysics, v. 550, p. 1-16.

Poppe, L., V. Paskevich, J. Hathaway, and D. Blackwood, 2001, A laboratory manual for X-ray powder diffraction: US Geological Survey Open-File Report, v. 1, p. 1-88.

Steiger, R. H., and E. Jäger, 1977, Subcommission on geochronology: convention on the use of decay constants in geo-and cosmochronology: Earth and Planetary Science Letters, v. 36, p. 359-362.

Torgersen, E., G. Viola, H. Zwingmann, and I. H. Henderson, 2015, Inclined K–Ar illite age spectra in brittle fault gouges: effects of fault reactivation and wall-rock contamination: Terra Nova, v. 27, p. 106-113.

van der Pluijm, B. A., C. M. Hall, P. J. Vrolijk, D. R. Pevear, and M. C. Covey, 2001, The dating of shallow faults in the Earth's crust: Nature, v. 412, p. 172-175.

van der Pluijm, B. A., P. J. Vrolijk, D. R. Pevear, C. M. Hall, and J. Solum, 2006, Fault dating in the Canadian Rocky Mountains: Evidence for late Cretaceous and early Eocene orogenic pulses: Geology, v. 34, p. 837-840.

Viola, G., H. Zwingmann, J. Mattila, and A. Käpyaho, 2013, K-Ar illite age constraints on the Proterozoic formation and reactivation history of a brittle fault in Fennoscandia: Terra Nova, v. 25, p. 236-244.

Warren, J., C. Morley, T. Charoentitirat, I. Cartwright, P. Ampaiwan, P. Khositchaisri, M. Mirzaloo, and J. Yingyuen, 2014, Structural and fluid evolution of Saraburi Group sedimentary carbonates, central Thailand: A tectonically driven fluid system: Marine and Petroleum Geology.

Weaver, C. E., 1989, Clays, muds, and shales, Elsevier.

Wiltschko, D. V., G. R. Lambert, and W. Lamb, 2009, Conditions during syntectonic vein formation in the footwall of the Absaroka Thrust Fault, Idaho–Wyoming–Utah fold and thrust belt: Journal of Structural Geology, v. 31, p. 1039-1057.

Yamasaki, S., H. Zwingmann, K. Yamada, T. Tagami, and K. Umeda, 2013, Constraining the timing of brittle deformation and faulting in the Toki granite, central Japan: Chemical Geology, v. 351, p. 168-174.

Zwingmann, H., and N. Mancktelow, 2004, Timing of Alpine fault gouges: Earth and Planetary Science Letters, v. 223, p. 415-425.

Zwingmann, H., N. Mancktelow, M. Antognini, and R. Lucchini, 2010, Dating of shallow faults: New constraints from the AlpTransit tunnel site (Switzerland): Geology, v. 38, p. 487-490.

Chapter 6

Conclusions

This project intended to build on our current understanding of structural deformation in shale detachment zones, and the properties which govern the nature of deformation in fine-grained sediments, with the aims:

1. To investigate the detailed structure of the Sap Bon Formation detachment zone in the Khao Khwang Fold-Thrust belt of central Thailand in order to better understand the nature of deformation in a shale detachment zone.
2. To use suite of analytical techniques to investigate the transient (deformational conditions, fluid flow, and changes in mineralogy) and intrinsic (protolith mineralogy, rheology) in order to better understand the influence these properties have on the nature of deformation in a shale detachment zone.
3. To compare these properties in the Sap Bon Formation to other know detachment zones in order to build on the understanding of the influence changes in these properties may have on the structural behaviour of shale detachment zones.

Chapter 2

Chapter two focuses on building a detailed picture of the structures and styles of deformation within the Sap Bon Formation, particularly in the 'proximal domain' located directly above the Eagle Thrust and interpreted to be acting as a detachment zone.

This was achieved be detailed structural mapping of series of quarry benches, resulting in construction of a cross section through approximately 180 meters of the Sap Bon Formation above the Eagle Thrust.

We interpret that the distribution of continuous vs. discontinuous deformational styles is governed by the distribution of contrasting competency domains related to the heterogeneity of the protolith Sap Bon Formation shale. Weak phases (incompetent domains composed of fine-grained shales) have localised strain and host shear-zone like faults which form an anastomosing network through the detachment zone. These shear zones characterise a three-dimensionally complex fault system in the proximal domain, surrounding three-dimensional lenses of competent rock. Extreme structural heterogeneity occurs both in-section and laterally through the proximal domain. This exposure of Sap Bon Formation is divided into structural domains (proximal, intermediate, and distal) based on the observed changes in structural behaviour with proximity to the basal Eagle Thrust.

Chapter 3

This chapter employed illite crystallinity, carbon and oxygen stable isotopes, vitrinite reflectance, and total organic carbon content analyses to constrain deformational conditions and rock properties influencing rheology within the Sap Bon Formation. Illite crystallinity data indicates the peak deformational temperature reached in the Sap Bon Formation to be between 160-220 °C.

Higher crystallinity is found in incompetent shale shear zones than the more competent domains, implying higher temperature or strain rate within the incompetent domains.

Fluid flow pathways through the evolution of the complex fault zone in the proximal domain are unravelled using stable isotope results, which indicate the basal Eagle Thrust, as well as other large faults constituted the primary source of permeability during orogenesis, once rock-matrix permeability had been lost. Building on the results of chapter two and evidence from strain localisation and fluid-flow history, we conceptualise a schematic model of fault-zone development within the Sap Bon Formation, from burial through to deformation in the Indosinian Orogeny. This chapter also highlighted the impracticality of using vitrinite reflectance (commonly used in basin settings) to constrain deformational temperature in a deformed sequence.

Chapter 4

This chapter builds on the evidence for strain localisation in incompetent domains within the Sap Bon Formation to test illite crystallinity as a potential tool for tracking finite strain variation in low-grade rocks, devoid of other appropriate strain markers. Two new field areas in Norway and New Zealand were introduced and sampled for finite strain and illite crystallinity analysis. The findings in this chapter indicate that illite crystallinity can be used as a proxy for finite strain, and data supports the previous interpretation of higher finite strain and strain localisation within the incompetent domains of the Sap Bon Formation.

Mineralogical mapping of thin sections from the competent and incompetent domains of the Sap Bon Formation detachment zone further strengthen this interpretation: results indicate a significantly more developed strain fabric, as well as higher maturity of clay mineralogy in the incompetent domain sample. Higher and more interconnected porosity also strengthens the interpretation in chapter three of shear zones in incompetent domains acting as conduits, and primary permeability, for orogenic fluid flow.

Chapter 5

This chapter aimed to constrain the timing of shale shear zone deformation within the Sap Bon Formation using K-Ar dating of illite from fault gouges. Data from XRD mineralogy and stable isotopes analysis is used to scrutinise the ages yielded from five samples in the Sap Bon Formation and a sixth from an adjacent fault block, to indicate the influence of detrital, diagenetic, and orogenic illites on the ages produced. From these results and comparison to recent zircon provenance studies in the Khao Khwang Fold-Thrust Belt we interpret that deposition of the Sap Bon Formation had occurred by 262.1±5.4 Ma, while the formation had been incorporated into the fold-thrust belt no later than 230.0±4.6 Ma. Evidence for out-of-sequence thrusting in the adjacent fault block at 208.0±4.6 Ma is supported by evidence for contemporaneous deposition in a nearby piggy-back basin.

Implications for the understanding of the nature of shale detachment zones and the history of the Khao Khwang Fold-Thrust Belt

The overall contributions and implications of the case studies (chapters 2-5) in this project have been:

1. Identification and detailed structural analysis of an ancient shale detachment zone in the Khao Khwang Fold-Thrust Belt, exhibiting strong evidence for the influence of competency contrast on the development of complex fault geometries and combined brittle/ductile deformational mechanisms in deformed shales
2. Presenting strong evidence to suggest faulting and shear zone formation in fined-grained rocks provide permeability conduits during orogenesis.
3. Confirmation (building on previous studies) of the potential for illite crystallinity as a proxy from finite strain in low-grade deformation of fine-grained rocks, while providing the first quantitative evidence for this relationship.
4. Providing new age-constraints of deposition and deformation of the Saraburi Group during the Indosinian Orogeny.

Supplementary Data

Appendix A

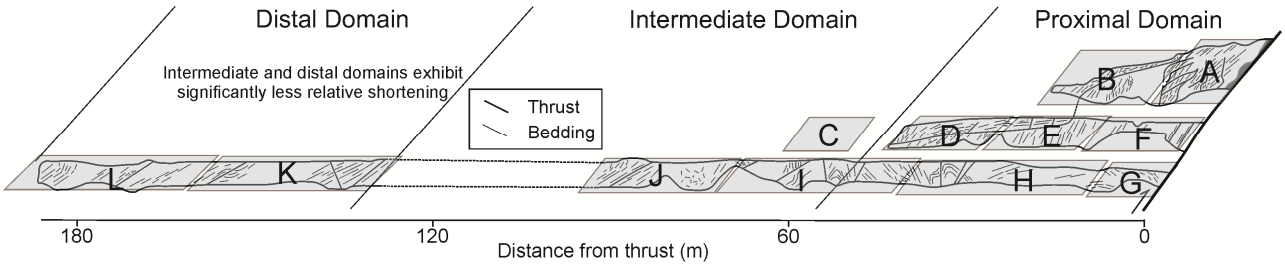

Fig. 1. Illustration of position of original field sketches in relation to the cross sections in Chapter 2.

Structural data from the Siam City Cement Quarry exposure of the Sap Bon Formation and associated detachment thrust is here presented in tables corresponding to the indicated section corresponding to the original field sketches for the cross sections constructed through this area (Chapter 2, Figs. 5 and 6; Appendix A, Fig. 1). Each reading is noted as a measurement of one of the following structural features: bedding (B), shear surface, fault, or foliation plane (S), fracture (F), fold hinge (FH), tension gash where the long axis parallel to σ1 is measure as a plane, or a line in relation to a plane (TG), slickenfibres, measured as a line, or as a pitch on the preceding plane in the table (SL).

Table A1 – Structural data

Section (Fig. 1)	GPS	Structure type	Reading
A	N 14°38'28.1" E 101°05'25.5"	S	55/189
		B	70/195
		B	88/196
		B	53/045
		S	90/176
		B	85/165
		S	68/167
		B	71/199
		B	58/333
		S	80/167
		B	88/207
		B	87/190
		S	71/170
		S	70/173
		FH	40→332
		TG	18/316
		TG	16/276
		TG	16/267
		S	63/167
		B	41/344
		B	56/230
		B	48/180
		SL	46→160
		SL	85E
		SL	49→104
		SL	42→102
B	N 14°38'27.9" E 101°05'24.9"	FH	12→277
		FH	18→279
		B	69/022
		B	40/024
		B	66/197
		S	80/016
		S	54/070
		TG	56/246
		B	80/344
		S	66/224
		S	70/220
		B	60/011
		FH	10→291
		FH	04→290
		S	60/210
		SL	39→148
		SL	39→235
		B	75/181
		B	84/191
		TG	61/288
		TG	63/294
		S	84/228

Table A1 – Structural data

		S	90/190
		SL	80E
		B	82/211
C	N 14°38’27.3” E 101°05’22.4”	S	44/179
		SL	90E/W
		S	78/200
		S	20/239
		B	76/024
		S	56/356
		S	70/211
		F	62/053
		F	46/334
		S	78/225
		S	50/351
		FH	50→012
		FH	52→004
		S	64/358
		S	55/200
		SL	55W
		SL	80E
		SL	70W
		SL	58W
		B	54/186
		S	42/160
		S	85/025
		B	84/197
		S	44/038
		SL	10E
		SL	90E/W
		SL	60W
		S	32/212
		SL	50E
		SL	70W
		S	82/206
		S	64/197
		S	34/129
		SL	85W
		B	71/231
		SL	55E
		B	16/167
		S	26/200
		B	15/069
		B	60/238
		B	79/200
		S	82/198
		SL	70E
		S	50/204
		SL	42→160
		s	72/202
		SL	90E/W

Table A1 – Structural data

			S	30/348
			B	45/218
			SL	42→180
			SL	41→247
			S	34/332
			B	44/344
			S	52/184
			SL	60E
			S	58/214
			SL	50→238
			S	74/198
			SL	60E
			B	74/271
			B	68/189
			B	31/194
			B	71/304
			B	72/190
			SL	70E
			S	65/180
			SL	68→140
			S	73/175
			SL	58→120
			SL	37→340
			S	84/223
			S	84/200
			B	56/177
			F	52/319
			S	36/187
			SL	18E
			SL	23→291
			B	25/186
			SL	29→144
			S	70/082
			B	36/193
			S	66/180
			SL	35W
			S	53/195
			B	31/187
			SL	70W
			SL	12E
			S	25/111
D	N 14°38'26.4"	E 101°05'25.4"	S	43/039
			S	12/240
			S	37/178
			S	44/160
			S	32/191
			SL	60E
			S	43/160
			SL	84E
			FH	44→300

Table A1 – Structural data

			F	71/095
			B	74/160
			S	60/163
			SL	70E
			B	38/210
			FH	14→116
			FH	20→108
			B	60/178
			S	20/231
			SL	15→168
			B	78/231
			B	24/172
			TG	80W
			TG	41E
			B	48/003
E	N 14°38'27.2"	E 101°05'26.5"	B	82/215
			S	14/189
			S	04/195
			S	87/214
			S	24/169
			B	90/195
			B	50/149
			SL	50E
			S	80/202
			SL	80E
			B	90/174
			S	72/162
			SL	45E
			TG	46/302
			B	82/008
			FH	54→082
			B	88/189
			SL	46→110
			B	88/192
			S	73/019
F	N 14°38'27.1"	E 101°05'27.1"	S	60/202
			B	73/210
			S	60/272
			S	45/010
			SL	70W
			S	69/220
			SL	54E
			B	78/213
			S	65/199
			SL	60E
			SL	40W
			S	85/195
			SL	78E
			S	62/188
			SL	45E

Table A1 – Structural data

G	N 14°38’27.1”	E 101°05’27.3”	S	85/146
			SL	60E
			S	50/181
			SL	70E
			SL	85E
			B	54/333
			B	72/325
			B	86/137
			B	41/053
			SL	90E/W
			B	70/153
			SL	28E
			B	88/147
			B	64/162
			FH	53→131
			B	50/136
			B	51/161
			S	45/190
			S	40/126
H	N 14°38’27.0”	E 101°05’27.1”	B	53/198
			S	79/000
			B	88/349
			SL	30E
			FH	28→102
			B	78/189
			B	39/160
			B	35/100
			S	54/001
			B	50/170
			SL	85E
			S	68/191
			SL	60W
			S	84/190
			SL	68E
			B	72/344
			S	34/072
			SL	42E
			S	62/190
			SL	70W
			S	76/206
			SL	90E/W
			S	82/032
			SL	60W
I	N 14°38’26.8”	E 101°05’26.4”	S	77/021
			SL	80E
			B	28/028
			F	72/109
			FH	16→097
			B	88/354
			B	32/339

Table A1 – Structural data

			B	30/355
			SL	54E
			S	65/010
			SL	85E
			B	66/050
			B	42/044
			S	81/153
			SL	70W
			SL	05W
			B	64/008
			SL	85W
			S	54/200
			B	86/162
			S	80/186
			FH	16→088
			S	88/216
			SL	86W
			FH	28→118
			B	58/060
			B	50/180
			S	72/007
			SL	85E
			S	82/036
			B	60/029
			FH	72→095
J	N 14°38'26.0"	E 101°05'26.0"	B	66/185
			S	54/239
			SL	20W
			B	64/219
			B	60/207
			S	68/209
			SL	60E
			B	80/207
			TG	44/340
			S	59/186
			SL	70E
			B	78/194
			S	64/205
			B	87/212
			S	60/218
			SL	70E
			B	79/275
			FH	10→270
			S	60/013
			SL	50E
			B	90/187
			B	60/020
			FH	62→089
			B	80/330
			B	61/051

Table A1 – Structural data

			B	62/135
			B	67/188
			S	62/185
			SL	80W
K	N 14°38’25.0”	E 101°05’24.5”	S	48/194
			SL	20E
			B	53/197
			F	63/092
			F	53/062
			S	62/196
			SL	80E
			S	88/147
			B	51/210
			S	62/179
			B	48/168
			S	76/189
			B	40/222
			S	50/201
			S	80/358
			S	37/200
			B	24/258
			B	22/194
			F	22/194
			S	75/196
			S	79/194
			B	38/220
			S	55/208
			S	85/109
			S	44/022
			B	48/209
			SL	04/107
			S	51/193
			S	72/186
L	N 14°38’24.1”	E 101°05’24.8”	B	54/204
			SL	50E
			S	38/198
			FH	20→109
			S	47/189
			TG	88/083
			B	55/190
			S	58/202
			B	39/204
			B	60/192
			S	54/240
			B	63/200
			B	32/190
			B	89/181
			B	48/218
			S	85/186

Appendix B

Table B1 – Sample descriptions

Khao Khwang Fold-Thrust Belt, Central Thailand

Sample	Description	Section GPS
EAG12001	Sample of Khao Khad Formation packstone, no calcite vein material present. Structurally this sample was taken from approximately 10 metres below the Eagle Thrust in Shale Quarry S (Chapter 3, figs. 1 and 4).	N 14° 38' 28.2" E 101° 05' 25.7"
EAG12002	Sample of Khao Khad Formation packstone, no calcite vein material present. Structurally this sample was taken from approximately 7 metres below the Eagle Thrust.	N 14° 38' 28.2" E 101° 05' 25.7"
EAG12003	Sample of Khao Khad Formation packstone, no calcite vein material present. Structurally this sample was taken from approximately 5 metres below the Eagle Thrust.	N 14° 38' 28.2" E 101° 05' 25.7"
EAG12004	Sample of Khao Khad Formation packstone, no calcite vein material present. Structurally this sample was taken from approximately 3 metres below the Eagle Thrust.	N 14° 38' 28.2" E 101° 05' 25.7"
EAG12005	Sample of Khao Khad Formation packstone, no calcite vein material present. Structurally this sample was taken from 1 metre below the Eagle Thrust.	N 14° 38' 28.2" E 101° 05' 25.7"
EAG12006	Sample of calcite vein material in Khao Khad Formation packstone. Structurally this sample was taken from 2 metres below the Eagle Thrust.	N 14° 38' 28.2" E 101° 05' 25.7"
EAG12007	Sample of calcite vein material in Khao Khad Formation packstone. Structurally this sample was taken from 7 metres below the Eagle Thrust.	N 14° 38' 28.2" E 101° 05' 25.7"
EAG12008	Sap Bon Formation. Sample of extremely fissile/smeared shale along the fault plane of the Eagle Thrust on the top bench of three which were measured for cross-sections (Chapter 2, figs 5 and 6).	N 14° 38' 28.1" E 101° 05' 24.9"
EAG12010	Sap Bon Formation. Sample of extremely fissile/smeared shale along the fault plane of the Eagle Thrust on the top bench of three which were measured for cross-sections.	N 14° 38' 28.1" E 101° 05' 24.9"
EAG12011	Sample of calcite vein material featuring slickenfibres along the fault plane of the Eagle Thrust. Top bench cross section.	N 14° 38' 28.1" E 101° 05' 24.9"

Table B1 – Sample descriptions

EAG12012	Sample of calcite vein material featuring slickenfibres along the fault plane of the Eagle Thrust. Top bench cross section.	N 14° 38' 28.1" E 101° 05' 24.9"
EAG12014	Sap Bon Formation. Sample of extremely fissile and smeared fault gouge material along a thrust plane approximately 1 metre above the Eagle Thrust. More competent material in 'wall rock' of fault was also sampled. This was a sandier package of carbonate cemented arenite. Top bench cross section.	N 14° 38' 28.1" E 101° 05' 24.9"
EAG12015	Sap Bon Formation. Sample of calcite vein material in tension gash approximately 4 metres above the Eagle Thrust. Host rock is more competent, sandier package. Top bench cross section.	N 14° 38' 28.1" E 101° 05' 24.9"
EAG12016	Sap Bon Formation. Sample of competent carbonate cemented arenite in relatively undeformed package of rock approximately 9 metres above the Eagle Thrust. Top bench cross section.	N 14° 38' 28.1" E 101° 05' 24.9"
EAG12017	Sap Bon Formation. Sample of calcite vein material in tension gash approximately 12 metres above the Eagle Thrust. Host rock is more competent, sandier package. Top bench cross section.	N 14° 38' 27.3" E 101° 05' 24.8"
EAG12018	Sap Bon Formation. Sample of fissile, heavily sheared shale approximately 13 metres above the Eagle Thrust. Top bench cross section.	N 14° 38' 27.3" E 101° 05' 24.8"
EAG12019	Sap Bon Formation. Sample of fissile, heavily sheared shale approximately 12 metres above the Eagle Thrust. Top bench cross section.	N 14° 38' 27.3" E 101° 05' 24.8"
EAG12020	Sap Bon Formation. Sample of less fissile but still sheared shale with fine, dark laminations approximately 16 metres above the Eagle Thrust. Top bench cross section.	N 14° 38' 27.3" E 101° 05' 24.8"
EAG12021	Sample of calcite vein material featuring slickenfibres along fault plane approximately 25 metres above the Eagle Thrust. Top bench cross section.	N 14° 38' 27.3" E 101° 05' 24.8"
EAG12022	Sample of calcite vein material in vein cross cutting fault orientation approximately 25 metres above the Eagle Thrust. Top bench cross section.	N 14° 38' 27.3" E 101° 05' 24.8"
EAG12023	Sap Bon Formation. Sample of fissile, sheared shale as well as calcite vein material around fault plane approximately 40 metres above the Eagle Thrust. Lateral section of middle bench of cross sections (Chapter 2, Figs 9 and 10).	N 14° 38' 27.3" E 101° 05' 22.4"
EAG12024	Sap Bon Formation. Sample of fissile, sheared shale as well as calcite vein material around fault plane approximately 40 metres above the Eagle Thrust. Lateral section of middle bench of cross sections.	N 14° 38' 27.3" E 101° 05' 22.4"

Table B1 – Sample descriptions

EAG12025	Sap Bon Formation. Sample of calcite vein material from conjugate fracture fills approximately 50 metres above the Eagle Thrust. Lateral section of middle bench of cross sections.	N 14° 38' 27.3" E 101° 05' 22.4"
EAG12027	Sap Bon Formation. Sample of calcite vein material from conjugate fracture fills approximately 50 metres above the Eagle Thrust. Lateral section of middle bench of cross sections.	N 14° 38' 27.3" E 101° 05' 22.4"
EAG12028	Sap Bon Formation. Sample of calcite vein material from thrust parallel slickenfibres approximately 50 metres above the Eagle Thrust. Lateral section of middle bench of cross sections.	N 14° 38' 27.3" E 101° 05' 22.4"
EAG12029	Sap Bon Formation. Sample of calcite vein material in thick, massive vein along fault plane approximately 45 metres above the Eagle Thrust. Lateral section of middle bench of cross sections.	N 14° 38' 27.3" E 101° 05' 22.4"
EAG12030	Sap Bon Formation. Sample of calcite vein material from thrust parallel slickenfibres approximately 45 metres above the Eagle Thrust. Lateral section of middle bench of cross sections.	N 14° 38' 26.4" E 101° 05' 25.4"
EAG12031	Sap Bon Formation. Sample of calcite vein material in tension gash approximately 45 metres above Eagle Thrust. Lateral section of middle bench of cross sections.	N 14° 38' 26.4" E 101° 05' 25.4"
EAG12032	Sap Bon Formation. Sample of extremely fissile and smeared fault gouge material along a thrust plane approximately 40 metre above the Eagle Thrust. More competent material in 'wall rock' of fault was also sampled. This was a sandier package of carbonate cemented arenite. Lateral section of middle bench of cross sections.	N 14° 38' 26.4" E 101° 05' 25.4"
EAG12033	Sap Bon Formation. Sample of fissile, heavily sheared shale approximately 50 metres above the Eagle Thrust. Lateral section of middle bench of cross sections.	N 14° 38' 26.4" E 101° 05' 25.4"
EAG12034	Sap Bon Formation. Sample of fissile, sheared shale as well as calcite vein material around fault plane approximately 45 metres above the Eagle Thrust. Middle bench of cross sections (Chapter 2, Fig. 6).	N 14° 38' 27.1" E 101° 05' 27.1"
EAG12035	Sap Bon Formation. Sample of competent carbonate cemented arenite in relatively undeformed package of rock approximately 25 metres above the Eagle Thrust. Middle bench cross section.	N 14° 38' 27.1" E 101° 05' 27.1"
EAG12036	Sap Bon Formation. Brecciated and smeared shale along Eagle Thrust fault plane in middle bench cross section.	N 14° 38' 27.1" E 101° 05' 27.1"

Table B1 – Sample descriptions

EAG12037	Sap Bon Formation. Sample of calcite vein material from thrust parallel slickenfibres along the Eagle Thrust. Middle bench of cross sections.	N 14° 38' 27.1" E 101° 05' 27.1"
EAG12038	Sap Bon Formation. Sample of calcite vein material from thrust orthogonal vein immediately above the Eagle Thrust. Middle bench of cross sections.	N 14° 38' 27.1" E 101° 05' 27.1"
EAG12039	Sample of Khao Khad Formation packstone, no calcite vein material present. Structurally this sample was taken from approximately 2 metres below the Eagle Thrust.	N 14° 38' 27.1" E 101° 05' 27.1"
EAG12040	Sap Bon Formation. Sample of calcite vein material from thrust parallel slickenfibres along the Eagle Thrust. Middle bench of cross sections.	N 14° 38' 27.0" E 101° 05' 27.3"
EAG12041	Sap Bon Formation. Sample of sheared shale from otherwise generally competent shale and calcite vein material featuring slickenfibres approximately 20 metres above the Eagle Thrust. Bottom Bench of cross sections (Chapter 2, Fig. 6).	N 14° 38' 27.0" E 101° 05' 27.3"
EAG12042	Sap Bon Formation. Sample of shale with mixed competent and heavily sheared material. Approximately 25 metres above the Eagle Thrust, bottom bench of cross section.	N 14° 38' 27.0" E 101° 05' 27.3"
EAG12043	Sap Bon Formation. Sample of calcite vein material from thrust parallel slickenfibres along fault plane. Approximately 75 metres above the Eagle Thrust, bottom bench of cross sections.	N 14° 38' 26.8" E 101° 05' 26.4"
EAG12044	Sap Bon Formation. Sample of calcite vein material from thrust orthogonal slickenfibres along fault plane. Sheared shale material also sampled. Approximately 80 metres above the Eagle thrust, bottom bench of cross sections.	N 14° 38' 25.6" E 101° 05' 25.2"
EAG12045	Sap Bon Formation. Sample of fissile, heavily sheared shale approximately 90 metres above the Eagle Thrust. Lateral section of middle bench of cross sections.	N 14° 38' 25.0" E 101° 05' 24.5"
EAG12046	Sap Bon Formation. Sample of both fissile fault gouge material in fault plane and relatively undeformed shale/carbonate cemented arenite approximately 90 metres above the Eagle Thrust. Lateral section of middle bench of cross sections.	N 14° 38' 25.0" E 101° 05' 24.5"
EAG12047	Sap Bon Formation. Sample of relatively undeformed shale/carbonate cemented arenite displaying well developed sub-vertical cleavage. Material from gouge around fault plane at the base of this rock package also taken. Approximately 125 metres above the Eagle Thrust. Lateral section of middle bench of cross sections.	N 14° 38' 23.7" E 101° 05' 24.9"

Table B1 – Sample descriptions

EAG12048	Sap Bon Formation. Sample of calcite vein material from thrust parallel slickenfibres along fault plane. Sheared shale material also sampled. Approximately 130 metres above the Eagle thrust, bottom bench of cross sections.	N 14° 38' 23.7" E 101° 05' 24.9"
EAG12049	Sap Bon Formation. Sample of calcite vein material from thrust parallel slickenfibres along fault plane. Sheared shale material also sampled. Approximately 145 metres above the Eagle thrust, bottom bench of cross sections.	N 14° 38' 23.7" E 101° 05' 24.9"
EAG12051	Sap Bon Formation. Sample of fissile fault gouge shale approximately 145 metres above the Eagle Thrust. Bottom bench of cross sections.	N 14° 38' 23.7" E 101° 05' 24.9"
EAG12052	Sap Bon Formation. Sample of calcite vein material from thrust parallel slickenfibres approximately 165 metres above the Eagle Thrust. Bottom bench of cross sections.	N 14° 38' 23.7" E 101° 05' 24.9"
EAG12053	Sap Bon Formation. Sample of sheared shale from otherwise generally competent shale approximately 170 metres above the Eagle Thrust. Bottom Bench of cross sections.	N 14° 38' 23.7" E 101° 05' 24.9"
EAG12055	Sap Bon Formation? Unconfirmed stratigraphic association. Sample of fissile fault gouge shale from middle ridge thrust in Siam City Cement Quarry (Chapter 3, fig. 4; chapter 5, fig. 1).	N 14° 38' 06.6" E 101° 05' 04.0"
EAG13001	Sample of calcite vein material in Khao Khad Formation packstone. Structurally this sample was taken from 2 metres below the Eagle Thrust and from a vein parallel to the fault plane. Top bench of cross sections.	N 14° 38' 28.2" E 101° 05' 25.7"
EAG13002	Sample of calcite vein material in Khao Khad Formation packstone. Structurally this sample was taken from 4 metres below the Eagle Thrust and from a vein parallel to the fault plane. Top bench of cross sections.	N 14° 38' 28.2" E 101° 05' 25.7"
EAG13003	Sample of calcite vein material in Khao Khad Formation packstone. Structurally this sample was taken from 2 metres below the Eagle Thrust and from a vein orthogonal to the fault plane. Top bench of cross sections.	N 14° 38' 28.2" E 101° 05' 25.7"
EAG13004	Sample of calcite vein material in Khao Khad Formation packstone. Structurally this sample was taken from 4 metres below the Eagle Thrust and from a vein orthogonal to the fault plane. Top bench of cross sections.	N 14° 38' 28.2" E 101° 05' 25.7"
EAG13005	Sample of calcite vein material in Khao Khad Formation packstone. Structurally this sample was taken from 5 metres below the Eagle Thrust and from a vein orthogonal to the fault plane. Top bench of cross sections.	N 14° 38' 28.2" E 101° 05' 25.7"

Table B1 – Sample descriptions

EAG13007A	'Alum Shales' undifferentiated formation in Shale Quarry A (Chapter 3, figs. 1 and 4). Sample of calcite vein material in vein orientated parallel to foliation.	WGS84 0723475E 1618161N
EAG13007B	'Alum Shales' undifferentiated formation in Shale Quarry A. Sample of calcite vein material in vein orientated parallel to foliation. 2/3 samples in stack of slickenfibres.	WGS84 0723475E 1618161N
EAG13007C	'Alum Shales' undifferentiated formation in Shale Quarry A. Sample of calcite vein material in vein orientated parallel to foliation. 3/3 samples in stack of slickenfibres.	WGS84 0723475E 1618161N
EAG13008	'Alum Shales' undifferentiated formation in Shale Quarry A. Sample of calcite vein material hosted in igneous sill.	WGS84 0723475E 1618161N
EAG13009	'Alum Shales' undifferentiated formation in Shale Quarry A. Sample of calcite vein material parallel to foliation and hosted in igneous sill.	WGS84 0723475E 1618161N
EAG13010	'Alum Shales' undifferentiated formation in Shale Quarry A. Sample of calcite vein material parallel to foliation and hosted in igneous sill.	WGS84 0723440E 1618205N
EAG13011	'Alum Shales' undifferentiated formation in Shale Quarry A. Sample of calcite vein material orthogonal to foliation and hosted in igneous sill.	WGS84 0723440E 1618205N
EAG13017	'Alum Shales' undifferentiated formation in Shale Quarry A. Sample of calcite vein material in vein orientated parallel to foliation.	WGS84 0723440E 1618205N
EAG13018	'Alum Shales' undifferentiated formation in Shale Quarry A. Sample of calcite vein material in vein orientated parallel to foliation.	WGS84 0723440E 1618205N
EAG13019	'Alum Shales' undifferentiated formation in Shale Quarry A. Sample of calcite vein material in vein orientated orthogonal to foliation.	WGS84 0723415E 1618231N
EAG13020	'Alum Shales' undifferentiated formation in Shale Quarry A. Sample of calcite vein material in vein orientated parallel to foliation.	WGS84 0723415E 1618231N
EAG13021	'Alum Shales' undifferentiated formation in Shale Quarry A. Sample of calcite vein material in vein orientated parallel to foliation.	WGS84 0723415E 1618231N

Table B1 – Sample descriptions

EAG13022	'Alum Shales' undifferentiated formation in Shale Quarry A. Sample of calcite vein material in vein orientated parallel to foliation.	WGS84 0723404E 1618263N
EAG13023	'Alum Shales' undifferentiated formation in Shale Quarry A. Sample of calcite vein material in vein orientated parallel to foliation.	WGS84 0723404E 1618263N
EAG13024	'Alum Shales' undifferentiated formation in Shale Quarry A. Sample of calcite vein material in vein orientated parallel to foliation.	WGS84 0723404E 1618263N
EAG13025	'Alum Shales' undifferentiated formation in Shale Quarry A. Sample of calcite vein material in vein orientated orthogonal to foliation.	WGS84 0723376E 1618261N
EAG13026	'Alum Shales' undifferentiated formation in Shale Quarry A. Sample of calcite vein material in vein orientated orthogonal to foliation.	WGS84 0723376E 1618261N
EAG13028	'Alum Shales' undifferentiated formation in Shale Quarry A. Sample of calcite vein material in vein orientated parallel to foliation.	WGS84 0723376E 1618261N
EAG13029	'Alum Shales' undifferentiated formation in Shale Quarry A. Sample of calcite vein material in vein orientated parallel to foliation.	WGS84 0723399E 1618236N
EAG13030	'Alum Shales' undifferentiated formation in Shale Quarry A. Sample of calcite vein material parallel to foliation and hosted in igneous sill.	WGS84 0723399E 1618236N
EAG13031	'Alum Shales' undifferentiated formation in Shale Quarry A. Sample of calcite vein material parallel to foliation and hosted in igneous sill.	WGS84 0723399E 1618236N
EAG13032	'Alum Shales' undifferentiated formation in Shale Quarry A. Sample of calcite vein material parallel to foliation and hosted in igneous sill.	WGS84 0723399E 1618236N
EAG13033	'Alum Shales' undifferentiated formation in Shale Quarry A. Sample of calcite vein material parallel to foliation and hosted in igneous sill.	WGS84 0723420E 1618191N
EAG13034	'Alum Shales' undifferentiated formation in Shale Quarry A. Sample of calcite vein material in vein orientated parallel to foliation.	WGS84 0723420E 1618191N
EAG13035	'Alum Shales' undifferentiated formation in Shale Quarry A. Sample of calcite vein material parallel to foliation and hosted in igneous sill.	WGS84 0723420E 1618191N

EAG13036	'Alum Shales' undifferentiated formation in Shale Quarry A. Sample of calcite vein material in vein orientated parallel to foliation.	WGS84 0723420E 1618191N
EAG13037	'Alum Shales' undifferentiated formation in Shale Quarry A. Sample of calcite vein material in vein orientated parallel to foliation.	WGS84 0723450E 1618157N
EAG13038	'Alum Shales' undifferentiated formation in Shale Quarry A. Sample of calcite vein material in vein orientated parallel to foliation.	WGS84 0723450E 1618157N
EAG13039	'Alum Shales' undifferentiated formation in Shale Quarry A. Sample of calcite vein material in vein orientated parallel to foliation.	WGS84 0723450E 1618157N
EAG13040	'Alum Shales' undifferentiated formation in Shale Quarry A. Sample of calcite vein material in vein orientated parallel to foliation.	WGS84 0723450E 1618157N
EAG13041	'Alum Shales' undifferentiated formation in Shale Quarry A. Sample of calcite vein material in vein orientated parallel to foliation.	WGS84 0723462E 1618114N
EAG13042	'Alum Shales' undifferentiated formation in Shale Quarry A. Sample of calcite vein material in vein orientated parallel to foliation.	WGS84 0723462E 1618114N
EAG13043	'Alum Shales' undifferentiated formation in Shale Quarry A. Sample of calcite vein material in vein orientated parallel to foliation.	WGS84 0723462E 1618114N
EAG13044	'Alum Shales' undifferentiated formation in Shale Quarry A. Sample of calcite vein material in vein orientated parallel to foliation.	WGS84 0723425E 1618160N
EAG13045	'Alum Shales' undifferentiated formation in Shale Quarry A. Sample of calcite vein material parallel to foliation and hosted in igneous sill.	WGS84 0723425E 1618160N
EAG13046	'Alum Shales' undifferentiated formation in Shale Quarry A. Sample of calcite vein material in vein orientated parallel to foliation.	WGS84 0723425E 1618160N
EAG13047	'Alum Shales' undifferentiated formation in Shale Quarry A. Sample of calcite vein material in vein orientated parallel to foliation.	WGS84 0723385E 1618215N

Table B1 – Sample descriptions

EAG13048	'Alum Shales' undifferentiated formation in Shale Quarry A. Sample of calcite vein material in vein orientated parallel to foliation.	WGS84 0723385E 1618215N
EAG13049	'Alum Shales' undifferentiated formation in Shale Quarry A. Sample of calcite vein material in vein orientated parallel to foliation.	WGS84 0723385E 1618215N
EAG13050	'Alum Shales' undifferentiated formation in Shale Quarry A. Sample of calcite vein material in vein orientated parallel to foliation.	WGS84 0723352E 1618247N
EAG13051	'Alum Shales' undifferentiated formation in Shale Quarry A. Sample of calcite vein material parallel to foliation and hosted in igneous sill.	WGS84 0723352E 1618247N
EAG13052	'Alum Shales' undifferentiated formation in Shale Quarry A. Sample of calcite vein material in vein orientated parallel to foliation.	WGS84 0723352E 1618247N
EAG13053	'Alum Shales' undifferentiated formation in Shale Quarry A. Sample of calcite vein material in vein orientated parallel to foliation.	WGS84 0723312E 1618249N
EAG13054	'Alum Shales' undifferentiated formation in Shale Quarry A. Sample of calcite vein material orthogonal to foliation and hosted in igneous sill.	WGS84 0723312E 1618249N
EAG13055	'Alum Shales' undifferentiated formation in Shale Quarry A. Sample of calcite vein material in vein orientated parallel to foliation.	WGS84 0723312E 1618249N
EAG13056	'Alum Shales' undifferentiated formation in Shale Quarry A. Sample of calcite vein material in vein orientated parallel to foliation.	WGS84 0723329E 1618196N
EAG13057	'Alum Shales' undifferentiated formation in Shale Quarry A. Sample of calcite vein material orthogonal to foliation and hosted in igneous sill.	WGS84 0723329E 1618196N
EAG13058	'Alum Shales' undifferentiated formation in Shale Quarry A. Sample of calcite vein material in vein orientated parallel to foliation.	WGS84 0723329E 1618196N
EAG13068	'Alum Shales' undifferentiated formation in Shale Quarry A. Sample of calcite vein material in vein orientated parallel to foliation.	WGS84 0723366E 1618136N

Table B1 – Sample descriptions

EAG13070	'Alum Shales' undifferentiated formation in Shale Quarry A. Sample of calcite vein material in vein orientated orthogonal to foliation.	WGS84 0723366E 1618136N
EAG13071	'Alum Shales' undifferentiated formation in Shale Quarry A. Sample of calcite vein material in vein orientated parallel to foliation.	WGS84 0723366E 1618136N
EAG13072	'Alum Shales' undifferentiated formation in Shale Quarry A. Sample of calcite vein material parallel to foliation and hosted in igneous sill.	WGS84 0723397E 1618108N
EAG13073	'Alum Shales' undifferentiated formation in Shale Quarry A. Sample of calcite vein material in vein orientated parallel to foliation.	WGS84 0723397E 1618108N
EAG13074	'Alum Shales' undifferentiated formation in Shale Quarry A. Sample of calcite vein material in vein orientated parallel to foliation.	WGS84 0723306E 1618171N
EAG13075	'Alum Shales' undifferentiated formation in Shale Quarry A. Sample of calcite vein material in vein orientated parallel to foliation.	WGS84 0723306E 1618171N
EAG13077	'Alum Shales' undifferentiated formation in Shale Quarry A. Sample of calcite vein material in vein orientated parallel to foliation.	WGS84 0723306E 1618171N
EAG13078	'Alum Shales' undifferentiated formation in Shale Quarry A. Sample of calcite vein material in vein orientated orthogonal to foliation.	WGS84 0723313E 1618114N
EAG13079	'Alum Shales' undifferentiated formation in Shale Quarry A. Sample of calcite vein material parallel to foliation and hosted in igneous sill.	WGS84 0723313E 1618114N
EAG13080	'Alum Shales' undifferentiated formation in Shale Quarry A. Sample of calcite vein material in vein orientated parallel to foliation.	WGS84 0723342E 1618146N
EAG13081	'Alum Shales' undifferentiated formation in Shale Quarry A. Sample of calcite vein material in vein orientated parallel to foliation.	WGS84 0723342E 1618146N
EAG13082	'Alum Shales' undifferentiated formation in Shale Quarry A. Sample of calcite vein material in vein orientated parallel to foliation.	WGS84 0723342E 1618146N

Table B1 – Sample descriptions

EAG13083	'Alum Shales' undifferentiated formation in Shale Quarry A. Sample of calcite vein material orthogonal to foliation and hosted in igneous sill.	WGS84 0723342E 1618146N
EAG13084	'Alum Shales' undifferentiated formation in Shale Quarry A. Sample of calcite vein material orthogonal to foliation and hosted in igneous sill.	WGS84 0723360E 1618101N
EAG13085	'Alum Shales' undifferentiated formation in Shale Quarry A. Sample of calcite vein material orthogonal to foliation and hosted in igneous sill.	WGS84 0723360E 1618101N
EAG13086A	'Alum Shales' undifferentiated formation in Shale Quarry A. Sample of calcite vein material orthogonal to foliation and hosted in igneous sill.	WGS84 0723360E 1618101N
EAG13086B	'Alum Shales' undifferentiated formation in Shale Quarry A. Sample of calcite vein material orthogonal to foliation and hosted in igneous sill.	WGS84 0723360E 1618101N
EAG13087	'Alum Shales' undifferentiated formation in Shale Quarry A. Sample of calcite vein material orthogonal to foliation and hosted in igneous sill.	WGS84 0723386E 1618078N
EAG13088	'Alum Shales' undifferentiated formation in Shale Quarry A. Sample of calcite vein material orthogonal to foliation and hosted in igneous sill.	WGS84 0723386E 1618078N
EAG13090	'Alum Shales' undifferentiated formation in Shale Quarry A. Sample of calcite vein material in vein orientated parallel to foliation.	WGS84 0723386E 1618078N
EAG13091	'Alum Shales' undifferentiated formation in Shale Quarry A. Sample of calcite vein material in vein orientated parallel to foliation.	WGS84 0723386E 1618078N
EAG13092	'Alum Shales' undifferentiated formation in Shale Quarry A. Sample of calcite vein material in vein orientated parallel to foliation.	WGS84 0723275E 1618187N
EAG13093	'Alum Shales' undifferentiated formation in Shale Quarry A. Sample of calcite vein material in vein orientated parallel to foliation.	WGS84 0723275E 1618187N
EAG13094	'Alum Shales' undifferentiated formation in Shale Quarry A. Sample of calcite vein material in vein orientated parallel to foliation.	WGS84 0723275E 1618187N

EAG13095	'Alum Shales' undifferentiated formation in Shale Quarry A. Sample of calcite vein material in vein orientated parallel to foliation.	WGS84 0723251E 1618246N
EAG13096	Phu Phe Formation. Sample of vein in packstone, structurally this unit is in variably thrust and stratigraphic contact with the underlying 'alum shales'.	WGS84 0723251E 1618246N
EAG13097	Phu Phe Formation. Sample of packstone, structurally this unit is in variably thrust and stratigraphic contact with the underlying 'alum shales'.	WGS84 0723251E 1618246N
EAG13099	Phu Phe Formation. Sample of vein in packstone, structurally this unit is in variably thrust and stratigraphic contact with the underlying 'alum shales'.	WGS84 0723251E 1618246N
EAG13100	Phu Phe Formation. Sample of packstone, structurally this unit is in variably thrust and stratigraphic contact with the underlying 'alum shales'.	WGS84 0723251E 1618246N

Chrystalls Beach Complex, Southern Otago, New Zealand

NNAE1002	Alum Shales Formation. Sample of finely laminated and foliated dark shale from the Nærsnes beach cross section through a series of imbricates along the Grundvik Peninsula.	WGS84 0584338E 6620710N
NNAE7001	Alum Shales Formation. Sample of finely laminated and foliated dark shale from the Nærsnes beach cross section through a series of imbricates along the Grundvik Peninsula.	WGS84 0584381E 6626763N
NV001	Venstøp Formation. FJellstad Farm in the Ringerike area Sample from shales which sit approximately 300 metres stratigraphically above the basal Alum shales. Sample material was on finely foliated grey-brown shales.	WGS84 0584381E 6626763N
NV004	Venstøp Formation. FJellstad Farm in the Ringerike area. Sample from shales which sit approximately 300 metres stratigraphically above the basal Alum shales. Sample material was on finely foliated grey-brown shales.	WGS84 0567240E 6661503N

Osen Røa Thrust Sheet, Oslo Region, Norway

NZBCK1001	Sample of continuous deformation style shale matrix of the Chrystalls Beach Complex accretionary melange. Very thin (2 cm) band of shale matrix as this site is dominated almost entirely by competent material (Chapter 4, fig. 2).	WGS84 0432908E 4885618N

Table B1 – Sample descriptions

NZCB2002	Sample of continuous deformation style shale matrix of the Chrystalls Beach Complex accretionary melange.	WGS84 0431431E 4884345N
NZCB5002	Sample of continuous deformation style shale matrix of the Chrystalls Beach Complex accretionary melange.	WGS84 0431510E 4884399N
NZCBR003	Sample of continuous deformation style shale matrix of the Chrystalls Beach Complex accretionary melange. Considerably high ratio (50:50?) of competent lenses to incompetent shale matrix at this location.	WGS84 0431948E 4884649N
NZCBR006	Sample of continuous deformation style shale matrix of the Chrystalls Beach Complex accretionary melange. Considerably high ratio (50:50?) of competent lenses to incompetent shale matrix at this location.	WGS84 0432358E 4885003N
NZWBR002	Sample of continuous deformation style shale matrix of the Chrystalls Beach Complex accretionary melange. Minimal shale matrix present at this location (<10%), dominated by competent packages and quartz mineralisation of fractures.	WGS84 0433199E 4885837N
NZWBR005	Sample of continuous deformation style shale matrix of the Chrystalls Beach Complex accretionary melange. Packages of seemingly separated (boudinage or thrust emplacement) shale matrix here in dominantly competent rock. Very little fracture mineralisation present.	WGS84 0434578E 4887497N

Appendix C

Step no.	Action	Comments
	1. SAMPLE MILLING	
Step 1	Wash sample chips to remove any fine material	Removes artificially ground particles
Step 2	Run through disc mill at initial setting determined by width of rock chips. Through to 1.0mm disc gap	Start at half maximum width of chip size and decrease step wise to reach 5.0 > 2.0 > 1.0 mm
	2. CLAY PURIFICATION	
	2.1 CARBONATE REMOVAL	
Step 1	Place 1.0 g of sample in 50 ml centrifuge vial	
Step 2	Add 10 ml of sodium acetate/acetic acid buffer	To make up buffer solution, dissolve 136 g of sodium acetate trihydrate in 900 ml of DI water, then add 45 ml glacial acetic acid and bring total volume up to 1000 ml with further DI water
Step 3	Loosely screw on cap and place all samples in a rack, then in water bath at 90 °C until effervescence ceases	If reacting too violently remove samples from bath and allow water in bath to cool before continuing
Step 4	Fill vial with sample up to 50 ml with DI water	
Step 5	Centrifuge for 5 minutes at 3000 rpm, discard supernatant	Supernatant = clear fluid on top of sample, discard in appropriate acid waste container
Step 6	Repeat steps 2-5 twice more	On these occasions the samples may need to sit in hot water bath for up to 30 minutes
Step 7	Fill vial to 50 ml with DI water and shake vigorously, centrifuge for 5 minutes at 3000 rpm, discard supernatant	This step is to rinse the sample of remaining buffer solution, still discard supernatant in appropriate acid waste container
Step 8	Repeat the rinse (step 7) twice more	The sample is now purified of carbonates for XRD, if the sample needs to be left overnight at this point, fill vial with DI water first

Note: samples must be purified of carbonates (2.1) before organic matter removal

2.2 ORGANIC MATTER REMOVAL

Step 1	Adjust the required amount of sodium hypochlorite bleach to a pH of 9.5 using 4M HCL. This solution is unstable and should be used the day of preparation	Use a pH meter as you add 4M HCL, allowing you to accurately adjust. Use the fume hood as this step releases a dangerous gas
Step 2	Dispense 10 ml of the pH adjusted bleach into centrifuge vial contacting sample	
Step 3	Loosely screw on cap and place all samples in a rack, then in water bath at 90 °C for 15 minutes	
Step 4	Remove vials from bath fill to 50 ml with DI water	
Step 5	Centrifuge for 5 minutes at 3000 rpm, discard supernatant	Discard in appropriate bleach water container
Step 6	Repeat steps 2-5 until samples no longer react upon addition of further bleach	This usually takes 1-3 repeats depending on organic content, purified samples should appear light grey, brown or reddish with the darker organic matter removed
Step 7	After the last bleach repeat, fill vial to 50 ml with DI water and shake vigorously, centrifuge for 5 minutes at 3000 rpm, discard supernatant	This step is to rinse the sample of remaining bleach, still discard supernatant in appropriate bleach waste container
Step 8	Repeat the rinse (step 6) twice more	The sample is now purified of organic matter for XRD, if the sample needs to be left overnight at this point, fill vial with DI water first

Note: each sample must be thoroughly rinsed following organic matter removal (2.2)

3. CLAY FRACTION SEPERATION

Step 1	Fill samples with DI water to the 20 ml mark	Depending on the amount of rock material remaining you may need more to allow for the ultrasonic needle to be submersed
Step 2	Use the ultrasonic machine to agitate each sample for 30 seconds at a setting of 30%	This machine is loud and high pitched, so always use ear protection, ensure the sides of the vial do not touch the ultrasonic needle
Step 3	Centrifuge each sample for 4 minutes at 900 rpm	

Step 4	Pour of the supernatant into a beaker labelled with the sample name	The supernatant should be cloudy
Step 5	Repeat steps 1-4 until the supernatant is clear	
Step 6	Place a teaspoon of $CaCL_2$ in each sample beaker and cover, then allow to settle for at least 36 hours	Check the beakers for settling, when the suspended particles have settled leaving an entirely clear supernatant they are ready for step 7
Step 7	Pour material into centrifuge vials and centrifuge for 20 minutes at 3000 rpm, discard supernatant which should be clear	If using the same centrifuge tubes ensure they are cleaned and dried thoroughly. This step will need to be repeated due to the volume of fluid in the beakers compared to the centrifuge tube capacity
Step 8	Continue step 7 until all material has been transferred back to centrifuge tubes	The final portion in the beakers will require adding DI water to remove
Step 10	Add 10 ml of $CaCL_2$ solution to each sample and then shake with the vortex mixer	
Step 11	Fill to the 50 ml mark with DI water and centrifuge for 10 minutes at 3000 rpm, discard supernatant	
Step 12	Fill vial to 50 ml with DI water, centrifuge for 10 minutes at 3000 rpm, discard supernatant	This is a final rinse to remove $CaCL_2$ solution, if the sample needs to be left overnight at this point, fill vial with DI water first

3.1 SAMPLE PREPERATION FOR XRD

Step 1	Take clean silicon slides for XRD and write sample numbers on the dull side of each, place these shinny-side-up on the Perspex XRD Slides and label these as well	

Step 2	Fill centrifuge vial with sample to 20 ml with DI water, agitate using the ultrasonic machine set to 30% for 30 seconds	The samples should now not settle too quickly (as the $CaCL_2$ should be removed), if they do, a further rinse is required
Step 3	Shake samples well and centrifuge for 4 minutes at 900 rpm	
Step 4	Pipette from the middle of each centrifuge tube, carefully taking only from the centre of the suspended material and dispense onto the corresponding labelled slide	
Step 5	Allow the suspension to dry overnight	The samples are then ready for XRD analysis

Diffraction patterns from all samples were collected using a Bruker D8 Advance X-Ray Diffractometer at the following instrument settings: CuKα radiation at 40 kV/40 mA; 0.6 mm divergence slit; 0.05 (2θ) step size, 1.5s counting time. Diffraction patterns were collected from 3.5 to 45° 2θ.

Document C2 – Illite crystallinity standardisation

Six standards were provided by Hugh Rice to calibrate raw X-ray diffraction illite crystallinity measurements to the Crystallinity Index Standard (CIS). The six samples were prepared for XRD analysis as per the same procedure in Document C1. Each standard was then analysed with the same procedure and machine settings as in Document C1. The following data were obtained:

Standard sample No.	FWHM of 10Å peak	10Å data set from CIS
sw1	0.28	0.63
sw2	0.30	0.47
sw3	0.26	0.46
sw4	0.16	0.38
sw5	0.18	0.36
sw6	0.10	0.25

These data provided the regression curve which was used to correct all illite crystallinity values in this study to CIS values:

$$y = 1.4357x + 0.119$$

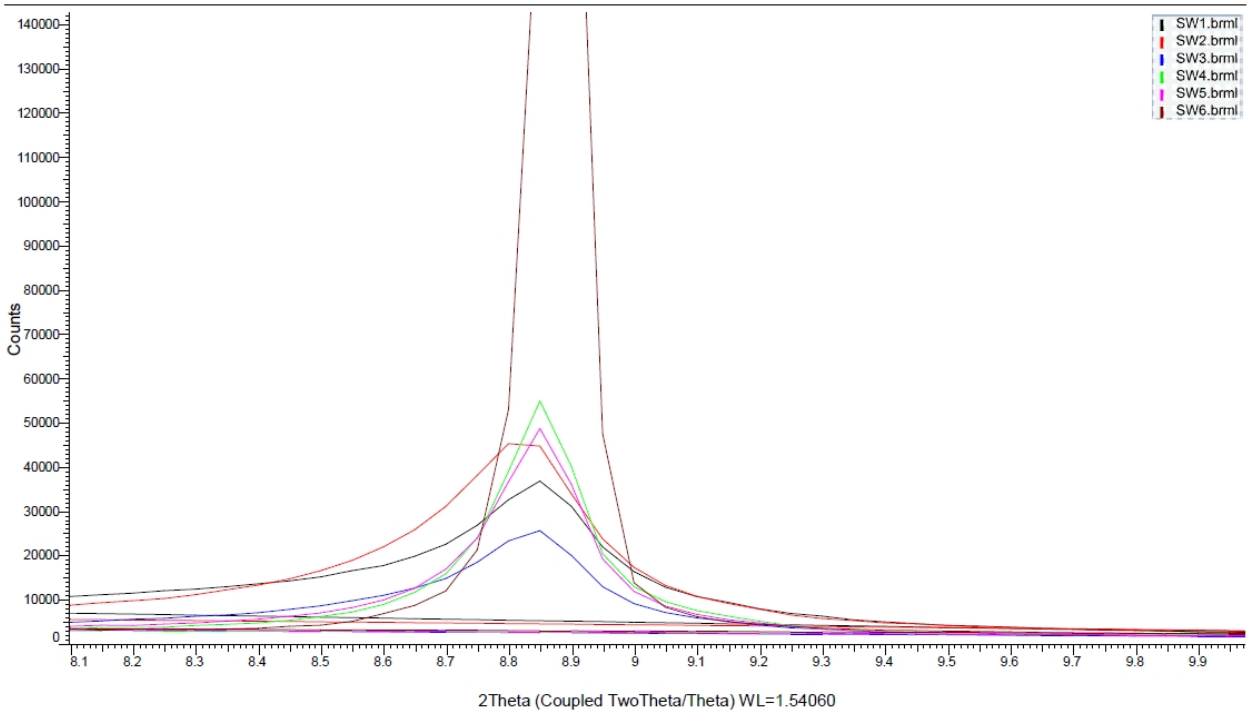

XRD Diffractogram of 10Å peak from the six standard samples.

Figure C2 – XRD diffractograms of samples

Each sample is shown with an air-dried (black) and ethylene glycol treated (red) diffractogram.

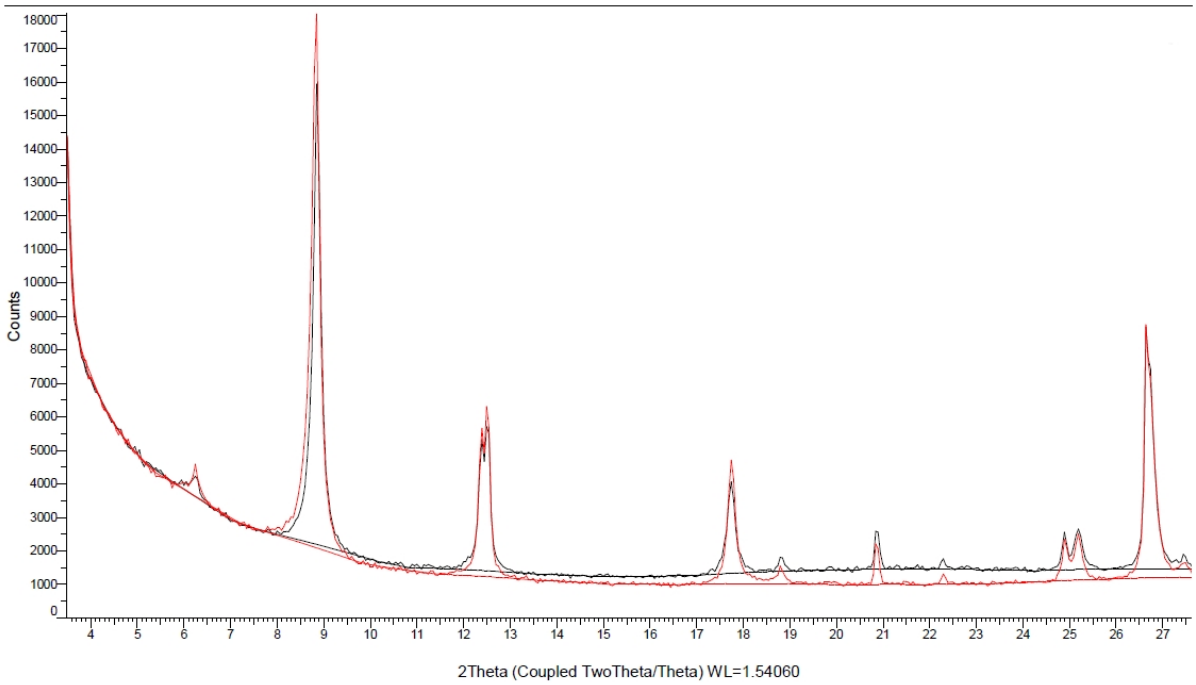

EAG12008

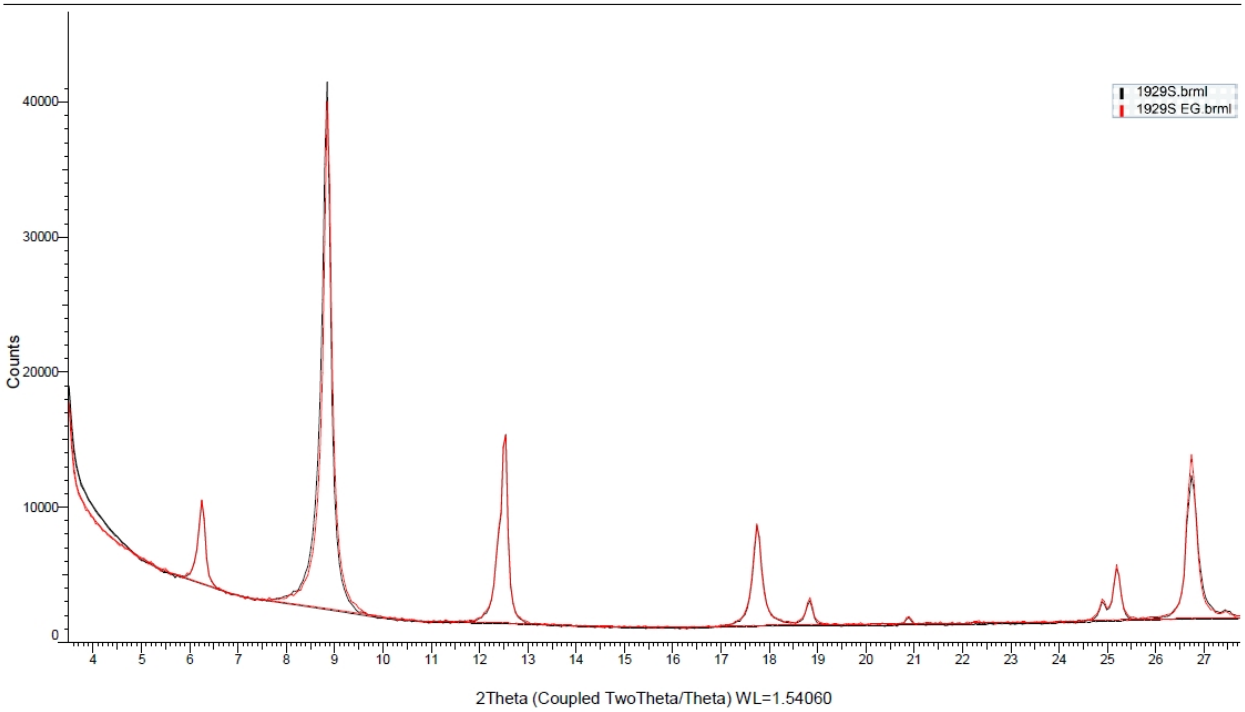

EAG12014

Figure C1 – XRD diffractograms of samples

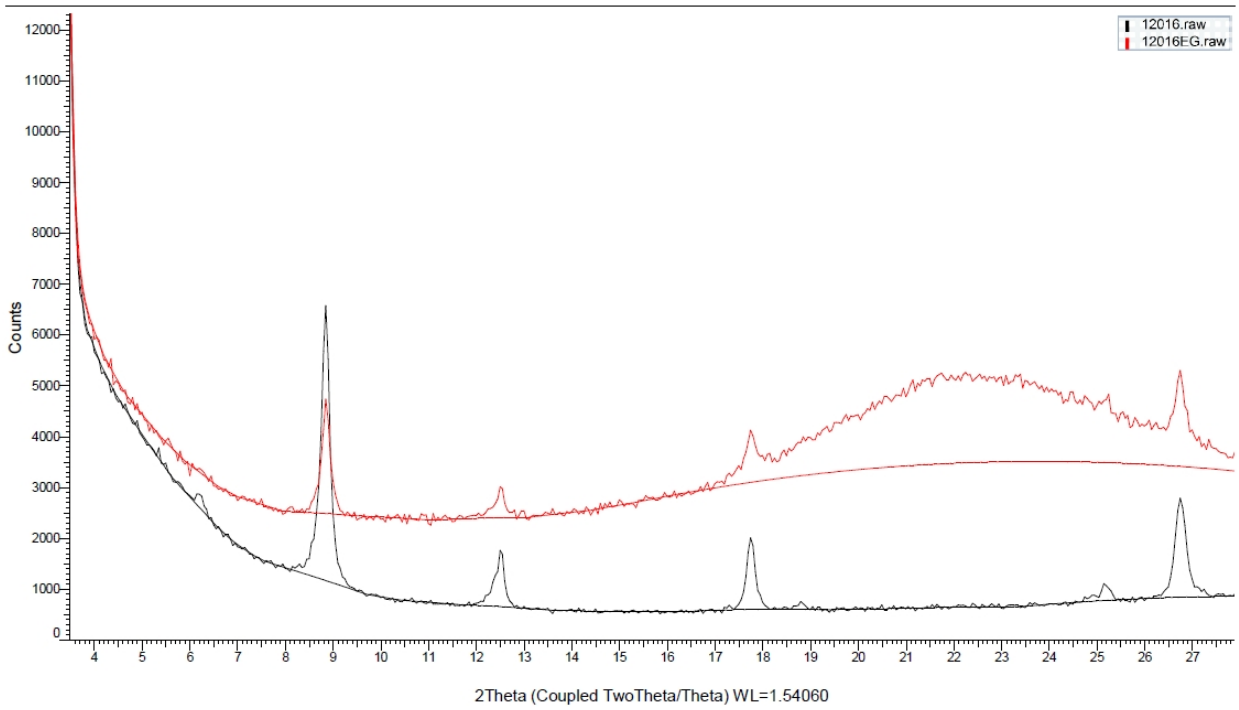

EAG12016

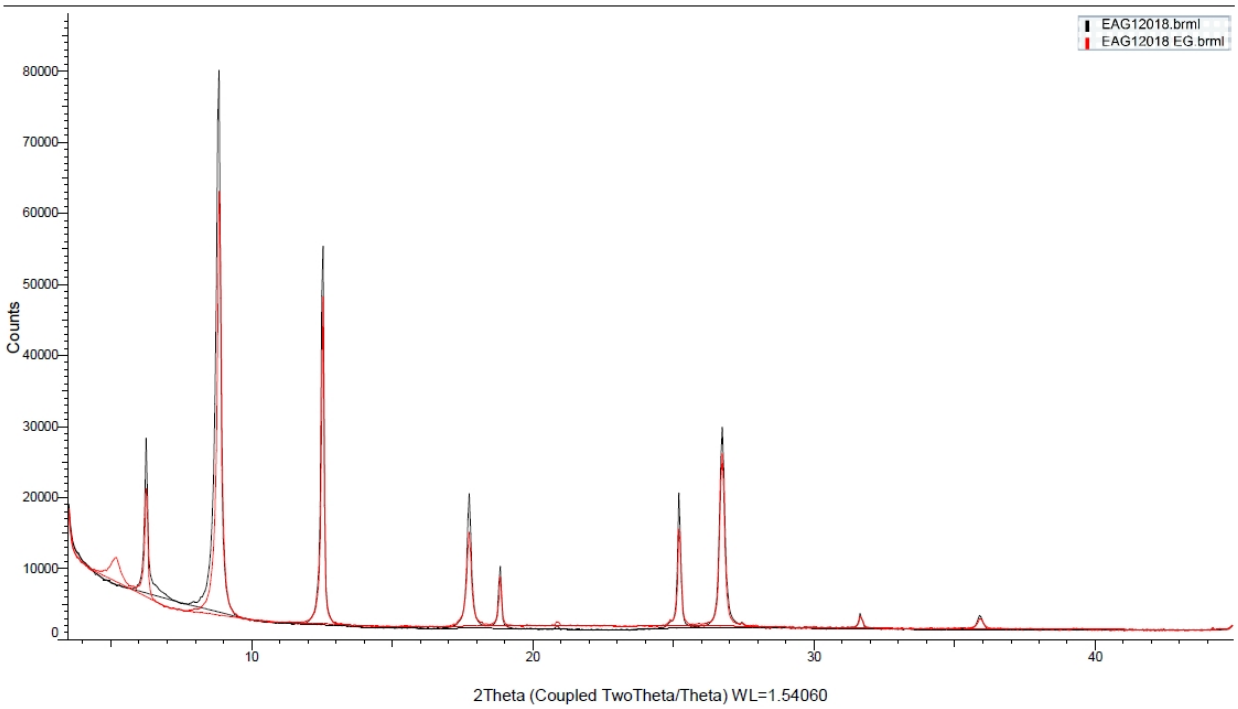

EAG12018

Figure C1 – XRD diffractograms of samples

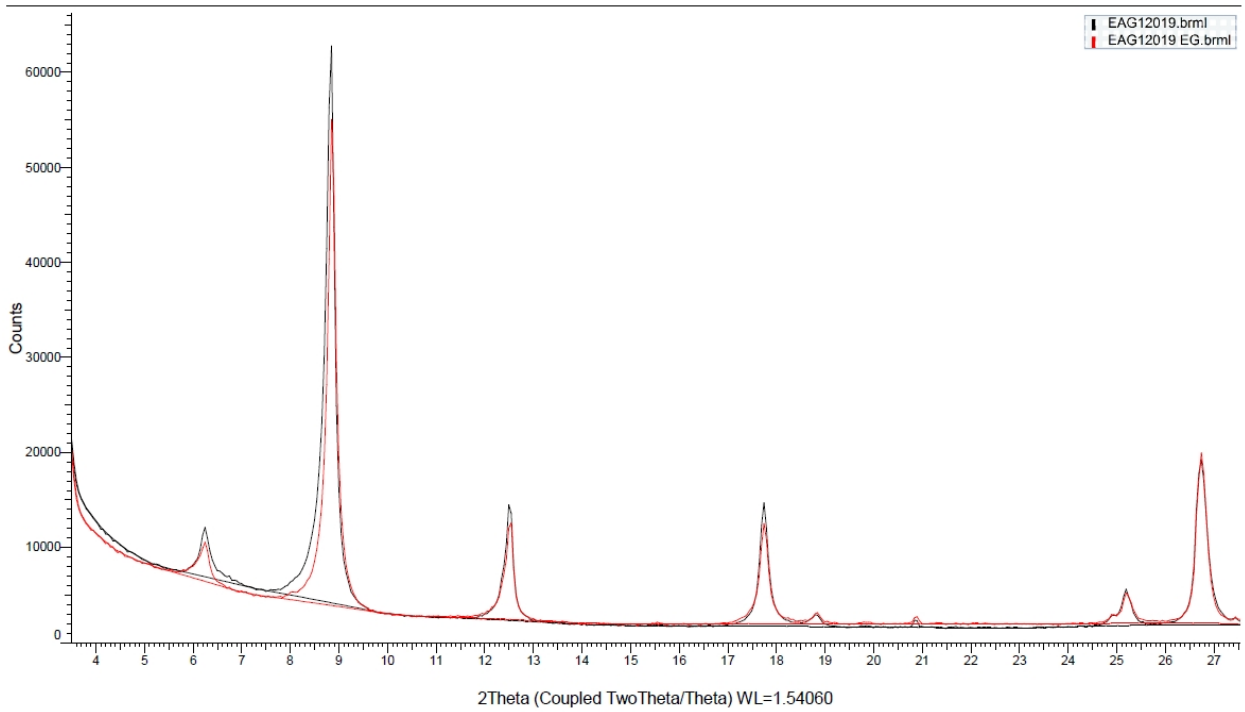

EAG12019

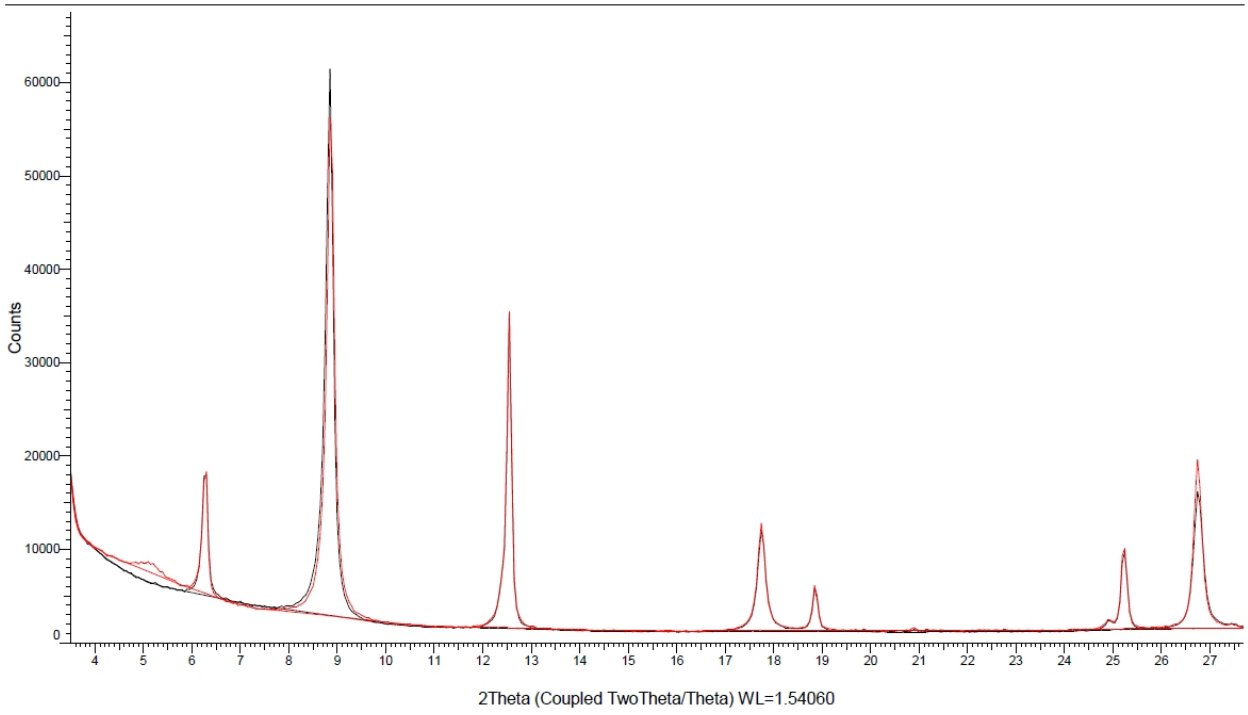

EAG12032

Figure C1 – XRD diffractograms of samples

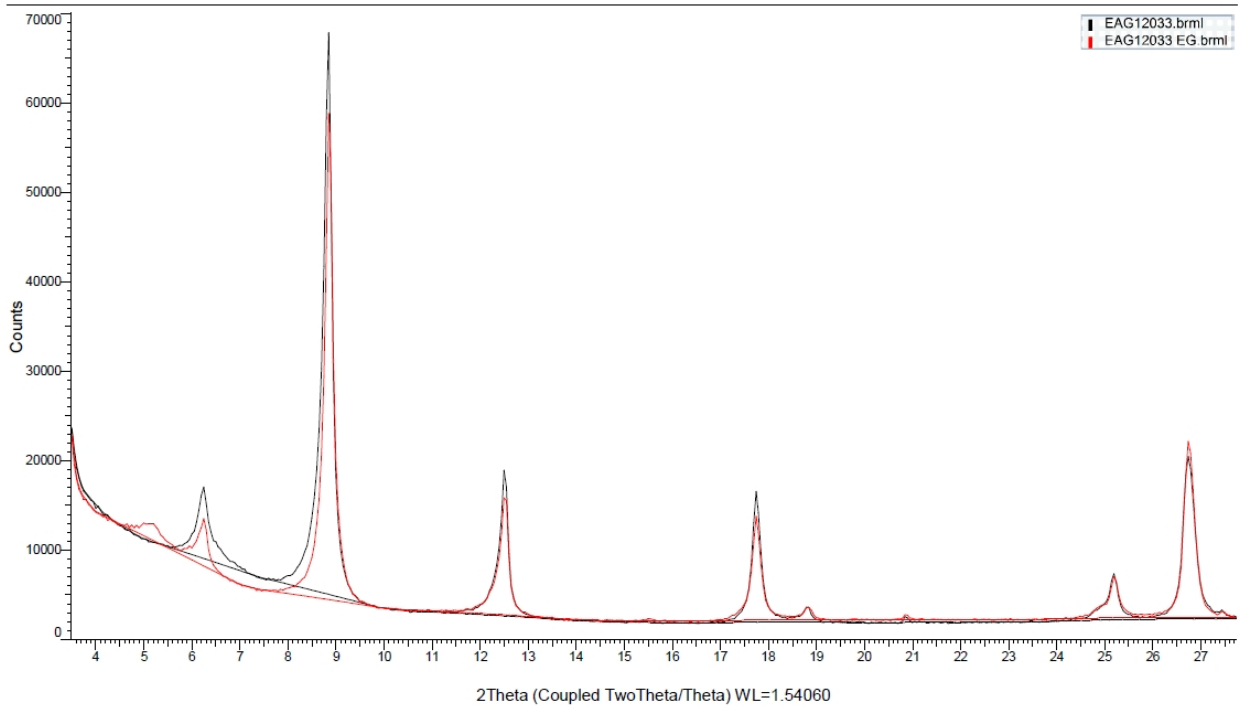

EAG12033

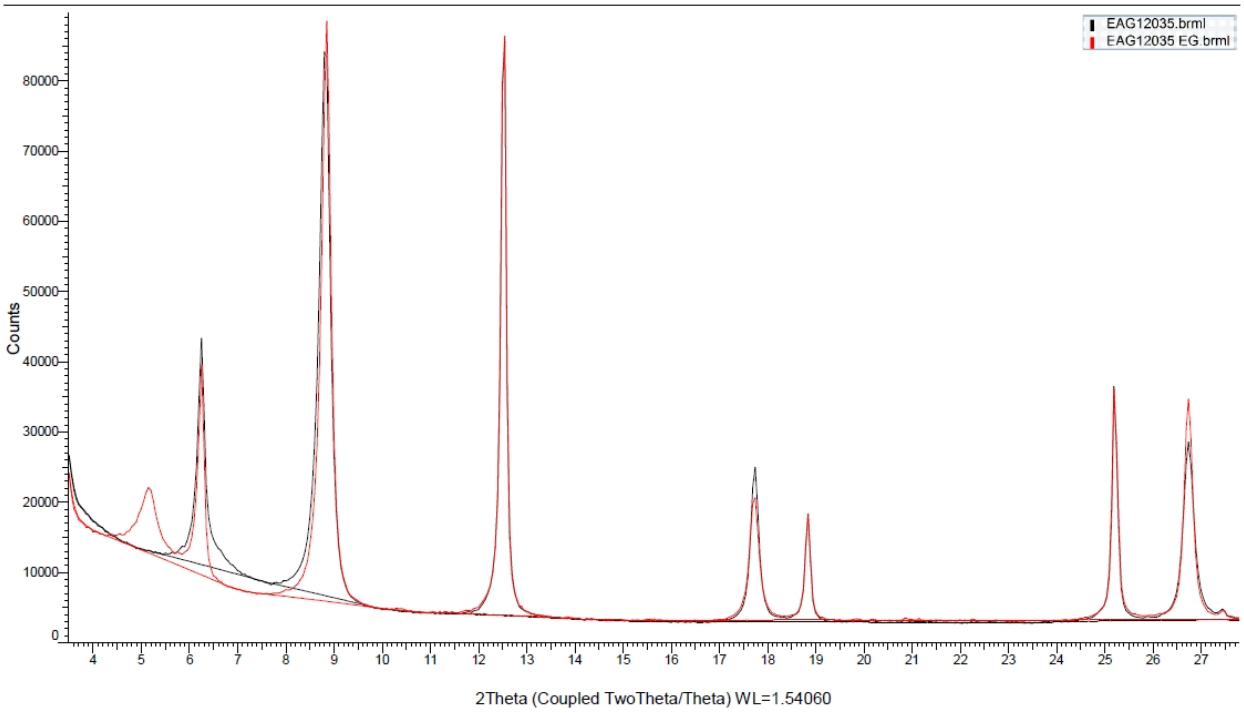

EAG12035

Figure C1 – XRD diffractograms of samples

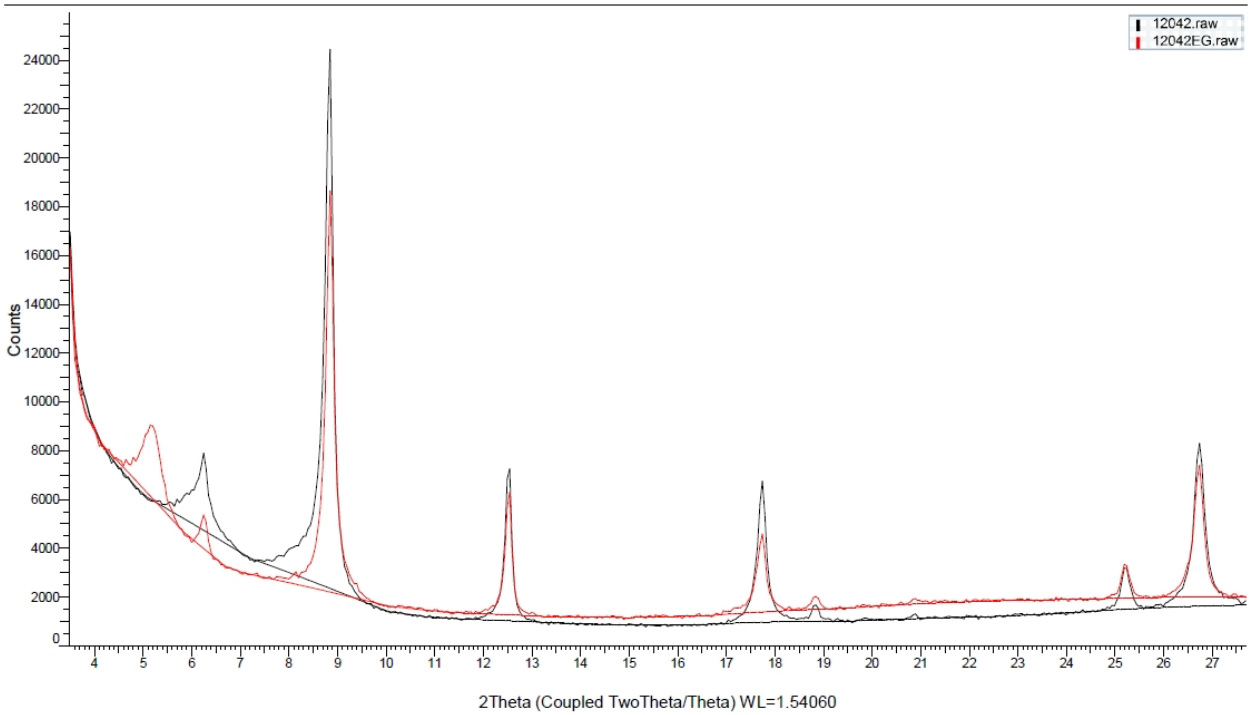

EAG12042

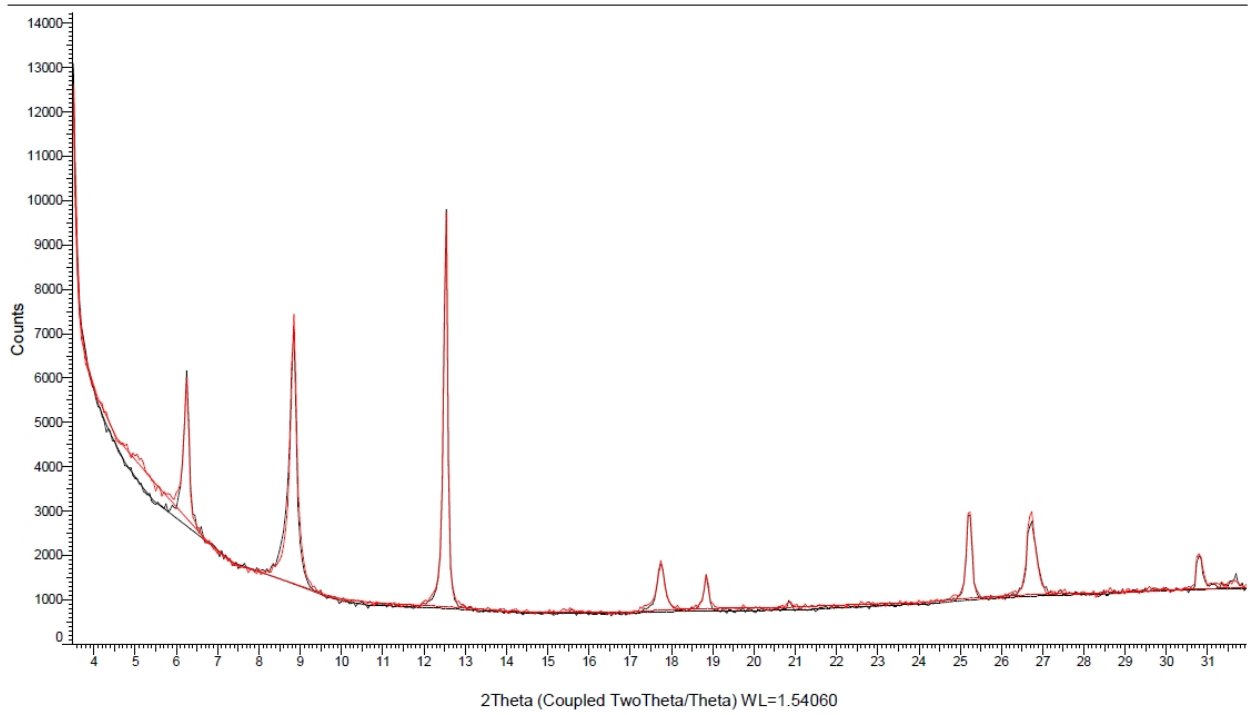

EAG12046

Figure C1 – XRD diffractograms of samples

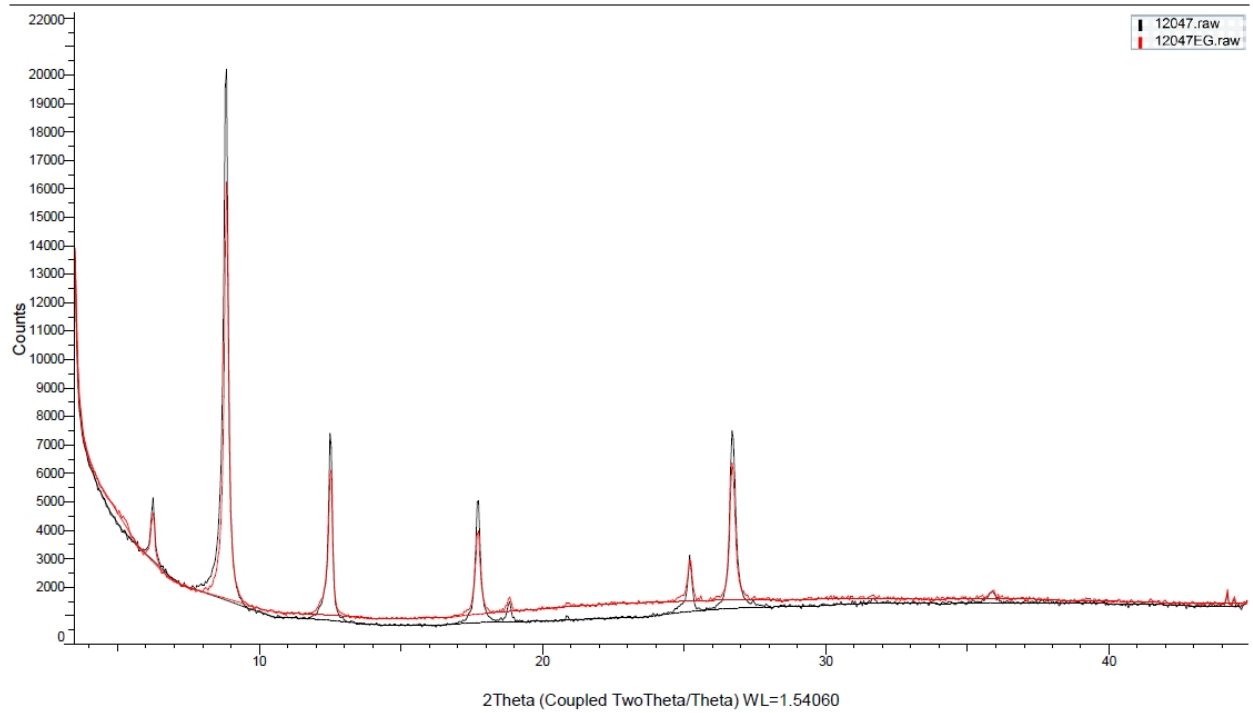

EAG12047

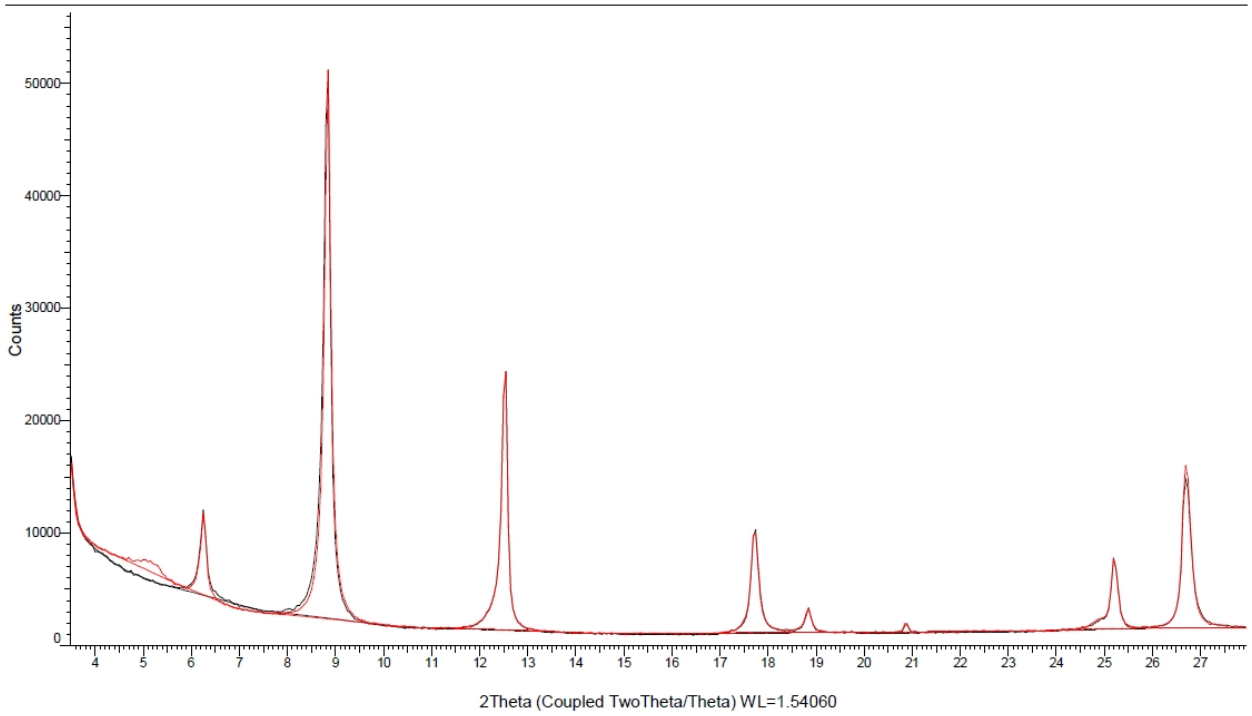

EAG12048

Figure C1 – XRD diffractograms of samples

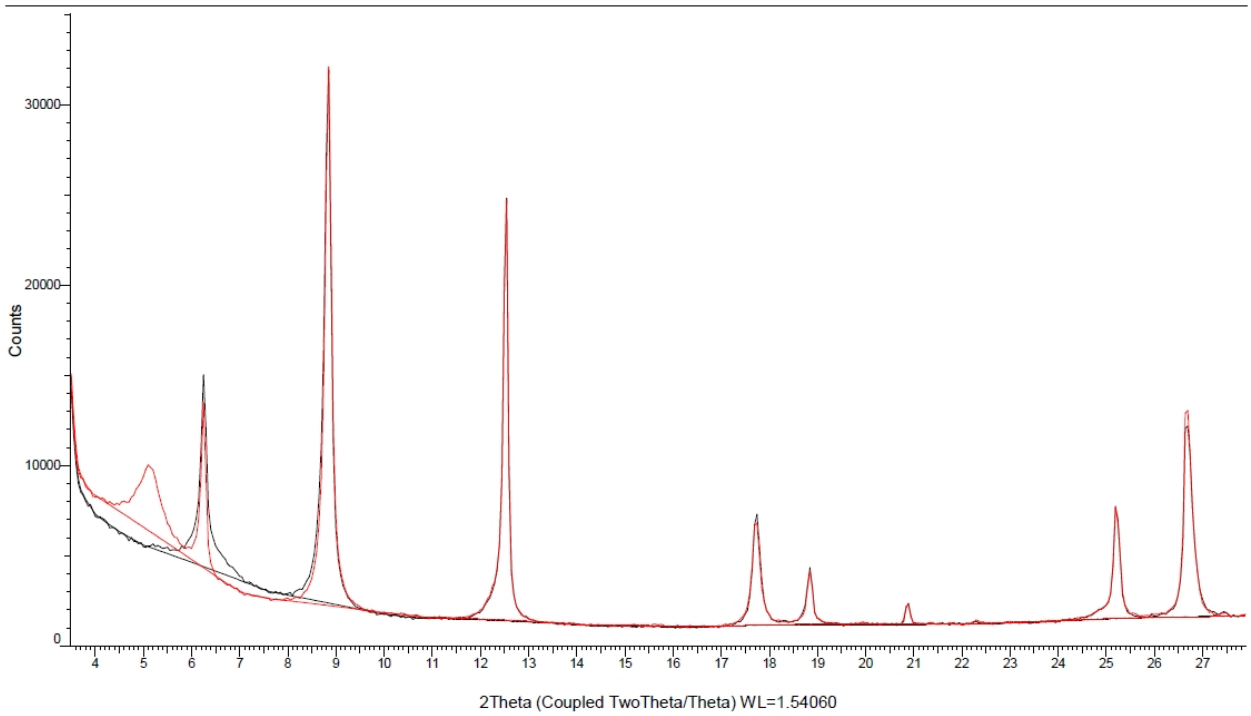

EAG12051

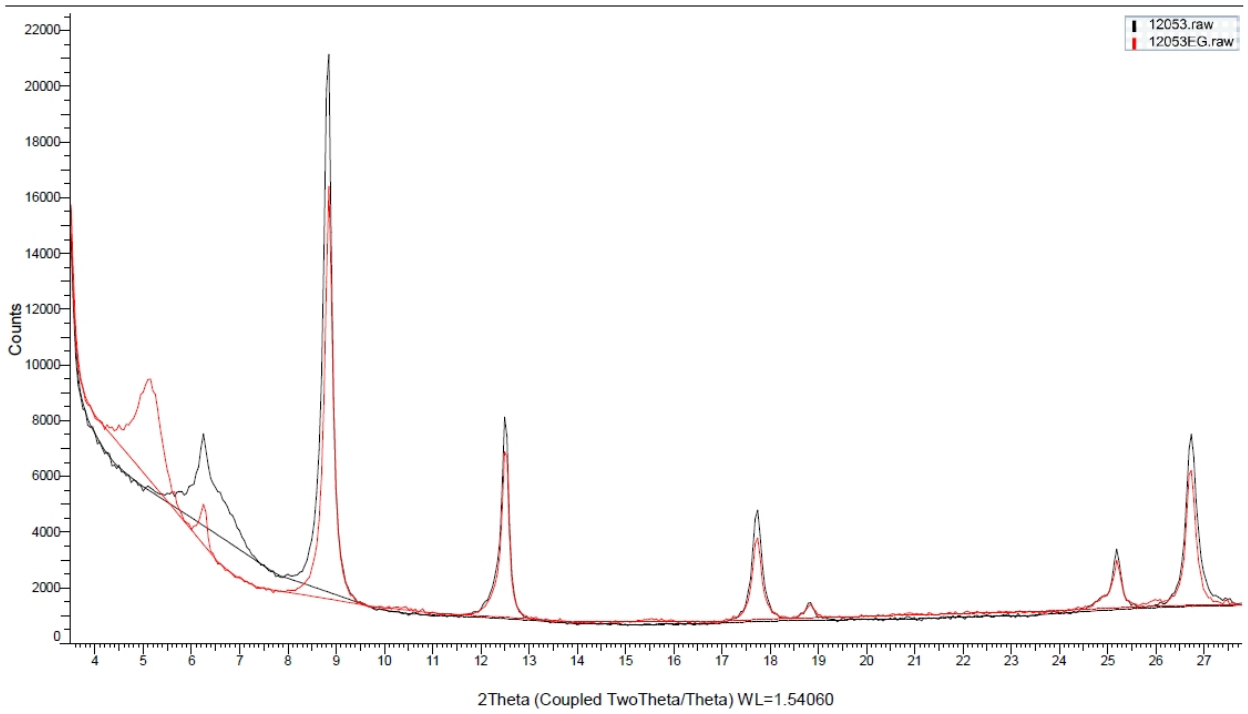

EAG12053

Figure C1 – XRD diffractograms of samples

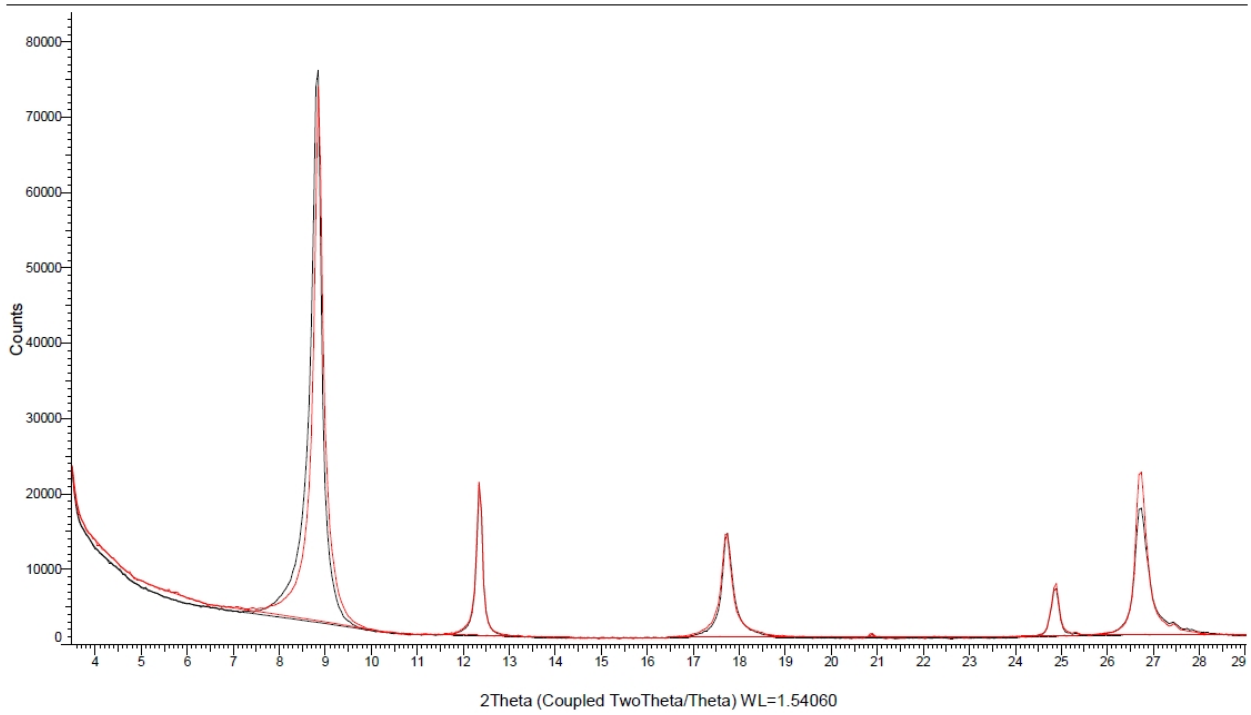

EAG12055

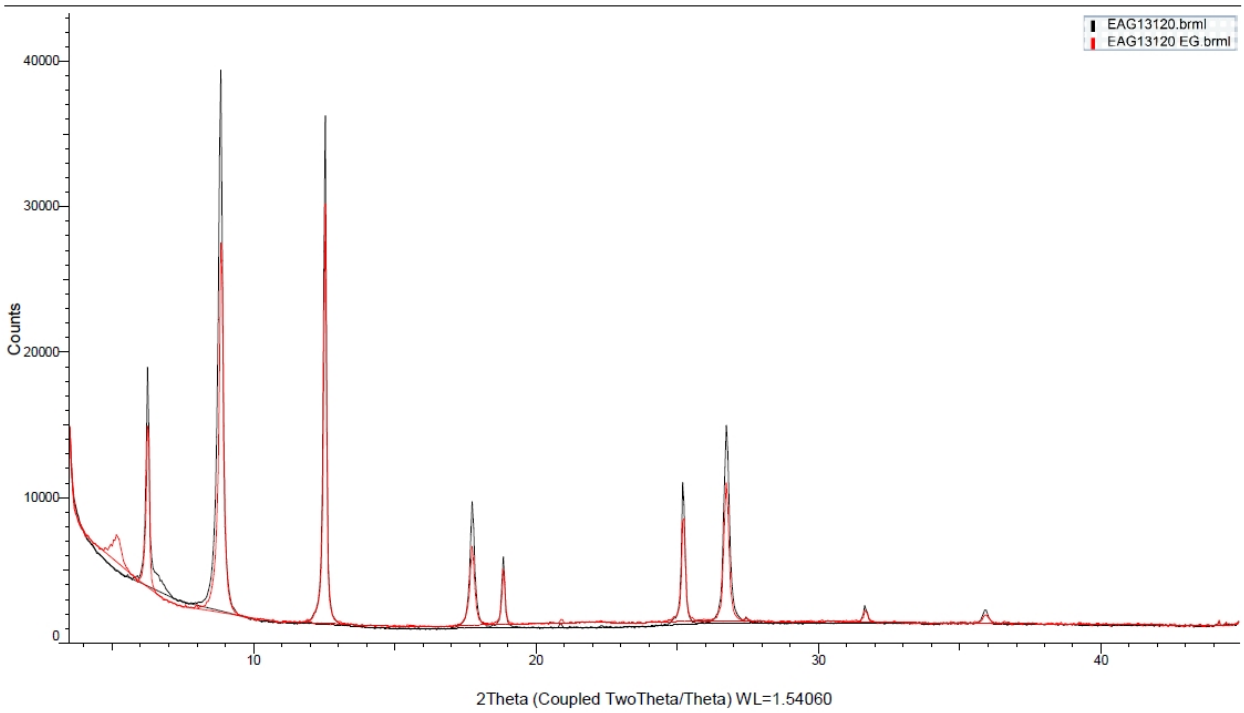

EAG13120

Figure C1 – XRD diffractograms of samples

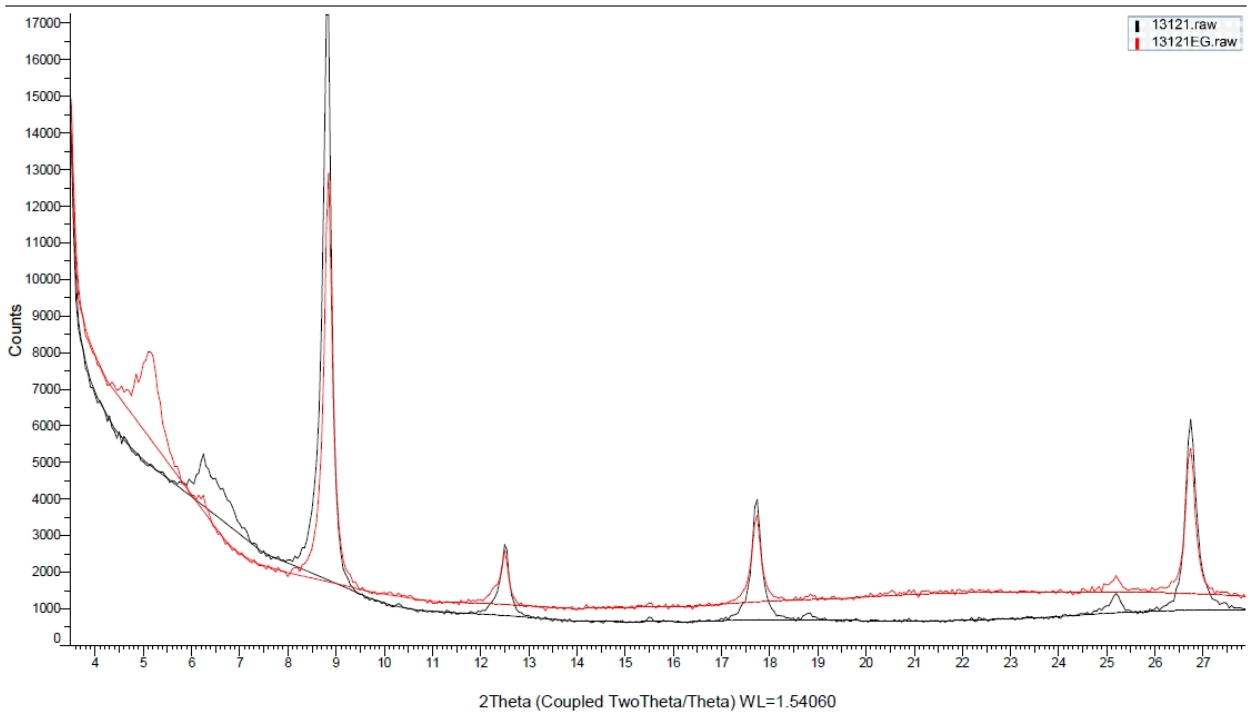

EAG13121

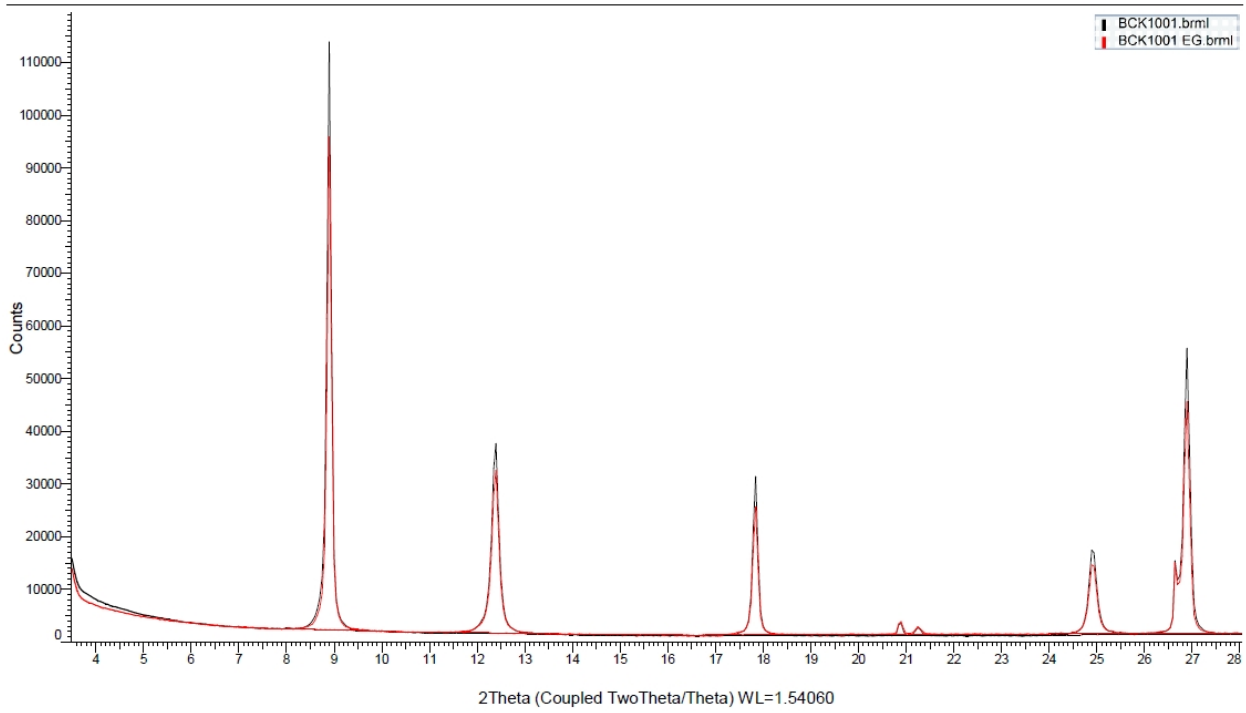

NZBCk1001

Figure C1 – XRD diffractograms of samples

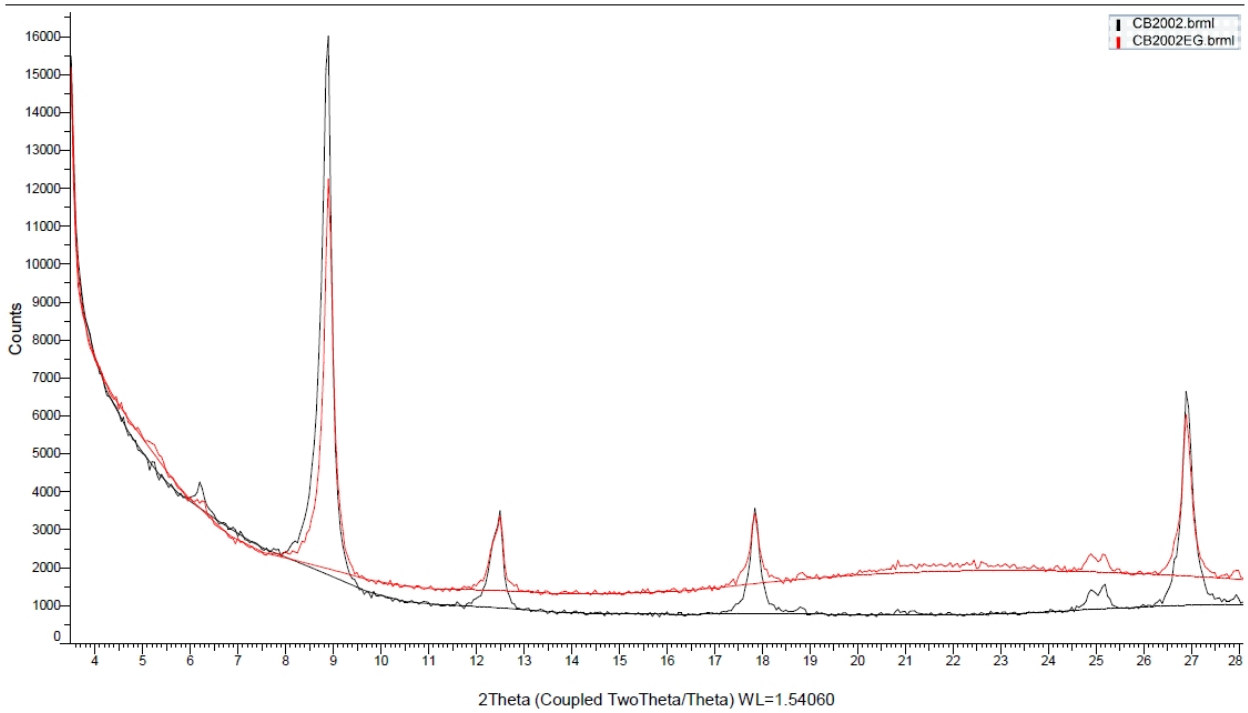

NZCB2002

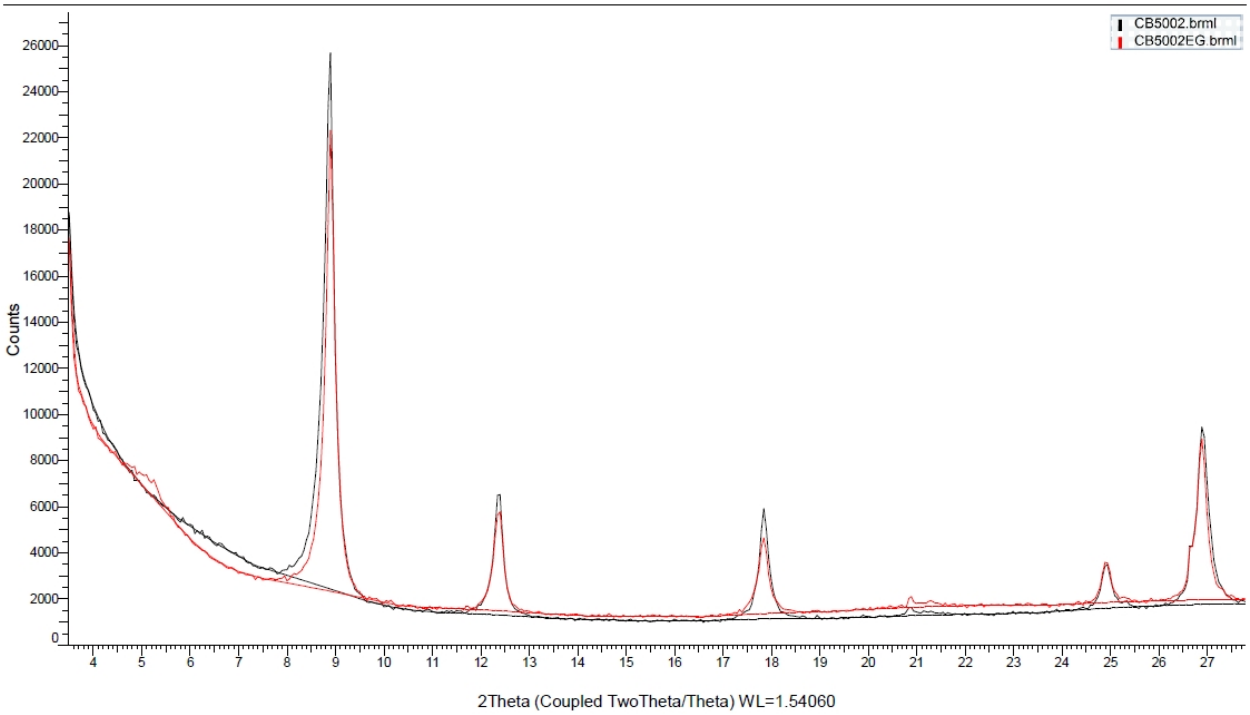

NZCB5002

Figure C1 – XRD diffractograms of samples

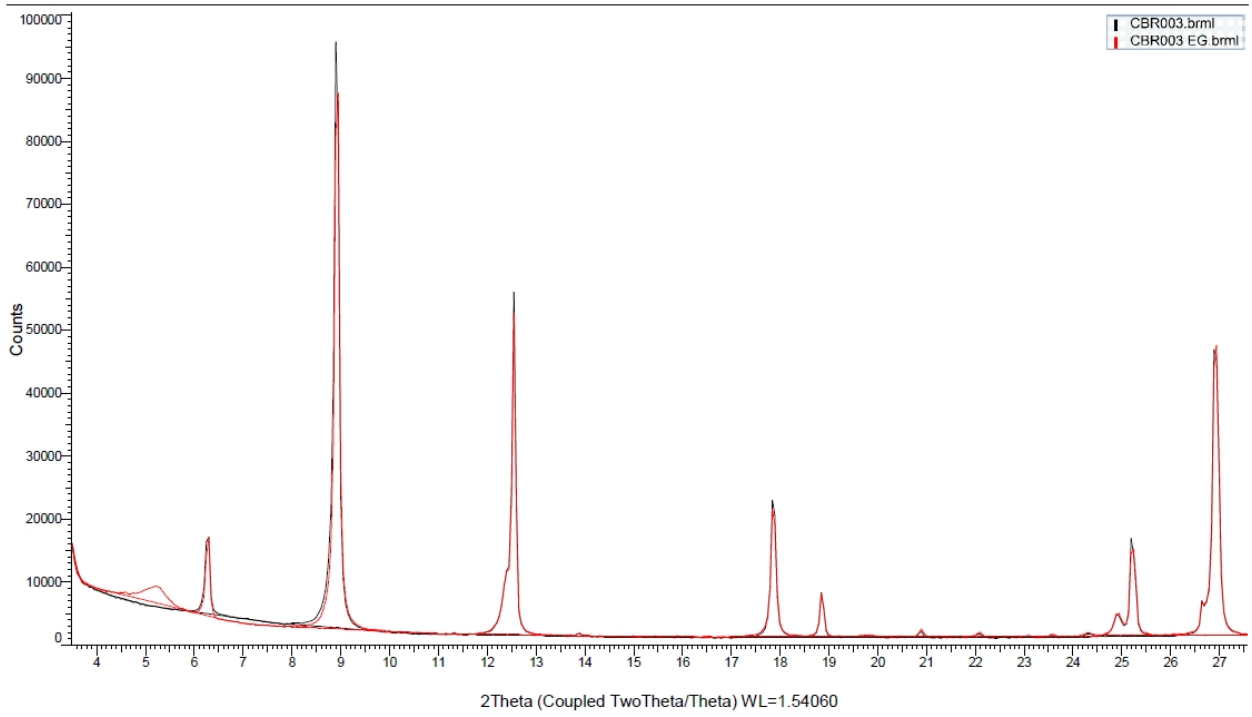

NZCBR003

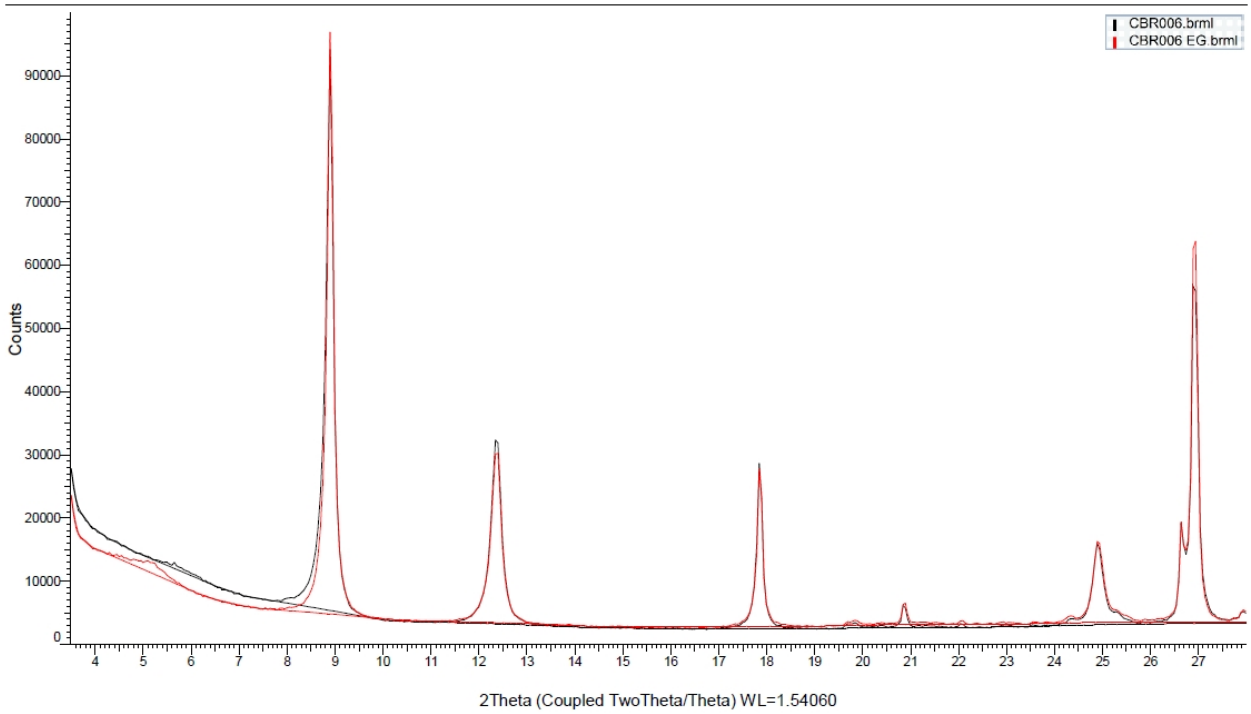

NZCB006

Figure C1 – XRD diffractograms of samples

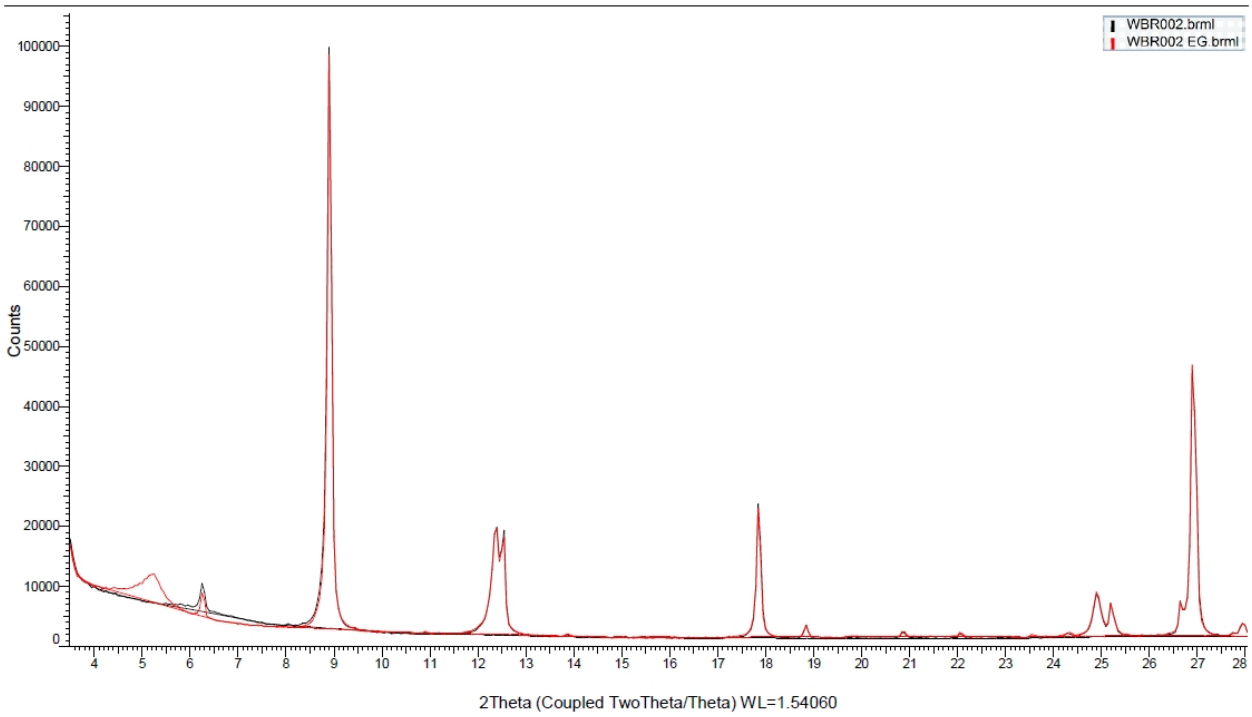

NZWBR002

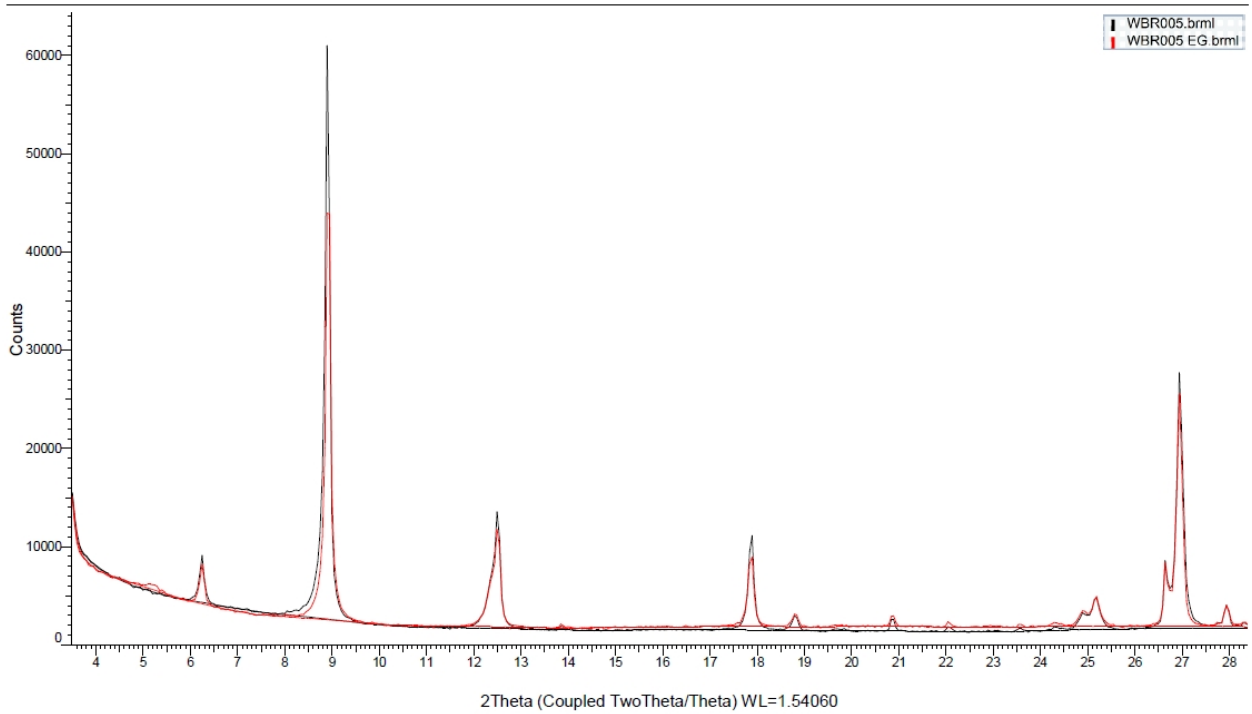

NZWBR005

Figure C1 – XRD diffractograms of samples

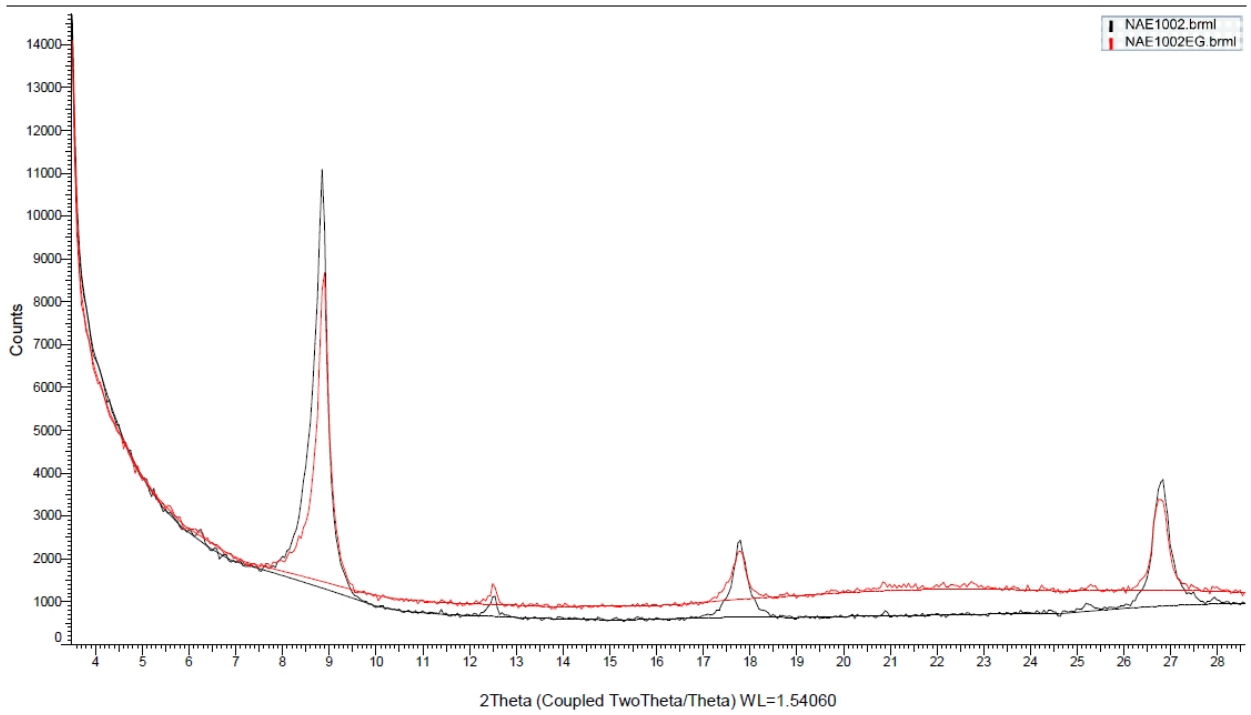

NNAE1002

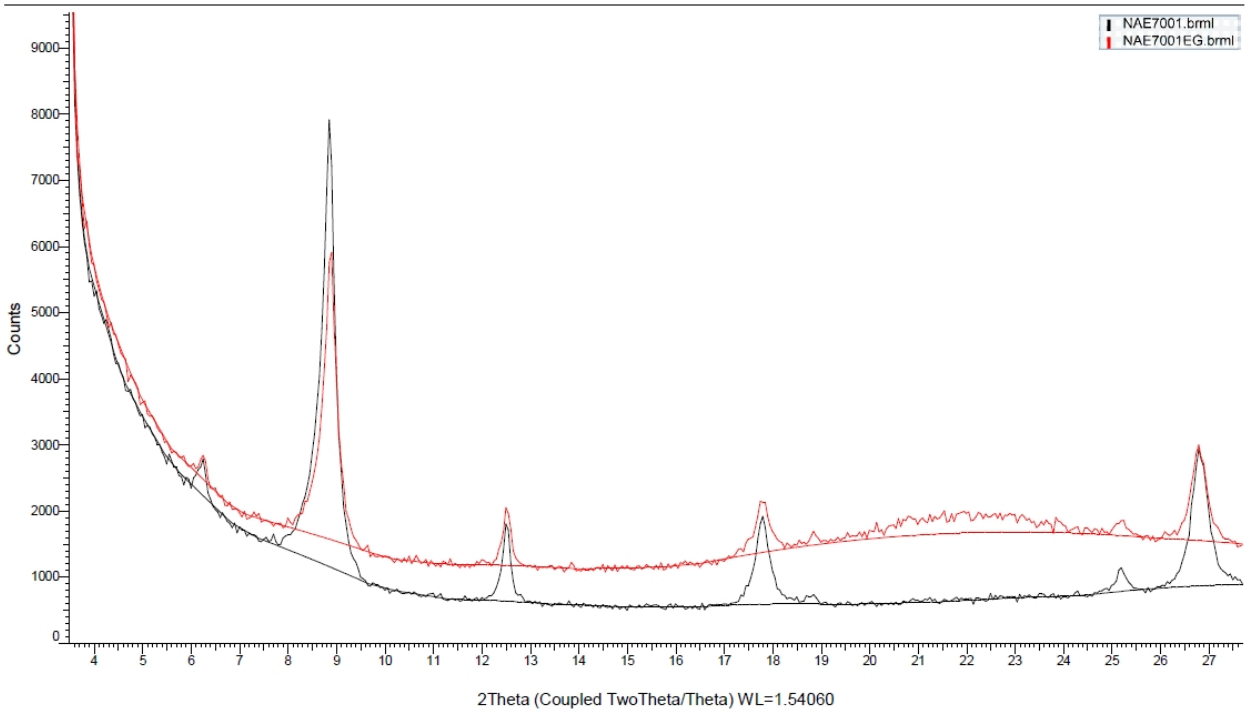

NNAE7001

Figure C1 – XRD diffractograms of samples

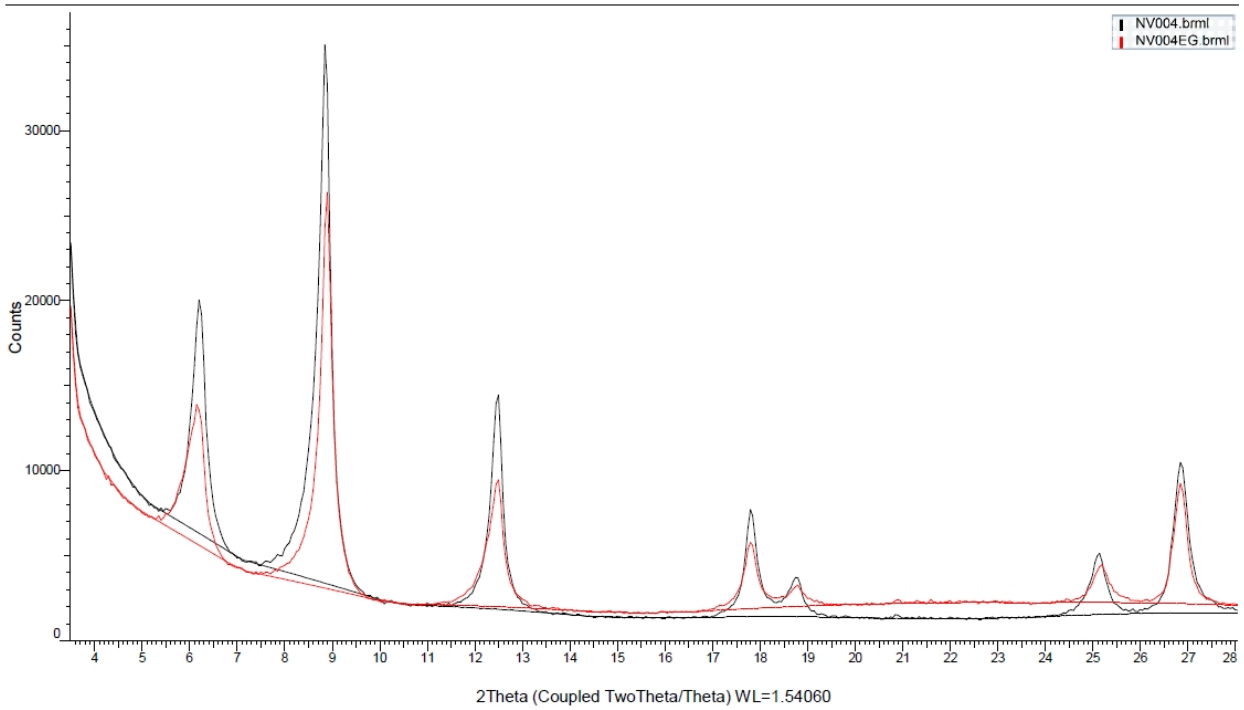

NV001

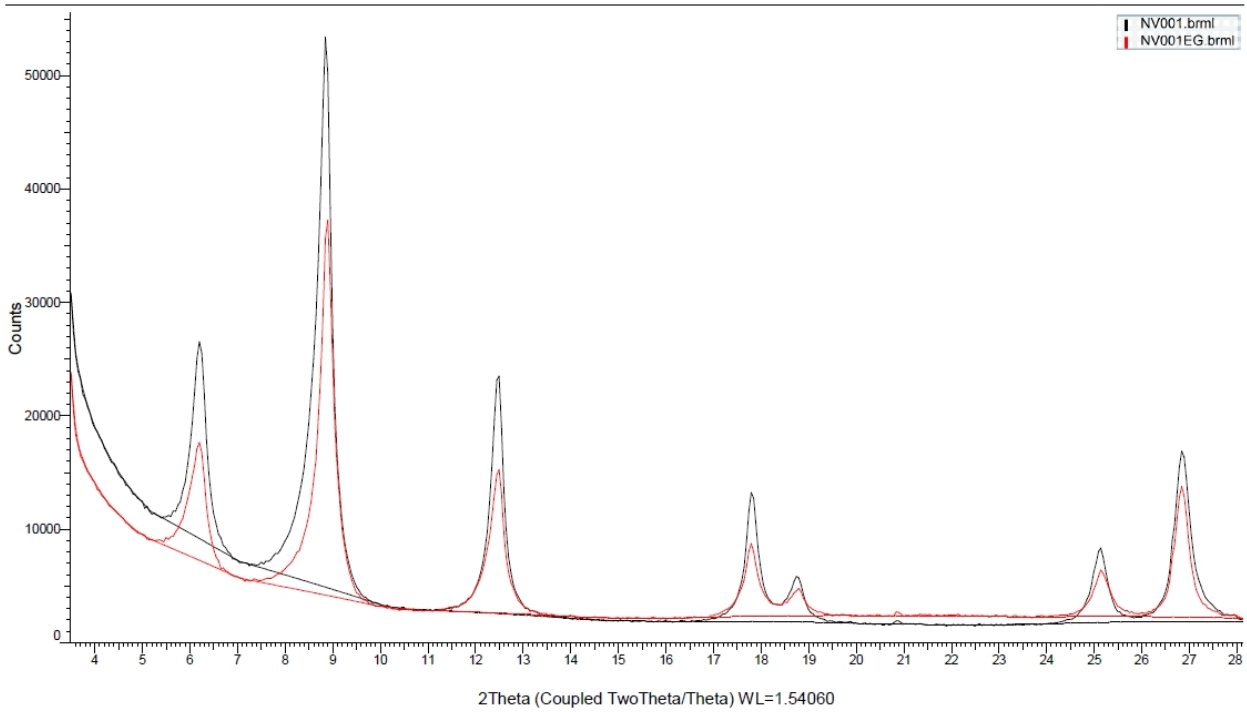

NV004

Appendix D

1. Sample collection and preparation

Sampling for δ13C and δ18O stable isotopes analysis was carried out with consistent spacing through Shale Quarry S, as well as the nearby exposure of alum shales (Shale Quarry A) to the south-east of Shale Quarry S (Chapter 3, Fig. 4). Samples were taken from calcite vein material throughout the Sap Bon Formation and alum shales, along thrusts, bedding planes and in tension gashes. Samples were also taken from bioclastics in the Khao Khad Formation in Shale Quarry S, as well as the Phu Phe Formation in Shale Quarry A (Chapter 3, Fig. 4, 7C-D). In all, we collected 45 samples from Shale Quarry S; nine from the Khao Khad Formation below the Eagle Thrust (both packestone and veins were sampled), 15 of calcite veins in the shales. 97 samples were collected from Shale Quarry A, 93 of calcite veins in the alum shales and associated basaltic sills, and four from the overlying Phu Phe Formation packstones.

Sample material was powdered using a dental technicians drill, with 500-1000 mg of powdered calcite collected from each sample. Care was taken to ensure organic material and/or shales were not collected with the calcite. Optical microscopy of thin sections from 11 samples showed no dolomite present in any of the vein fill calcite samples.

2. Analysis

Stable isotope (δ18O and δ13C) measurements were performed on ~0.8 mg powders using continuous-flow isotope-ratio mass spectrometry. Samples were weighed using a high-precision Mettler analytical balance. The vials (with piercable septum caps) were placed onto a hot block set to 70 degrees Celsius which was integrated with a helium purging system. Each vial was purged with helium to remove ambient air using a double-holed needle. The vials were then acidified using 105% orthophosphoric acid. Measurements were made on the evolved CO2 gas from the acid digestion using an Analytical Precision AP2003 at the School of Geography, The University of Melbourne. Results were normalized to the Vienna Pee Dee Belemnite scale using an internal working standard of Carrara Marble (NEW1), which was previously calibrated against the international standards of NBS18 and NBS19. Mean analytical precision for both δ18O and δ13C is better than 0.1‰.

Table D1 – Results of stable isotopes analysis

Sample	δ18O	δ13C	Sample	δ18O	δ13C
EAG12-001	-6.98	4.79	EAG13018	-10.73	1.14
EAG12-002	-7.42	4.91	EAG13019	-10.83	3.17
EAG12-003	-6.8	4.39	EAG13020	-10.63	2.90
EAG12-004	-8.68	4.68	EAG13021	-10.64	4.00
EAG12-005	-9.33	4.92	EAG13022	-10.28	4.32
EAG12-006	-9.24	3.23	EAG13023	-10.24	4.47
EAG12-007	-13.51	2.73	EAG13024	-10.73	4.94
EAG12-011	-11.29	3.05	EAG13025	-12.98	4.54
EAG12-012	-11.12	3.02	EAG13026	-9.87	4.50
EAG12-015	-9.8	3.22	EAG13028	-11.14	4.85
EAG12-021	-10.69	2.24	EAG13029	-10.28	4.56
EAG12-022	-10.66	1.29	EAG13030	-10.84	0.49
EAG12-024	-11.17	1.42	EAG13031	-10.04	0.22
EAG12-025	-11.13	1.53	EAG13032	-11.21	3.19
EAG12-028	-11.4	1.64	EAG13033	-11.06	2.94
EAG12-029	-11.32	1.87	EAG13034	-11.16	4.27
EAG12-030	-11.41	1.5	EAG13035	-11.96	0.52
EAG12-034	-11.43	1.2	EAG13037	-11.15	4.04
EAG12-037	-10.97	1.4	EAG13039	-10.70	3.64
EAG12-038	-9.44	4.93	EAG13040	-11.65	4.08
EAG12-039	-9.01	4.2	EAG13041	-11.53	3.23
EAG12-040	-10.88	3.38	EAG13042	-11.38	3.77
EAG12-043	-11.14	1.94	EAG13043	-11.48	4.07
EAG12-044	-10.9	1.84	EAG13044	-11.35	2.71
EAG12-048	-11.55	2.18	EAG13045	-11.52	1.95
EAG12-049	-11.68	1.72	EAG13046	-11.50	3.81
EAG12-052	-11.41	1.27	EAG13047	-11.78	4.18
EAG12-056	-9.93	1.68	EAG13048	-11.69	4.12
EAG12-058	-10.4	1.94	EAG13049	-11.56	4.03
EAG12-059	-8.13	4.39	EAG13050	-12.06	4.14
EAG12-060	-7.97	4.19	EAG13051	-11.55	3.80
EAG12-061	-9.4	3.48	EAG13052	-11.30	4.14
EAG12-062	-9.1	2.78	EAG13053	-12.67	4.63
EAG13001	-7.47	4.68	EAG13054	-9.93	4.69
EAG13002	-7.90	4.60	EAG13055	-11.51	4.68
EAG13003	-7.84	4.68	EAG13056	-10.13	4.44
EAG13004	-7.76	4.76	EAG13057	-9.84	4.39
EAG13005	-11.63	3.84	EAG13058	-10.64	4.72
EAG13007A	-11.07	0.62	EAG13060	-11.17	4.31
EAG13007B	-10.95	1.17	EAG13060Y	-9.87	4.16
EAG13007C	-10.82	1.24	EAG13061	-11.46	4.41
EAG13008	-10.87	-0.27	EAG13062	-11.27	3.70
EAG13009	-11.06	-1.39	EAG13063	-11.48	3.72
EAG13010	-11.26	-0.87	EAG13064	-15.96	2.21
EAG13011	-10.91	0.49	EAG13065	-11.44	4.35
EAG13012A	-12.19	1.17	EAG13068	-11.41	3.77
EAG13012B	-12.75	0.57	EAG13070	-8.60	4.49
EAG13013	-11.55	1.67	EAG13071	-11.04	3.97
EAG13014	-12.19	1.27	EAG13072	-8.85	4.38
EAG13015	-11.88	1.90	EAG13073	-16.02	4.39
EAG13016	-17.30	0.11	EAG13074	-11.63	3.05
EAG13017	-11.03	1.50	EAG13075	-13.10	4.37
EAG13077	-14.65	4.62			

Table D1 – Results of stable isotopes analysis

EAG13078	-7.97	3.70
EAG13079	-10.00	3.51
EAG13080	-11.50	4.08
EAG13081	-12.48	3.71
EAG13082	-11.44	4.23
EAG13083	-9.07	3.73
EAG13084	-8.62	3.74
EAG13086A	-6.32	2.80
EAG13086B	-8.41	4.74
EAG13087	-9.80	2.98
EAG13088	-7.49	3.29
EAG13090	-14.34	2.62
EAG13091	-14.24	3.18
EAG13093	-12.01	3.31
EAG13094	-15.64	2.86
EAG13095	-9.07	2.61
EAG13096	-16.68	2.42
EAG13097	-6.99	4.68
EAG13099	-10.50	4.82
EAG13100	-7.68	4.60

Appendix E

1. Total organic carbon content analysis method

To acquire total organic carbon content values samples were analysed using a PE 2400 CHNS elemental analyser. This gave the total amount of carbon (as a weight %). Analysis using acid digestion and a pressure calcimeter was then used to analyse the amount of inorganic ($CaCO_3$) present in the sample. The original source rock TOC was estimated using the calculator of *Pepper, A. S., and P. J. Corvi, 1995, Simple kinetic models of petroleum formation. Part I: oil and gas generation from kerogen : Marine and Petroleum Geology, v. 12, pp.291-319.*

Table E1 – Results of total organic carbon content analysis

Sample	Location*	TOC (%)	S1	S2	HI	Original rock TOC (%)
EAG12008	Shale Quarry S[1]	**3.978**	0.04	0.04	1.00563	4.01
EAG12009	Shale Quarry S	**0.335**	0.03	0.04	11.9335	0.37
EAG12010	Shale Quarry S	**0.362**	0.04	0.04	0.887	3.62
EAG12012	Shale Quarry S	**3.277**	0.05	0.03	0.91558	3.30
EAG12016	Shale Quarry S	**1.400**	0.04	0.03	3.887	1.44
EAG12018	Shale Quarry S	**2.971**	0.04	0.04	3.4011	2.86
EAG12019	Shale Quarry S	**2.948**	0.02	0.02	0.67843	2.96
EAG12020	Shale Quarry S	**1.580**	0.02	0.02	0.11	1.58
EAG12023	Shale Quarry S	**1.890**	0.05	0.04	1.091	1.90
EAG12024	Shale Quarry S	**1.976**	0.03	0.05	2.53026	2.01
EAG12027	Shale Quarry S	**1.254**	0.09	0.1	7.97632	1.33
EAG12028	Shale Quarry S	**1.612**	0.1	0.17	10.5485	1.74
EAG12031	Shale Quarry S	**1.450**	0.04	0.04	2.7568	1.48
EAG12032	Shale Quarry S	**1.839**	0.02	0.01	0.54375	1.85
EAG12033	Shale Quarry S	**0.959**	0.01	0.01	1.04254	0.97
EAG12034	Shale Quarry S	**1.038**	0.03	0.02	1.92714	1.05
EAG12035	Shale Quarry S	**2.402**	0.02	0.01	0.41625	2.41
EAG12036	Shale Quarry S	**1.665**	0.03	0.08	4.80419	1.73
EAG12041	Shale Quarry S	**0.061**	0.02	0.07	114.116	0.47
EAG12042	Shale Quarry S	**1.225**	0.03	0.02	1.63208	1.24
EAG12044	Shale Quarry S	**0.310**	0.03	0.07	22.6013	0.37
EAG12045	Shale Quarry S	**1.040**	0.02	0.01	0.96136	1.05
EAG12046	Shale Quarry S	**1.439**	0.02	0.02	1.3897	1.45
EAG12047	Shale Quarry S	**0.721**	0.04	0.03	4.16195	0.74
EAG12048	Shale Quarry S	**1.429**	0.07	0.15	10.4957	1.55
EAG12049	Shale Quarry S	**1.898**	0.06	0.09	4.74189	1.96
EAG12053	Shale Quarry S	**1.637**	0.03	0.01	0.61095	1.64
SQ13016	Highway 21[1]	**11.74**	-	-	-	-
SQ13001	Highway 21	**3.45**	-	-	-	-
SQ13006	Highway 21	**7.16**	-	-	-	-
SQ13011	Highway 21	**9.83**	-	-	-	-
SQ13022	Highway 21	**13.22**	-	-	-	-
NNAE3002	Nærsnes[2]	**0.74**	-	-	-	-
NNAE1002	Nærsnes	**0.26**	-	-	-	-
NNAE7001	Nærsnes	**0.18**	-	-	-	-
NV001	Hole, Ringerike[2]	**1.41**	-	-	-	-
NV004	Hole, Ringerike	**1.06**	-	-	-	-
NZBCK1001	Bull Creek[3]	**0.83**	-	-	-	-
NZCB2002	Chrystalls Beach	**1.77**	-	-	-	-
NZCB4002	Chrystalls Beach	**3.35**	-	-	-	-
NZCB5002	Chrystalls Beach	**0.26**	-	-	-	-
NZCB5008	Chrystalls Beach	**0.31**	-	-	-	-
NZCBR003	Chrystalls Beach	**0.24**	-	-	-	-
NZCBR006	Chrystalls Beach	**0.18**	-	-	-	-
NZQPR1001	Quoin Point	**0.03**	-	-	-	-
NZWRB002	Watsons Beach	**0.13**	-	-	-	-
NZWRB005	Bull Creek	**0.14**	-	-	-	-

[1] Chapter 3, Fig. 1; [2] Chapter 4, Fig. 3; [3] Chapter 4, Fig. 2.

Appendix F

1. Fry method

In the absence of suitable marker grains or other ovoids, the Fry method of point-to-point strain analysis can be used to determine the two-dimensional geological strain recorded by a material. This method is based on the underlying assumption that in the grain centres of the undeformed protolith have an essentially normal distribution. This arises as a result of grains having a characteristic initial size, meaning the distances between grain centres are controlled by the geometric constraints of the packing of the grains. When this distribution of grains are deformed, the relative distances between grain centres increases in the direction of the long (S1) axis of the strain ellipse, and decreases in the direction of the short axis (S2). The Fry method is a simple, practical method for finding the best fit solution to the strain ellipse. Usually this method is undertaken by hand through marking and numbering the particle centres. A central reference point is marked on tracing paper and the positions of each point traced onto the overlay. This process is repeated for all other points on the base sheet. Around the central reference point a region with very low point concentration will be visible. This vacancy arises from the fact that any two original particles cannot lie closer than the sum of their radii. Finally the elliptical distribution of point densities allows the shape and orientation of the strain ellipse to be determined. In this study a grain centre mapping software package (GeoFryPlots, developed by Rod Holcombe, see Chapter 4) was employed. This program allows the user to manual identify grain centres while producing a plot of centre-to-centre distances. The user may then fit a strain ellipse to the centre vacancy (Chapter 4, Fig. 5).

All samples were orientated in the field and thin sections were cut parallel to lineation (X-axis) and perpendicular to foliation (XY plane) in order to assess finite strain in the XZ plane of the finite strain ellipsoid, providing the greatest change in strain, and in the direction of transport. Each thin section was photographed under an optical microscope with five photographs at x10 zoom taken of each 20x40 mm thin section and analysed using the software GeoFryplots. Two analyses were run on each photograph for a total of 10 per sample, with each analysis using between 80-200 grains. The 10 RS values for the strain ellipse were then averaged for each sample and a standard error calculated.

Table F1 – Results of strain analysis

Sample ID	Rs measurements										Avg.	St. dev.	SE
EAG12008	1.92	2.24	2.33	1.93	1.91	2.10	2.08	1.99	2.20	1.86	**2.056**	0.152	0.048
EAG12016	1.91	1.51	1.54	1.57	1.59	1.71	1.73	1.55	1.7	1.75	**1.656**	0.119	0.038
EAG12019	1.75	1.74	1.82	1.9	1.77	1.88	1.82	1.72	1.72	1.7	**1.782**	0.066	0.021
EAG12033	1.5	1.76	1.6	1.62	1.59	1.71	1.66	1.51	1.67	1.66	**1.628**	0.078	0.025
EAG12035	1.52	1.31	1.37	1.39	1.41	1.5	1.32	1.36	1.36	1.36	**1.39**	0.066	0.021
EAG12042	1.81	1.8	1.72	1.84	1.79	1.77	1.85	1.83	1.86	1.93	**1.82**	0.054	0.017
EAG12053	1.94	2.06	1.78	1.99	1.95	1.99	1.81	1.97	1.99	1.94	**1.942**	0.081	0.026
EAG13120	2.21	1.88	1.98	2.04	2.01	2.11	1.93	1.91	2.06	1.91	**2.004**	0.099	0.031
EAG13121	1.3	1.6	1.46	1.43	1.49	1.55	1.39	1.41	1.53	1.58	**1.474**	0.089	0.028
NNAE102	1.29	1.13	1.21	1.23	1.22	1.27	1.19	1.2	1.19	1.21	**1.214**	0.042	0.013
NNAE701	1.14	1.17	1.1	1.14	1.14	1.11	1.1	1.15	1.14	1.09	**1.128**	0.025	0.008
NV01	1.01	1	1.06	1.04	1.03	1	1.01	1.05	1.04	1.02	**1.026**	0.020	0.006
NV04	1.05	1.03	1.02	1.02	1.04	1.03	1.01	1.04	1.06	1.06	**1.036**	0.016	0.005
NzBCk01	2.79	2.91	2.63	2.88	2.78	2.81	2.77	2.76	2.81	2.72	**2.786**	0.074	0.023
NZCB202	1.77	1.7	1.76	1.71	1.79	1.65	1.66	1.72	1.76	1.64	**1.716**	0.051	0.016
NZCB502	1.28	1.30	1.38	1.36	1.30	1.37	1.29	1.36	1.40	1.40	**1.344**	0.044	0.014
NZCBR03	2.62	2.50	2.56	2.41	2.40	2.50	2.48	2.61	2.54	2.44	**2.506**	0.073	0.023
NZCBR06	2.2	2.15	2.15	2.05	2.19	2.11	2.17	2.06	2.11	2.09	**2.128**	0.050	0.016
NZWBR02	2.52	2.46	2.38	2.34	2.44	2.51	2.36	2.41	2.43	2.45	**2.43**	0.056	0.018
NZWBR05	2.65	2.41	2.48	2.58	2.51	2.46	2.66	2.42	2.43	2.36	**2.496**	0.098	0.031

SE = Standard error of the mean

Appendix G

1. QEMSCAN method

The QEMSCAN system located at the Ian Wark Research Institute integrates the Zeiss Evo scanning electron microscope with two Bruker Silicon Drift Detectors (SDD) and iDiscover software. This fully automated instrument provides the capabilities for rapid characterisation of minerals and non-crystalline phases with distinct elemental composition. The system is able to measure thousands of points on a sample within seconds and display compositional images.

The thin sections were measured with 10 µm spacing resolution using the Field Image method of the QEMSCAN measurements. In this form of analysis, each of the thin section was split into a grid. The analysed fields (1000 µm in size each) were then stitched into a single composite image allowing mineral associations to be visually represented for interpretation. In this study, a voltage of 25keV and a beam current of 5nA were used.

2. Mineral phase characterisation

During the QEMSCAN analyses, 1000 count X-ray spectra were collected from each analytical point and were automatically compared against the mineral phases present in the SIP (Species Identification Protocol). In the first part of the study, the SIP files were examined to see if all of the phases were identified correctly. A typical SIP list may have hundreds of entries which contain information on the BSE response, the elemental composition as well as the X-ray count rate information. Most of the mineral definitions are created based on analysis of standards. The SIP contains also the 'boundary phase' entries which refer to the EDX data collected from the boundaries between two (or more) intergrown phases. If 'unknown' minerals are present in the sample, the additional definitions are then created and the assumed chemical composition (based on the collected X-ray spectra) along with the density values are assigned to those entries.

In this study, the additional definition, named 'Porosity', was created to highlight voids and fractures observed in the analysed samples. It has to be noticed, that the Porosity in this case refers to the enclosed background illustrated in the two-dimensional image.

Figure G1 – Mapped areas of this sections

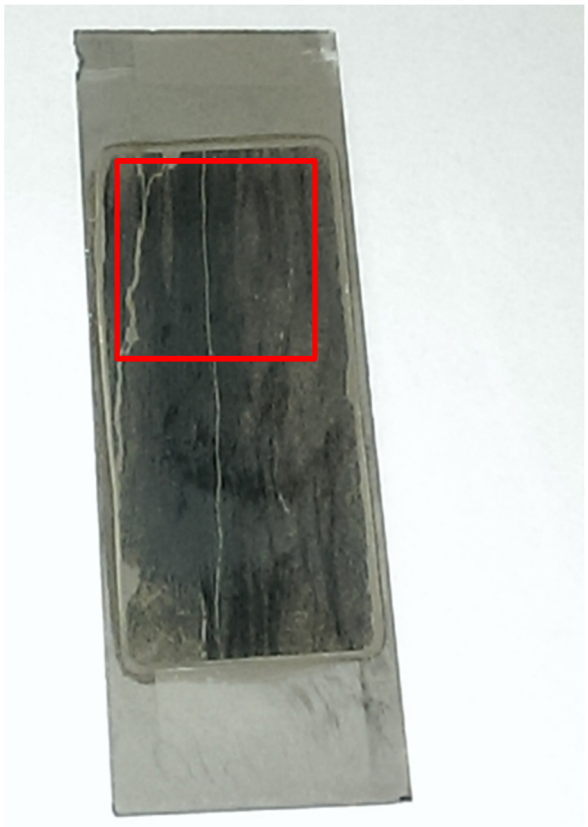

Sample EAG12016 (left) and EAG12019 (bottom) area mapped highlighted in red.

Table G1 – Scanned minerals

Sample	Description
Porosity	the enclosed background (2D)
Silicates (C)	Any silicates (quartz and aluminosilicate) with a high concentration of a carbon. The carbon peak might refer either to the organic material present in the samples (particularly in the thin section 016) or it is due to the coating of fine minerals present at the edge (including the fractures) of the thin sections.
Quartz	any SiO2
Illite/Muscovite	illite and/or muscovite
Pyrophyllite	assumed pyrophyllite (the thin section 016) and fine interfaces between silica, mica and feldspars
Biotite	biotite and/or phlogopite
Kaolinite	Kaolinite
Chlorite/Smectite	Mg-Fe chlorite and possible smectite
K Feldspars	any K-feldspars
Albite	Albite
Fe Ox/CO3	any Fe oxides, hydroxides and/or siderite
Carbonates	mostly ankerite - 016; mostly calcite/aragonite – 019
Ti(Fe) Oxides	mostly Ti oxides; possible Ti-Fe oxides in the thin section 13120
Al Oxides	any Al oxides, hydroxides
Pyrite	any Fe sulphides
Others*	traces of zircon, apatite, monazite, Ca Sulphates, chalcopyrite, sphalerite and other unclassified traces

Table G2 – Modal mineralogy

	Sample	13120	13121	019	016
Mineral Mass (%)	Porosity	0	0	0	0
	Silicates (C)	0.62	0.71	1.79	0.74
	Quartz	72.53	48.2	42.15	74.32
	Illite/Muscovite	12.46	39.47	44.39	13.68
	Pyrophyllite	6.08	2.32	0.84	1.33
	Biotite	0.03	2.01	1.87	1.56
	Kaolinite	1.06	0.8	0.41	0.38
	Chlorite/Smectite	0.54	0.99	0.82	1.42
	K Feldspars	0.3	0.73	0.9	0.54
	Albite	0.5	1.42	0.08	0.15
	Fe Ox/CO3	2.28	0.9	1.21	1.05
	Carbonates	0.08	0.3	3.55	3.82
	Ti(Fe) Oxides	1.5	1.25	1.32	0.8
	Al Oxides	1.87	0.36	0	0
	Pyrite	0.01	0.22	0.49	0.04
	Others	0.14	0.34	0.18	0.17
Mineral Volume(%)	Porosity	6.27	2.63	5.03	1.78
	Silicates (C)	0.64	0.75	1.85	0.8
	Quartz	69.68	48.61	41.54	74.6
	Illite/Muscovite	11.41	37.59	41.37	12.98
	Pyrophyllite	5.22	2.09	0.74	1.21
	Biotite	0.02	1.72	1.56	1.33
	Kaolinite	1.03	0.82	0.41	0.38
	Chlorite/Smectite	0.49	0.97	0.78	1.21
	K Feldspars	0.3	0.76	0.92	0.56
	Albite	0.47	1.42	0.07	0.15
	Fe Ox/CO3	1.77	0.69	0.96	0.87
	Carbonates	0.07	0.29	3.31	3.41
	Ti(Fe) Oxides	1.07	0.92	0.96	0.58
	Al Oxides	1.44	0.3	0	0
	Pyrite	0.01	0.15	0.36	0.03
	Others	0.1	0.29	0.13	0.11

Table G2 – Modal mineralogy

Calculated ESD Size (µm)	**Porosity**	24	32	24	31
	Silicates (C)	16	19	17	21
	Quartz	67	65	49	130
	Illite/Muscovite	20	43	42	28
	Pyrophyllite	16	16	16	21
	Biotite	15	18	16	18
	Kaolinite	16	17	21	22
	Chlorite/Smectite	15	20	19	20
	K Feldspars	15	15	15	15
	Albite	15	29	16	16
	Fe Ox/CO3	20	16	16	16
	Carbonates	15	18	35	44
	Ti(Fe) Oxides	16	18	17	19
	Al Oxides	22	22	18	31
	Pyrite	15	19	17	16
	Others	15	25	21	23

Figure G2 – Scan images from EAG12019

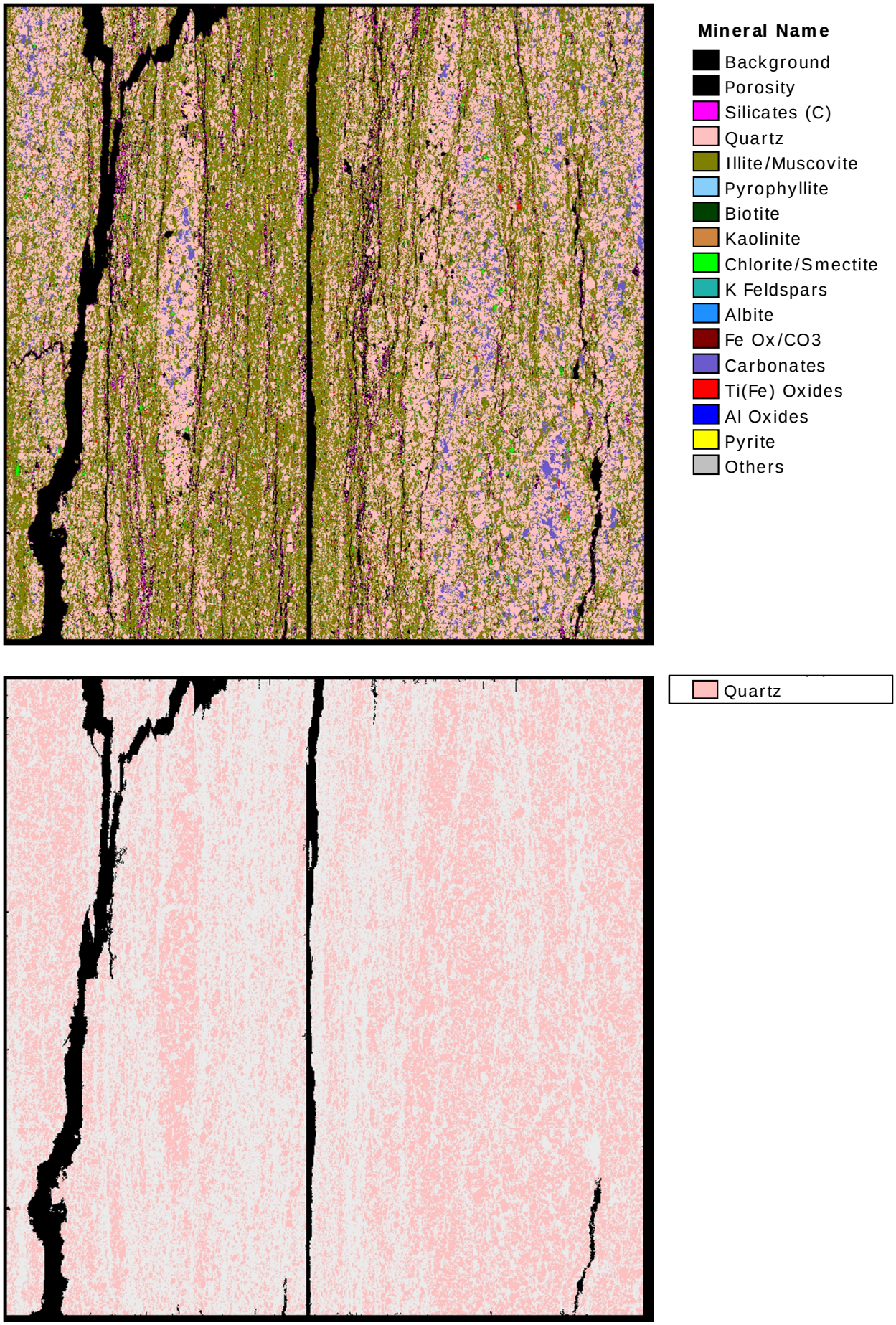

Figure G2 – Scan images from EAG12019

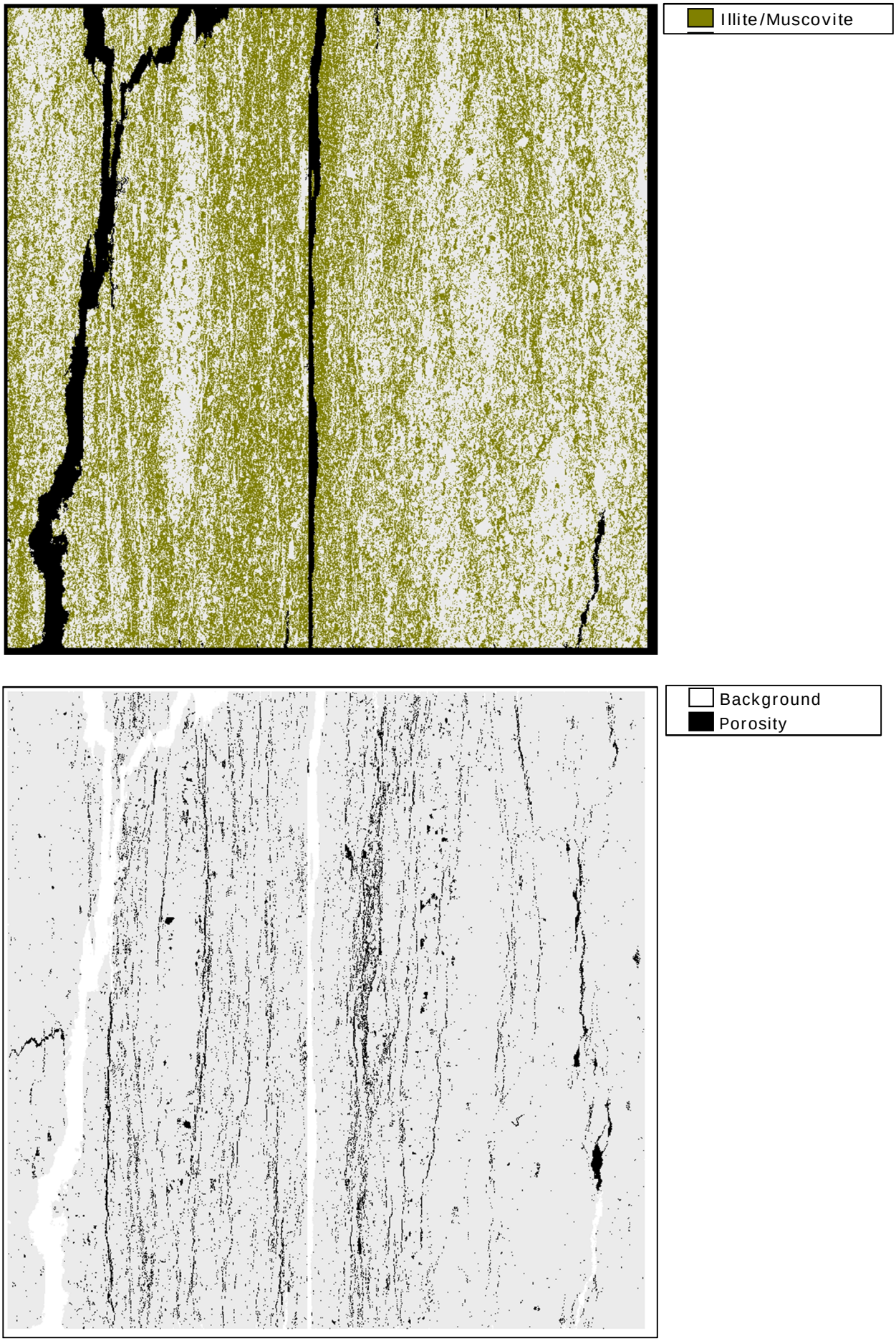

Figure G2 – Scan images from EAG12016

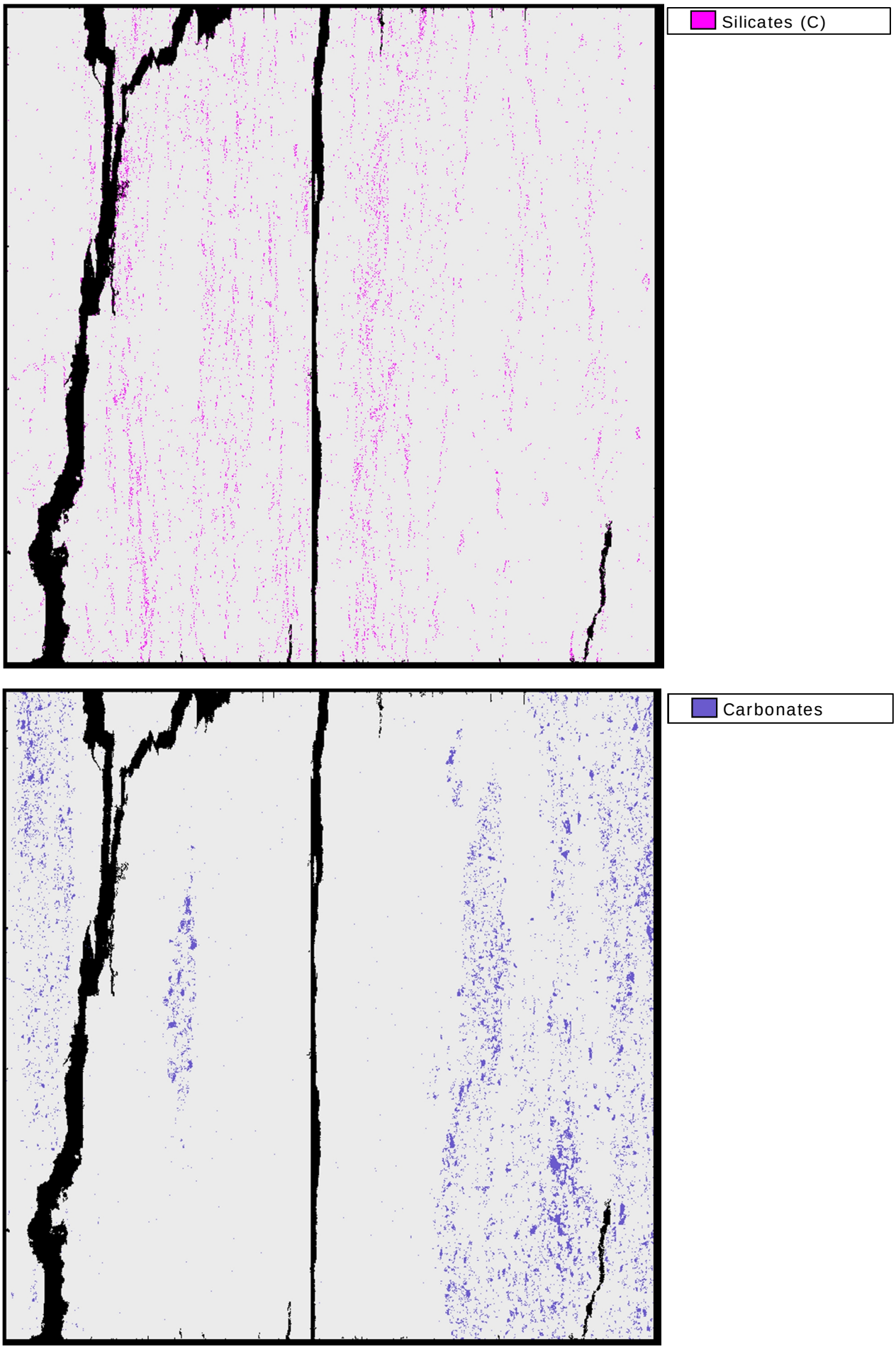

Figure G2 – Scan images from EAG12016

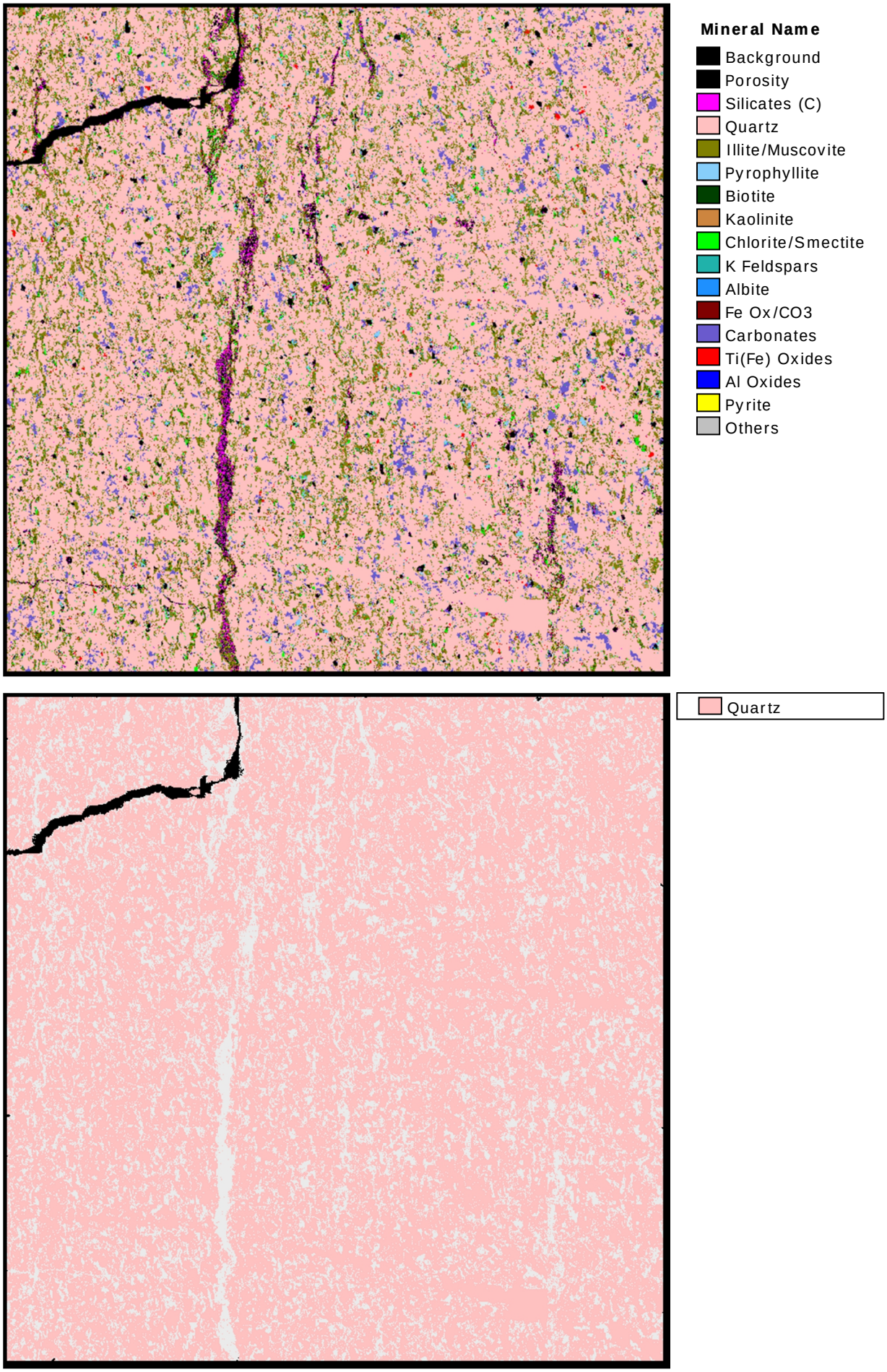

Figure G2 – Scan images from EAG12016

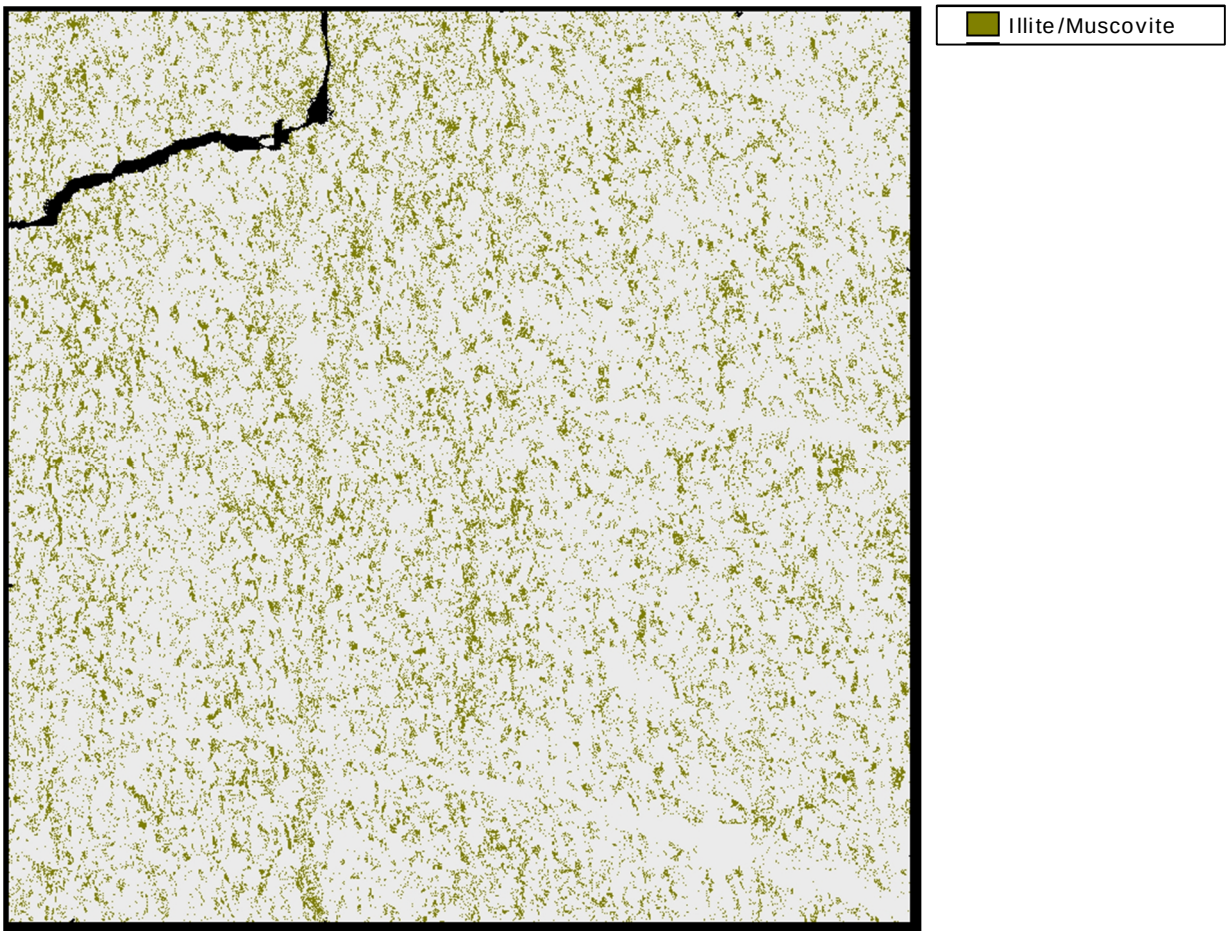

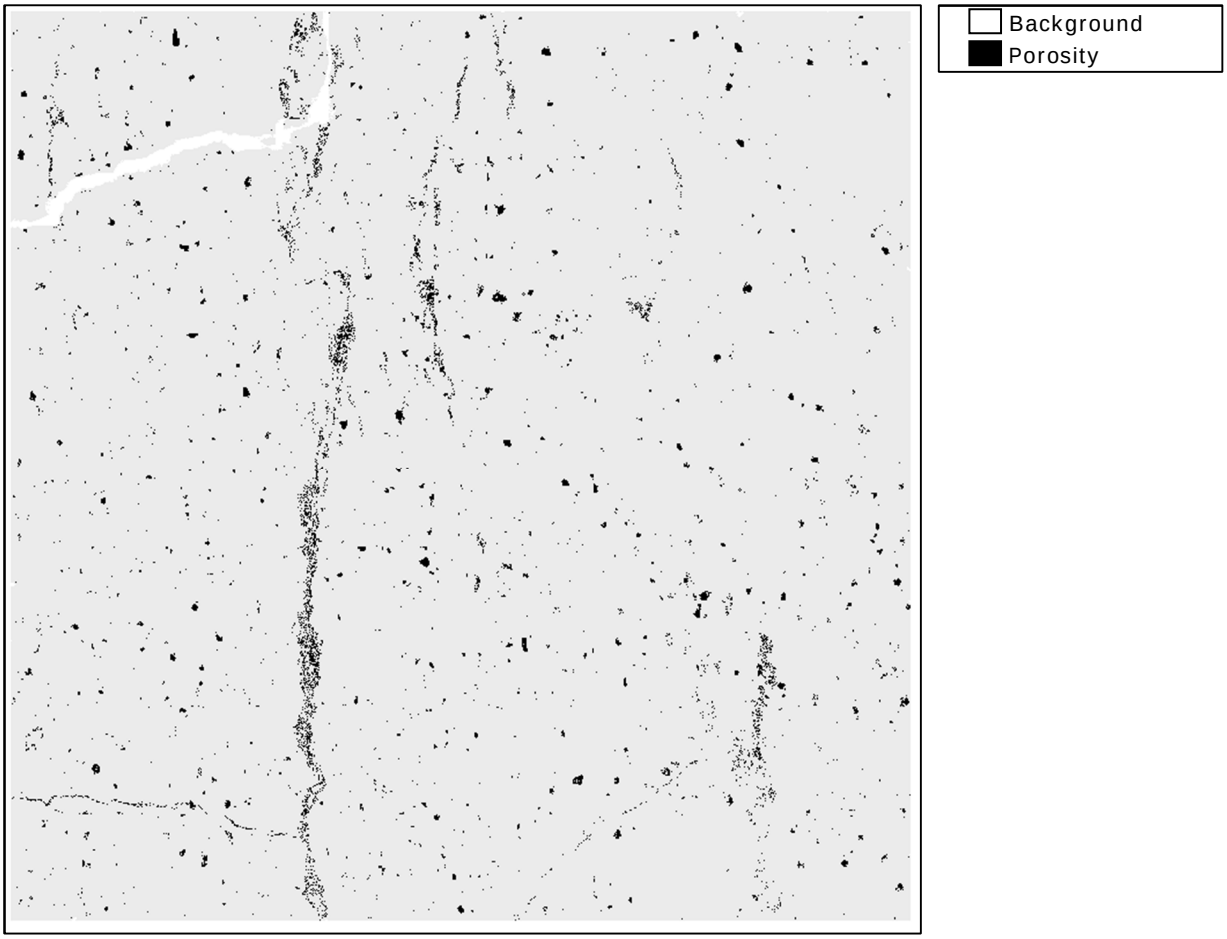

Figure G2 – Scan images from EAG12016

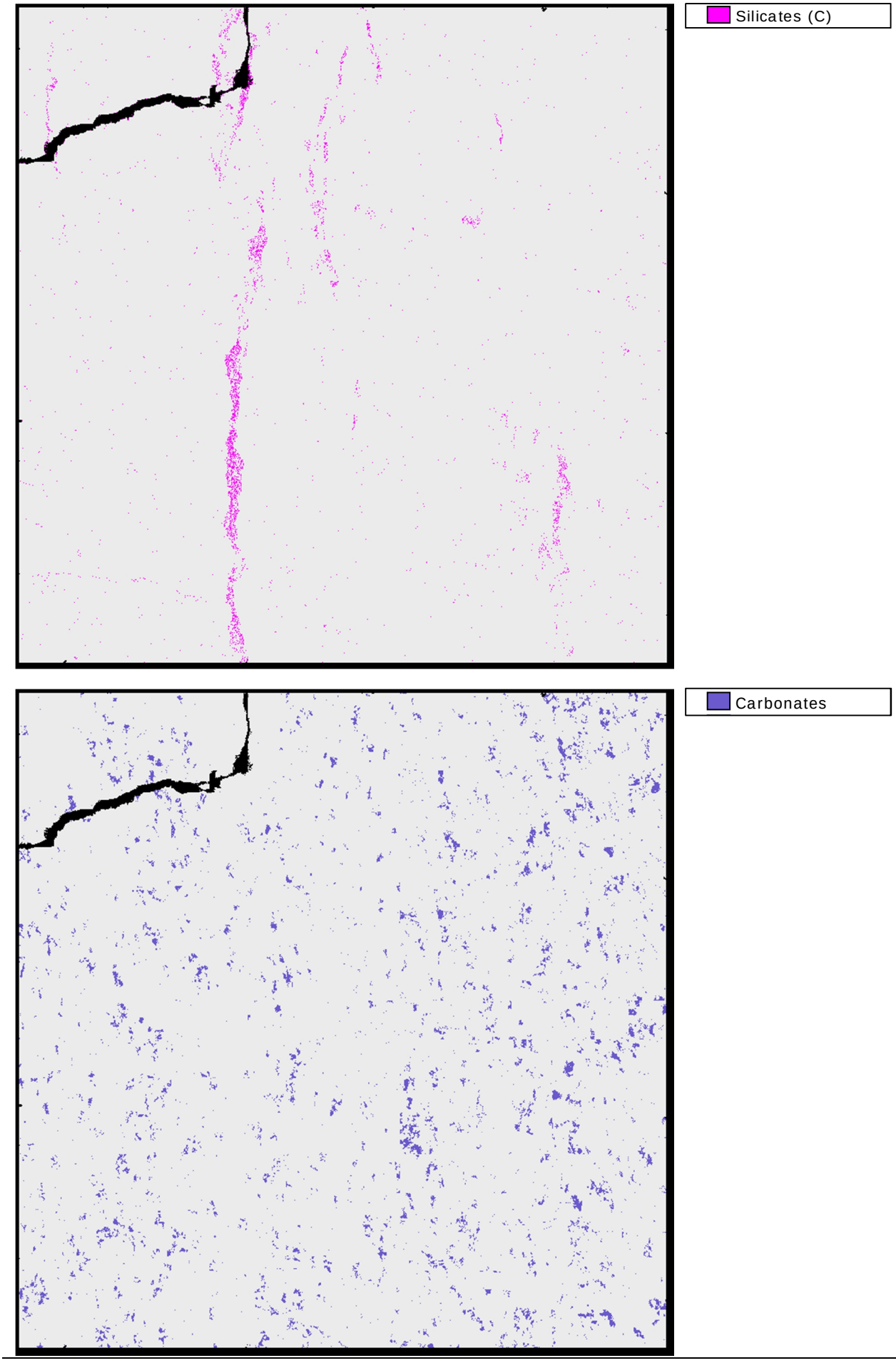

Appendix H

Document H – K-Ar dating

1. K-Ar dating method

All samples were provided to Horst Zwingmann and Andrew Todd of CSIRO ESRE Laboratory, 26 Dick Perry Ave, Kensington, WA 6151. Samples were disaggregated, prepared and analysed according to the method set out in *Zwingmann, Horst, and Neil Mancktelow. "Timing of Alpine fault gouges." Earth and Planetary Science Letters 223.3 (2004): 415-425.* The method is transcribed here, with edits where appropriate for the context of this study.

1. Sample preparation

Each sample consisted of ca. 150-300 g of fresh fault gouge and/or host rock material. Larger pieces were first crushed into chips <10 mm in size. Sample chips were then gently disaggregated by using a repetitive freezing and thawing technique to avoid artificial reduction of rock components and contamination of finer size fractions with relict K-bearing minerals (e.g. K-feldspar).

2. Dating procedure

K content was determined by atomic absorption. The pooled error of duplicate K determinations on several samples and standards is better than 2.0%. Samples were pre-heated under vacuum at 80 °C for several hours to reduce the amount of atmospheric Ar adsorbed onto the mineral surfaces during sample preparation. Ar was extracted from the mineral fractions by fusing samples using a low blank resistance furnace within a vacuum line serviced by an on-line ^{38}Ar spike pipette. The ^{38}Ar spike was calibrated against GA1550 biotite. The isotopic composition of the spiked Ar was measured with an on-line VG3600 mass spectrometer via Faraday cup. The released gases were subjected to a two-stage purification procedure via CuO and Ti getters. Blanks for the extraction line and mass spectrometer were systematically determined and the mass discrimination factor was determined by airshots. About 25 mg of sample material was required for Ar analyses. The error for Ar analyses is below 0.40% and the ^{40}Ar/^{36}Ar value for airshots averaged 295.82±0.36 (n=3) (Table H1). The K–Ar ages were calculated using ^{40}K abundance and decay constants recommended by *Steiger, R_H, and Emilie Jäger. "Subcommission on geochronology: convention on the use of decay constants in geo-and cosmochronology." Earth and planetary science letters 36.3 (1977): 359-362.*

Table H1 – K-Ar dating results and standard data

Sample [<2 µm]	K(%)	Rad. ^{40}Ar (mol/g)	Rad. ^{40}Ar (%)	Age (Ma)	Error (Ma)
EAG12014	4.67	1.9870E-09	94.1	230.0	4.6
EAG12032	4.86	2.0207E-09	95.1	225.1	4.6
EAG12046	3.86	1.8883E-09	93.7	262.1	5.4
EAG12047	4.38	1.9050E-09	93.4	234.8	4.9
EAG12051	3.07	1.3789E-09	94.8	242.0	5.1
EAG12055	5.24	2.0088E-09	92.0	208.5	4.4

Argon standard data

Sample ID	K [%]	Rad. 40Ar [mol/g]	Rad. 40Ar [%]	Age [Ma]	Error [Ma]	Remark [%] *
HD-B1-112	7.96	3.3820E-10	93.69	24.34	0.39	+ 0.54%
HD-B1-113	7.96	3.3357E-10	92.38	24.01	0.36	- 0.83%
HD-B1-122	7.96	3.3607E-10	92.17	24.19	0.38	- 0.08%
HD-B1-123	7.96	3.3590E-10	92.07	24.18	0.37	- 0.12%

Airshot data

Airshot ID	40Ar/36Ar	+/-
AS108-AirS-1	297.59	0.51
AS109-AirS-1	294.57	0.27
AS119-AirS-1	296.36	0.34
AS119-AirS-2	294.76	0.30